

Electron Spectroscopy: Theory, Techniques and Applications

Volume 2

Edited by

C. R. Brundle

*IBM Research
5600 Cottle Road
San Jose
California 95193, U.S.A.*

and

A. D. Baker

*Queens College
The City University of New York
Kissena Boulevard
Flushing, New York 11367, U.S.A.*

1978



Academic Press

London · New York · San Francisco

A Subsidiary of Harcourt Brace Jovanovich, Publishers

Contents

Contributors to Volume 2	v
Preface	vii

1. Basic Concepts of X-ray Photoelectron Spectroscopy

C. S. Fadley

I. Introduction	2
II. Experimental Considerations	7
III. The Photoemission Process	23
IV. Core Electron Binding Energy Shifts	75
V. Final-state Effects	94
VI. Angular-resolved Measurements on Solids	124
VII. Concluding Remarks	142
References	145

2. The Photoionization of Atoms: Cross-sections and Photoelectron Angular Distributions

S. T. Manson and D. Dill

I. Introduction	158
II. General Theory of Photoionization Cross-sections and Photo- electron Angular Distributions	159
III. Accurate Calculations of Photoionization Cross-sections and Angular Distributions	172
IV. Hartree-Fock Calculations	182

Basic Concepts of X-ray Photoelectron Spectroscopy

C. S. FADLEY*

Department of Chemistry, University of Hawaii, Honolulu, Hawaii 96822

	<i>Page</i>
I. Introduction	2
II. Experimental Considerations	7
A. Radiation Sources	7
B. Specimen Preparation	11
C. Electron Energy Analysis	17
D. Detection and Control	21
E. Data Analysis	22
III. The Photoemission Process	23
A. Wave Functions, Total Energies, and Binding Energies	23
B. The Hartree-Fock Method and Koopmans' Theorem	29
C. More Accurate Wavefunctions via Configuration Interaction	38
D. Transition Probabilities and Photoelectric Cross-sections	39
E. Inelastic Scattering in Solids	65
F. Photoelectron Peak Intensities	69
IV. Core Electron Binding Energy Shifts	75
V. Final-state Effects	94
A. Introduction	94
B. Relaxation Effects	95
C. Multiplet Splittings	98
D. Multi-electron Excitations	110
E. Vibrational Effects	121
VI. Angular-resolved Measurements on Solids	124
A. Introduction	124
B. Surface Sensitivity Enhancement at Grazing Electron Exit Angles	125
C. Surface Sensitivity Enhancement at Grazing X-ray Incidence Angles	131
D. Single-crystal Effects	132
VII. Concluding Remarks	142
Acknowledgements	144
References	145

* Alfred P. Sloan Foundation Research Fellow.

I. INTRODUCTION

X-ray photoelectron spectroscopy has by now become a widely-used technique for studying the properties of atoms, molecules, solids, and surfaces. The extent of development between the first experiments of this type by Robinson and Rawlinson in 1914¹ and the present state of the art is indeed great, with most of this growth occurring within the last 10–20 years under the stimulation of pioneering studies begun in the early 1950s,^{2, 3} particularly those carried out at Uppsala University.³ From the first observations that core photoelectron peak intensities could be used for quantitative analysis by Steinhardt and co-workers² and that core electron binding energies exhibited chemically-induced shifts by Siegbahn and co-workers,³ the number of distinct physical and chemical effects noted has expanded considerably. Thus, together with numerous developments in interpretive theory, this expansion has provided a rich panoply of information that can be derived by analysing different aspects of an x-ray photoelectron spectrum. To be sure, a greater understanding of the theoretical models underlying these phenomena has not always led to results as directly interpretable in simple chemical or physical terms as was initially imagined, but the overall scope of information derivable is nonetheless large enough to be useful in a broad range of disciplines.

The number of publications involving x-ray photoelectron spectroscopy (which is commonly referred to by one of the two acronyms *XPS* or *ESCA* ≡ electron spectroscopy for chemical analysis) is thus by now quite large, and includes several prior reviews^{3, 4–10} and conference proceedings,^{11, 12} as well as other chapters in this series on specific problems or areas of application.^{13, 14} Thus, no comprehensive review of the literature will be attempted here, but rather only a concise discussion of various basic experimental and theoretical concepts, together with selected examples exhibiting different effects. In certain more newly developed areas, or for subjects in which confusion seems to exist in the literature, a somewhat more detailed treatment will be made. The instrumentation and experimental data discussed will be primarily restricted to that involving exciting radiation produced in a standard type of x-ray tube, thus providing an operational definition of XPS. Thus, photon energies of $\gtrsim 100$ eV will be considered, with principal emphasis on the most common 1.2–1.5 keV range. The more recently initiated photoemission studies utilizing synchrotron radiation¹⁵ will thus not be included. The theoretical models discussed may, on the other hand, often apply directly to photoelectron emission experiments performed at lower photon energies as, for example, in conventional ultraviolet photoelectron spectroscopy (UPS) for which $h\nu$ is typically in the 5–40 eV range or in synchrotron studies. Alternatively, the models utilized in XPS may represent some particular

limit that cannot be used at lower energies. Thus, at several points, comparisons between low-energy- and high-energy-photoemission experiments will be made.

The fundamental experiment in photoelectron spectroscopy involves exposing the specimen to be studied to a flux of nearly monoenergetic radiation with mean energy $h\nu$, and then observing the resultant emission of photoelectrons, whose kinetic energies will be described most simply by the photoelectric equation:

$$h\nu = E_b^V(k) + E_{kin} \quad (1)$$

in which $E_b^V(k)$ is the binding energy or ionization potential of the k th level as referred to the vacuum level and E_{kin} is the photoelectron kinetic energy. (A more exact definition of binding energy, including a discussion of reference levels, is presented in Section II.B.3.) In general, both Auger electrons and secondary electrons (usually resulting from inelastic scattering processes) will also be emitted from the specimen, but it is generally possible to distinguish these electrons from true photoelectrons by methods to be discussed later in this section. There are three fundamental properties characterizing each emitted photoelectron: its kinetic energy, its directions of emission with respect to the specimen and the exciting radiation, and, for certain rather specialized experimental situations, the orientation of its spin. These three properties thus give rise to three basic types of measurements that are possible on the emitted electron flux.

(1) *The number distribution of photoelectrons with kinetic energy.* This measurement produces an electron spectrum or energy distribution curve (EDC) and, of course, requires some sort of electron energy analyser or spectrometer, of which several types are currently being utilized. In the dispersive spectrometers most commonly used in XPS, electron spectra are usually measured at fixed angles of electron emission (or over a small range of emission angles) relative to both the photon source and the specimen.

(2) *The distribution of photoelectron intensity with angle of emission.* Such angular-resolved measurements can be made relative to the photon propagation direction or to axes fixed with respect to the specimen. Generally, these measurements require kinetic energy distribution determinations at each of several angles of emission.

(3) *The spin polarization or spin distribution of the photoelectron intensity.* These measurements require a specimen that has somehow been magnetically polarized, usually by an external field, so that more photoelectrons may be emitted with one of the two possible spin orientations than with the other. Then the relative numbers of spin-up and spin-down photoelectrons are measured.¹⁶ Such spin polarization measurements have so far only been

made with ultraviolet radiation for excitation, and they will not be discussed further here.

The additional time and experimental complexity required for angular distribution or spin polarization measurements have resulted in the fact that most XPS studies up to the present time have involved only kinetic energy distributions with a fixed geometry of the photon source, specimen, and spectrometer. However, measurements of both types (2) and (3) seem fruitful from several points of view, and angular-resolved XPS studies in particular have grown in importance in recent years.¹⁷

As an illustration of certain typical features observed in fixed-angle XPS spectra, Fig. 1 shows data obtained from an aluminum specimen exposed to monochromatized x-rays of 1487 eV energy. In Fig. 1(a), a broad-scan spectrum of 1000 eV width is displayed, and various prominent photoelectron peaks are labelled according to their level of origin from O1s to valence. The oxygen KLL Auger structure is also partially visible at the low-kinetic-energy end of the spectrum. The oxygen peaks arise from oxygen atoms present in a surface oxide layer; the C1s peak is due to an outermost surface layer of contaminants containing carbon. As is usually the case, the photoelectron peaks are considerably narrower and simpler in structure than the Auger peaks. Each electron peak exhibits to one degree or another an approximately constant background on its low-kinetic-energy side that is due to inelastic scattering; that is, electrons arising via the primary photoemission or Auger process that produces the sharp "no-loss" peak have been inelastically scattered in escaping from the specimen so as to appear in an "inelastic tail" or energy-loss spectrum.¹⁸ Depending upon the types of excitation possible within the specimen, the inelastic tails may exhibit pronounced structure also, as is evident in the multiple peaks formed below the Al2s and Al2p no-loss features (which are due to the excitation of collective valence electron oscillations or plasmons¹⁹ in aluminium metal), as well as the single broad peak in the O1s inelastic tail (which is due to one-electron excitations from the occupied to the unoccupied valence levels of aluminum oxide). The inelastic tail below C1s is considerably weaker due to the relatively thin layer of carbon-containing species present (approximately two atomic layers); thus, for this sample, C1s photoelectrons could escape with a relatively low probability of being inelastically scattered.

In Fig. 1(b), an expansion of the low-kinetic-energy region of the same aluminum spectrum is shown, and several other features are more clearly discernible. The plasmon loss structure is well resolved, and peaks associated with the excitation of up to four plasmons are seen. A magnified view of the rather low-intensity valence photoelectron region also shows complex spectral structure associated primarily with the overlapping metal- and oxide-valence levels. In general, XPS valence photoelectron intensities are approximately

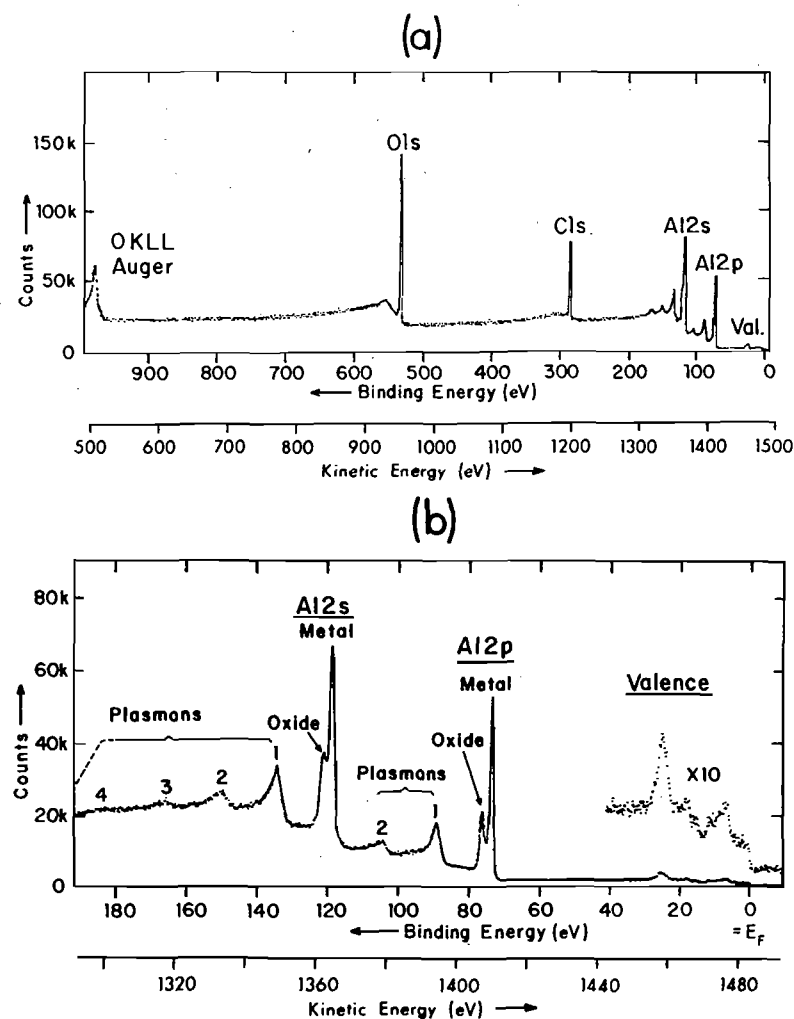


Fig. 1. Typical XPS spectra obtained from an oxidized aluminium specimen with a carbonaceous contaminant overlayer. Monochromatized AlK α radiation was used for excitation. (a) Overall spectrum with all major no-loss features labelled. (b) Expanded-scale spectrum of the Al2s, Al2p, and valence regions. Chemically-shifted oxide- and metal-core peaks are indicated, as well as inelastic loss peaks due to bulk plasmon creation.

an order of magnitude lower than those of the most intense core levels in a given specimen, but they are nonetheless high enough to be accurately measured and studied by using longer data acquisition times to improve statistics. An additional and chemically very significant feature in Fig. 1(b) is the splitting of the Al2s and Al2p photoelectron peaks into two components,

one associated with oxide and one associated with metal. This splitting or chemical shift is caused by the change in the aluminum chemical environment between oxide and metal.

In analysing XPS spectra, it is important to be able to distinguish as well as possible intensity resulting from Auger processes and inelastic scattering events. An Auger peak can be identified by: (1) comparing the observed peak energy with other experimental or theoretical Auger energies expected to be associated with the atom or atoms present, and (2) changing the photon energy by some amount $\Delta(h\nu)$ and then noting whether the peak shifts in kinetic energy by $\Delta(h\nu)$ according to Eq. (1) (and thus is a photoelectron peak) or remains fixed in kinetic energy (and thus has an Auger origin). Inelastic loss structure is often not as easily discernible in complex photoelectron spectra as for the examples shown in Fig. 1, but can be identified by: (1) looking for nearly identical features at kinetic energies below different no-loss peaks, as all high-energy electrons will be capable of the same excitations in inelastic scattering (although perhaps with probabilities that show a weak dependency on kinetic energy), and (2) comparing observed structure with independently-determined energy-loss spectra for the specimen material.¹⁸

A further very important point in connection with XPS studies of solid specimens is that the probability of inelastic scattering during escape from the sample is high enough that the mean depth of emission of no-loss electrons may be as small as a few atomic layers, and is never much larger than approximately 10 atomic layers.^{20, 21} Thus, any analysis based on these no-loss peaks is inherently providing information about a very thin layer near the specimen surface, and this is, for example, the reason why O1s and C1s peaks due to thin surface overlayers are readily apparent in Fig. 1. This surface sensitivity of XPS (or any form of electron spectroscopy) can be exploited for studying various aspects of surface physics and chemistry,²² but, on the other hand, must also be viewed as a potential source of error in trying to derive the true bulk properties of a given specimen.

In the following sections, various aspects of x-ray photoelectron spectroscopy are treated in more detail. In Section II, the instrumentation and experimental procedures required are reviewed. In Section III, the theoretical description of the photoemission process is discussed in detail so as to provide an accurate background for the consideration of various specific effects or areas of application; the use of XPS for the study of valence levels in molecules and solids is also considered. Section IV discusses chemical shifts of core-electron binding energies and various models used for interpreting them. Several effects primarily related to complexities in the final state of photoemission (namely relaxation phenomena, multiplet splittings, various many-electron interactions, and vibrational broadenings) are considered in Section V. In Section VI, various aspects of angular distribution measurements on

solids are considered. Finally, Section VII summarizes the present state of the technique and points out certain likely areas for future development.

II. EXPERIMENTAL CONSIDERATIONS

The basic components necessary for performing an XPS experiment consist of a radiation source for excitation, the specimen to be studied, an electron energy analyser, and some form of detection and control system. Each of these four distinct aspects of the experimental system is considered below. There are by now several commercial sources for complete XPS spectrometer systems²³⁻³⁰ which represent various design approaches to each of these components.

A. Radiation Sources

The standard x-ray tube consists of a heated-filament cathode from which electrons are accelerated toward a suitable solid anode (usually water-cooled) over a potential of the order of 5–20 kV. Holes formed in the inner levels of the anode atoms by electron bombardment are then radiatively filled by transitions from higher-lying levels, with the resultant emission of x-rays. A thin, x-ray-transmitting window separates the excitation region from the specimen in most tubes. In general, more than one relatively sharp x-ray line will be emitted by any anode material, and the energy widths associated with various lines can also vary considerably from line to line or from element to element.³¹ An additional source of radiation from such a tube is a continuous background of bremsstrahlung.³¹ The choice of an anode material and operating conditions is thus made so as to achieve the closest possible approximation to a single, intense, monochromatic x-ray line. Various design geometries for such x-ray tubes are discussed in the literature,^{3, 4, 31-36} with one obvious choice being whether to hold the anode or cathode at ground potential.

The anode materials most commonly utilized in XPS studies are Mg and Al, and, to a much lesser degree, Na and Si. Each of the members of this sequential series of second-row atoms gives rise to an x-ray spectrum that is dominated by a very intense, unresolved, $K\alpha_1$ - $K\alpha_2$ doublet resulting from transitions of the type $2p_{3/2} \rightarrow 1s$ and $2p_{1/2} \rightarrow 1s$, respectively. The first demonstrations that such low-Z anodes could be utilized in XPS studies were by Henke.³² These were followed approximately five years later by higher resolution applications by Siegbahn and co-workers.³ The mean energies of the x-rays produced in such sources are: $\text{Na}K\alpha_{1,2}$ —1041.0 eV,³⁵ $\text{Mg}K\alpha_{1,2}$ —1253.6 eV,³⁷ $\text{Al}K\alpha_{1,2}$ —1486.6 eV³⁸ and $\text{Si}K\alpha_{1,2}$ —1739.5 eV.³⁹ At these x-ray energies, aluminium or beryllium windows of 10–30 μm thickness are sufficiently transmitting for use in separating the tube and specimen region. Additional x-ray lines are also produced in such tubes, as indicated in Fig. 2

for a magnesium anode³⁷ (note the logarithmic scale). These consist of satellites arising from $2p \rightarrow 1s$ transitions in atoms that are doubly-ionized (KL in Fig. 2), triply-ionized (KL^2), etc., and are denoted variously as $K\alpha'$, $K\alpha_3$, $K\alpha_4$, ..., $K\alpha_{14}$. $K\alpha_3$ and $K\alpha_4$ are by far the most intense, and, in Mg and Al, they occur at about 10 eV above the $K\alpha_{1,2}$ peak and with intensities of approximately 8% and 4% of $K\alpha_{1,2}$, respectively. Photoelectron spectra obtained with non-monochromatized sources of this type thus always exhibit a characteristic double peak at kinetic energies ~ 10 eV above the strong

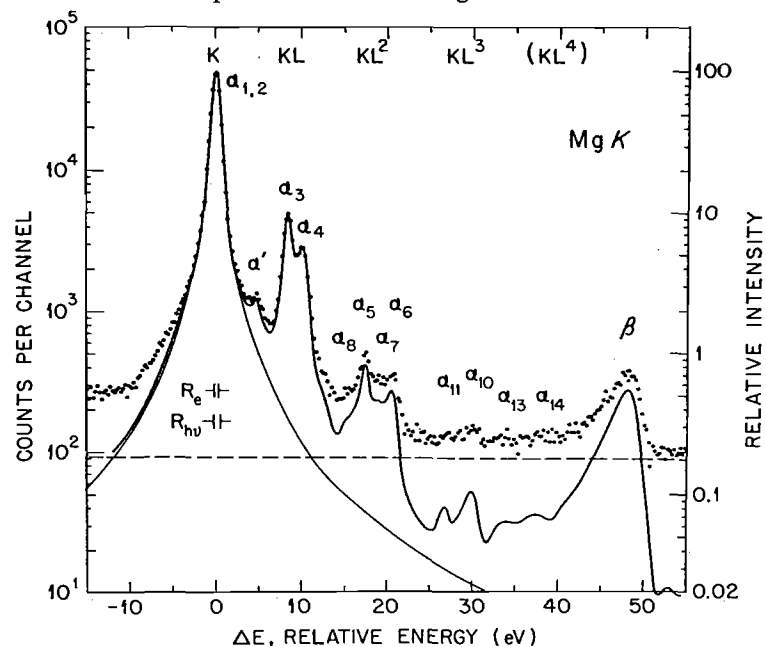


Fig. 2. The K x-ray emission spectrum of Mg metal as emitted by a non-monochromatized x-ray source. The peaks indicated $\alpha_{1,2}$, ..., β correspond to various transitions into the $K=1s$ subshell. The dashed line is an average background and the solid line is the net spectrum. Note the logarithmic intensity scale. The notation K corresponds to a single initial $1s$ hole, KL to initial holes in both $1s$ and $2s$ or $2p$, KL^2 to a single initial hole in $1s$ and two initial holes in $2s$, $2p$, etc. (From Krause and Ferreira, ref. 37.)

$K\alpha_{1,2}$ peaks. The $K\alpha'$, $K\alpha_5$, ..., $K\alpha_{14}$ satellites are $\lesssim 1\%$ of $K\alpha_{1,2}$ in magnitude, and so, for most applications, can be neglected. An additional band of $K\beta$ x-rays arises at energies approximately 45–50 eV above $K\alpha_{1,2}$ and is the result of valence $\rightarrow 1s$ transitions; the $K\beta$ intensity is approximately 1% of $K\alpha_{1,2}$ for Mg and Al.³⁷ Thus, to a first approximation, the x-ray spectrum consists only of the very intense $K\alpha_{1,2}$ x-ray and most work has been based solely on an analysis of $K\alpha_{1,2}$ -produced photoelectron peaks. However, in any study involving weak photoelectron peaks, or peaks generated by $K\alpha_{1,2}$ which overlap with satellite-generated peaks due to other

electronic levels, the non-monochromatic character of the x-ray source must be taken into account. For such non-monochromatized x-ray sources, the primary limiter of instrumental resolution is thus the natural linewidth of the $K\alpha_{1,2}$ line. As judged by the full width at half maximum intensity (FWHM), this resolution limit is approximately 0.4 eV for $NaK\alpha_{1,2}$,³⁵ 0.7 eV for $MgK\alpha_{1,2}$,³⁵ 0.8 eV for $AlK\alpha_{1,2}$,³⁸ and 1.0–1.2 eV for $SiK\alpha_{1,2}$.³⁹ This width decreases with decreasing atomic number for two reasons: the $2p_{3/2}-2p_{1/2}$ spin-orbit splitting decreases and the $1s$ hole lifetime increases. Materials of lower atomic number are thus favoured for width, but Mg and Al are generally utilized because of their lower chemical reactivity and vapor pressure in comparison to Na, and thus their easier fabrication and use as anodes. Although neon is expected to yield a $K\alpha_{1,2}$ line at 848.6 eV of only $\sim 0.2-0.3$ eV width, no attempts at constructing such a source for use in XPS have as yet been successful. The use of $K\alpha_{1,2}$ x-rays of F in highly ionic compounds have been used recently in XPS.⁴⁰

The monochromatization of such $K\alpha_{1,2}$ x-rays by Bragg reflection from a suitable single crystal has also been utilized to achieve narrower excitation sources, as well as to eliminate satellite lines and bremsstrahlung radiation.^{3, 23, 25, 41, 42} Although the intensity loss in such reflections is considerable, photoelectron peaks as narrow as 0.4 eV have been observed with monochromatized $AlK\alpha$ excitation;^{25, 41, 42} this width is to be compared to the $\gtrsim 0.9$ eV typically found without monochromatization. To compensate for the loss in intensity due to monochromatization, various procedures have been utilized, including the use of very high-intensity x-ray tubes involving rotating anodes,⁴¹ monochromator systems with more than one crystal,^{25, 41} multichannel detection systems,^{25, 41} and dispersion-compensating x-ray- and electron-optics.^{3, 25} In dispersion compensation, all photon energies within the $K\alpha_{1,2}$ linewidth are spatially dispersed by Bragg reflection and utilized for photoelectron excitation, but their line-broadening influence is nullified by the action of the dispersive electron energy analyzer; the commercial Hewlett-Packard system based upon this mode of operation yields optimum photoelectron peak widths with $AlK\alpha_{1,2}$ of ~ 0.5 eV FWHM.²⁵

An additional type of ultra-soft x-ray transition that has been utilized successfully in XPS studies is the $M\zeta$ transition ($4p_{3/2} \rightarrow 3d_{3/2}$) in the sequential elements Y to Mo. The use of such x-rays in XPS was first suggested by Krause,³⁴ who pointed out that they yield sufficiently intense and monochromatic sources in the very interesting energy range of $100 \lesssim h\nu \lesssim 200$ eV, even though various satellite x-rays are present. The most narrow and thus

most used lines of this type are those for Y ($h\nu=132.3$ eV, FWHM=0.5 eV) and Zr ($h\nu=151.4$ eV, FWHM=0.8 eV), and they have been successfully applied to studies of both valence levels and outer core levels.³⁴⁻³⁶ The ultra-soft character of these x-rays and their resultant decreased ability to penetrate through matter, as well as the significant sensitivity of their linewidths to surface chemical alterations of the anode surface, lead to several special features of tube design. Thin polymeric windows must be used. Relatively high excitation voltages as compared to $h\nu$ of $\sim 4-6$ kV are also beneficial to maximize the intensity originating in the metallic anode interior (as distinct from its oxidized exterior).³⁵ And, in the highest resolution designs, a continuous deposition of fresh anode material is provided during operation.^{34, 36}

A final rather new development in x-ray sources by Hovland⁴³ that deserves mention here leads to what has been termed *scanning* XPS. A thin layer of specimen material is directly deposited on one side of a thin Al foil (~ 6 μm thick). A high-resolution scanning electron beam is directed at the other side of this foil, so that, at any given time, $\text{AlK}\alpha$ x-rays are produced over only a very small spot with dimensions comparable to the beam diameter. These x-rays readily pass through the thin foil and specimen, exciting photoelectrons from a corresponding spot near the specimen surface. Lateral spatial resolutions of as low as 20 μm have so far been achieved, and a number of potential applications for such scanning XPS measurements exist.⁴³ The only significant limitation is that it must be possible to prepare sufficiently thin specimens ($\sim 1000-10,000$ \AA) that x-ray attenuation in penetrating to the surface is not appreciable.

The x-ray sources discussed up to this point thus permit high-resolution measurements to be carried out in the two approximate photon-energy ranges 100-200 eV and 1000-2000 eV, with a relatively little explored region from $\sim 200-1000$ eV separating them. Another source of radiation in the photon energy region from 100 to 2000 eV of principal interest here is the so-called synchrotron radiation that is emitted in copious quantities by centripetally-accelerated electrons moving with highly relativistic velocities.^{15, 44} This continuous spectrum of radiation is sufficiently intense to permit selection of a narrow range on the order of tenths of eV or lower with a suitable monochromator (usually a grating) while still maintaining fluxes adequate for photoemission studies. A number of excellent photoemission studies have by now been performed using such radiation,¹⁵ although these have so far been restricted to photon energies between approximately 10 and 350 eV, principally because of the difficulty of achieving adequate monochromatization without severe intensity loss for soft x-rays of ≥ 350 eV. Such radiation has the advantages of being both continuously variable in energy, as well as linearly polarized to a high degree;⁴⁴ thus, the exploration of phenomena dependent upon photon energy and/or polarization are much more easily

studied than with more standard ultraviolet or soft x-ray sources. By contrast the soft x-ray tubes discussed previously emit radiation that is randomly polarized to a very good approximation.

B. Specimen Preparation

1. *Introduction.* X-ray photoelectron spectra have been obtained from specimens present as gases, solids, or liquids. The preparation and handling of any specimen requires considering two important factors: (1) In order to avoid excessive inelastic scattering during photoelectron traversal through the energy analyzer, pressures between the specimen and the detector must be maintained at $\lesssim 10^{-4}$ torr. This limit is easily estimated by considering a typical path length during analysis of 100 cm, and requiring that the total number of atoms/molecules encountered along this path be no greater than the analogous number encountered along the mean no-loss distance of emission from a typical solid specimen of ~ 20 \AA . (2) As the emission of photoelectrons, Auger electrons, and secondary electrons from any specimen constitutes a net loss of negative charge, it is also necessary to minimize or in some other way correct for the possible occurrence of a significant positive potential build-up in the emitting region. One way in which this is accomplished to some degree in any system is by the flux of similar electrons emitted *toward* the specimen by various portions of the specimen chamber and holder which are also in general exposed to exciting x-rays and/or electrons, although this can in fact lead to the opposite problem: a negative potential build-up.⁴⁵ The charging potential V_c produced by any net imbalance between charge input and output may vary throughout the specimen volume and in effect cause a range of energy level shifts from the values corresponding to the limiting situation in which no charging occurs. Thus, if \mathbf{r} is the spatial coordinate of the emission point within the specimen, and $E_b^V(k)^0$ and E_{k1n}^0 are the binding energy and kinetic energy expected for emission from level k in the absence of charging, the photoelectric equation [Eq. (1)] can be rewritten as

$$\begin{aligned} h\nu &= E_b^V(k, \mathbf{r}) + E_{k1n}(\mathbf{r}) \\ &= E_b^V(k)^0 + E_{k1n}(\mathbf{r}) + V_c(\mathbf{r}) \end{aligned} \quad (2)$$

Thus, if $V_c(\mathbf{r})$ is significant with respect to the typical instrumental resolution of ~ 0.1 eV (which it indeed can be in certain cases^{4, 45}), the measured binding energies $E_b^V(k, \mathbf{r})$ will in general be different from $E_b^V(k)^0$, and peak broadening also may occur. To minimize or correct for such effects, studies of peak position versus x-ray flux can be made,^{45, 46} and a variable external source of electrons can be provided.²⁵ For gaseous specimens, the pressure can also be varied.⁴ For solids, it is also customary to connect the specimen electrically to the specimen chamber as well as possible. Also, the presence

of a certain reference atom (for example, gold or carbon) on the surface of the specimen can be used to correct for charging,⁴⁷ although this procedure is often not completely unambiguous. A method recently developed by Grunthaner⁴⁸ involves floating a solid specimen at a variable negative potential and noting that potential at which an external source of monoenergetic electrons just begins to reach the surface; although not widely used as yet, this method seems to provide a very direct way of measuring surface potential distributions and thus correcting for them.

2. *Gaseous Specimens.* The basic requirement for gas-phase studies is a chamber to contain the gas with an x-ray-transparent window separating it from the x-ray source and a small opening or slit to permit photoelectron exit into the energy analyzer.^{4, 33, 47, 49-51} Typical gas pressures required in the chamber are from 10^{-2} to 1 torr, and therefore some form of differential pumping is generally necessary between the exit slit and the analyzer in order to minimize gas-phase inelastic scattering effects,⁴ as discussed previously. Typical specimen volumes are of the order of 1 cm^3 . The first gas-phase XPS studies were performed by Krause and Carlson,⁴⁹ followed shortly thereafter by the more extended investigations of Siegbahn *et al.*⁴ The gas in the chamber can be provided by a room-temperature gas-phase source, or can be the result of heating liquid-⁴ or solid-³³ phase reservoirs. With such devices, metals and other vaporizable solids can be studied by photoelectron spectroscopy in the gas phase.^{33, 50} In certain studies, rather significant changes in peak positions and relative intensities due to the combined effects of charging and kinetic energy-dependent inelastic scattering have been noted,⁴ but, in general, these are relatively small, especially at lower pressures.

For gas-phase spectra, the vacuum level is the naturally-occurring reference level, so that Eqs (1) and (2) are directly related to measurable quantities.

3. *Solid Specimens.* There are various methods of preparing solid specimens suitable for study by XPS. Typical specimen areas are $\sim 1 \text{ cm}^2$ or smaller, and, because inelastic scattering effects limit the no-loss emission to a mean depth of only 10–80 Å below the surface (as discussed in more detail in Section III.E), this corresponds to an active specimen volume of only approximately 10^{-6} cm^3 . Thus, total masses of only 1–10 μg are involved, and amounts of material on the order of 10^{-9} g can be detected under certain circumstances. Any change of the chemical composition in the first few atomic layers near the surface can thus also have a significant influence on results.

Machineable solids can simply be cut, cleaved, and/or polished into shapes suitable for mounting in the specimen position. For materials that can be prepared as fine powders at room temperature, specimens can also be prepared by pressing the powder into a uniform pellet (perhaps supported by an imbedded conducting-wire mesh) or by dusting the powder onto an adhesive backing such as that provided by double-sided tape (although this procedure

has the rather undesirable characteristics of limiting temperature excursions and providing a steady source of surface-contaminating carbonaceous volatiles). In order to minimize atmospheric contamination or alteration of specimens, final preparation in an inert-atmosphere glove box or bag, perhaps attached to the specimen chamber, can be useful. Elements and certain compounds can also be heated *in situ* and vapor-deposited on a supporting substrate to form specimens. Alternatively, dissolved materials can be deposited from solution on a substrate, either by evaporating off the solvent or by selectively electroplating out various components.⁵² Materials that normally exist as liquids or gases can also be condensed onto suitably cooled substrates for study in the solid state.⁴ A broad range of specimen temperatures has by now been investigated, ranging from near that of liquid helium (4 K)⁵³ to several thousand degrees Kelvin.⁵⁴

The extreme surface sensitivity of XPS also leads in many applications to the requirement that the specimen region be held at pressures of $\lesssim 10^{-9}$ torr in order to permit adequate control of surface composition. For example, for O_2 at 10^{-9} torr and 25°C , the gas-phase collision rate with a surface will be such that, if each molecule striking the surface remains there (corresponding to a sticking coefficient of 1.0), a full atomic layer will be deposited in approximately 50 min.⁵⁵ This minimum monolayer coverage time varies inversely with pressure, so that pressures of the order of 10^{-10} torr are necessary to insure the maintenance of a highly reactive surface in a clean state over the period of time of several hours usually required for a series of XPS measurements. In preparing such surfaces, *in situ* cleaning by vapor deposition, cleaving, scraping, or inert-gas ion bombardment is thus often used.⁵⁵

For the case of solid specimens, an electrical connection is made to the spectrometer in an attempt to minimize charging effects and maintain a well-defined and fixed potential during photoemission. For the simplest possible case of a metallic specimen in a metallic spectrometer, the energy levels and kinetic energies which result are as shown in Fig. 3. Thermodynamic equilibrium between specimen and spectrometer requires that their electron chemical potentials or Fermi levels be equal as shown. In a metal at absolute zero, the Fermi level E_F has the interpretation of being the highest occupied level, as indicated in the figure; this interpretation of E_F is also very nearly true for metals at normal experimental temperatures. For semiconductors and insulators, however, it is not so simple to locate the Fermi level, which lies somewhere between the filled valence bands and the empty conduction bands. The work function ϕ_s for a solid is defined to be the energy separation between the vacuum level and the Fermi level. When connected as shown in Fig. 3, the respective vacuum levels for specimen and spectrometer need not be equal, however, so that in passing from the surface of the specimen into the spectrometer, an electron will feel an accelerating or retarding potential

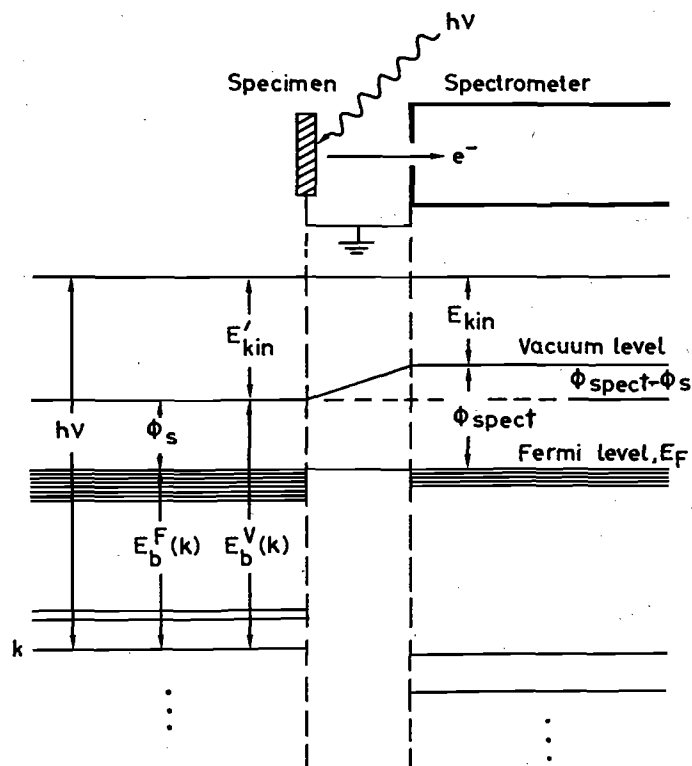


Fig. 3. Energy level diagram for a metallic specimen in electrical equilibrium with an electron spectrometer. The closely spaced levels near the Fermi level E_F represent the filled portions of the valence bands in specimen and spectrometer. The deeper levels are core levels. An analogous diagram also applies to semi-conducting or insulating specimens, with the only difference being that E_F lies somewhere between the filled valence bands and the empty conduction bands above.

equal to $\phi_s - \phi_{\text{spect}}$, where ϕ_s is the specimen work function and ϕ_{spect} is the spectrometer work function. Thus, an initial kinetic energy E_{kin}' at the surface of the specimen becomes E_{kin} inside the spectrometer, and

$$E_{\text{kin}} = E_{\text{kin}}' + \phi_s - \phi_{\text{spect}} \quad (3)$$

From Fig. 3 it is thus clear that binding energies in a metallic solid can be measured quite easily relative to the identical Fermi levels of specimen and spectrometer. The pertinent equation is

$$h\nu = E_b^F(k) + E_{\text{kin}} + \phi_{\text{spect}} \quad (4)$$

where the superscript F indicates a Fermi level reference. Provided that it is also possible to determine the specimen work function ϕ_s from some other

measurement, vacuum-referenced binding energies can then be obtained from

$$E_b^V(k) = E_b^F(k) + \phi_s \quad (5)$$

In fact, photoelectron spectra can be used to derive vacuum-referenced binding energies by measuring the position of the zero-kinetic-energy cut-off of the usually very intense secondary electron peak. Such a cut-off is shown in Fig. 4 in XPS data obtained for metallic Au by Baer.⁵⁶ This procedure for determining work functions has been used extensively in UPS studies,⁵⁷ but only in a more limited way in XPS^{56, 58} due to the greater range of

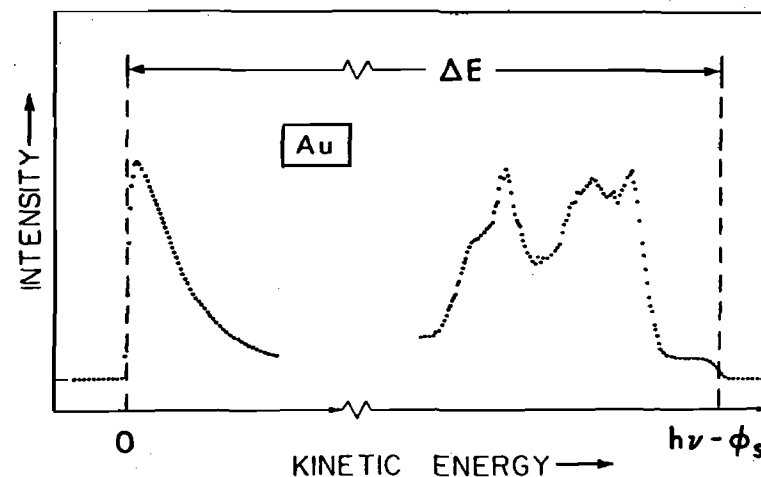


Fig. 4. Full XPS spectral scan for a polycrystalline Au specimen, showing both the cut-off of the secondary electron peak at zero kinetic energy and the high-energy cut-off for emission from levels at the metal Fermi level. The measurable distance ΔE thus equals $h\nu - \phi_s$, provided that suitable specimen biasing has been utilized. For this case, $h\nu$ was 1253.6 eV and ϕ_s was 5.1 eV. (From Baer, ref. 56.)

energies involved. In the simplest situation, both specimen and spectrometer are metallic and the energy diagram of Fig. 3 applies. All electrons emitted from the specimen are thus accelerated or decelerated by the same work function difference or contact potential $\phi_s - \phi_{\text{spect}}$ before analysis. With no voltage bias between specimen and spectrometer, the zero-energy cut-off corresponds to electrons propagating in final states exactly at the spectrometer vacuum level. For the implicit decelerating sign of $\phi_s - \phi_{\text{spect}}$ shown in Fig. 3, electrons propagating in final states at the specimen vacuum level are thus not observed. However, if the specimen is biased negatively with respect to the spectrometer by an amount greater than $\phi_s - \phi_{\text{spect}}$, then the low-energy cut-off does represent electrons at the specimen vacuum level or what can be defined as the true zero of kinetic energy. For the opposite accelerating sign of

$\phi_s - \phi_{\text{spect}}$, the true zero is observable and negative biasing is necessary only to insure that the cut-off is easily distinguishable against other sources of low-energy electrons.^{56, 58} The low-energy cut-off thus establishes the zero of kinetic energy, and a distance $h\nu$ above this on the measured spectral scale corresponds to the point at which excitation from states at the specimen vacuum level would occur. On the same scale, the high-kinetic-energy cut-off observable for metal specimens (also shown in Fig. 4) is caused by excitation from occupied states at the Fermi level, and the difference between these two positions is thus the specimen work function. That is, if the measured difference in kinetic energy between the two cut-offs is denoted by ΔE , then

$$\phi_s = h\nu - \Delta E \quad (6)$$

In more complex situations where semiconducting or insulating specimens are involved, initial states at E_F are not occupied so as to yield the same type of high-energy cut-off, although the low-energy cut-off can still be determined. The location of E_F in spectra can in this case be determined by using a reference metal specimen under the same biasing conditions, and assuming that electronic equilibrium is fully established between specimen, reference, and spectrometer. Possible charging effects make the latter assumption uncertain in many cases, however.

Whether it is determined from photoemission measurements or not, in general some additional information concerning ϕ_s is necessary to determine $E_b^V(k)$ for a solid specimen. Inasmuch as ϕ_s is also very sensitive to changes in surface composition, it is thus often Eq. (4) that is used in analyzing data for metals and other solid specimens. From this discussion, it is clear that Fermi-referenced binding energies are operationally very convenient for solid specimens, although they may not always be the most directly comparable to the results of theoretical calculations, in which the vacuum level often emerges as the natural reference.

4. *Liquid Specimens.* The requirement that pressures in the analyzer region be maintained at reasonably low levels of $\lesssim 10^{-4}$ torr means that measurements on common liquids with relatively high vapor pressures can be performed only with difficulty. However, Siegbahn and co-workers^{41, 59} have developed techniques for carrying out such studies; these involve a continuously-replenished liquid source in the form of either a free jet or a thin film carried on a translating wire, together with a high-speed differential pumping system between specimen chamber and analyzer. With such an apparatus, it has been possible to study relatively non-volatile liquids such as formamide (HOCNH_2), as well as solutions of the ionic solid KI dissolved in formamide. Certain liquid metals and other very low vapor pressure materials can, on the other hand, be studied with relatively little special equipment.⁶⁰

C. Electron Energy Analysis

1. *Brief Overview.* The various specific types of energy analyzers utilized in electron spectroscopy are discussed in detail in the literature,^{10, 61, 62} as well as in a special chapter in this series.⁶³ Thus, only certain salient features relevant to x-ray photoelectron studies will be reviewed here. In general, there are several criteria that an analyzer should satisfy: (1) A resolution capability of $\Delta E_{\text{kin}}/E_{\text{kin}} \approx 0.01\%$. This corresponds to 0.1 eV for 1000 eV electrons. Most XPS spectrometers presently operate in the 0.01–0.10% range. (2) The highest possible efficiency (sensitivity, intensity). That is, the highest possible fraction of electrons leaving the sample should be energy-analyzed and detected at the same time. (3) Unrestricted physical access to the sample and detector regions. This permits a wide variety of excitation sources, specimen geometries, and detector systems to be used.

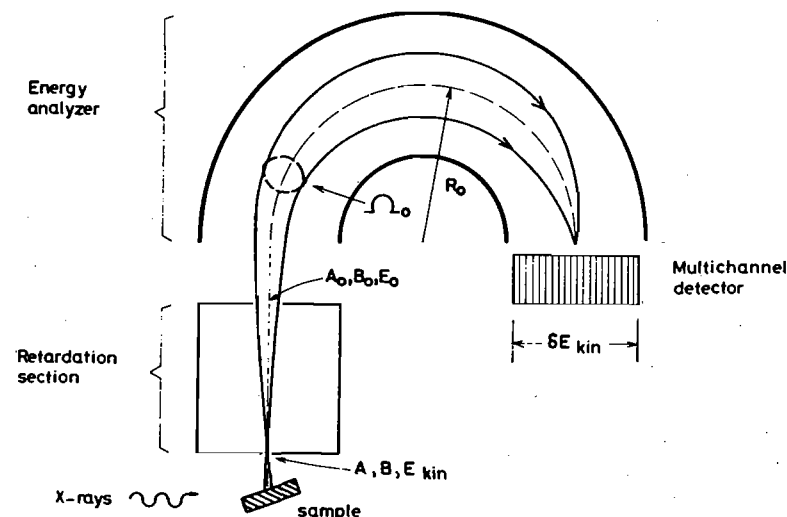


Fig. 5. Schematic illustration of an XPS spectrometer system indicating the primary components of radiation source, sample, electron energy analyser, and detector. For the specific example shown here, the energy analysis is accomplished by a pre-retardation section followed by a hemispherical electrostatic analyzer. A multichannel detector is also shown for generality.

(4) Ultra-high-vacuum capability for work on solid samples if surface composition is to be precisely controlled. (5) Ease of construction. One design philosophy often used for increasing the ease of construction is to insert a retardation section before the analyzer as shown schematically in Fig. 5, so that the energy of a given electron can be reduced from its initial value of E_{kin} to the final value at which it is analyzed of E_0 . For a given absolute resolution of ΔE_{kin} , the relative resolution required from the analyzer is thus

reduced from $\Delta E_{\text{kin}}/E_{\text{kin}}$ to $\Delta E_{\text{kin}}/E_0$, thereby permitting looser tolerances on many mechanical and electrical components. The net effects of such retardations on intensity may or may not be deleterious, however, and are discussed in more detail in the next section. (6) Relative insensitivity to external environment, particularly as regards the shielding of extraneous magnetic fields. The vast majority of spectrometers currently in use are based on interaction with electrostatic fields and for these, μ -metal shielding is generally used to exclude extraneous magnetic fields. Only for the relatively few magnetic spectrometers in use are Helmholtz-coil systems required for magnetic field cancellation.^{3, 4} Quantitative estimates of the degrees to which extraneous magnetic fields must be excluded for a given resolution have been calculated previously.⁶⁴ (7) If angular distribution studies are intended, well-defined, and perhaps also variable, angles of electron exit and x-ray incidence. This requirement generally acts counter to that for high efficiency, as it implies detecting only electrons emitted in a relatively small element of solid angle, thus reducing the total number that can be analyzed and detected.

With these constraints, there are several possible analyzer configurations,^{61, 62} but the three that have been most used in XPS are all of the spatially dispersive type, and consist of the hemispherical electrostatic (schematically shown in cross-section in Fig. 5),^{3, 61, 65} the cylindrical mirror electrostatic (CMA),^{61, 66-68} and the double-focussing magnetic with a $1/\sqrt{r}$ field form.^{3, 64, 69} In all of these analyzers, electrons are dispersed on the basis of kinetic energy along a radial or axial coordinate. For reasons of both ease of construction and magnetic shielding, the two electrostatic analyzers are much more common than the double-focussing magnetic, although a number of important early studies were performed on such instruments,^{3, 33} and a fully-optimized spectrometer based upon the $1/\sqrt{r}$ field form is presently under construction.^{64, 70} In addition to these dispersive analyzers, limited use has also been made in XPS of non-dispersive analyzers based upon the retarding grid principle.⁷¹⁻⁷³ Such analyzers are usually of relatively limited resolution ($\sim 1\%$), however, so that their use has been restricted to the obtaining of chemical composition information similar to that derived from Auger spectra. Such low-resolution Auger and XPS spectra can, in fact, be generated by using the spherical grids of a low-energy electron diffraction (LEED) system as a retarding grid analyzer. A further type of commercial analyzer developed specifically for XPS studies by the DuPont Corporation²⁴ is a hybrid with both dispersive and non-dispersive characteristics. Its first stage consists of an electrostatic deflection section that selects a band of energies in a dispersive mode; two subsequent retarding grid sections act as low-pass and high-pass filters with the net result that only a narrow band of energies is detected after the high-pass filter. A final type of XPS spectrometer with certain unique features is that formerly produced by

the Hewlett Packard Company,²⁵ which makes use of dispersion-compensating x-ray- and electron-optics.^{3, 74} In this system, an x-ray monochromator is matched to a retarding-lens/hemispherical-electrostatic-analyzer unit in such a way as to maximize intensity and minimize linewidths without the use of any slits in the x-ray optics; the detailed performance of this spectrometer has been analyzed recently.⁷⁴

2. *Spectrometer Efficiency and Retardation.* The resolution and efficiency of any spectrometer are of critical importance. These properties are highly dependent upon one another, since for operation at lower resolution (higher $\Delta E_{\text{kin}}/E_{\text{kin}}$), a higher fraction of electrons can usually be energy-analyzed and detected. For operation at a given resolution, the overall efficiency E of a dispersive analyzer can be written as proportional to the following product⁶⁴

$$E \propto BA\Omega \cdot \delta E_{\text{kin}} \quad (7a)$$

in which B is the brightness or intensity of the electron source for the energy analyzer in electrons per unit area and per unit solid angle, A is the area of the source, Ω is the solid angle over which electrons from the source are accepted into the energy analyzer and detected, and δE_{kin} is the range of electron energies or spectral width which can be analyzed at one time (as, for example, by a multi-channel detector). B , A , and Ω in general depend on E_{kin} for a given spectrometer. δE_{kin} will thus be proportional to N , the number of distinct energy channels simultaneously detected. If B and A vary over the area of the source, then a more correct statement of this efficiency involves an integration over the surface as

$$E \propto \int B\Omega \cdot dA \cdot \delta E_{\text{kin}} \quad (7b)$$

The effective electron source as seen by the analyzer is often defined by an aperture in front of the photoemitting sample, and, depending upon the system, B , A , and Ω may refer to this aperture or to the true specimen surface. If a multichannel detector is utilized, δE_{kin} may in principle be as large as 10% of E_{kin} ,^{25, 64} whereas the resolution ΔE_{kin} will be $\geq 0.01\%$ of E_{kin} . In this case, the detector would correspond to $\lesssim 1000$ channels. The notation used in this discussion is indicated in the schematic drawing of Fig. 5, where subscript zeros have been used on all quantities after a hypothetical retarding section. Such a retarding section may or may not be present, according to the specific system under consideration.

Helmer and Weichert⁷⁵ first pointed out that, for the general class of dispersive analyzers used in XPS, it is possible to retard before analysis, and, for a given absolute resolution ΔE_{kin} , to gain in overall efficiency in a system with single-channel detection (for which $\delta E_{\text{kin}} \approx \Delta E_{\text{kin}}$ and $N=1$), and this result has proven useful in several specific spectrometer designs.^{23, 25, 27, 28, 30}

Their analysis (which has also been extended to apply to systems with multi-channel detection by Hagström and Fadley⁶) compares the operation of a given dispersive analyzer with and without retardation for a fixed resolution ΔE_{kin} , and with a primary electron source of fixed brightness B (cf. Fig. 5). It also requires that the source area A_0 and solid angle Ω_0 utilized at the analyzer entrance (and thus perhaps after the retardation section) be adjusted to the maximum values consistent with a resolution of ΔE_{kin} in either mode of operation *and* that the primary source (for example, a first entrance aperture) be capable of supplying electrons over sufficient area and solid angle to fill or illuminate both A_0 and Ω_0 with electrons. There are then two factors to be considered: (1) *The loss of brightness with retardation.* This loss of brightness has been derived for a few geometries involving a source and a *non-absorbing* retardation (or acceleration) section. If θ is defined to be the angle between the electron emission direction and a planar source surface, these geometries include a source emitting with a $\sin \theta$ intensity distribution into an arbitrary point-to-point imaging lens system,⁷⁶ and a source with either a $\sin \theta$ ⁷⁷ or an isotropic⁷⁵ intensity distribution emitting into a uniform retarding field perpendicular to its surface. These derivations, which often (but not always) make use of the Abbe sine law^{75, 76} or its paraxial-ray approximation the Langrange-Helmholtz relation,^{3, 76} result in a simple brightness variation of the form:

$$B_0 = B \left(\frac{E_0}{E_{\text{kin}}} \right) \quad (8)$$

in which B_0 and E_0 are the brightness and kinetic energy after retardation. The cases for which this relationship has been shown to hold thus represent limits that are relatively easily achieved experimentally. Without retardation, the efficiency of a spectrometer conforming to this brightness law and possessing only a single channel of detection will be

$$E \propto BA\Omega \quad (9)$$

whereas with retardation it will be

$$E' \propto B_0 A_0 \Omega_0 \quad (10)$$

or, from Eq. (8),

$$E' \propto B \left(\frac{E_0}{E_{\text{kin}}} \right) A_0 \Omega_0 \quad (11)$$

(2) *The gain in efficiency associated with the increase of A_0 and Ω_0 relative to A and Ω permitted by the decrease in relative resolution from $(\Delta E_{\text{kin}}/E_{\text{kin}})$ to $(\Delta E_{\text{kin}}/E_0)$.* As a specific example, consider the hemispherical electrostatic analyzer, which is shown in Fig. 5. Its resolution is controlled by the radial source width s , the axial (out-of-plane) source height h , the radial detector

width d , the radial angle of emission α_r , the axial (out-of-plane) angle of emission α_z , and the optic circle radius R_0 , according to^{3, 61}

$$\frac{\Delta E_{\text{kin}}}{E_{\text{kin}}} = \frac{s}{4R_0} + 0.125 \left(\frac{h}{R_0} \right)^2 + \frac{d}{4R_0} + 0.61\alpha_r^2 + \text{smaller terms in } \alpha_r, \alpha_z^3, \text{ etc.} \quad (12)$$

The system is thus first-order focussing in h and α_r , and second-order focussing in α_z . Also, $sh = A$ (or A_0 with retardation) and $\alpha_z \alpha_r \propto \Omega$ (or Ω_0 with retardation). Optimizing the selection of each of the four parameters s , h , d and α_r by the reasonable procedure of requiring an approximately equal contribution from each term to $\Delta E_{\text{kin}}/E_{\text{kin}}$ ⁶⁹ thus means that

$$s \propto \frac{\Delta E_{\text{kin}}}{E_{\text{kin}}}, \quad h \propto \left(\frac{\Delta E_{\text{kin}}}{E_{\text{kin}}} \right)^{\frac{1}{2}}, \quad \alpha_r \propto \left(\frac{\Delta E_{\text{kin}}}{E_{\text{kin}}} \right)^{\frac{1}{2}} \quad (13)$$

and α_z can conservatively be assumed to be held constant. Thus, without retardation,

$$A \propto \left(\frac{\Delta E_{\text{kin}}}{E_{\text{kin}}} \right)^{\frac{1}{2}}, \quad \Omega \propto \left(\frac{\Delta E_{\text{kin}}}{E_{\text{kin}}} \right)^{\frac{1}{2}} \quad (14)$$

whereas with retardation

$$A_0 \propto \left(\frac{\Delta E_{\text{kin}}}{E_0} \right)^{\frac{1}{2}}, \quad \Omega_0 \propto \left(\frac{\Delta E_{\text{kin}}}{E_0} \right)^{\frac{1}{2}} \quad (15)$$

The ratio of efficiencies with and without retardation is then after cancellations

$$\frac{E'}{E} = \frac{E_{\text{kin}}}{E_0} \quad (16)$$

Thus, a tenfold retardation yields a tenfold loss in B , but a one hundredfold increase in the useable $A\Omega$ product, so that a net tenfold gain in efficiency results. Similar considerations apply to the other dispersive analyzers used in XPS,⁷⁵ provided that an appropriate retardation section is utilized. The application of such an analysis to a spectrometer in which a maximum degree of multichannel detection is incorporated is, by contrast, found to yield an approximately constant overall efficiency with retardation.⁶

D. Detection and Control

With very few exceptions, the detectors presently used in x-ray photoelectron spectroscopy are based on continuous-dynode electron multipliers of the "channeltron" type.^{62, 78, 79} These consist of fine-bore lead-doped glass tubes treated by hydrogen reduction at high temperature to leave the surface coated with a semiconducting material possessing a high secondary-electron emissive power.⁶² Tube inner diameters vary from 1 mm down

to 10 μm . A high voltage of a few kV is applied between the ends of such a tube, and multiplications of 10^6 – 10^8 are achieved by repeated wall collisions as electrons travel down the inside of the tube. These multipliers are available in various configurations, often involving tube curvature to minimize ion-induced after-pulsing. Stacks of parallel tubes in the so-called "channel-plate" geometry are also available for use in multichannel detection schemes. Parallel-plate multipliers based upon the same principle have also been attempted.⁸⁰

The efficiency gains concomitant with multichannel detection have led to the use of such a system in one commercial spectrometer,²⁵ in which the multiplied electron pulses from a channel plate are accelerated into a phosphorescent screen, behind which (and external to vacuum) is situated a vidicon camera for translating the optical signal into countable electronic pulses. Other forms of multichannel detection system based upon channel-plate/resistive strip combinations have also been used⁸¹ to a limited degree, and solid-state image sensors of a different type appear to offer good possibilities for future applications of this nature.⁶²

As the appropriate voltages or currents in the analyzer are swept so as to generate electron counts at different kinetic energies, there are various ways of storing and outputting the data. Most simply, a ratemeter can be directly coupled to a plotter or printer during a single continuous sweep. Generally, however, it is desirable to make repeated scans over a given spectral region to average out instrument drifts and certain types of noise; this results in the closest possible approximation to a spectrum with statistically-limited noise. Such repeated scanning requires some form of multiscalar memory, which is often expanded to involve on-line computer control.³³ The use of a more or less dedicated computer has additional advantages in that it can be used to control various functions of the spectrometer in a more automated way, as well as to carry out different types of data analysis such as background subtraction and curve fitting, and commercial systems usually offer this option.

E. Data Analysis

The aim of spectral analyses in XPS is to determine the locations, intensities, and, in certain cases, also the shapes of the various peaks observed, many of which are not clearly resolved from one another. Several complexities must be allowed for in doing this: (1) All peaks will exhibit inelastic tails toward low kinetic energy and these tails may in turn exhibit structure (see, for example, Fig. 1). As a rough approximation that is useful for many solid materials, a major portion of the inelastic tail can be assumed to have a linear or constant form, with extra features perhaps superimposed on it. Valence spectra from solids have been corrected for inelastic scattering by using a close-lying core level to derive the form of the inelastic tail,^{33, 82} as well as by the more

approximate procedure of assuming an asymptotically-constant tail at low kinetic energy whose value at any energy is proportional to the integrated no-loss peak intensity at higher kinetic energies.⁸³ (2) All peaks ride on a background of secondary electrons from higher-kinetic-energy peaks. This background also can often be approximated as linear or constant. (3) The basic peak shapes observed in XPS are a convolution of several variable factors: the exciting x-ray lineshape, contributions from weaker x-rays such as satellites in non-monochromatized sources, the analyzer lineshape, possible non-uniform specimen charging, a Lorentzian hole-state lifetime contribution, Doppler broadening in gases,⁴ and various final-state effects involving many-electron excitations⁸⁴ and vibrational excitations^{41, 85} (as discussed further in Section V). Thus, no universal peak shape of, for example, Gaussian, Lorentzian, or Voigt-function form can be used, and most analyses have involved a somewhat trial-and-error fit for each specific problem. One rather general least-squares program for carrying out such fits permits choosing several basic peak shapes of Gaussian or Lorentzian form, to which are smoothly added an asymptotically-constant inelastic tail of variable height.³³ The effects of satellite x-rays can also automatically be included in the basic peak shape chosen, and a variable linear background is also present. Examples of spectral analyses for atomic 4d core levels using this program are shown in Fig. 6.⁸⁶ Lorentzian shapes have been used for Xe and Yb, and Gaussians for Eu, and the overall fits to these spectra are very good.

Beyond spectral analyses involving fits of certain functional forms to the data, Wertheim^{87, 88} and Grunthaner⁸⁹ have also developed techniques for *deconvoluting* XPS spectra so as to mathematically remove instrumental linewidth contributions. The form of the instrumental linewidth has, in turn, been derived from the shape of the high-energy cut-off at the Fermi energy for a metallic specimen (cf. Fig. 4). This is possible because, to a good approximation, the density of occupied states ends in a vertical step function at E_F . The term "deconvolution" is also often incorrectly used to describe the results of peak-fitting procedures.

III. THE PHOTOEMISSION PROCESS

In this section, various aspects of the basic photoemission process are discussed in detail, with the primary aim of providing a unified theoretical framework for the subsequent discussion of various experimental observations. In discussing photoelectric cross-sections for atoms, molecules, and solids, applications to the interpretation of experimental results are also presented here.

A. Wave Functions, Total Energies, and Binding Energies

In any photoelectron emission experiment, the basic excitation process

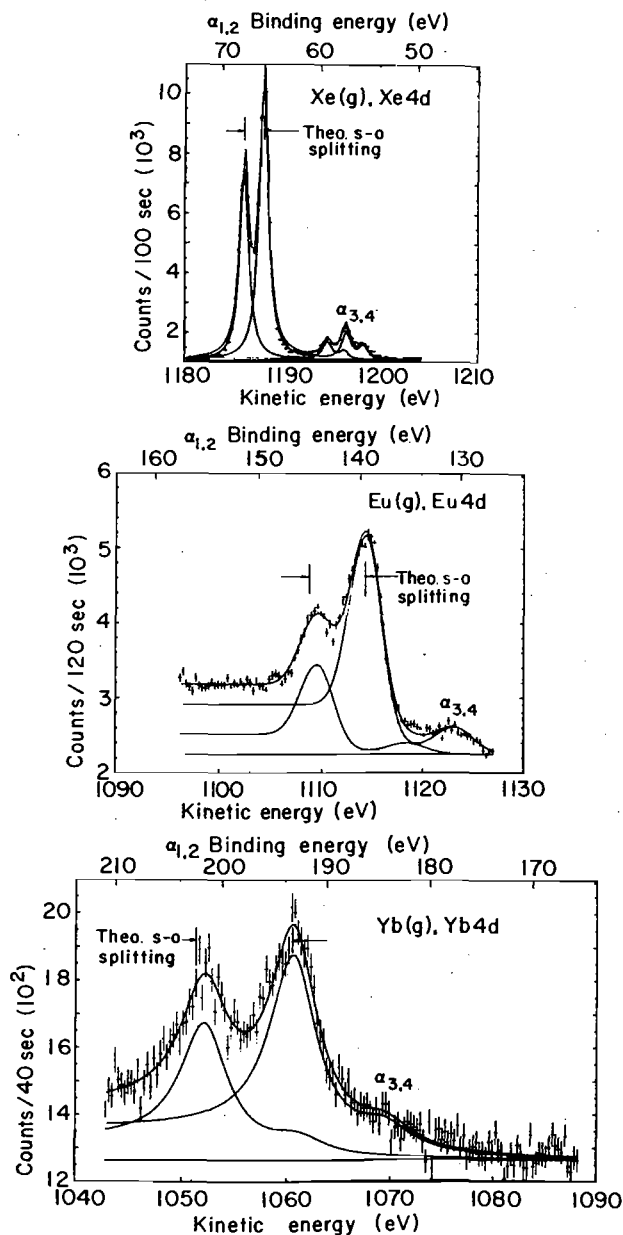


Fig. 6. $4d$ core photoelectron spectra from gaseous Xe, Eu, and Yb produced by excitation with non-monochromatized $MgK\alpha$ x-rays (cf. Fig. 2). The spectra have been resolved into components by least-squares fits of peak shapes including the $\alpha_{3,4}$ satellites and an asymptotically-constant inelastic tail. Lorentzian shapes were used for Xe and Yb, Gaussian for Eu. (From Fadley, ref. 33 (where the curve fitting program is described) and Fadley and Shirley, ref. 86.)

involves absorption of a photon of energy $h\nu$ according to

$$\Psi_{\text{tot}}^i(N), E_{\text{tot}}^i(N) \xrightarrow{h\nu} \Psi_{\text{tot}}^f(N, K), E_{\text{tot}}^f(N, K) \quad (17)$$

Here $\Psi_{\text{tot}}^i(N)$ is the initial-state N -electron wave function corresponding to a total energy $E_{\text{tot}}^i(N)$, and $\Psi_{\text{tot}}^f(N, K)$ is the K th final-state N -electron wave function (including the photoelectron) corresponding to a total energy of $E_{\text{tot}}^f(N, K)$. The relevant energy conservation equation is

$$E_{\text{tot}}^i(N) + h\nu = E_{\text{tot}}^f(N, K) \quad (18)$$

In the simplest situation, the index K thus labels the one-electron orbital k from which emission occurs (as discussed below), but in general it should describe all modes of excitation possible within the final state, including electronic, vibrational, and translational. In all forms of higher-energy photoelectron spectroscopy, it is customary to assume that the photoelectron is sufficiently weakly coupled to the $(N-1)$ -electron ion left behind so as to permit separating the final state of the excitation process to yield

$$\Psi_{\text{tot}}^i(N), E_{\text{tot}}^i(N) \xrightarrow{h\nu} \Psi_{\text{tot}}^f(N-1, K), E_{\text{tot}}^f(N-1, K) + \phi^f(1)\chi^f(1), E_{\text{kin}} \quad (19)$$

in which $\Psi_{\text{tot}}^f(N-1, K)$ and $E_{\text{tot}}^f(N-1, K)$ refer to the K th $(N-1)$ -electron ionic state that can be formed, E_{kin} is the kinetic energy of the K th photoelectron peak, $\phi^f(1)$ is the spatial part of a one-electron orbital describing the photoelectron and $\chi^f(1)$ is the spin part of the photoelectron orbital ($\chi = \alpha$ or β). The form of $\phi^f(1)$ thus depends on kinetic energy. (For simplicity here, any change in kinetic energy due to work function differences between specimen and analyzer is neglected.) $\Psi_{\text{tot}}^f(N-1, K)$ and $\phi^f(1)$ can, if desired, be combined in a suitable sum of products to yield the correct overall antisymmetry with respect to electronic coordinates necessary in the final state. This can be written with an antisymmetrizing operator \hat{A} as:^{90, 91}

$$\Psi_{\text{tot}}^f(N, K) = \hat{A}(\phi^f(1)\chi^f(1), \Psi_{\text{tot}}^f(N-1, K)) \quad (20)$$

The energy conservation equation which then results is that most useful in analyzing XPS spectra:

$$E_{\text{tot}}^i(N) + h\nu = E_{\text{tot}}^f(N-1, K) + E_{\text{kin}} \quad (21)$$

The binding energy corresponding to leaving the ion in a state describable by $\Psi_{\text{tot}}^f(N-1, K)$ is thus given by

$$E_b^v(K) = E_{\text{tot}}^f(N-1, K) - E_{\text{tot}}^i(N) \quad (22)$$

in which the vacuum-level reference is implicit.

One inherent source of linewidth in any binding energy measurement is thus energy broadening due to lifetime effects in either the initial or final state. If the relevant lifetime is denoted by τ , uncertainty principle arguments thus lead to a broadening that is Lorentzian in shape, with a FWHM in eV given by $\sim \hbar/\tau = 6.58 \times 10^{-16} / \tau(\text{s})$. The initial state lifetime is usually very long, and so contributes negligible broadening. However, final-state lifetimes are estimated to be as short as 10^{-18} s in certain cases, so that such effects can play a major role in limiting XPS resolution, particularly for inner subshell excitation.

In general, for a system containing N electrons with spatial coordinates $\mathbf{r}_1, \mathbf{r}_2, \dots, \mathbf{r}_N$ and spin coordinates $\sigma_1, \sigma_2, \dots, \sigma_N$ and P nuclei with spatial coordinates $\mathbf{R}_1, \mathbf{R}_2, \dots, \mathbf{R}_p$, any of the total wave functions considered will depend upon all of these coordinates

$$\Psi_{\text{tot}}(N) = \Psi_{\text{tot}}(\mathbf{r}_1, \sigma_1, \mathbf{r}_2, \sigma_2, \dots, \mathbf{r}_N, \sigma_N; \mathbf{R}_1, \mathbf{R}_2, \dots, \mathbf{R}_p) \quad (23)$$

Nuclear spin coordinates can be neglected on the resolution scale of electron spectroscopy. In the non-relativistic limit that usually serves as the starting point for calculations on such systems, the relevant Hamiltonian in electrostatic units is

$$\begin{aligned} \hat{H}_{\text{tot}} = & -\frac{\hbar^2}{2m} \sum_{i=1}^N \nabla_i^2 - \sum_{i=1}^N \sum_{l=1}^P \frac{Z_l e^2}{r_{il}} + \sum_{i=1}^N \sum_{j>i}^N \frac{e^2}{r_{ij}} \\ & + \sum_{l=1}^P \sum_{m>l}^P \frac{Z_l Z_m e^2}{r_{lm}} - \frac{\hbar^2}{2} \sum_{l=1}^P \frac{\nabla_l^2}{M_l} \end{aligned} \quad (24)$$

Electron kinetic Electron-nuclear attraction Electron-electron repulsion Nuclear-nuclear repulsion Nuclear kinetic

Here, m is the electronic mass, Z_l is the charge of the l th nucleus, $r_{il} = |\mathbf{r}_i - \mathbf{R}_l|$, $r_{ij} = |\mathbf{r}_i - \mathbf{r}_j|$, $r_{lm} = |\mathbf{R}_l - \mathbf{R}_m|$ and M_l is the mass of the l th nucleus. To this must be added relativistic effects, usually via a perturbation approach;⁹²⁻⁹⁴ the additional term in the Hamiltonian most often considered is spin-orbit splitting, which for atomic orbitals has the form:^{93, 95, 96}

$$\hat{H}_{\text{so}} = \sum_{i=1}^N \xi(r_i) \hat{l}_i \cdot \hat{s}_i \quad (25)$$

in which $\xi(r_i)$ is an appropriate function of the radial coordinate r_i ,⁹⁵ \hat{l}_i is the one-electron operator for orbital angular momentum, and \hat{s}_i is the one-electron operator for spin angular momentum. The total wave function then must satisfy a time-independent Schroedinger equation of the form

$$\hat{H}_{\text{tot}} \Psi_{\text{tot}}(N) = E_{\text{tot}}(N) \Psi_{\text{tot}}(N)$$

For such an overall Hamiltonian, the Born-Oppenheimer approximation⁹⁵ permits separating the total wave function into a product of an electronic part Ψ and a nuclear part Ψ_{nuc} as

$$\Psi_{\text{tot}}(\mathbf{r}_1, \dots, \mathbf{R}_p) = \Psi(\mathbf{r}_1, \sigma_1, \mathbf{r}_2, \sigma_2, \dots, \mathbf{r}_N, \sigma_N) \Psi_{\text{nuc}}(\mathbf{R}_1, \mathbf{R}_2, \dots, \mathbf{R}_p) \quad (26)$$

In this approximation, the electronic wave function $\Psi(N)$ depends only parametrically on $\mathbf{R}_1, \mathbf{R}_2, \dots, \mathbf{R}_p$ via the nuclear-nuclear Coulombic repulsion potential, and is the solution to a Schroedinger equation in which the Hamiltonian is that of Eq. (24) with the nuclear kinetic energy term subtracted off:

$$\left(\hat{H}_{\text{tot}} + \frac{\hbar^2}{2} \sum_{l=1}^P \frac{\nabla_l^2}{M_l} \right) \Psi(N) \equiv \hat{H}(N) \Psi(N) = E(N) \Psi(N) \quad (27)$$

(\hat{H}_{tot} here can include spin-orbit effects via Eq. (25) if desired). The total energy of the system can then be written as the sum of the electronic energy E and the nuclear energy E_{nuc} , as

$$E_{\text{tot}} = E + E_{\text{nuc}} \quad (28)$$

with E_{nuc} arising from various forms of internal nuclear motion such as vibrations, rotations, and translations (center-of-mass motions). If the various modes of nuclear motion are furthermore independent, the energy becomes

$$E_{\text{tot}} = E + E_{\text{vib}} + E_{\text{rot}} + E_{\text{trans}} + \dots \quad (29)$$

The overall quantum numbers K describing any initial or final state thus must include a complete specification of all of these modes of motion.

For example, in the limit of a diatomic molecule with a very nearly harmonic oscillator form for the curve of electronic energy, E , versus internuclear separation,

$$E_{\text{vib}} = \hbar \nu_{\text{vib}} (v + \frac{1}{2}) \quad (30)$$

in which ν_{vib} is the classical vibration frequency and $v=0, 1, 2, \dots$, is the vibrational quantum number. Such vibrational excitations in the final state ion give rise to the pronounced vibrational bands well known in UPS studies of gas-phase molecules,⁹⁷ and have also recently been noted in XPS studies of both gases⁴¹ and solids⁸⁵ (see Section V.E). Rotational excitations are sufficiently low in energy as to be so far unresolvable in XPS studies of molecules.

Translational motion of the center of mass of an atom or molecule can influence energies in two ways: (1) The conservation of linear momentum in the excitation process requires that

$$\mathbf{p}_{\hbar\nu} + \mathbf{0} = \mathbf{p}^f + \mathbf{p}_r \quad (31)$$

where $\mathbf{p}_{h\nu}$ is the photon momentum and has a magnitude of $h\nu/c$, the momentum associated with E^i is taken for simplicity to be zero, \mathbf{p}^f is the photoelectron momentum, and \mathbf{p}_r is the recoil momentum of the atom or molecule, treated as a center-of-mass translation. If v is the magnitude of the photoelectron velocity, for $E_{\text{kin}} = 500$ eV, $v/c = 0.044$ and for $E_{\text{kin}} = 1500$ eV, $v/c = 0.076$. Thus, the photoelectrons typically encountered in XPS can be considered to a good approximation to be non-relativistic. In this approximation, it is a simple matter to show that $|\mathbf{p}_{h\nu}| \approx v/2c |\mathbf{p}^f|$ for the example of photoelectrons originating from valence electronic levels (for which $E_{\text{kin}} \approx h\nu$). Therefore, in general $|\mathbf{p}_{h\nu}| \ll |\mathbf{p}^f|$ and $\mathbf{p}^f \approx \mathbf{p}_r$, indicating that the ion recoils in a direction opposite to that of photoelectron emission. By conserving both energy and momentum, it can be shown that for a given $h\nu$ and E_{kin} , the recoil energy $E_r = p_r^2/2M$ increases with decreasing atomic or molecular mass M .³ For excitation of valence shell photoelectrons with AlK α radiation ($h\nu = 1487$ eV), Siegbahn *et al.*³ have calculated the following recoil energies for different atoms: H—0.9 eV, Li—0.1 eV, Na—0.04 eV, K—0.02 eV, and Rb—0.01 eV. It is thus clear that only for the lightest atoms H, He, and Li does the recoil energy have a significant magnitude in comparison with the present 0.4–1.0 eV instrumental linewidths in XPS spectra. For almost all cases, E_r can thus be neglected. (2) A more generally applicable limit on resolution in gas-phase studies is set by the Doppler broadening associated with the thermal translational motion of the emitting molecules. For center-of-mass motion of a molecule of total molecular weight M with a velocity \mathbf{V} , the electron kinetic energy appropriate for use in Eq. (1) is

$$E_{\text{kin}}'' = \frac{1}{2}m|\mathbf{v} - \mathbf{V}|^2 \quad (32)$$

Thus, the measured kinetic energy $E_{\text{kin}} = \frac{1}{2}mv^2$ will differ from that of Eq. (32) by varying amounts, according to the thermal distribution of velocities. If the mean measured kinetic energy in a peak is denoted by $\overline{E_{\text{kin}}}$, then it can be shown using simple kinetic theory that the Doppler width ΔE_d (in eV) is given by⁹⁸

$$\Delta E_d = 0.723 \times 10^{-3} \left(\frac{T \cdot \overline{E_{\text{kin}}}}{M} \right)^{\frac{1}{2}} \quad (33)$$

in which $\overline{E_{\text{kin}}}$ is in eV, T is the absolute temperature in $^{\circ}\text{K}$ and M is the molecular weight. At room temperature and a typical XPS energy of 1000 eV, ΔE_d is thus $\lesssim 0.10$ eV for molecules with $M \geq 10$. In general, such Doppler broadening is thus not a significant factor in comparison to typical XPS resolutions of ~ 0.4 – 1.0 eV, although they can be important in limiting gas-phase UPS resolution.

In many instances, it is adequate to neglect nuclear motion entirely, and use Eqs (17) and (19) with the quantities $\Psi^i(N)$, $E^i(N)$, $\Psi^j(N)$, $E^j(N)$, $\Psi^j(N-1, K)$, and $E^j(N-1, K)$ relating to only electronic motion. Note that this means

accurate calculations must in principle be made on both initial state and final state. The overall designations for such N -electron or $(N-1)$ -electron states are obtained from the various irreducible representations of the symmetry group corresponding to the mean nuclear positions.⁹⁵ For example, in atoms for which spin-orbit coupling is small, Russell-Saunders or L, S coupling can be utilized, yielding states specified by L, S , and perhaps also M_L and M_S , where L is the quantum number for total orbital angular momentum L , S is the quantum number for total spin angular momentum S , and M_L and M_S relate to the z components of orbital- and spin-angular momentum. In the limit of zero spin-orbit splitting, energies depend only on L and S , yielding different L, S terms or multiplets with degeneracies of $(2L+1)(2S+1)$. Analogous overall quantum numbers apply for molecules,⁹⁵ but they are seldom used in describing total electronic wave functions in solids. Multiplet splittings such as those discussed in Section V.C are the result of energy differences between such many-electron states.

B. The Hartree-Fock Method and Koopmans' Theorem

In attempting to determine reasonably accurate approximations to N -electron wave functions, a common starting point is the non-relativistic Hartree-Fock (HF) self-consistent-field (SCF) method.^{95, 99} As the Hartree-Fock method has been widely used in calculations on atoms, molecules, and solids at different levels of exactness and also serves as a reference method for several more accurate and less accurate methods of computing electronic energy levels, it is outlined here in simplest form. The wave function Ψ for an N -electron system is approximated as a single Slater determinant Φ of N orthonormal one-electron spin-orbitals. Each one-electron orbital is composed of a product of a spatial part $\phi_i(\mathbf{r})$ ($i = 1, 2, \dots, N$) and a spin part $\chi_i(\sigma)$ which is equal to either α ($m_s = +\frac{1}{2}$), or β ($m_s = -\frac{1}{2}$), for which the orthonormality relations are

$$\begin{aligned} \int \phi_i^*(\mathbf{r})\phi_j(\mathbf{r}) d\tau &\equiv \langle \phi_i | \phi_j \rangle = \delta_{ij} \\ \int \chi_i^*(\sigma)\chi_j(\sigma) d\sigma &\equiv \langle \chi_i | \chi_j \rangle = \delta_{m_i, m_j} = \begin{cases} 1 & \text{for } \alpha\alpha \text{ or } \beta\beta \\ 0 & \text{for } \alpha\beta \text{ or } \beta\alpha \end{cases} \end{aligned} \quad (34)$$

Ψ can then be written as a normalized determinant of the form:

$$\Psi \approx \Phi = \frac{1}{\sqrt{N!}} \begin{vmatrix} \phi_1(1)\chi_1(1) & \phi_2(1)\chi_2(1) & \dots & \phi_{N-1}(1)\chi_{N-1}(1) & \phi_N(1)\chi_N(1) \\ \phi_1(2)\chi_1(2) & \phi_2(2)\chi_2(2) & \dots & \phi_{N-1}(2)\chi_{N-1}(2) & \phi_N(2)\chi_N(2) \\ \vdots & \vdots & \ddots & \vdots & \vdots \\ \phi_1(N)\chi_1(N) & \phi_2(N)\chi_2(N) & \dots & \phi_{N-1}(N)\chi_{N-1}(N) & \phi_N(N)\chi_N(N) \end{vmatrix} \quad (35a)$$

or in terms of the antisymmetrizer \hat{A} as

$$\Phi = \hat{A}(\phi_{1X_1}, \phi_{2X_2}, \dots, \phi_{NX_N}) \quad (35b)$$

where the integers 1, ..., N label the space and spin coordinates \mathbf{r}_j and σ_j for each orbital.

The spatial one-electron orbitals are furthermore assumed to have symmetries belonging to the set of irreducible representations of the symmetry group of the equilibrium nuclear geometry, and are in this sense often referred to as "delocalized". Thus, for example, in atoms, the orbitals have the form⁹⁵

$$\phi_{nlm_l}(r, \theta, \phi) = R_{nl}(r) Y_{lm_l}(\theta, \phi) \quad (36)$$

in which $R_{nl}(r)$ is the radial part and the angular part is given by the spherical harmonic $Y_{lm_l}(\theta, \phi)$. In molecules, various symmetry types arise, as, for example, 1σ , $3\pi_g$, $2a_1$, ..., ⁹⁵ and the orbitals are often approximated as linear combinations of atomic orbitals (LCAO's). In solids, the translational periodicity of the crystal requires that all such delocalized orbitals be of the Bloch-function type:^{95, 96, 99}

$$\phi_{\mathbf{k}}(\mathbf{r}) = u_{\mathbf{k}}(\mathbf{r}) \exp(i\mathbf{k} \cdot \mathbf{r}) \quad (37)$$

in which \mathbf{k} is the electron wave vector with a quasi-continuous distribution of values and $u_{\mathbf{k}}(\mathbf{r})$ is a function characteristic of each $\phi_{\mathbf{k}}$ that has the same translational periodicity as the lattice. A free electron moving under the influence of no forces corresponds to a constant $u_{\mathbf{k}}(\mathbf{r})$, and yields a plane-wave (PW) one-electron orbital of the form

$$\phi_{\mathbf{k}}(\mathbf{r}) = C \exp(i\mathbf{k} \cdot \mathbf{r}) \quad (38)$$

in which C is a normalization constant and the momentum \mathbf{p} and energy E are given by

$$\mathbf{p} = \hbar\mathbf{k} \quad (39)$$

$$E = E_{\text{kin}} = p^2/2m = \hbar^2 k^2/2m \quad (40)$$

In the often-used spin-restricted Hartree-Fock method, each spatial orbital ϕ_i is also taken to be multiplied by either α and β in the Slater determinant (that is, to have a maximum occupation number of two). Thus only $N/2$ unique ϕ_i 's are involved in describing a system with an even number of electrons in doubly-occupied orbitals.

If the Hamiltonian of Eq. (27) is used together with the variational principle to determine the optimum Φ for which the total energy $E = \langle \Phi | \hat{H} | \Phi \rangle$ is a minimum, the Hartree-Fock equations are obtained. These N equations can be used to determine a self-consistent set of orbitals ϕ_i , as well as to calculate the total energy E of the state described by Φ . In atomic units (1 a.u. = 1 Hartree = 27.21 eV, 1 Bohr = $a_0 = 0.529 \text{ \AA}$), the Hartree-Fock equations in

diagonal form are

$$\begin{aligned} & \left[-\frac{1}{2}\nabla_1^2 - \sum_{l=1}^P \frac{Z_l}{r_{1l}} \right] \phi_i(1) + \left[\sum_{j=1}^N \int \phi_j^*(2) \frac{1}{r_{12}} \phi_j(2) d\tau_2 \right] \phi_i(1) \\ & \quad \text{Kinetic} \quad \text{Electron-nuclear} \quad \text{Electron-electron} \\ & \quad \quad \quad \text{attraction} \quad \quad \quad \text{Coulombic} \\ & \quad \text{repulsion} \\ & - \delta_{m_{s_i}, m_{s_j}} \sum_{j=1}^N \left[\int \phi_j^*(2) \frac{1}{r_{12}} \phi_i(2) d\tau_2 \right] \phi_j(1) = \epsilon_i \phi_i(1), \quad i=1, 2, \dots, N \end{aligned} \quad (41)$$

where the ϵ_i 's are termed energy eigenvalues, one-electron energies, or orbital energies. The origins of the individual terms are labelled. The exchange interaction is only possible between spin-orbitals with parallel spins (that is, $\alpha\alpha$ or $\beta\beta$), and the Kronecker delta $\delta_{m_{s_i}, m_{s_j}}$ allows for this. It is convenient to re-express Eq. (41) more simply in terms of the Fock operator $\hat{F}(1)$ as:

$$\hat{F}(1)\phi_i(1) \equiv \left\{ -\frac{1}{2}\nabla_1^2 - \sum_{l=1}^P \frac{Z_l}{r_{1l}} + \sum_{j=1}^N [J_j - \delta_{m_{s_i}, m_{s_j}} \hat{K}_j] \right\} \phi_i(1) = \epsilon_i \phi_i(1) \quad (42)$$

by defining the Coulomb and exchange operators J_j and \hat{K}_j such that

$$J_j \phi_i(1) \equiv \int \phi_j^*(2) \frac{1}{r_{12}} \phi_j(2) \phi_i(1) d\tau_2 \quad (43)$$

$$\hat{K}_j \phi_i(1) \equiv \int \phi_j^*(2) \frac{1}{r_{12}} \phi_i(2) \phi_j(1) d\tau_2 \quad (44)$$

Thus, the matrix elements of these operators are the two-electron Coulomb integrals J_{ij} and exchange integrals K_{ij} :

$$J_{ij} \equiv \langle \phi_i(1) | J_j | \phi_i(1) \rangle = \iint \phi_i^*(1) \phi_j^*(2) \frac{1}{r_{12}} \phi_i(1) \phi_j(2) d\tau_1 d\tau_2 \quad (45)$$

$$K_{ij} \equiv \langle \phi_i(1) | \hat{K}_j | \phi_i(1) \rangle = \iint \phi_i^*(1) \phi_j^*(2) \frac{1}{r_{12}} \phi_i(2) \phi_j(1) d\tau_1 d\tau_2 \quad (46)$$

From these definitions, it is clear that $J_{ij} = J_{ji}$, $K_{ij} = K_{ji}$, and $J_{ii} = K_{ii}$. Once the Hartree-Fock equations have been solved to the desired self-consistency, the orbital energies ϵ_i can be obtained from

$$\epsilon_i = \epsilon_i^0 + \sum_{j=1}^N (J_{ij} - \delta_{m_{s_i}, m_{s_j}} K_{ij}) \quad (47)$$

where ϵ_i^0 is the expectation value of the one-electron operator for kinetic energy and electron-nuclear attraction

$$\epsilon_i^0 = \langle \phi_i(1) | -\frac{1}{2}\nabla_1^2 - \sum_{l=1}^P \frac{Z_l}{r_{1l}} | \phi_i(1) \rangle \quad (48)$$

By comparison, the total energy of the state approximated by Φ is given by

$$E = \langle \Phi | \hat{H} | \Phi \rangle = \sum_{i=1}^N \epsilon_i^0 + \sum_{i=1}^N \sum_{j>i}^N (J_{ij} - \delta_{m_i, m_j} K_{ij}) + \sum_{l=1}^P \sum_{m>l}^P \frac{Z_l Z_m}{r_{lm}} \quad (49)$$

Note that the first two summations over electronic indices are not simply the sum of all of the one-electron energies for the N electrons in the system, as the sum of the Coulomb and exchange terms in the total energy is made with $i < j$ to avoid counting these terms twice. This means that measured binding energies (which will be shown shortly to be very close to the ϵ_i 's in value) cannot be directly used to determine total energies and hence such quantities as reaction energies.

Mann¹⁰⁰ has compiled very useful tables of accurate Hartree-Fock calculations for all atoms in the periodic table. These include one-electron energies, Slater F^k and G^k integrals for calculating J_{ij} and K_{ij} , radial expectation values, and wave-function tabulations. Herman and Skillman⁹³ and Carlson *et al.*¹⁰¹ have also calculated energies, radial expectation values, and local one-electron potentials for all atoms, using a Hartree-Fock Slater approximation with relativistic corrections.

In utilizing the Hartree-Fock method for computing binding energies, the most accurate procedure is to compute the difference between $E^i(N-1, K)$ and $E^i(N)$ corresponding to the Hartree-Fock wave functions $\Psi^i(N-1, K)$ and $\Psi^i(N)$, respectively. In the one-electron-orbital picture provided by this method, the final-state wave function can be characterized as having a hole in the k th subshell, and, for a closed-shell system with all ϕ_i 's doubly occupied, the overall index K can be replaced simply by k . As the photoemission process by which this hole is formed occurs on a time scale very short compared to that of nuclear motion ($\sim 10^{-16}$ s compared to $\sim 10^{-13}$ s), the nuclear positions in $\Psi^i(N-1, K)$ can be assumed to be identical to those in $\Psi^i(N)$, and the nuclear-nuclear repulsion sum in Eq. (49) will thus cancel in an energy difference. However, the ion left behind by the exiting photoelectron may not possess a nuclear geometry consistent with the ionic ground-state vibrational motion, an effect which leads to the possibility of exciting various final vibrational states. If the excitation is also fast in comparison to the motions of the $(N-1)$ passive electrons in $\Psi^i(N-1, K)$ (a less rigorously justifiable limit termed the "sudden approximation"), it is also possible to show that various final electronic states can be reached. (See Sections III.D.1, V.D.2, and V.E for more detailed discussions.) For now, only the electronic ground state of the ion corresponding to the minimum binding energy will be considered. In this usually dominant final state, it is expected that the passive electrons will not have the same spatial distribution as those in $\Psi^i(N)$ due to relaxation or rearrangement around the k hole. Although the overall change in the spatial form of the passive orbitals due to relaxation

around an inner hole is not large (for example, the mean radius of an atomic orbital changes by only $\sim 1-10\%$),¹⁰² the resulting change in energy can have an appreciable effect on calculated binding energies. Such relaxation effects can have significant consequences in interpreting binding energy data such as, for example, chemical shifts, and they are discussed in more detail in Sections IV and V.B. Hole-state calculations in which initial and final states are treated with equal accuracy in the Hartree-Fock sense have been performed by various authors for atoms,¹⁰³⁻¹⁰⁵ small molecules,¹⁰⁶⁻¹⁰⁹ and inorganic clusters.¹¹⁰ If binding energies determined in this way are corrected for relativistic effects where necessary, very good agreement with experimental core electron binding energies has been obtained. For example, an agreement of approximately 0.2% is found between theoretical and experimental 1s binding energies of Ne ($E_b^V(1s) = 870$ eV) and Ar ($E_b^V(1s) = 3205$ eV).¹⁰³

Relativistic effects generally increase core electron binding energies, as well as leading to spin-orbit splittings, and their magnitudes depend on the ratio of the characteristic orbital velocity to the velocity of light.^{93, 94} The atomic Hartree-Fock Slater calculations of Herman and Skillman⁹³ and Carlson and Pullen⁹⁴ provide a direct tabulation of such corrections for all atoms as determined by perturbation theory. For example, the correction for Cl 1s is only about 0.2 eV out of 290 eV ($\sim 0.08\%$), whereas for the deeper core level Ar 1s, it is about 22 eV out of 3180 eV ($\sim 0.69\%$).

An additional type of correction which should in principle be made to any type of Hartree-Fock calculation is that dealing with electron-electron correlation. In connection with hole-state Hartree-Fock binding energy calculations, the intuitive expectation for such corrections might be that because the initial-state SCF calculation does not include favorable correlation between a given core electron and the other $(N-1)$ electrons, the calculated E^i value would be too large and thus that the binding energy $E_b^V(K) = E^i(N-1, K) - E^i(N)$ would be too small. However, in comparing relativistically-corrected hole-state calculations on several small atoms and ions with experimental binding energies, the remaining error due to correlation has been found to change sign from level to level within the same system.^{103, 111} Such deviations from simple expectations appear to have their origins primarily in the different types of correlation possible for final hole states in different core or valence levels. For example, $E_b^V(1s)$ for Ne shows a correlation correction δE_{corr} in the expected direction (that is, so as to increase E_b) of approximately 0.6 eV out of 870.2 eV ($\sim +0.07\%$)¹¹² whereas δE_{corr} for $E_b^V(2s)$ acts in the opposite direction by approximately 0.9 eV out of 48.3 eV ($\sim -1.8\%$).¹¹¹ For core levels in closed-shell systems such as Ne, such corrections can be computed approximately from a sum of electron pair correlation energies $\epsilon(i, j)$ calculated for the ground state of the system.¹¹¹ For example, in computing the 1s binding energy in Ne, the

correction has the form of a sum over pair correlation energies between the $1s$ electron and all other electrons in the atom. Such correlation energies are dependent upon both overlap and spin orientation, as the exchange interaction partially accounts for correlation of electrons with parallel spin. For Ne $1s$, this sum is thus:

$$\delta E_{\text{corr}} = \epsilon(1s\alpha, 1s\beta) + \epsilon(1s\alpha, 2s\alpha) + \epsilon(1s\alpha, 2s\beta) \\ + 3\epsilon(1s\alpha, 2p\alpha) + 3\epsilon(1s\alpha, 2p\beta) \quad (50)$$

with values of $\epsilon(1s\alpha, 1s\beta) = +1.09$ eV, $\epsilon(1s\alpha, 2s\alpha) = +0.01$ eV, $\epsilon(1s\alpha, 2s\beta) = +0.06$ eV, $\epsilon(1s\alpha, 2p\alpha) = +0.11$ eV, $\epsilon(1s\alpha, 2p\beta) = +0.15$ eV. Note the smaller magnitudes of $\epsilon(i, j)$ for electrons with parallel spins. Also, it is clear that most of the correlation correction arises from the strongly overlapping $1s$ electrons. Equation (50) is only a first approximation, however, and more exact calculations involving explicit estimates of all types of correlation in both Ne and Ne $^+$ with a $1s$ hole give better agreement with the experimental $1s$ binding energy.¹¹² The experimental value is $E_b^V(1s) = 870.2$ eV, in comparison to $\delta E_{\text{corr}} = 1.9$ eV, $E_b^V(1s) = 870.8$ eV based on Eq. (50)¹¹¹ and $\delta E_{\text{corr}} = 0.6$ eV, $E_b^V(1s) = 870.0$ eV based on the more accurate calculation.¹¹² δE_{corr} is decreased in the latter calculation primarily because of correlation terms that are present in Ne $^+$ but not in Ne. The sum of pair correlation energies $\epsilon(i, j)$ in Ne $^+$ is larger than that in Ne by about 30%, and other terms not describable as pair interactions are present in Ne $^+$ but not Ne.

Aside from verifying that Hartree-Fock hole-state energy difference calculations can yield very accurate values for core electron binding energies in atoms and molecules, such investigations have also led to another important consideration concerning the final hole state formed by photoelectron emission. This concerns the correct extent of delocalization of the hole, which is implicitly assumed to have a symmetry dictated by the entire nuclear geometry (or to exhibit a maximum degree of delocalization) in the diagonal Hartree-Fock method discussed here. Hole-state calculations by Bagus and Schaefer¹⁰⁷ have shown that *core-orbital* holes will tend to be localized on one atomic center, as opposed to being distributed over all centers as might be expected in certain cases from a linear-combination-of-atomic-orbitals (LCAO) Hartree-Fock calculation including all electrons. In the simple example of O $_2$, a hole in the $1\sigma_g$ or $1\sigma_u$ molecular orbitals (which can be considered to a very good approximation to be made up of a sum or difference of $1s$ atomic orbitals on the two oxygen atoms, respectively) is predicted by such a calculation to result in a net charge of $+\frac{1}{2}e$ on each oxygen atom in the molecule. However, Snyder¹⁰⁸ has pointed out that such a state does not minimize the total energy associated with the final state Hamiltonian. Thus, the lowest energy state is found¹⁰⁷ to localize the $1s$ core hole entirely on

either oxygen atom. These pairs of equivalent final states (which no longer possess one-electron orbitals with the full symmetry of the molecule) yield the correct values of $E^V(N-1, K)$ for computing binding energies. For O $_2$, the localized hole-states yield a value of $E_b^V(1s) = 542$ eV, in comparison with an experimental value of 543 eV, and a delocalized hole-state value of 554 eV. Thus, localizing the hole represents a large correction of 12 eV ($\sim 2.2\%$). More recently, Cederbaum and Domcke¹¹³ have shown from a more rigorous point of view why the use of such localized core-hole states is valid.

Although localization of final-state core holes is thus to be expected in general, the question of localization becomes more complex in dealing with valence electrons in molecules or solids. Molecular orbitals with lone-pair character or which exhibit a predominance of atomic-orbital make-up from a single atom in an LCAO description are inherently localized, even though they are describable in terms of the overall symmetry species of the molecule, and such orbitals would be expected to exhibit hole localization to a great degree. Other molecular valence hole states may or may not show localization that deviates significantly from a description with full-symmetry molecular orbitals. Similarly, the spatially-compact $4f$ valence levels in solid rare-earth elements and compounds are found to yield highly-localized hole states, as is evidenced by the atomic-like multiplet splittings observed¹¹⁴ (see Section V.C). The valence d electrons in solid transition metals and their compounds or the valence electrons in free-electron-like metals may not always be so simply described, however. Nonetheless, Ley *et al.*¹¹⁵ have concluded that, even for the highly delocalized valence states of free-electron metals such as Li, Na, Mg, and Al, the energy associated with final-state relaxation around a valence hole can be calculated equally well in terms of either a localized- or delocalized-hole-state description; in this case, however, the delocalized hole state is still best considered to be an itinerant localized hole propagating through the solid.

Although a localized-orbital description of the *initial* state can always be obtained from a Hartree-Fock determinant by means of a suitable unitary transformation of the various orbitals ϕ_i without changing the overall N -electron determinantal wave function or total energy,¹¹⁶ the transformation is not unique. Payne¹¹⁷ has also recently presented a new method for performing molecular Hartree-Fock calculations in which relatively unique localized-orbital character is built in by constraining each LCAO molecular orbital to be composed only of atomic orbitals centered on a small set of nearest-neighbor atoms. Although either of these two procedures for obtaining localized initial-state orbitals can provide chemically intuitive and transferable bonding orbitals between two or three bonding centers,^{116, 117} it is not clear that they would necessarily lead to a more correct description of the final state with one electron removed. More theoretical and experimental work is thus necessary to characterize fully the best one-electron-orbital

description of the final states of many systems, if indeed such a one-electron picture is always adequate or necessary.

In order to avoid the difficulties associated with hole-state calculations in determining binding energies, a very often used approximation is to assume that Koopmans' Theorem well describes the relationship between initial and final state total energies. The basis of this theorem is the assumption that the initial one-electron orbitals ϕ_i making up the determinant $\Phi^i(N)$ are precisely equal to the final orbitals ϕ_i' making up $\Phi^f(N-1, k)$ with a single k -subshell hole. The final state total energy $E^f(N-1, k)$ can then be calculated from the formula for $E^i(N)$ [cf. Eq. (49)] simply by eliminating those terms dealing with the electron occupying the k th orbital initially. This procedure leaves as the Koopmans' Theorem value for $E^f(N-1, k)$ (neglecting nuclear repulsion):

$$\begin{aligned} E^f(N-1, k)^{\text{KT}} &= \sum_{i \neq k}^N \epsilon_i^0 + \sum_{i \neq k}^N \sum_{j > i, j \neq k}^N (J_{ij} - \delta_{m_{s_i}, m_{s_j}} K_{ij}) \\ &= \sum_{i \neq k}^N \epsilon_i^0 + \sum_{i=1}^N \sum_{j > i}^N (J_{ij} - \delta_{m_{s_i}, m_{s_j}} K_{ij}) \\ &\quad - \sum_{i=1}^N (J_{ik} - \delta_{m_{s_i}, m_{s_k}} K_{ik}) \end{aligned} \quad (51)$$

The Koopmans' Theorem binding energy of the k th electron is then by the difference method [cf. Eq. (22)],

$$\begin{aligned} E_b^{\text{V}}(k)^{\text{KT}} &= E^f(N-1, k)^{\text{KT}} - E^i(N) \\ &= -\epsilon_k^0 - \sum_{i=1}^N (J_{ik} - \delta_{m_{s_i}, m_{s_k}} K_{ik}) \end{aligned}$$

or, making use of Eq. (47) for the orbital energy ϵ_k ,

$$E_b^{\text{V}}(k)^{\text{KT}} = -\epsilon_k \quad (52)$$

Thus, the binding energy of the k th electron is in this approximation equal to the negative of the orbital energy ϵ_k . For bound-state orbitals ϵ_k is negative, so that the binding energy has the appropriate positive sign. This result is Koopmans' Theorem, as is indicated by the superscript KT. In reality, the relaxation of the $(N-1)$ passive orbitals about the k hole in the ionic ground state will tend to lower $E^f(N-1, k)^{\text{KT}}$, and thus, as long as relativistic and correlation corrections are not too large, binding energies estimated with Koopmans' Theorem should be greater than the true values. If the error due to such electronic relaxation is denoted by $\delta E_{\text{relax}} > 0$, then a binding energy can be written as (neglecting relativistic and correlation effects):

$$\begin{aligned} E_b^{\text{V}}(k) &= E_b^{\text{V}}(k)^{\text{KT}} - \delta E_{\text{relax}} \\ &= -\epsilon_k - \delta E_{\text{relax}} \end{aligned} \quad (53)$$

It should be noted, however, that Koopmans' Theorem as it is derived here applies only to closed-shell systems (that is, systems that are adequately represented by a single Slater determinant with doubly-occupied one-electron orbitals), or to solids which contain many electrons in highly delocalized valence orbitals with quasi-continuous energy eigenvalues. For any other case, there will in general be several possible couplings of spin- and orbital-angular momenta in the open shell or shells, and each distinct coupling will give rise to a different initial or final state energy. These states in atoms might, for example, be described in terms of L, S coupling, and would in general be represented by a linear combination of Slater determinants.¹¹⁸ Although each of these determinants would have the same gross electronic configuration (for example, $3d^5$), various possible combinations of $m_s = \pm \frac{1}{2}$ and m_l would be possible within the open shells. Provided that final-state relaxation is neglected, Slater¹¹⁸ has pointed out that a binding energy $E_b^{\text{V}}(k)^{\text{KT}}$ computed as the difference between the *average* total energy for all states within the final configuration and the *average* total energy for all states within the initial configuration is equal to the one-electron energy ϵ_k computed from an initial-state Hartree-Fock calculation utilizing Coulomb and exchange potentials averaged over all states possible within the initial configuration. This we can write as

$$\overline{E_b^{\text{V}}(k)^{\text{KT}}} = \overline{E^f(k)^{\text{KT}}} - \overline{E^i} = -\epsilon_k \quad (54)$$

and it represents a generalization of Koopmans' Theorem to open-shell systems. The various final states discussed here are the cause of the multiplet splittings to be considered in Section V.C.

Although the orbital energies ϵ_k in Koopmans' Theorem as stated here refer to fully delocalized orbitals, Payne¹¹⁷ has recently pointed out that near-Hartree-Fock calculations in which different atomic-orbital basis sets are chosen for different molecular orbitals to yield effectively localized final results *also* yield a set of one-electron energies that can be interpreted via Koopmans' Theorem. As these one-electron energies are not the same as those for fully delocalized orbitals, it is thus of interest to determine whether any such localization effects are clearly discernible in experimental valence binding energies.

The most direct way of calculating δE_{relax} is of course to carry out SCF Hartree-Fock calculations on both the initial and final states and to compare $E_b^{\text{V}}(k)$ as calculated by a total energy difference method with $E_b^{\text{V}}(k)^{\text{KT}} = -\epsilon_k$. Such calculations have been performed by various authors on both atoms and molecules.^{3, 104-109} As representative examples of the magnitudes of these effects, for the neon atom, $E_b^{\text{V}}(1s) = 868.6$ eV and $E_b^{\text{V}}(1s)^{\text{KT}} = 891.7$ eV, giving $\delta E_{\text{relax}} \approx 23$ eV ($\sim 2.6\%$), and $E_b^{\text{V}}(2s) = 49.3$ eV and $E_b^{\text{V}}(2s)^{\text{KT}} = 52.5$ eV, giving $\delta E_{\text{relax}} \approx 3$ eV ($\sim 6.0\%$). Effects of similar magnitude are

found in the $1s$ levels of molecules containing first-row atoms.^{106, 109} Also, in certain cases, the presence of a localized hole may cause considerable valence electron polarization relative to the initial state.^{106, 107, 110} Thus δE_{relax} lies in the range of 1–10% of the binding energy involved, with greater relative values for more weakly bound electrons. Several procedures have also been advanced for estimating δE_{relax} ^{105, 119–121} and these are discussed in more detail in Section V.B. It has also been pointed out by Manne and Åberg⁹⁰ that a Koopmans' Theorem binding energy represents an average binding energy as measured over all states K associated with emission from the k th orbital, including those describable as both "one-electron" and "multi-electron" in character. This analysis is discussed in more detail in Section III.D.1. Implicit in the use of Koopmans' Theorem is the idea of a predominantly one-electron transition in which the $(N-1)$ passive electrons are little altered.

To summarize, the use of Hartree–Fock theory and Koopmans' Theorem permits writing any binding energy approximately as

$$E_b^V(k) = -\epsilon_k - \delta E_{\text{relax}} + \delta E_{\text{relat}} + \delta E_{\text{corr}} \quad (55)$$

in which δE_{relax} , δE_{relat} , and δE_{corr} are corrections for relaxation, relativistic effects, and correlation effects, respectively.

C. More Accurate Wave Functions via Configuration Interaction

In explaining certain many-electron phenomena observed in XPS spectra it is absolutely essential to go beyond the single-configuration Hartree–Fock approximation, and the most common procedure for doing this is by the configuration interaction (CI) method.¹²² In this method, an arbitrary N -electron wave function $\Psi(N)$ is represented as a linear combination of Slater determinants $\Phi_j(N)$ corresponding to different N -electron configurations:

$$\Psi(N) = \sum_{j=1} C_j \Phi_j(N) \quad (56)$$

The coefficients C_j , and perhaps also the set of one-electron orbitals ϕ_i used to make up the Φ_j 's, are optimized by seeking a minimum in total energy to yield a more accurate approximation for $\Psi(N)$. In the limit of an infinite number of configurations, the exact wave function is obtained by such a procedure. In practice, the dominant C_j 's are usually those multiplying determinants with the same configurations as those describing the Hartree–Fock wave function for the system.

For example, for Ne, a highly accurate CI calculation by Barr involving 1071 distinct configurations of spatial orbitals¹²³ yields the following absolute values for the coefficients multiplying the various members of a few more

important configurations: $\Phi_1 = 1s^2 2s^2 2p^6 =$ Hartree–Fock configuration—0.984; $\Phi_2 = 1s^2 2s^1 2p^6 3s^1 = 0.005$; $\Phi_3 = 1s^2 2s^2 2p^5 3p = 0.009$; $\Phi_4 = 1s^2 2s^2 2p^4 4p^2 = 0.007–0.030$; and $\Phi_5 = 1s^2 2s^2 2p^4 3p 4p = 0.007–0.022$. Approximately 70 distinct configurations have coefficients larger than 0.010 in magnitude, but only that for Φ_1 is larger than 0.030.

Manson⁹¹ has discussed the influence of configuration interaction on the calculation of photoelectron peak intensities (see the more detailed discussion in the next section), and in particular has noted that it may be important to allow for CI effects in both initial and final states. Specific effects of configuration interaction in XPS spectra are also discussed in Sections V.C and V.D, as well as in the chapter by Martin and Shirley¹⁴ in this series.

D. Transition Probabilities and Photoelectric Cross-sections

1. *General Considerations and the Sudden Approximation.* In order to predict the intensities with which various photoelectron peaks will occur, it is necessary to calculate their associated transition probabilities or photoelectric cross-sections. The photoelectric cross-section σ is defined as the transition probability per unit time for exciting a single atom, single molecule, or solid specimen from a state $\Psi^i(N)$ to a state $\Psi^f(N)$ with a unit incident photon flux of $1 \text{ cm}^{-2} \text{ s}^{-1}$. If the direction of electron emission relative to the directions of photon propagation and polarization is specified in $\Psi^f(N)$, as well as perhaps its direction of emission with respect to axes fixed in the specimen, such a cross-section is termed differential, and is denoted by $d\sigma/d\Omega$. The differential solid angle $d\Omega$ is that into which electron emission occurs, and it is indicated in Fig. 7. From $d\sigma/d\Omega$ for a given system, the total cross-section for electron excitation into any direction is given by

$$\sigma = \int \frac{d\sigma}{d\Omega} d\Omega \quad (57)$$

Such differential or total cross-sections can be calculated by means of time-dependent perturbation theory, utilizing several basic assumptions that are discussed in detail elsewhere^{124–131} and reviewed briefly below.

In a semi-classical treatment of the effect of electromagnetic radiation on an N -electron system, the perturbation \hat{H}' due to the radiation can be approximated in a weak-field limit as:¹³¹

$$\hat{H}' = -\frac{e}{2mc} (\hat{p} \cdot \mathbf{A} + \mathbf{A} \cdot \hat{p}) \quad (58)$$

in which $\hat{p} = -i\hbar\nabla$ and $\mathbf{A} = \mathbf{A}(\mathbf{r}, t)$ is the vector potential corresponding to the field. For an electromagnetic wave traveling in a uniform medium, it is possible to choose \mathbf{A} such that $\nabla \cdot \mathbf{A} = 0$ and thus $\hat{p} \cdot \mathbf{A} = 0$, so that in all applications to XPS it is appropriate to consider only the $\mathbf{A} \cdot \hat{p}$ term in Eq.

(58). (In UPS studies of solids, it has, however, been pointed out that the change in properties near a surface can result in a "surface photoeffect" due to the $\hat{p} \cdot \mathbf{A}$ term.¹³²) The electromagnetic wave is further assumed to be a traveling plane wave of the form:

$$\mathbf{A}(\mathbf{r}, t) = \mathbf{e}A_0 \exp [i(\mathbf{k}_{h\nu} \cdot \mathbf{r} - 2\pi\nu t)] \quad (59)$$

where \mathbf{e} is a unit vector in the direction of polarization (\mathbf{e} is parallel to the electric field \mathbf{E}), A_0 is an amplitude factor, $\mathbf{k}_{h\nu}$ is the wave vector of propagation, $|\mathbf{k}_{h\nu}| = 2\pi/\lambda$, and λ is the wavelength of the radiation. Within this approximation the transition probability per unit time for a transition from $\Psi^i(N)$ to $\Psi^f(N)$ can be shown to be proportional to the following squared matrix-element^{124, 131}

$$\begin{aligned} |M_{if}|^2 &= \left| \langle \Psi^f(N) | \sum_{i=1}^N \mathbf{A}(\mathbf{r}_i) \cdot \hat{p}_i | \Psi^i(N) \rangle \right|^2 \\ &= \hbar^2 A_0^2 \left| \langle \Psi^f(N) | \sum_{i=1}^N \exp(i\mathbf{k}_{h\nu} \cdot \mathbf{r}_i) \mathbf{e} \cdot \nabla_i | \Psi^i(N) \rangle \right|^2 \end{aligned} \quad (60)$$

in which the time dependence of \mathbf{A} has been integrated out and the integration remaining in the matrix element is over the space and spin coordinates of all N electrons. The intensity or photon flux of the incident radiation is proportional to A_0^2 . If the final state $\Psi^f(N)$ corresponds to electron emission with a wave vector \mathbf{k}^f (or momentum $\mathbf{p}^f = \hbar\mathbf{k}^f$) oriented within a solid angle $d\Omega$ (cf. Fig. 7), the differential cross-section can then be shown to be:¹²⁴

$$\frac{d\sigma}{d\Omega} = C \left(\frac{1}{h\nu} \right) \left| \langle \Psi^f(N) | \sum_{i=1}^N \exp(i\mathbf{k}_{h\nu} \cdot \mathbf{r}_i) \mathbf{e} \cdot \nabla_i | \Psi^i(N) \rangle \right|^2 \quad (61)$$

in which C is a combination of fundamental constants, and A_0^2 is eliminated in the normalization to unit photon flux. In dealing with atoms and molecules, it is often necessary to sum further over various experimentally-indistinguishable symmetry-degenerate final states, and to average over various symmetry-degenerate initial states to determine a correct cross-section. If the degeneracy of the initial state is g_i and if each such initial state is equally populated, this yields

$$\frac{d\sigma}{d\Omega} = \frac{C}{g_i} \left(\frac{1}{h\nu} \right) \sum_{i,f} \left| \langle \Psi^f(N) | \sum_{i=1}^N \exp(i\mathbf{k}_{h\nu} \cdot \mathbf{r}_i) \mathbf{e} \cdot \nabla_i | \Psi^i(N) \rangle \right|^2 \quad (62)$$

Also, if unpolarized radiation is utilized for excitation, a summation or integration over the various possible orientations of \mathbf{e} is necessary in deriving $d\sigma/d\Omega$, yielding finally a summation $\sum_{i,f,e}$ in Eq. (62). Furthermore, for a randomly oriented set of atoms or molecules as appropriate to studies of gaseous- or polycrystalline-specimens, $d\sigma/d\Omega$ must also be averaged over all

possible orientations of the target system with respect to each possible relative geometry of the radiation and the emitted electron.

A final point of general concern is the influence of nuclear motion, specifically vibration, on such cross-sections. If the Born–Oppenheimer approximation [Eq. (26)] is valid and the influence of the perturbing radiation on

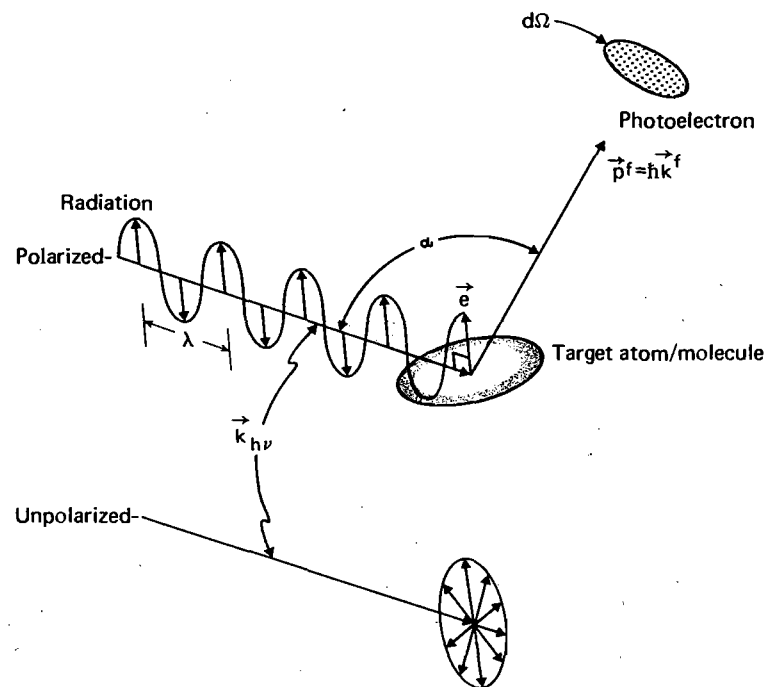


Fig. 7. General geometry for defining the differential cross-section $d\sigma/d\Omega$, showing both polarized and unpolarized incident radiation. The polarization vector \mathbf{e} is parallel to the electric field \mathbf{E} of the radiation. In order for the dipole approximation to be valid, the radiation wave length λ should be much larger than typical target dimensions (that is, the opposite of what is shown here).

the nuclear coordinates is neglected, the differential cross-section [Eq. (62)] becomes:

$$\frac{d\sigma}{d\Omega} = \frac{C}{g_i} \left(\frac{1}{h\nu} \right) \sum_{i,f} \left| \langle \Psi^f(N) | \sum_{i=1}^N \exp(i\mathbf{k}_{h\nu} \cdot \mathbf{r}_i) \mathbf{e} \cdot \nabla_i | \Psi^i(N) \rangle \right|^2 \left| \langle \Psi_{vib}^f(P) | \Psi_{vib}^i(P) \rangle \right|^2 \quad (63)$$

in which the squared overlap between the initial and final vibrational wave functions is simply a Franck–Condon factor. Vibrational effects in XPS spectra are discussed in Section V.E. Only the electronic aspects of matrix elements and cross-sections are considered further here.

In proceeding further, it is assumed that the photon wavelength λ is much larger than the typical dimensions of the system, which will generally be of the order of a few Å. This is a reasonably good, although borderline, approximation for MgK α or AlK α x-rays with $\lambda \approx 10$ Å. This assumption permits treating $\exp(i\mathbf{k}_{h\nu} \cdot \mathbf{r}_i)$ as unity in the integration, yielding for Eq. (62):

$$\frac{d\sigma}{d\Omega} = \frac{C}{g_i} \left(\frac{1}{h\nu} \right) \sum_{i,f} \left| \mathbf{e} \cdot \langle \Psi^f(N) | \sum_{i=1}^N \nabla_i | \Psi^i(N) \rangle \right|^2 \quad (64)$$

and is termed "neglect of retardation" or "the dipole approximation". A further convenience that thus arises is being able to write the matrix element in Eq. (64) in any of the three forms:¹²⁴

$$\begin{aligned} \langle \Psi^f(N) | \sum_{i=1}^N \nabla_i | \Psi^i(N) \rangle &= \frac{i}{\hbar} \langle \Psi^f(N) | \sum_{i=1}^N \hat{p}_i | \Psi^i(N) \rangle \\ &= \frac{m(h\nu)}{\hbar^2} \langle \Psi^f(N) | \sum_{i=1}^N \mathbf{r}_i | \Psi^i(N) \rangle \\ &= \frac{1}{h\nu} \langle \Psi^f(N) | \sum_{i=1}^N \nabla_i V | \Psi^i(N) \rangle \end{aligned} \quad (65)$$

The equality of these three forms can be proven by means of commutation relations for the exact wave functions corresponding to any Hamiltonian of the form of Eq. (24); the first form is denoted "momentum" or "dipole-velocity", the second "dipole-length", and the third "dipole-acceleration". In the last form, $V = V(\mathbf{r}_1, \mathbf{r}_2, \dots, \mathbf{r}_N)$ is the potential represented by the electron-electron repulsion and electron-nuclear attraction terms in the Hamiltonian.

There are several levels of accuracy that can be used for the evaluation of matrix elements such as those in Eq. (64). The most often used approximation begins by assuming a strongly "one-electron" character for the photoemission process, and represents the initial state as an antisymmetrized product of the "active" k th orbital $\phi_k(1)$ from which emission is assumed to occur and an $(N-1)$ -electron remainder $\Psi_R(N-1)$ representing the "passive" electrons:

$$\Psi^i(N) = \hat{A}(\phi_k(1)\chi_k(1), \Psi_R(N-1)) \quad (66)$$

In the weak-coupling limit, the final state is further given very accurately by

$$\Psi^f(N) = \hat{A}(\phi^f(1)\chi^f(1), \Psi^f(N-1)) \quad (67)$$

where for brevity the index K (or most simply k) on the ionic wave function $\Psi^f(N-1)$ has been suppressed, and f specifies the kinetic energy and any additional quantum numbers necessary for the continuum orbital $\phi^f(1)$. If it is further assumed that the primary $k \rightarrow f$ excitation event is rapid or

"sudden" with respect to the relaxation times of the passive-electron probability distribution, the evaluation of N -electron matrix elements for a general one-electron transition operator \hat{i} depending only on spatial coordinates (such as any of those in Eq. 65) yields:^{90, 131}

$$\langle \Psi^f(N) | \sum_{i=1}^N \hat{i}_i | \Psi^i(N) \rangle = \langle \phi^f(1) | \hat{i} | \phi_k(1) \rangle \langle \Psi^f(N-1) | \Psi_R(N-1) \rangle \quad (68)$$

The use of this expression is often termed the "sudden approximation", and it has proven to be very successful for predicting the intensities of various types of many-electron fine structure observed in XPS spectra (see, for example, Sections V.C, and V.D). Transition probabilities and cross-sections are thus in this limit proportional to

$$|\langle \phi^f(1) | \hat{i} | \phi_k(1) \rangle|^2 |\langle \Psi^f(N-1) | \Psi_R(N-1) \rangle|^2 \quad (69)$$

and involve a one-electron matrix element and an $(N-1)$ -electron overlap integral between the ionic wave function and the passive-electron remainder $\Psi_R(N-1)$. It should be noted that $\Psi_R(N-1)$ is thus not a valid ionic wave function, but rather a non-unique "best" representation of the initial-state passive electrons. In order for the overlap integral to be non-zero, symmetry requirements further dictate that both $\Psi^f(N-1)$ and $\Psi_R(N-1)$ must correspond to the same overall irreducible representation; this is the origin of the so-called "monopole selection rule", which is discussed in more detail in Section V.D.2.

It is necessary also to consider criteria for determining whether the sudden approximation can be used or not.^{133, 134} If the excitation from a given subshell k gives rise to a set of final state energies $E^f(N-1, K)$; $K=1, 2, \dots$, then the simplest criterion for the validity of the sudden approximation is that¹³³

$$[E^f(N-1, K) - E^f(N-1, K')] \tau' / \hbar \ll 1 \quad (70)$$

where τ' is the time required for the $k \rightarrow f$ photoelectron to leave the system, and K and K' can range over any pair of final energies with significant intensity in the set. As an indication of the orders of magnitude occurring in this inequality, for a typical x-ray photoelectron of $E_{\text{kin}} = 1000$ eV, $v/c \approx 0.06$ or $v \approx 2 \times 10^9$ cm/s. For a typical atomic diameter of 2 Å, the escape time can thus be roughly estimated as $\tau' \approx (2 \times 10^{-8}) / (2 \times 10^9) \approx 10^{-17}$ s. Thus, $\tau' / \hbar \approx 1/65$ eV $^{-1}$, and for final state separations much larger than 10 eV, the sudden approximation would appear to be violated. However, calculations by Åberg¹³³ and by Carlson, Krause, and co-workers¹³⁵ using the sudden approximation have given reasonable agreement with experiment for several systems for which this inequality was not fully satisfied. On the other hand, Gadzuk and Sunjic¹³⁴ have considered in more detail the question of transit

times and relaxation times in XPS, and have concluded that even the typical excitation energies in XPS of ~ 1.5 keV may not be sufficient to reach fully the sudden limit. This question thus requires further study.

An alternative, and in certain respects more general, description of the initial and final states in the transition matrix element is to use single-determinant Hartree-Fock wave functions. If these are calculated accurately for both states, thus including relaxation effects, the relevant wave functions are

$$\Psi^i(N) = \hat{A}(\phi_1\chi_1, \phi_2\chi_2, \dots, \phi_k\chi_k, \dots, \phi_N\chi_N) \quad (71)$$

$$\Psi^f(N) = \hat{A}(\phi_1'\chi_1, \phi_2'\chi_2, \dots, \phi^f\chi^f, \dots, \phi_N'\chi_N) \quad (72)$$

and the transition matrix element becomes^{136, 137}

$$\langle \Psi^f(N) | \sum_{i=1}^N \hat{i}_i | \Psi^i(N) \rangle = \sum_m \sum_n \langle \phi_m'(1) | \hat{i} | \phi_n(1) \rangle D^{fi}(m|n) \quad (73)$$

where the double sum on m and n is over *all* occupied orbitals and $D^{fi}(m|n)$ is an $(N-1) \times (N-1)$ passive-electron overlap determinant. $D^{fi}(m|n)$ is thus equal to the signed minor formed by removing the m th row and n th column from the $N \times N$ determinant D^{fi} whose elements are overlaps between initial- and final-state one-electron orbitals. That is, the pq element is $(D^{fi})_{pq} = \langle \phi_p'\chi_p | \phi_q\chi_q \rangle$. Many of the N^2 matrix elements contributing to Eq. (73) are zero or near-zero for three reasons: (1) one-electron matrix-element selection rules associated with $\langle \phi_m'(1) | \hat{i} | \phi_n(1) \rangle$; (2) monopole selection rules arising from the one-electron overlaps $\langle \phi_p'\chi_p | \phi_q\chi_q \rangle$, since ϕ_p' and ϕ_q must have the same spatial symmetry and the spin functions χ_p and χ_q must be equal for the overlap to be non-zero; and (3) the near orthogonality of the passive-orbital sets $\phi_1, \dots, \phi_{k-1}, \phi_{k+1}, \dots, \phi_N$ and $\phi_1', \dots, \phi_{k-1}', \phi_{k+1}', \dots, \phi_N'$, so that $\langle \phi_p' | \phi_p \rangle \approx 1.0$ and $\langle \phi_p' | \phi_q \rangle \approx 0$ for $p \neq q$. Additional matrix elements corresponding to transitions other than $k \rightarrow f$ that cannot be ruled out on these bases have furthermore been shown by Åberg¹³³ to be negligible for a high-excitation-energy limit, which leaves finally a first-order result analogous to the sudden-approximation expression

$$\langle \Psi^f(N) | \sum_{i=1}^N \hat{i}_i | \Psi^i(N) \rangle = \langle \phi^f(1) | \hat{i} | \phi_k(1) \rangle D^{fi}(f|k) \quad (74)$$

Various methods for calculating such overlap determinants for atoms have been investigated by Mehta *et al.*,¹⁰² and it has been concluded that the use of a diagonal-element product is accurate to within $\sim 1-2\%$:

$$\langle \Psi^f(N) | \sum_{i=1}^N \hat{i}_i | \Psi^i(N) \rangle = \langle \phi^f(1) | \hat{i} | \phi_k(1) \rangle \sum_{j=1, j \neq k}^N \langle \phi_j' | \phi_j \rangle \quad (75)$$

Proceeding one step further to an unrelaxed, "frozen orbital", or "Koopmans' Theorem" final state in which $\phi_j' = \phi_j$ for $j \neq k$ finally leads to the simplest approximation for such matrix elements:

$$\langle \Psi^f(N) | \sum_{i=1}^N \hat{i}_i | \Psi^i(N) \rangle = \langle \phi^f(1) | \hat{i} | \phi_k(1) \rangle \quad (76)$$

The majority of matrix element and cross-section calculations to date have used this last form.

At the level of sudden approximation calculations utilizing Eq. (68) or (74), two experimentally useful spectral sum rules have been pointed out. The first states that the weighted-average binding energy over all final ionic states $\Psi^f(N-1, K)$ associated with a given primary $k \rightarrow f$ excitation, is simply equal to the Koopmans' Theorem binding energy of $-\epsilon_k$. That is, if I_K is the intensity of a transition to $\Psi^f(N-1, K)$ corresponding to a binding energy $E_b(K)$, then

$$-\epsilon_k = \frac{\sum_K I_K E_b(K)}{\sum_K I_K} = \sum_K \frac{|\langle \Psi^f(N-1, K) | \Psi_{\mathbf{R}}(N-1) \rangle|^2 E_b(K)}{\sum_K I_K} \quad (77)$$

This was first pointed out in connection with XPS by Manne and Åberg,⁹⁰ and has also been derived in a somewhat different context by Lundquist.¹³⁸ The significance of this sum rule is illustrated in Fig. 8, and it requires that,

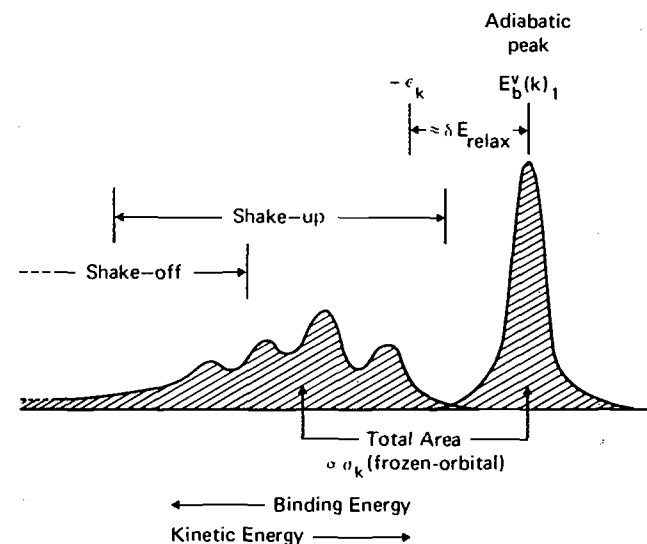


Fig. 8. Schematic illustration of a photoelectron spectrum involving shake-up and shake-off satellites. The weighted average of all binding energies yields the Koopmans' Theorem binding energy $-\epsilon_k$ [sum rule (77)], and the sum of all intensities is proportional to a frozen-orbital cross section σ_k [sum rule (78)]. The adiabatic peak corresponds to formation of the ground state of the ion [$E_b(k)_1 \equiv E_b(K=1)$].

in order for relaxation to occur in forming the lowest-binding-energy "primary" or "adiabatic" final state corresponding to the ionic ground state, excited ionic states corresponding to binding energies higher than $-\epsilon_k$ must also arise. The peaks due to these states have been variously called "shake-up", "shake-off", "many-electron transitions", "configuration-interaction satellites", or "correlation peaks", and more specific illustrations are given in Section V.D. The high-intensity lowest-binding-energy peak has often been associated with a "one-electron transition", although this name is unduly restrictive in view of the inherently many-electron nature of the photoemission process. Thus, the intimate relationship between relaxation and correlation is demonstrated, although it still is possible to determine uniquely a relaxation energy with initial- and final-state Hartree-Fock wave functions that are often assumed to be uncorrelated in the sense that E_{corr} is measured relative to them. The second sudden-approximation sum rule deals with intensities, and it states that the sum of all intensities associated with the states $\Psi^f(N-1, K)$ is given by

$$I_{\text{tot}} = \sum_K I_K = C \sum_K |\langle \phi^f(1) | \hat{t} | \phi_k(1) \rangle|^2 |\langle \Psi^f(N-1, K) | \Psi_{\text{R}}(N-1) \rangle|^2 \\ = C |\langle \phi^f(1) | \hat{t} | \phi_k(1) \rangle|^2 \quad (78)$$

where C is a constant for a given photon energy. One experimental consequence of this sum rule is that matrix elements and cross-sections calculated with unrelaxed final-state orbitals and thus using Eq. (76) apply only to absolute intensities summed over all states $\Psi^f(N-1, K)$, as was first pointed out by Fadley.¹³⁷ Thus, absolute photoelectron intensities for the usually-dominant ionic-ground-state peaks may be below those predicted by unrelaxed or frozen-orbital cross-sections, as has been noted experimentally by Wuilleumier and Krause;¹³⁹ by contrast, x-ray absorption coefficients, which inherently sum over all final states for a given $k \rightarrow f$ excitation, are well predicted by unrelaxed cross-sections.¹³⁷

At a higher level of accuracy than any of the approximations discussed up to this point, configuration-interaction wave functions can also be used in the calculation of matrix elements and cross-sections.^{91, 127} In particular, Manson⁹¹ has discussed in a general way the effects that this can have, pointing out several mechanisms by which calculated intensities can be significantly modified by the inclusion of CI in the initial-state wave function and the final-state wave function. For computational convenience, it is customary (although not essential) to use the same set of orthonormal one-electron orbitals $\phi_1, \phi_2, \dots, \phi_M$ ($M > N$) in making up the configurations of both initial and final states. This apparent lack of allowance for relaxation in the final state can be more than compensated by using a large number of configurations with mixing coefficients C_j^i and C_j^f that are optimized for

both states:

$$\Psi^i(N) = \sum_j C_j^i \Phi_j^i(N) \quad (79)$$

$$\Psi^f(N) = \sum_m C_m^f \Phi_m^f(N) \quad (80)$$

The exact expressions for matrix elements determined with such wave functions are rather complex, particularly if more than one continuum orbital is included, corresponding to an allowance for continuum CI (also referred to as interchannel coupling or close coupling).⁹¹ Although such continuum effects may be important in certain special cases (see Section V.D.5), several many-electron phenomena noted in XPS spectra can be well explained in terms of only initial-state CI and final-state-ion CI. In visualizing these effects, it is thus useful to take a sudden approximation point of view, in which a single primary $k \rightarrow f$ transition is considered and the individual configurations $\Phi_j^i(N)$ and $\Phi_m^f(N)$ are thus written as antisymmetrized products with forms analogous to Eqs (66) and (67):

$$\Phi_j^i(N) = \hat{A}(\phi_k(1)\chi_k(1), \Phi_j^i(N-1)) \quad (81)$$

$$\Phi_m^f(N) = \hat{A}(\phi^f(1)\chi^f(1), \Phi_m^f(N-1)) \quad (82)$$

In these equations, the $(N-1)$ -electron factors can if desired be indexed identically, so that, for the fixed one-electron basis set, $\Phi_j^i(N-1) = \Phi_m^f(N-1)$ if $j=m$ and thus also $\langle \Phi_j^i(N-1) | \Phi_m^f(N-1) \rangle = \delta_{jm}$. Matrix elements in this limit are then given by repeated application of Eq. (68) as

$$\langle \Psi(N) | \sum_{i=1}^N \hat{t}_i | \Psi^i(N) \rangle = \langle \phi^f(1) | \hat{t} | \phi_k(1) \rangle \left[\sum_j (C_j^f)^* C_j^i \right] \quad (83)$$

Thus, the mixing of various configurations into either the initial or final states can affect the observed intensity of a given final state appreciably, as it is only if a certain configuration has a non-zero coefficient in both states that it will contribute a non-zero $(C_j^f)^* C_j^i$ product. For the useful limiting case in which a single configuration $j=1$ dominates the initial state, then $C_j^i \approx 1.0$, $C_j^f \approx 0$ for $j \neq 1$, and the square of the matrix element (83) for transitions to a given final state is simply

$$\left| \langle \Psi^f(N) | \sum_{i=1}^N \hat{t}_i | \Psi^i(N) \rangle \right|^2 \propto |C_1^f|^2 \quad (84)$$

(If relaxation is permitted in the final-state one-electron orbitals, then overlap integrals of the form $\langle \Phi_m^f(N-1) | \Phi_j^i(N-1) \rangle \equiv S_{jm}$ must be computed,¹⁴ and Eqs (83) and (84) become more complex. However, in general $S_{jm} \approx \delta_{jm}$.) Such CI effects are important in understanding the simplest forms of multiplet

splittings (Section V.C), many-electron effects in multiplet splittings (Section V.C), and the intensities of various many-electron satellites (Section V.D).

The inherent requirement of relaxed final-state orbitals in sudden approximation calculations using single-determinant Hartree-Fock wave functions has led to a certain amount of confusion when comparing this model with the results of CI calculations. Manson,⁹¹ for example, has pointed out that the use of relaxed final-state orbitals in such single-determinant calculations yields matrix elements of no higher accuracy than those resulting from the inclusion of only a limited form of initial-state configuration interaction. Thus, there are several types of effects that can only be adequately discussed in terms of a more complete CI treatment.

In the next three sections, matrix element and cross-section calculations for atoms, molecules, and solids are discussed at the often-used level of unrelaxed final-state orbitals that results in Eq. (76).

2. *Atoms.* For a closed-shell atom in the limit of no final-state passive-electron relaxation and a non-relativistic Hamiltonian, each emission event is characterized by a well-defined transition from spin-orbital $\phi_{k\chi k} = \phi_{nlm_l\chi_{m_s}}$ to spin-orbital $\phi^f\chi^f = \phi_{E^f l^f m_l^f \chi_{m_s^f}}$, where E^f is the photoelectron kinetic energy $h\nu - E_b^V(nl)$. The usual dipole selection rules then require that

$$\Delta l = l^f - l = \pm 1 \quad (85)$$

$$\Delta m_l = m_l^f - m_l = 0, \pm 1 \quad (86)$$

$$\Delta m_s = m_s^f - m_s = 0$$

Photoemission is thus divided into two "channels" for $l^f = l + 1$ and $l^f = l - 1$, with the $l + 1$ channel usually being much more important at XPS energies.

The most commonly encountered experimental situation is a collection of atoms whose orientations are random with respect to one another that is exposed to a flux of unpolarized radiation with an angle α between the propagation directions of the radiation and photoelectron (cf. Fig. 7). For this situation, the total photoelectric cross-section for all events involving emission from a given nl subshell can be calculated by summing transition probabilities for all possible one-electron events according to Eq. (63). A general derivation^{124, 126, 127, 140} then shows that the total subshell cross section σ_{nl} is, in the dipole-length form,¹⁴¹ given by

$$\sigma_{nl}(E^f) = \frac{4\pi\alpha_0 a_0^2}{3} (h\nu) [lR_{l-1}^2(E^f) + (l+1)R_{l+1}^2(E^f)] \quad (87)$$

in which α_0 is the fine structure constant, a_0 is the Bohr radius, and the $R_{l\pm 1}(E^f)$ are radial matrix elements common to all one-electron dipole matrix elements between ϕ_{nlm_l} and $\phi_{E^f l^f m_l^f}$. (ϕ_{nlm_l} and $\phi_{E^f l^f m_l^f}$ both have

the general form of Eq. (36).) These radial integrals are given by

$$R_{l\pm 1}(E^f) = \int_0^\infty R_{nl}(r)rR_{E^f, l\pm 1}(r)r^2 dr = \int_0^\infty P_{nl}(r)rP_{E^f, l\pm 1}(r) dr \quad (88)$$

where $P_{nl}(r)/r \equiv R_{nl}(r)$ is the radial part of the ϕ_{nlm_l} orbital and $P_{E^f, l\pm 1}(r)/r \equiv R_{E^f, l\pm 1}(r)$ is the radial part of the continuum photoelectron orbital $\phi_{E^f l^f m_l^f}$. The differential photoelectric cross-section for a given subshell is furthermore given by the expression^{124, 127, 140}

$$\begin{aligned} \frac{d\sigma_{nl}}{d\Omega}(E^f) &= \frac{\sigma_{nl}}{4\pi} [1 - \frac{1}{2}\beta_{nl}(E^f)P_2(\cos \alpha)] \\ &= \frac{\sigma_{nl}}{4\pi} [1 + \frac{1}{2}\beta_{nl}(E^f)(\frac{3}{2}\sin^2 \alpha - 1)] \end{aligned} \quad (89)$$

where $\beta_{nl}(E^f)$ is termed the asymmetry parameter, α is the angle between photon propagation direction and electron emission direction, and $P_2(\cos \alpha) = \frac{1}{2}(3\cos^2 \alpha - 1)$. $\beta_{nl}(E^f)$ can in turn be calculated from the radial integral $R_{l\pm 1}(E^f)$ and certain continuum-orbital phase shifts $\delta_{l\pm 1}(E^f)$ that represents the shift in the sinusoidally oscillating character of $R_{E^f, l\pm 1}(r)$ at large radii relative to the continuum wave functions for a hydrogen atom at energy E^f . The equation for $\beta_{nl}(E^f)$ is

$$\beta_{nl}(E^f) = \frac{\{l(l-1)R_{l-1}^2(E^f) + (l+1)(l+2)R_{l+1}^2(E^f) - 6l(l+1)R_{l+1}(E^f)R_{l-1}(E^f)\cos[\delta_{l+1}(E^f) - \delta_{l-1}(E^f)]\}}{(2l+1)[lR_{l-1}^2(E^f) + (l+1)R_{l+1}^2(E^f)]} \quad (90)$$

and the term in $\cos[\delta_{l+1} - \delta_{l-1}]$ represents an interference between outgoing $l+1$ and $l-1$ waves. Such phase shifts are illustrated for $C2p$ emission into s and d waves at different $h\nu$ in Figs 9(d) and 9(e).

The allowed range for β_{nl} is $-1 \leq \beta \leq +2$. A positive value of β indicates that photoelectrons are preferentially emitted at angles perpendicular to the photon direction ($\alpha = 90^\circ$), whereas a negative value indicates preferential emission either parallel or anti-parallel to this direction ($\alpha = 0^\circ$ or 180°). A value of $\beta = 0$ yields an isotropic distribution. For s -electron emission, $l = 0$, and only transitions to $l^f = 1$ waves are possible. β is always $+2$ for this case, yielding a differential photoelectric cross-section of the form:

$$\frac{d\sigma_{ns}(E^f)}{d\Omega} = \frac{\sigma_{ns}(E^f)}{4\pi} \cdot \sin^2 \alpha \quad (91)$$

with maximum intensity at $\alpha = 90^\circ$ and zero intensity at $\alpha = 0^\circ$ and 180° . For the other limiting case of $\beta = -1$,

$$\frac{d\sigma_{nl}(E^f)}{d\Omega} = \frac{\sigma_{nl}(E^f)}{4\pi} \cdot \cos^2 \alpha \quad (92)$$

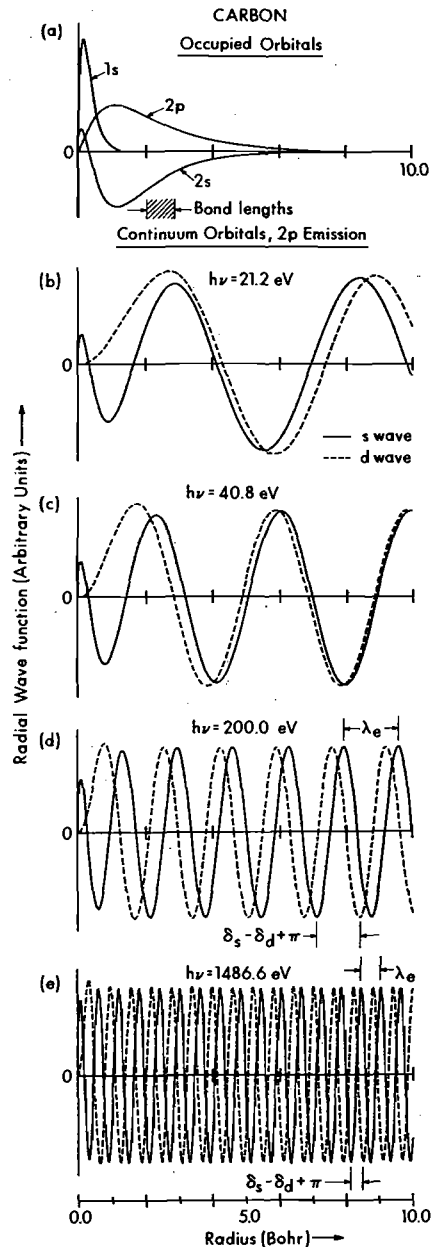


Fig. 9. Radial functions $P(r) = r \cdot R(r)$ for (a) the occupied orbitals of atomic carbon and (b)–(e) the continuum photoelectron orbitals resulting from $C2p$ excitation at different photon energies as indicated. Continuum wave functions for both allowed emission channels are shown ($l+1 \rightarrow d$ wave, $l-1 \rightarrow s$ wave). Note the non-sinusoidal character near the nucleus, and the decrease in the electron deBroglie wavelength λ_e with increasing kinetic energy. The definition of the phase shift $\delta_s - \delta_d + \pi$ is also indicated for $h\nu = 200.0$ eV and 1486.6 eV. In (a), the range of typical bond lengths between carbon and low-to-medium Z atoms is also shown for comparison. (S. M. Goldberg and C. S. Fadley, unpublished results.)

the photoelectron intensity is zero at $\theta = 90^\circ$, and has its maximum value at $\theta = 0^\circ$ and 180° . No matter what the value of β is, the form of Eq. (89) dictates that the distribution should be cylindrically symmetric about the photon propagation direction.

Equation (89) is also equivalent to

$$\frac{d\sigma_{nl}(E_f)}{d\Omega} = A + B \sin^2\alpha \quad (93)$$

where A and B are constants given by $A = (\sigma_{nl}/4\pi)(1 - \beta_{nl}/2)$ and $B = (\sigma_{nl}/4\pi) \cdot 3\beta_{nl}/4$. From an empirical determination of A and B , β can thus be calculated from $\beta_{nl} = 4B/(3A + 2B)$. A comparison between the function predicted by Eq. (93) and experimental results made by Krause¹⁴² is shown in Fig. 10. The parameters A and B have in this case been empirically adjusted to give the best fit to data obtained for photoemission from $Kr3s$, $Kr3p$, and $Kr3d$ levels with $MgK\alpha$ x-rays. The data are reasonably well described by Eq. (93), although a slight systematic deviation is apparent; this has been associated with effects due to the breakdown of the dipole approximation

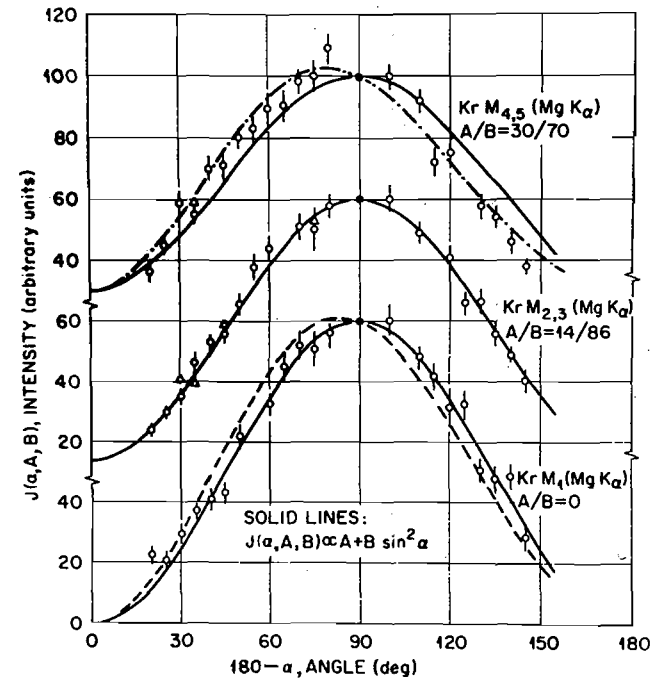


Fig. 10. Experimental angular distributions of $3s$ ($=M_1$), $3p$ ($=M_2, 3$), and $3d$ ($=M_4, 5$) photoelectrons excited from gaseous Kr with $MgK\alpha$ x-rays. The curves represent least-squares fits to the data points of a relationship of the form of Eq. (93), in which A and B were treated as empirical constants. (From Krause, ref. 142.)

(neglect of retardation).¹⁴² Note that the 3s data are consistent with Eq. (91) as expected. Also, a decrease in β with increasing orbital angular momentum is observed, although β is clearly positive for all three cases presented in Fig. 10. Wuilleumier and Krause¹³⁹ have also presented a similar analysis for Ne2p emission that extends up to XPS excitation energies.

Total atomic subshell cross-sections for photon energies relevant to XPS have been calculated in various studies.^{126, 143-151} These calculations have made use of both the non-relativistic theory outlined above, as well as relativistic methods based upon the Dirac equation.^{144, 145, 151} In the non-relativistic calculations, the method introduced by Cooper and Manson^{126, 146, 147} has been most utilized: cross-sections are calculated from matrix elements between initial-state orbitals determined in a Hartree-Fock-Slater approximation (as those generated by Herman and Skillman for all atoms)⁹³ and final-state orbitals determined from a one-electron radial Schroedinger equation with a central potential $V(r)$ representing the interaction with the nucleus and $(N-1)$ electrons in the ion (again of the form determined by Herman and Skillman). More recently, Scofield¹⁵¹ has used a relativistic analogue of this procedure to calculate MgK α and AlK α total subshell cross sections $\sigma_{nl, j=l\pm\frac{1}{2}}$ for all elements in the periodic table; spin-orbit effects split each subshell into two j components with occupancy $2j+1$. The use of such a cross-section tabulation in analyzing XPS spectral intensities is discussed below in Section III.F.3.

In general, it is found that for $h\nu$ well above threshold, as is the case in XPS measurements, transitions to $l'=l+1$ are much more probable than those to $l'=l-1$.^{126, 147} Thus, the term $(l+1)R_{l+1}^2(E^f)$ dominates the term $lR_{l-1}^2(E^f)$ in Eq. (87). Also, $\sigma_{nl}(E^f)$ is generally a decreasing function of E^f for $h\nu$ well above threshold. However, large oscillations and minima in the cross-section may occur as $h\nu$ is increased above threshold.^{126, 146, 147} Such oscillations can be explained in terms of the changing overlap character of an oscillatory $P_{nl}(r)$ and an oscillatory $P_{E^f, l\pm 1}(r)$ with changing E^f .¹²⁶ As E^f is increased, the effective wavelength of the radial oscillations in $P_{E^f, l\pm 1}$ decreases and the oscillations penetrate more deeply into the region of non-zero $P_{nl}(r)$ "within" the atom. This effect is illustrated quantitatively in Fig. 9 for continuum orbitals corresponding to emission from a C2p subshell at $h\nu=21.2, 40.8, 200,$ and 1486.6 eV, as calculated by Goldberg and Fadley using the Manson/Cooper program. For a given $h\nu$, the matrix element $R_{l\pm 1}(E^f)$ thus may consist of contributions due to the constructive overlap of one or more lobes in $P_{nl}(r)$ and $P_{E^f, l\pm 1}$. If, as E^f is varied, the relative signs of the overlapping lobes change, $R_{l\pm 1}(E^f)$ may change sign, and therefore at some kinetic energy intermediate between the sign change, a zero or minimum in $E_{l\pm 1}(E^f)$ and $\sigma_{nl}(E^f)$ can result. A corollary of this argument is that atomic orbitals $P_{nl}(r)$ which exhibit no oscillations with r

should show cross-sections which decrease smoothly with increasing E^f and exhibit no zeroes or minima.¹²⁶ Examples of such orbitals would be 1s, 2p, 3d, and 4f.

Comparisons of total cross-section calculations with experiment are often made through the total atomic absorption coefficient for x-rays, which at lower x-ray energies of $\lesssim 10$ eV consists essentially of a sum over the several subshell cross-sections. Such comparisons yield reasonably good agreement between experiment and theory ($\sim 5-10\%$) except near threshold where $h\nu \approx E_b^V(nl)$.^{137, 143, 145, 150, 152} Cooper and Manson¹⁴⁷ have also calculated relative subshell cross-sections in XPS which compare favorably with the experimental values of Krause¹⁴² shown in Fig. 10.

Asymmetry parameter calculations have also been performed for various atoms at the Manson/Cooper level, and the values obtained for $\beta_{nl}(E^f)$ are also in reasonable agreement with experiment ($\sim \pm 5\%$).¹⁴⁷ Manson¹⁵³ and Kennedy and Manson¹⁴⁹ have also pointed out that for certain subshells, theory predicts that $\beta_{nl}(E^f)$ may exhibit large oscillations with E^f . Finally, Reilman *et al.*¹⁵⁴ have calculated β values spanning all elements in the periodic table for the two common XPS x-rays MgK α and AlK α ; interpolations in this table can be made to any atomic subshell. Thus, the use of Scofield's σ_{nlj} values¹⁵¹ together with the β_{nl} tables of Reilman *et al.*¹⁵⁴ permits determining a reasonably accurate differential cross-section for any situation encountered in typical XPS experiments (even though it does represent a mixture of relativistic and non-relativistic calculations). The data of Fig. 10 make it clear that in order for comparisons of peak intensities in photoelectron spectra to be meaningful, the angular geometry of the experiment must be known and allowed for via $d\sigma/d\Omega$. Neglecting the effect of the asymmetry parameter is equivalent to assuming

$$\frac{d\sigma}{d\Omega} = \frac{\sigma}{4\pi} \quad (94)$$

a relationship that is only rigorously true for a "magic-angle" experimental geometry with $P_2(\cos \alpha) = 0$ or $\alpha = 54.74^\circ$.

A further important point in connection with atomic cross-sections is that, for systems initially possessing an open shell, the calculations outlined above will represent a sum of cross-sections leading to the various allowed final multiplet states (generally describable as L, S terms).¹²⁵ Provided that these multiplets are degenerate, no observable effects are suppressed by such a summation. However, in many cases of both core-level and valence-level emission, these multiplets are resolvable from one another, so that some procedure within a one-electron-transition model is needed for predicting the partitioning of the cross-section into the various multiplets. For emission from a closed inner subshell, the weight of each multiplet is just its total

multiplicity,¹⁵⁵ so that

$$\text{Intensity} \propto (2S^J + 1)(2L^J + 1) \quad (95)$$

For emission from a partially-filled valence subshell, more complex expressions involving fractional parentage coefficients arise; these have been discussed in detail by Cox and co-workers,^{155, 156} and by Bagus, Freeouf, and Eastman.¹⁵⁷ These references include extensive numerical tables. It has also recently been pointed out by Dill *et al.*¹⁵⁸ that for emission from a given nl subshell β_{nl} may vary from multiplet to multiplet, but such effects are small enough to be neglected in first approximation.

Finally, it should be noted that, although all of the foregoing has assumed randomly oriented atoms (as would be characteristic of gas-phase or polycrystalline specimens), the situation of an array of atoms with definite orientation can be important for the case of chemical bonding at a well-defined single-crystal surface. Gadzuk¹⁵⁹ has considered the theoretical expressions resulting for oriented transition-metal atoms on surfaces, and finds potentially significant effects on the angular dependence of photoelectron emission from such atoms.

3. *Molecules and Molecular-orbital Studies.* In general, less is known both experimentally and theoretically about molecular cross-sections, primarily due to the greater difficulty of accurately calculating either the initial-state orbitals or especially the final-state orbitals involved.

For core-level emission to typical XPS energies of a few hundred eV or more, the use of atomic subshell cross-sections is probably a very good approximation at the level of a one-electron model of photoemission, because the initial-state orbital is very little altered by chemical bonding and the final-state hole is highly localized and atomic-like, thus leading to a continuum orbital with very nearly atomic properties. (At very low energies of excitation, it is interesting to note however, that even core levels are predicted to show cross-section resonances due to molecular geometry.¹⁶⁰) Based upon theoretical calculations by Nefedov *et al.*,¹⁶¹ changes in the magnitudes of core-level cross-sections with ionization state are further expected to be very small ($\sim 0-1\%$ per unit charge), although in some cases such effects could be significant.

In valence-level emission, the determination of cross-sections becomes more complex. The initial-state orbital ϕ_k is usually written as a linear combination of atomic orbitals (LCAO):

$$\phi_k = \sum_{A\lambda} C_{A\lambda k} \phi_{A\lambda} \quad (96)$$

in which k represents a symmetry label appropriate for the molecule (e.g. $2\sigma_g$ or $1\pi_u$ in O_2), $\phi_{A\lambda}$ is an atomic orbital (AO) for which A designates the atom and λ the symmetry (e.g. $A = \text{oxygen}$ and $\lambda = 1s$ in O_2), and the $C_{A\lambda k}$'s

are expansion coefficients. Such an LCAO description can be made at any of various levels of accuracy, as is common in quantum-chemical calculations. The final-state orbital ϕ^f presents more of a problem, however, as it must be computed so as to take account of the full molecular geometry, even though at high excitation energies and large distances from the center of mass it will look very much like an atomic continuum orbital of the same kinetic energy. Various approximations have been used for such final states in cross-section calculations relevant to XPS: (1) A simple plane-wave (PW) of the form $\exp(i\mathbf{k} \cdot \mathbf{r})$ has been used in several studies,^{162, 163} although it seems doubtful that highly quantitative results can be achieved in this approximation because the plane-wave is in no way sensitive to the true potential near the atomic centers and neither is it properly orthogonal to the initial-state orbital. By analogy with the atomic case, one would expect correct final states to show behavior near the nucleus much like that shown in Fig. 9. (2) Plane-waves orthogonalized to the occupied core- and valence-orbitals (OPW's) have also been utilized, for example, by Rabalais, Ellison, and co-workers,¹⁶² but doubts concerning their quantitative accuracy at high energies have also been raised by Ritchie.¹⁶⁴ Also, the use of either PW or OPW approximations in the atomic case has been shown by Williams and Shirley¹⁶⁵ to be grossly inadequate. (3) Ritchie¹⁶⁴ has used an expansion in terms of partial waves of different l character, noting that the non-spherical symmetry of the molecular geometry may mix these, introducing complexities not found in the atomic case. (4) More recently, Dill,¹⁶⁰ Dehmer,¹⁶⁰ and Davenport¹⁶⁶ have discussed the use of the multiple-scattering $X\alpha$ ¹⁶⁷ method in molecular cross-section calculations and, at this point, it shows considerable promise of being able to provide very useful and reasonably accurate numerical results. The calculation of molecular cross-sections has been reviewed recently by Dehmer,¹⁶⁸ as well as by Huang and Rabalais¹³⁰ elsewhere in this series.

An additional factor that must be considered in molecular cross-section and lineshape analyses is that various final vibrational states may be reached in a given photoemission event, even in the simple case for which only a single vibrational mode is initially populated. These vibrational excitations are responsible for the bands observed in gas-phase UPS spectra,⁹⁷ for example, and similar effects have been noted in core-level XPS emission (see Section V.E). If the Born-Oppenheimer approximation is used, then the electronic cross-section (differential or total) can be partitioned among the various vibrational states simply by multiplying by appropriate Franck-Condon factors, as indicated previously in Eq. (63).

Whatever initial- and final-state approximations are utilized, it is nonetheless a general consequence of the conservation of parity and angular momentum that the overall form of the differential photoelectric cross-section of a randomly oriented collection of Born-Oppenheimer molecules exposed

to unpolarized radiation will have the same form as that for the atomic case,^{140, 168} namely, Eqs (89) or (93). The calculation of σ_k and β_k proceeds by a different method from that in atoms, of course. The UPS angular distributions of a number of small molecules have been measured by Carlson *et al.*^{169, 170} and they are found to follow the predicted form $A+B\sin^2\alpha$, with all members of each valence vibrational band showing very nearly the same distinct β value (with a few exceptions perhaps indicative of a partial breakdown of the Born–Oppenheimer approximation).

As in atoms, molecular cross-sections for open-shell systems also may represent emission into several non-degenerate multiplet states. Cox and Orchard¹⁵⁵ have derived the relative probabilities of reaching different final electronic states for emission from both filled and unfilled subshells. (A specialization of their results to filled-subshell emission from atoms yields Eq. (95).)

As a final general point concerning molecular cross-sections, it should be noted that, although all of the foregoing results assumed random orientation, the situation of surface chemical bonding on an atomically-ordered substrate may yield a set of molecules with a definite orientation. Dill¹⁷¹ has presented a general theoretical formalism for evaluating such oriented-molecule differential cross-sections, and Davenport¹⁶⁶ has performed numerical calculations for oriented carbon monoxide based upon the $X\alpha$ method. Primary emphasis in all such theoretical studies to date has been on ultra-violet excitation, however.

In analyzing XPS emission from molecular valence levels, much use has also been made of an approximation first suggested by Gelius.¹⁷² Although originally derived by assuming a plane-wave final state $\exp(i\mathbf{k}\cdot\mathbf{r})$, a slightly different procedure will be used here that both leads to the same result and also automatically includes certain correction terms that are often omitted. The initial-state molecular orbital (MO) ϕ_k is assumed to be of LCAO form [Eq. (96)] with the implicit restriction (not always stated) that the atomic orbitals $\phi_{A\lambda}$ be reasonable representations of *true* atomic orbitals, not just single-radial-lobe basis functions, for example, of Slater or Gaussian type. Consider a hypothetical final-state orbital ϕ^f corresponding to $E^f = h\nu - E_b^V(k)$ that has somehow been determined with arbitrary accuracy. The matrix element for photoemission from the molecular orbital will then be given by

$$\begin{aligned} \langle \phi^f | \mathbf{r} | \phi_k \rangle &= \langle \phi^f | \mathbf{r} | \sum_{A\lambda} C_{A\lambda k} \phi_{A\lambda} \rangle \\ &= \sum_{A\lambda} C_{A\lambda k} \langle \phi^f | \mathbf{r} | \phi_{A\lambda} \rangle \end{aligned} \quad (97)$$

The photoelectric cross-section will be proportional to the square of this matrix element. If the atomic orbitals and LCAO coefficients are assumed to

have been constructed as real, this square will be given by

$$\begin{aligned} |\langle \phi^f | \mathbf{r} | \phi_k \rangle|^2 &= \sum_{A'\lambda'} \sum_{A\lambda} C_{A'\lambda'k} C_{A\lambda k} \langle \phi^f | \mathbf{r} | \phi_{A'\lambda'} \rangle \langle \phi^f | \mathbf{r} | \phi_{A\lambda} \rangle \\ &= \sum_{A\lambda} |C_{A\lambda k}|^2 |\langle \phi^f | \mathbf{r} | \phi_{A\lambda} \rangle|^2 \\ &\quad + 2 \sum_{A'\lambda'} \sum_{\substack{A\lambda \\ (A\lambda > A'\lambda')}} C_{A'\lambda'k} C_{A\lambda k} \langle \phi^f | \mathbf{r} | \phi_{A'\lambda'} \rangle \langle \phi^f | \mathbf{r} | \phi_{A\lambda} \rangle \end{aligned} \quad (98)$$

The MO cross-section thus depends on matrix elements between a true molecular final state ϕ^f , and good approximations to atomic orbitals $\phi_{A\lambda}$. The strongly attractive potential near each atomic center will furthermore tend to make ϕ^f in the near-nuclear region look very much like the final-state orbital for photoemission from an isolated atom at the same kinetic energy. At XPS energies, the atomic continuum orbitals for all valence AO's should furthermore be very similar in oscillatory behavior, as the kinetic energies are all very close for a given $h\nu$. It can further be argued that it is the region near the nucleus in which most of the non-zero contributions to the matrix elements $\langle \phi^f | \mathbf{r} | \phi_{A\lambda} \rangle$ arise, because as the distance from each nucleus is increased, ϕ^f rapidly becomes an oscillatory function with periods of only $\sim 0.35 \text{ \AA}$ (the de Broglie wavelength λ_e of the photoelectron). This is illustrated for C2p emission from atomic carbon in Fig. 9. Thus, it is only near the nucleus that the initial-state AO's have sufficiently dense spatial variations to yield a largely non-cancelling contribution to the matrix element; in the diffuse, slowly-varying tails of the valence AO's between the atoms, the oscillations in ϕ^f will yield an approximate cancellation in the matrix element integration. (This same argument is made by Gelius¹⁷² using the more approximate plane-wave final state.) The squares of each of the matrix elements in Eq. (98) are therefore expected to be approximately proportional to the corresponding atomic cross-section:

$$\begin{aligned} |\langle \phi^f | \mathbf{r} | \phi_{A\lambda} \rangle|^2 &\propto d\sigma_{A\lambda}^{(\text{AO})}/d\Omega \\ \text{or} \quad \langle \phi^f | \mathbf{r} | \phi_{A\lambda} \rangle &\propto \pm (d\sigma_{A\lambda}^{(\text{AO})}/d\Omega)^{\frac{1}{2}} \end{aligned} \quad (99)$$

and the final result for the molecular cross-section can be rewritten as

$$\begin{aligned} d\sigma_k^{(\text{MO})}/d\Omega &\propto \sum_{A\lambda} |C_{A\lambda k}|^2 (d\sigma_{A\lambda}^{(\text{AO})}/d\Omega) \\ &\quad + 2 \sum_{A'\lambda'} \sum_{\substack{A\lambda \\ (A\lambda > A'\lambda')}} (\pm) C_{A'\lambda'k} C_{A\lambda k} (d\sigma_{A'\lambda'}^{(\text{AO})}/d\Omega)^{\frac{1}{2}} (d\sigma_{A\lambda}^{(\text{AO})}/d\Omega)^{\frac{1}{2}} \end{aligned} \quad (100)$$

The cross-terms in Eq. (100) are generally neglected, yielding the most commonly-used form of this model:

$$d\sigma_k^{(\text{MO})}/d\Omega \propto \sum_{A\lambda} |C_{A\lambda k}|^2 (d\sigma_{A\lambda}^{(\text{AO})}/d\Omega) \quad (101)$$

$|C_{A\lambda k}|^2$ is the net population of atomic orbital $A\lambda$ in molecular orbital k . In applications of Eq. (101), the net population is often replaced by the gross population $P_{A\lambda k}$ defined as

$$P_{A\lambda k} = |C_{A\lambda k}|^2 + \sum_{\substack{A'\lambda' \\ (A' \neq A)}} C_{A\lambda k} C_{A'\lambda' k} \langle \phi_{A\lambda} | \phi_{A'\lambda'} \rangle \quad (102)$$

although Eq. (100) makes it clear that this is only a very crude way of allowing for overlap effects. Discussions of additional theoretical complexities have also appeared in several studies.¹⁷²⁻¹⁷⁶

The model summarized in Eqs (101) and (102) has been used with reasonable success in analyzing valence spectra of both molecules^{172, 173} and solids in which quasi-molecular units (for example, polyatomic ions) exist.¹⁷⁴⁻¹⁷⁶ In general, empirical relative atomic cross-sections are determined for atoms or simple molecules, and then used, together with an LCAO calculation for the system under study, to generate a theoretical spectrum. One such example for CF_4 is shown in Fig. 11, and it is clear that it correctly predicts relative intensities to a very high accuracy.

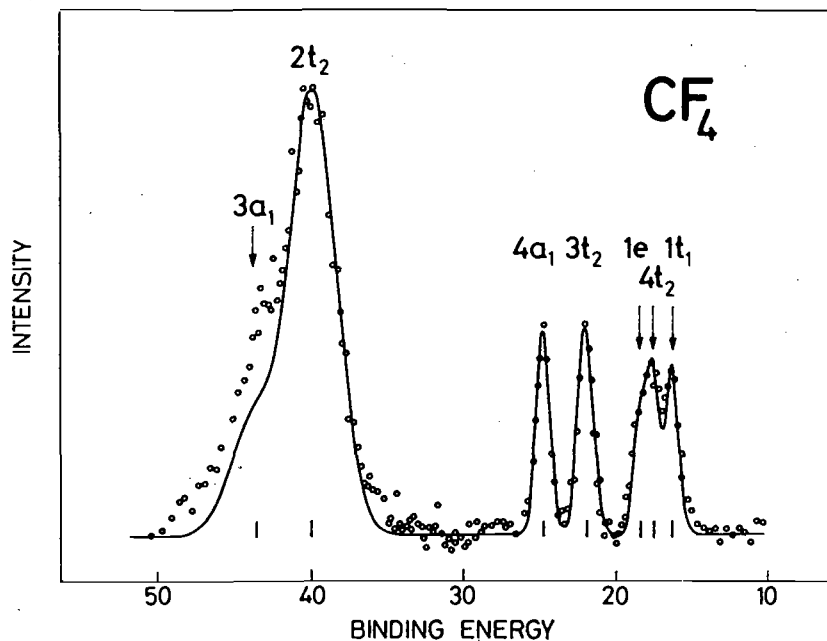


Fig. 11. Experimental XPS spectrum for the valence levels of gaseous CF_4 (points) in comparison with a theoretical curve based upon Eqs (101) and (102). Relative atomic subshell cross-sections were determined experimentally. $\text{MgK}\alpha$ radiation was used for excitation. (From Gelius, ref. 172.)

4. *Solids and Valence-band Studies.* X-ray photoemission from solids has been very successfully analyzed in terms of a three-step model first utilized in ultraviolet photoemission studies by Berglund and Spicer.¹⁷⁷ The steps involved are: (1) a one-electron excitation occurring somewhere below the solid surface from an initial-state orbital ϕ_k at energy E to a final-state orbital ϕ_f with an energy E^f greater by $h\nu$, (2) electron transport via ϕ_f to the surface, during which elastic and inelastic scattering events may occur, and (3) passage of the electron through the surface, at which a small potential barrier may cause refraction or back-reflection to occur. The electron states involved are generally assumed to be characteristic of the bulk material. The one-electron energies E and E^f may be measured with respect to the Fermi energy, the vacuum level, or some other reference; in any case E^f can be easily connected with the measured kinetic energy E_{kin} . An additional zeroth step involving penetration of the exciting radiation to the depth where excitation occurs might also be added to this model, but this has no significant consequence for XPS except at grazing incidence angles for which significant refraction and reflection begin to occur.^{17, 178, 179} As x-ray photoelectron escape depths are only of the order of 10–30 Å, the assumption of an initial excitation involving pure bulk electronic states might be questioned, and one-step theoretical models in which the surface is explicitly included in the photoemission process have been presented.^{180, 181} However, the bulk photoemission model correctly predicts most of the features noted in both UPS and XPS measurements on semiconductors and transition metals,^{57, 182} and also permits separating out the various important physical aspects of photoemission. The presence of distinct surface effects on the photoemission process cannot be discounted, however,¹³² with one much-discussed example being a surface-state peak observed in UPS spectra and other measurements on tungsten.¹⁸³ Primary emphasis here will be placed upon the excitation step in the three-step model, as it contains those elements of the problem that are most clearly related to the ground-state electronic structure of the system.

For emission from non-overlapping, highly-localized, core orbitals, the use of an atomic cross-section (differential or total) is a reasonable approximation for predicting the excitation strength. For emission from valence levels involved in only slightly overlapping quasi-molecular units, the methods discussed in the last section can be used. For emission from highly-overlapping band-like valence levels, a distinctly different procedure is necessary, as outlined below.

In a crystalline solid, both initial and final orbitals will be Bloch functions with wave vectors \mathbf{k} and \mathbf{k}' , respectively, so that $\phi_k(\mathbf{r}) \equiv \phi_{\mathbf{k}}(\mathbf{r}) = u_{\mathbf{k}}(\mathbf{r}) \exp(i\mathbf{k} \cdot \mathbf{r})$ and $\phi_{k'}(\mathbf{r}) \equiv \phi_{\mathbf{k}'}(\mathbf{r}) = u_{\mathbf{k}'}(\mathbf{r}) \exp(i\mathbf{k}' \cdot \mathbf{r})$, consistent with Eq. (37). Such an excitation is shown in Fig. 12 on a plot of one-electron potential energy versus distance from the surface. In traversing the surface barrier, the electron

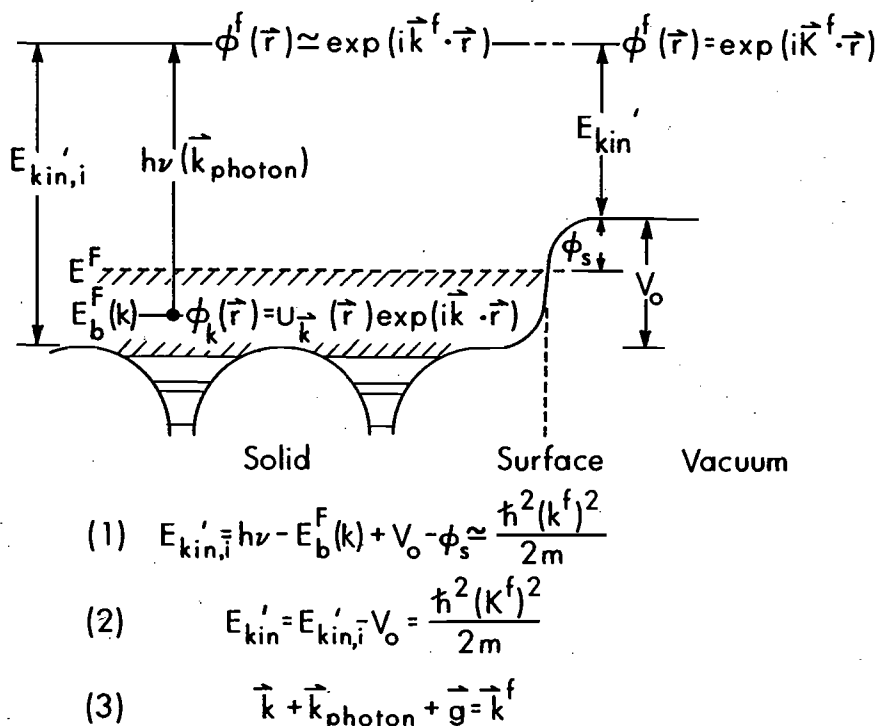


Fig. 12. One-electron model of photoemission in a metallic solid, shown as an energy-level diagram superimposed on the one-electron potential energy curve near the surface. The initial and final states inside the solid are assumed to have Bloch-wave character. Applicable conservation relations on energy and wave vector are also shown.

kinetic energy is reduced from its value inside the surface of $E_{kin,i}$ by an amount equal to the barrier height or inner potential V_0 . V_0 is generally measured with respect to the least negative portion of the potential energy inside the crystal which occurs midway between the strongly attractive atomic centers. Detection of an electron propagating in a definite direction outside of the surface implies a free-electron orbital $\phi_{k^f}(\mathbf{r}) = C \exp(i\mathbf{K}^f \cdot \mathbf{r})$ with momentum $\mathbf{P}^f = \hbar\mathbf{K}^f$, but it should be noted that \mathbf{K}^f need not be precisely equal to \mathbf{k}^f . One obvious source of a difference between \mathbf{K}^f and \mathbf{k}^f is refraction effects at the surface barrier, which are only expected to conserve the component of wave vector parallel to the surface ($k_{||}^f = K_{||}^f$), but such effects are rather small in XPS except for grazing-angles of electron emission with respect to the surface.¹⁷ A convenient convention for describing the electron wave vectors involved in such a transition is to choose the initial \mathbf{k} to lie inside the first or reduced Brillouin zone and the final \mathbf{k}^f to be expressed in an extended-zone scheme. Thus, initial states at several different energies may

possess the same reduced \mathbf{k} value, but each final state is associated with a unique \mathbf{k}^f value.

The basic one-electron matrix element associated with the cross-section for excitation is most generally written as $\langle \phi_{k^f} | \mathbf{A} \cdot \nabla | \phi_k \rangle$. This represents the one-electron analogue of Eq. (60). It is then a simple matter to show¹⁸⁴ that the translational symmetry properties of Bloch functions [Eq. (37)] imply that this matrix element can only be non-zero when \mathbf{k} and \mathbf{k}^f are related by a reciprocal lattice vector \mathbf{g} :

$$\mathbf{k}^f = \mathbf{k} + \mathbf{g} \quad (103)$$

Transitions satisfying this selection rule are termed "direct", and have been found to be very important in the analysis of UPS spectra and other optical absorption experiments from a variety of materials.^{57, 182} At the higher energies of excitation involved in XPS, it has been pointed out by Baird *et al.*¹⁸⁵ that the wave vector $\mathbf{k}_{h\nu}$ associated with the exciting x-ray in XPS has a magnitude sufficiently large that it must be included in this wave-vector conservation equation:

$$\mathbf{k}^f = \mathbf{k} + \mathbf{g} + \mathbf{k}_{h\nu} \quad (104)$$

For example, with $h\nu = 1486.6$ eV, $|\mathbf{k}^f| \approx 2\pi/\lambda_e \approx 19.7 \text{ \AA}^{-1}$ for valence emission, $|\mathbf{k}_{h\nu}| = 2\pi/\lambda \approx 0.7 \text{ \AA}^{-1}$, and typical magnitudes of the reduced wave vector are $|\mathbf{k}| \lesssim 2.0 \text{ \AA}^{-1}$. Transitions violating such selection rules are termed "non-direct", and can be induced in various ways, for example, by interaction with lattice vibrations (phonons), by the introduction of atomic disorder, or by considering emission from very localized valence levels (for example, rare-earth 4f) for which the localized initial and final hole states suppress the effects of translational symmetry. Shevchik¹⁸⁶ has recently made the important observation that phonon effects may lead to an almost total obscuring of direct-transition effects in the XPS spectra of most materials at room temperature. Phonons with a range of wave vectors \mathbf{k}_{phonon} are created or annihilated during the excitation process in a manner completely analogous to thermal diffuse scattering in x-ray diffraction,¹⁸⁷ with the net effect that only a certain fraction of the transitions are simply describable in terms of Eq. (104) (for which $\mathbf{k}_{phonon} \ll \mathbf{k}$). This fraction is most simply estimated from the Debye-Waller factor, as discussed in more detail in Section VI.D.2. Further study of such phonon effects is needed to assess quantitatively their importance, but they do appear to provide a likely mechanism whereby all occupied \mathbf{k} values can contribute to XPS spectra, even if electrons are collected along only a finite solid-angle cone with respect to the axes of a single-crystal in an angle-resolved experiment (see further discussion in Section VI.D.2).

If it is assumed for the moment (as in most prior XPS studies) that direct transitions *are* important, the total rate of excitation of electrons to a given

energy E^f will be given by a summation over all allowed $\mathbf{k} \rightarrow \mathbf{k}^f$ transitions in which energy and wave vector conservation are satisfied. Also, for experiments at non-zero temperature each transition must be weighted by the probability of occupation of the initial state, as given by the Fermi function:

$$F(E) = \frac{1}{\exp[(E - E_F)/kT] + 1} \quad (105)$$

This function allows for the thermal excitation of electrons lying within $\sim kT$ of the Fermi level. Finally, each transition can be weighted by an average probability \bar{T} for escape without inelastic scattering or back reflection at the surface, which will depend on both E^f and \mathbf{k}^f and can be denoted $\bar{T}(E^f, \mathbf{k}^f)$. The average indicated is over various depths of excitation below the surface. The final result will be proportional to the no-loss photoelectron spectrum finally observed, and is thus given by

$$\begin{aligned} N(E_{kin}) &= N(E^f + \Delta) = N(E + h\nu + \Delta) \\ &\propto \sum_{\text{Occupied bands}} \int |\langle \phi_{\mathbf{k}^f}(E^f) | \mathbf{A} \cdot \nabla | \phi_{\mathbf{k}}(E) \rangle|^2 \\ &\quad \times F(E) \bar{T}(E^f, \mathbf{k}^f) \delta(E^f - E - h\nu) \delta(\mathbf{k}^f - \mathbf{k} - \mathbf{g} - \mathbf{k}_{h\nu}) d^3k \quad (106) \end{aligned}$$

where Δ is a trivial energy-scale shift that allows for the binding-energy reference chosen, as well as any work function difference between specimen and spectrometer.

In evaluating the matrix elements in this equation to permit comparisons with XPS spectra, Kono *et al.*¹⁷⁶ have assumed an orthogonalized plane wave for the final state $\phi_{\mathbf{k}^f}$ and a tight-binding (or LCAO) initial state $\phi_{\mathbf{k}}$. Similar analyses have also been carried out more recently by Aleshin and Kucherenko,¹⁸⁸ and in Section VI.D.2, the application of a simpler form of this model to the analysis of angle-resolved XPS valence spectra from single crystals is discussed.

Several basic simplifications of Equation (106) have often been made so as to obtain a rather direct relationship between observed XPS spectra and the initial density of electronic states $\rho(E)$.⁸² Most of these simplifications cannot be made in considering UPS spectra, by contrast. The average no-loss escape function $\bar{T}(E^f, \mathbf{k}^f)$ will be essentially constant for all of the high-energy electrons in the XPS valence spectral region, and so can be eliminated. In UPS however, $\bar{T}(E^f, \mathbf{k}^f)$ can vary considerably over the spectrum. The Fermi function produces only relatively small effects within $\sim \pm kT$ of the Fermi energy, so that in either UPS or XPS carried out at or below room temperature, it is adequate to set it equal to a unit step function. A further simplification that can be justified in several ways for XPS but not UPS is

that the summation and integration in Eq. (106) ultimately yield for a polycrystalline specimen a result of the approximate form

$$N(E_{kin}) \propto \bar{\sigma}_E(h\nu) \rho(E) \quad (107)$$

in which $\bar{\sigma}_E(h\nu)$ is a mean photoelectric cross section for the initial states at energy E and $\rho(E)$ is the density of occupied initial states at energy E . The steps in this justification involve first noting the highly free-electron character of the very high energy final states in XPS (that is $\phi_{\mathbf{k}^f} \approx \exp(i\mathbf{k}^f \cdot \mathbf{r})$). Because the free-electron density of states is proportional to $(E^f)^{\frac{1}{2}}$, this results in an essentially constant total density of final states into which valence emission can occur.⁸² Furthermore, the relatively short electron mean free paths in XPS have been argued by Feibelman and Eastman¹⁸¹ to introduce an uncertainly-principle smearing in the surface-normal component of \mathbf{k}^f that is larger than the mean Δk spacing between final-state bands at a given energy, and so permits all initial states in a polycrystalline specimen to be equally involved in direct transitions as far as \mathbf{k} -conservation is concerned. Phonon effects also may lead to a uniform sampling of all initial states, as suggested by Shevchik.¹⁸⁶ Finally, Baird, Wagner, and Fadley have carried out model direct-transition calculations for single crystals of Au¹⁸⁵ and Al¹⁸⁹ in which all matrix elements were assumed to be equal and the only \mathbf{k}^f smearing included was associated with a finite spectrometer acceptance aperture; summing spectra predicted for all mean emission directions with respect to the crystal axes gave results essentially identical to the density of occupied states, suggesting again that all initial states are equally sampled. Thus, there are several reasons to expect XPS spectra from polycrystalline materials to have a form given approximately by Eq. (107).

XPS has been utilized to study the valence electronic structures of many solids.^{82, 190-193} Examples of comparisons between experiment and theory for the three principal classes of solids (metal, semiconductor, and insulator) are shown in Figs 13,¹⁹¹ 14,¹⁹² and 15.¹⁹³ Here, total densities of initial states $\rho(E)$ are compared directly with experiment, in some cases after a suitable broadening has been applied to theory to simulate natural and instrumental linewidth contributions. These comparisons show that all of the main features noted in the experimental spectra are also seen in the theoretical densities of states, although peak intensities are not always well predicted, probably due to non-constant cross-section effects. For example, in Fig. 15, the dotted curve indicates an empirical estimate by Ley *et al.*¹⁹³ of the relative cross-section variation that would be necessary to yield agreement between experiment and Eq. (107) for diamond. The form of this curve is furthermore consistent with the increasing C2s character expected toward higher binding energies in the diamond valence bands, as the C2s atomic cross-section is expected to be considerably larger than that for C2p.¹⁵¹ Similar conclusions have also been

reached for diamond in a recent more quantitative calculation of the matrix elements involved.¹⁸⁸ Cross-section variations over the valence bands thus clearly can play an important role in the analysis of such XPS data, but it is very encouraging that observed peak positions in general agree very well with those in the density of states. Thus, XPS has proven to be a very direct method for studying the density of states.

In summary, for studies of densities of states in solids, both UPS and XPS exhibit certain unique characteristics and advantages. Somewhat better resolution is possible in a UPS measurement, primarily due to the narrower

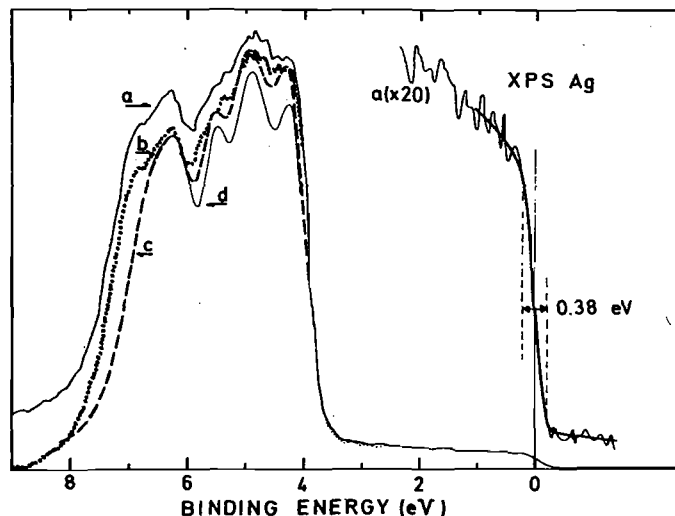


Fig. 13. XPS valence spectrum for polycrystalline silver excited by monochromatized $\text{AlK}\alpha$ radiation in comparison with a theoretical density of states. Curve *a* is the raw XPS data, curve *b* is the data after a smooth inelastic background correction has been subtracted, and curves *c* and *d* represent two different lineshape broadenings of the total theoretical density of states according to Eq. (158). These broadenings thus include effects due to both lifetime and shake-up type excitations in the metal. Note the steep cut-off in the data near $E_F=0$, which can be used to determine the instrumental resolution function. (From Barrie and Christensen, ref. 191.)

radiation sources presently available. Also, UPS spectra contain in principle information on both the initial and final density of states functions, together with certain k -dependent aspects of these functions. The interpretation of an XPS spectrum in terms of the initial density of states appears to be more direct, however. Also, the effects of inelastic scattering are more easily corrected for in an XPS spectrum (cf. Section II.E). Finally, the two techniques are very complementary in the sense that they are controlled by cross-sections which may have different relative values for different bands, thereby providing further information on the types of states involved.

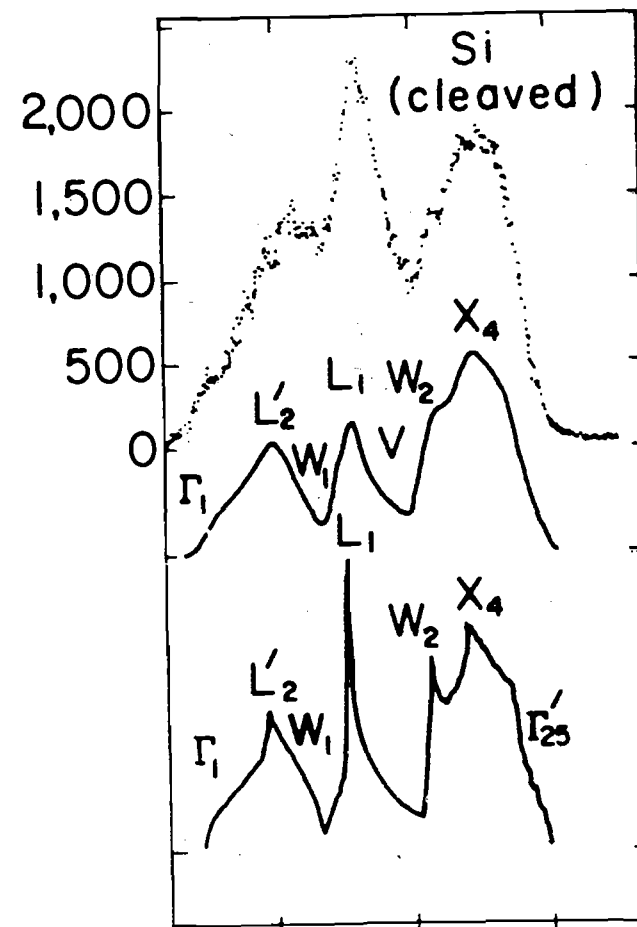


Fig. 14. XPS valence spectrum for a silicon single crystal cleaved in vacuum (points), together with a calculated total density of states (bottom curve), and a density of states broadened by the instrumental resolution function. Excitation was with monochromatized $\text{AlK}\alpha$. The spectrum has been corrected for inelastic scattering. The energy locations of state density primarily due to various high-symmetry points in the reduced Brillouin zone are also indicated. (From Ley *et al.*, ref. 192.)

E. Inelastic Scattering in Solids

Inelastic scattering acts to diminish the no-loss photoelectron current for any type of specimen (gas, liquid, or solid). The processes involved can be one-electron excitations, vibrational excitations, or, in certain solids, plasmon excitations. As it is in measurements on solids that inelastic scattering plays the most significant role in limiting no-loss emission to a mean depth of only a few atomic layers, only such effects will be considered in detail here.

is a maximum in the 30–100 eV kinetic-energy range. For the log–log plot of Fig. 16, the higher energy data are fairly well described by a single straight line that ultimately yields an empirical energy dependence of the form

$$\Lambda_e(E_{\text{kin}}) \propto (E_{\text{kin}})^{0.52} \quad (109)$$

This relationship is useful in rough estimates of Λ_e variation from peak to peak in a given specimen, although between different materials it is certainly not very reliable.

Powell²⁰ and Penn¹⁹⁶ have also recently discussed various theoretical models that can be used to predict attenuation lengths at XPS kinetic energies in terms of microscopic system electronic properties. Penn divides the attenuation length up into two parts involving core- and valence-level excitations according to a reciprocal addition procedure expected if the two types of losses are independent of one another:

$$\frac{1}{\Lambda_{e, \text{total}}} = \frac{1}{\Lambda_{e, \text{core}}} + \frac{1}{\Lambda_{e, \text{valence}}} \quad (110)$$

$\Lambda_{e, \text{core}}$ is determined from an equation of the form given by Powell:²⁰

$$\Lambda_{e, \text{core}} = 2.55 \times 10^{-3} M E_{\text{kin}} / \rho \sum_i \frac{N_i}{E_i} \ln \left[\frac{4E_{\text{kin}}}{\Delta E_i} \right] \quad (111)$$

in which M is the atomic or molecular weight of the solid, E_{kin} is in electron volts, ρ is the density in g/cm³, N_i is the number of electrons in the i th subshell at energy E_i , and ΔE_i is the mean energy loss involving these electrons (always greater than $E_i = E_b^{\text{F}}(i)$). $\Lambda_{e, \text{valence}}$ is determined by assuming that plasmon excitations are the dominant loss processes,¹⁹⁶ a situation that can also be shown to yield an overall relationship very similar to Eq. (111),²⁰ and the final results permit estimating XPS Λ_e values for all elements and compounds, albeit by means of a rather simplified model. In connection with such estimates, it is expected that *ratios* of Λ_e values for a given element or compound will be much more accurately determined than absolute values; this is a very useful result, as it is such ratios that are involved in quantitative analyses of homogeneous systems by XPS, as discussed further in the next section.

As a final comment concerning electron attenuation lengths, it has also been pointed out by Feibelman^{197, 198} that Λ_e may vary in magnitude from the bulk of a specimen to its surface because of changes in the dominant mode of extrinsic inelastic scattering (for example, from bulk- to surface-plasmon excitation). Thus, Λ_e need not be an isotropic constant of the material, although it does not much deviate from this for a free electron metal.¹⁹⁷

F. Photoelectron Peak Intensities

1. *Introduction.* The quantitative interpretation of x-ray photoelectron peak intensities requires developing a model for predicting their magnitudes from various properties of the excitation source, specimen, electron analyzer, and detection system. Detailed discussions of such models have been presented previously by Krause and Wuilleumier¹⁹⁹ for emission from gases and by Fadley¹⁷ for emission from polycrystalline solids. A brief outline of the essential assumptions involved will be presented here, followed by a summary of several important special cases for emission from solids in the next section.

In general, the photoelectron peak intensity N_k produced by subshell k can be calculated within a three-step-like model by integrating the differential intensities dN_k originating in the various volume elements of the specimen. Each of these differential intensities can be written as the following product, in which x, y, z denotes position within the specimen:

$$dN_k = \left[\begin{array}{c} \text{X-ray flux} \\ \text{at } x, y, z \end{array} \right] \times \left[\begin{array}{c} \text{Number of atoms (molecules)} \\ \text{in } dx \, dy \, dz \end{array} \right] \\ \times \left[\begin{array}{c} \text{Differential cross-} \\ \text{section for } k \text{ subshell} \end{array} \right] \times \left[\begin{array}{c} \text{Acceptance solid angle of} \\ \text{electron analyzer at } x, y, z \end{array} \right] \\ \times \left[\begin{array}{c} \text{Probability for no-loss} \\ \text{escape from specimen} \\ \text{with negligible} \\ \text{direction change} \end{array} \right] \times \left[\begin{array}{c} \text{Instrumental} \\ \text{detection} \\ \text{efficiency} \end{array} \right] \quad (112)$$

In most spectrometer systems, a non-monochromatized x-ray source with a broad flux emission pattern is utilized, and for this case it is reasonable to set the x-ray flux equal to some constant value I_0 over the entire specimen volume that is active in producing detectable photoelectrons. This assumption is valid because the exciting radiation is attenuated much more slowly with distance of travel into the specimen than are the electrons as they escape from the specimen. Thus, the region active in producing no-loss electrons is exposed to an essentially constant flux. Exceptions to this situation are monochromatized x-ray sources for which a focused beam is produced,⁷⁴ as well as grazing-incidence experiments on solid specimens in which x-ray refraction at the surface much increases the x-ray attenuation with distance below the surface.^{17, 178, 179} Neither of these special cases will be considered further here, but refraction effects are discussed in Section VI.C.

The acceptance solid angle Ω of the electron analyzer will vary over the specimen volume, becoming zero for those points from which emission is totally prohibited by the electron optics. Ω , as well as the effective specimen

area A over which $\Omega \neq 0$, also may vary with electron kinetic energy, as discussed previously in Sections II.C.1 and II.C.2.

The probability for no-loss escape from the specimen, which can in the present context be written as $T(E_{kin}, \mathbf{k}^f, x, y, z)$, is most simply given by an expression such as Eq. (108) involving the electron attenuation length, provided that elastic scattering events that change direction but not energy are neglected. \mathbf{k}^f thus specifies the direction of electron motion along the path length l from the excitation point x, y, z . In gases, such an escape probability must also take into account variations in density (and thus also Λ_e) along the electron trajectories.

The instrumental detection efficiency D_0 is defined to be the probability that a no-loss electron escaping from the specimen in a direction encompassed by the acceptance solid angle will yield a single final count (or equivalent current). This efficiency thus allows for all non-idealities in the analysis and detection system, and it can also depend on E_{kin} .

If the atomic or molecular density in cm^{-3} is denoted $\rho(x, y, z)$, the differential intensity element thus becomes

$$dN_k = I_0 \cdot \rho(x, y, z) dx dy dz \cdot \frac{d\sigma_k}{d\Omega} \cdot \Omega(E_{kin}, x, y, z) \cdot T(E_{kin}, \mathbf{k}^f, x, y, z) \cdot D_0(E_{kin}) \quad (113)$$

or for a uniform-density, but bounded, specimen:

$$dN_k = I_0 \cdot \rho dx dy dz \cdot \frac{d\sigma_k}{d\Omega} \cdot \Omega(E_{kin}, x, y, z) \cdot \exp[-l/\Lambda_e(E_{kin})] \cdot D_0(E_{kin}) \quad (114)$$

where l is the path length to escape from the specimen surface into vacuum.

2. *Peak Intensities from Solids.* With a few simplifying assumptions, Eq. (114) is readily integrated to obtain useful expressions for total peak intensity N_k for the idealized spectrometer shown in Fig. 17.^{17, 178} The specimen surface is assumed to be atomically flat. The specimen is taken to be polycrystalline to avoid single-crystal anisotropies in emission²⁰⁰ (see discussion in Section VI.D.1). An exponential inelastic attenuation law as in Eq. (108) is assumed, and elastic electron scattering effects are neglected. For a given kinetic energy, the electron spectrometer is further assumed to act as though a mean solid angle Ω_0 is applicable over all specimen volume included in the projection of an effective aperture A_0 along the mean electron emission direction (dotted lines in Fig. 17). Both Ω_0 and A_0 may be functions of the kinetic energy E_{kin} . The mean emission direction is assumed to be at an angle θ with respect to the surface. The exciting radiation is incident at an angle ϕ_x with respect to the surface, and, due to refraction, the internal

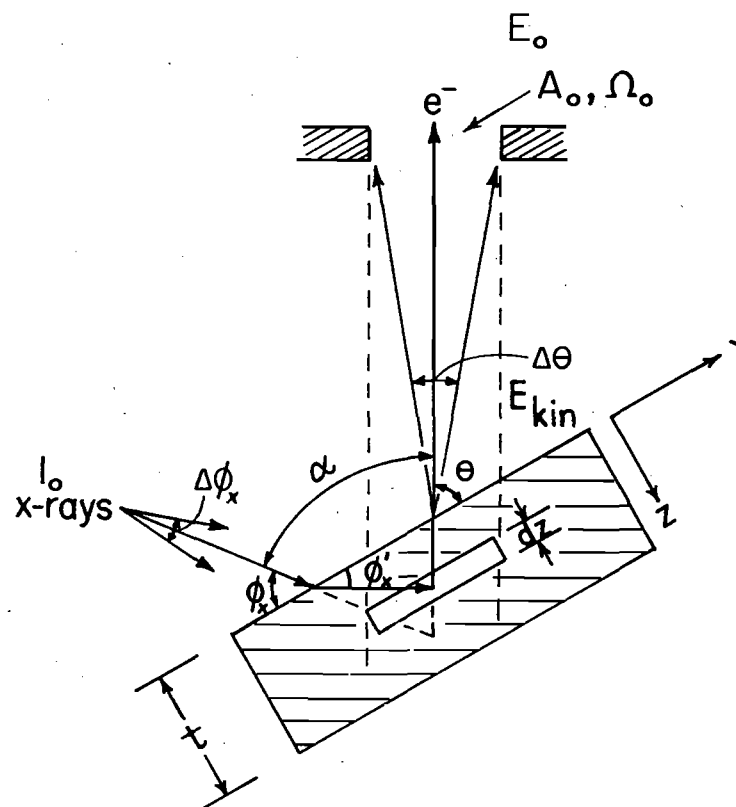


Fig. 17. Idealized spectrometer geometry for calculating photoelectron peak intensities from solid specimens.

angle ϕ_x' may be less than ϕ_x . Such refraction (and reflection) effects only occur for $\phi_x \lesssim 1^\circ$,^{178, 179} and will not be included here, although they are briefly discussed in Section VI.C. The angle α between the mean incidence- and exit-directions is held fixed at between approximately 45° and 105° in most current XPS spectrometers.

Within the approximations quoted above (which are very nearly achieved in a number of practical spectrometer systems), it is possible to derive intensity expressions for several important cases:^{17, 178, 201}

(a) Semi-infinite specimen, atomically clean surface, peak k with $E_{kin} \equiv E_k$:

$$N_k(\theta) = I_0 \Omega_0(E_k) A_0(E_k) D_0(E_k) \rho \frac{d\sigma_k}{d\Omega} \Lambda_e(E_k) \quad (115)$$

This case corresponds to an optimal measurement on a homogeneous specimen for which no surface contaminant layer is present. The expression given permits predicting the absolute peak intensities resulting for a given

specimen, or, of much more interest in practice, the relative intensities of the various peaks. If absolute intensities are to be derived, then the incident flux I_0 must be determined, as well as the kinetic energy dependences of effective solid angle Ω_0 , effective specimen area A_0 , and detection efficiency D_0 . In relative intensity measurements in which the quantity of interest is $N_k/N_{k'}$, for two peaks k and k' , I_0 will cancel, although $\Omega_0 A_0 D_0$ need not due to its kinetic energy dependence. The density ρ of the atoms or molecules on which subshell k or k' is located may be known beforehand, or may also be the desired end result in quantitative analyses using XPS. The differential cross-section $d\sigma_k/d\Omega$ can be calculated by the various methods discussed in Sections III.D.2–III.D.4. For core levels, the tabulations of σ_{nlj} by Scofield,¹⁵¹ combined with the β_{nl} values given by Reilman *et al.*,¹⁵⁴ provide a suitable means for estimating $d\sigma_k/d\Omega$ with good accuracy within the framework of a one-electron-transition model. Possible effects of multi-electron processes on the use of such cross-sections are discussed in Sections III.D.1 and V.D. Within a given specimen, $\Lambda_e(E_k)$ can be estimated from Penn's treatment,¹⁹¹ or, more simply, its dependence on kinetic energy can be assumed to follow the empirical square-root dependence of Eq. (109). Note that there is no θ dependence in N_k within this simple model, a prediction that has been verified experimentally by Henke;¹⁷⁸ this behavior is expected to hold as long as θ is not made so small that the edges of the specimen lie within the aperture A_0 .^{17, 222}

(b) Specimen of thickness t , atomically clean surface, peak k with $E_{kin} \equiv E_k$:

$$N_k(\theta) = I_0 \Omega_0(E_k) A_0(E_k) D_0(E_k) \rho \frac{d\sigma_k}{d\Omega} \Lambda_e(E_k) \times [1 - \exp(-t/\Lambda_e(E_k) \sin \theta)] \quad (116)$$

Here, the intensity of a peak originating in a specimen of finite thickness is predicted to increase with decreasing θ (again with the proviso that θ not be so small that the specimen edges lie within A_0).

(c) Semi-infinite substrate with uniform overlayer of thickness t —Peak k from substrate with $E_{kin} \equiv E_k$:

$$N_k(\theta) = I_0 \Omega_0(E_k) A_0(E_k) D_0(E_k) \rho \frac{d\sigma_k}{d\Omega} \Lambda_e(E_k) \times \exp(-t/\Lambda_e'(E_k) \sin \theta) \quad (117)$$

Peak l from overlayer with $E_{kin} \equiv E_l$:

$$N_l(\theta) = I_0 \Omega_0(E_l) A_0(E_l) D_0(E_l) \rho' \frac{d\sigma_l}{d\Omega} \Lambda_e'(E_l) \times [1 - \exp(-t/\Lambda_e'(E_l) \sin \theta)] \quad (118)$$

where

$\Lambda_e(E_k)$ = an attenuation length in the substrate

$\Lambda_e'(E_k)$ = an attenuation length in the overlayer

ρ = an atomic density in the substrate

ρ' = an atomic density in the overlayer.

Overlayer/substrate ratio:

$$\frac{N_l(\theta)}{N_k(\theta)} = \frac{\Omega_0(E_l) A_0(E_l) D_0(E_l) \rho' (d\sigma_l/d\Omega) \Lambda_e'(E_l)}{\Omega_0(E_k) A_0(E_k) D_0(E_k) \rho \frac{d\sigma_k}{d\Omega} \Lambda_e(E_k)} \times [1 - \exp(-t/\Lambda_e'(E_l) \sin \theta)] \exp(t/\Lambda_e'(E_k) \sin \theta) \quad (119)$$

This case represents a much more common experimental situation in which the primary specimen acts as substrate and possesses an intentional or unintentional contaminant overlayer (for example, oxide on a metal or a layer deposited from the spectrometer residual gases). Substrate peaks are attenuated by inelastic scattering in the overlayer, an effect that is much enhanced at low θ . The overlayer/substrate ratio is thus predicted to increase strongly as θ decreases, an effect that suggests a general method for increasing surface sensitivity by using grazing angles of electron escape; such angular-dependent studies are discussed in more detail in Section VI.B.

(d) Semi-infinite substrate with a non-attenuating overlayer at fractional monolayer coverage—Peak k from substrate: Eq. (115).

Peak l from overlayer:

$$N_l(\theta) = I_0 \Omega_0(E_l) A_0(E_l) D_0(E_l) \sigma' (d\sigma_l/d\Omega) (\sin \theta)^{-1} \quad (120a)$$

Overlayer/substrate ratio:

$$\frac{N_l(\theta)}{N_k(\theta)} = \frac{\Omega_0(E_l) A_0(E_l) D_0(E_l) s' (d\sigma_l/d\Omega)}{\Omega_0(E_k) A_0(E_k) D_0(E_k) s \frac{d\sigma_k}{d\Omega} (\Lambda_e(E_k) \sin \theta/d)} = \left[\frac{s'}{s} \right] \cdot \frac{D_0(E_l) \Omega_0(E_l) A_0(E_l) (d\sigma_l/d\Omega) d}{D_0(E_k) \Omega_0(E_k) A_0(E_k) \frac{d\sigma_k}{d\Omega} \Lambda_e \sin \theta} \quad (120b)$$

with

s' = the mean surface density of atoms in which peak l originates in cm^{-2}

s = the mean surface density of substrate atoms in cm^{-2}

s'/s = the fractional monolayer coverage of the atomic species in which peak l originates

d = the mean separation between layers of density s in the substrate (calculable from s/ρ).

These expressions are useful in surface-chemical studies at very low exposures to adsorbate molecules ($s'/s \lesssim 1$), as they permit an estimation of the fractional monolayer coverage from observed peak intensities. The assumption of no inelastic attenuation in the overlayer is an extreme one, but is justified because the macroscopic Λ_e' of case (c) is both difficult to estimate and dubious in its application to such thin, non-macroscopic layers, and also because it represents a correct limiting form for zero coverage.

The basic model presented here assumes an atomically-flat surface. As this will obtain only very rarely in actual experiments, assessments of the potential effects of surface roughness on XPS peak intensities have been made by Fadley *et al.*^{17, 202} It is found that roughness can appreciably affect both absolute and relative intensities, especially for systems with inhomogeneity as measured vertical to the surface,^{17, 203} with much depending upon the dimensional scale of the roughness relative to the attenuation lengths for x-rays and electrons involved. Roughness effects on angular-resolved measurements are discussed further in Section VI.B, and in considerably greater detail in other sources.^{17, 202, 203}

As a final comment concerning the equations presented here, it should be noted that, for complete generality, an angle-dependent instrument response function $R(E_k, \theta)$ must be included as a further factor in all of Eqs (115)–(120). The definition and determination of this response function are discussed elsewhere.^{17, 202} It is unity for the idealized geometry treated here (as long as θ is not too small). It has also been calculated and measured for one particular spectrometer system.⁷⁴ A further important property of this function is that it will generally be only weakly dependent on kinetic energy, and so will cancel to a very good approximation in peak intensity ratios obtained at a given angle θ . Thus, relative intensity measurements can be made in most cases without the necessity of evaluating the instrument response with θ .

3. *Applications to Quantitative Analysis.* The first detailed experimental tests of the simplest model for intensities originating in a uniform specimen represented by Eq. (115) above were carried out by Nefedov *et al.*¹⁶¹ and Carter *et al.*²⁰⁴ The study by Carter *et al.* made use of Eq. (94) to avoid the need of evaluating symmetry parameters, Eq. (109) for the energy dependence of attenuation lengths, and an empirically-determined instrument factor $\Omega_0(E_k)A_0(E_k)D_0(E_k)$. The Scofield calculations¹⁵¹ provided the cross-sections required. Theoretical relative intensities were calculated for subshells in a number of elements and comparisons were made with several sets of experimental data, including tabulations of measured relative intensities (or elemental sensitivities) by Wagner²⁰⁵ and Jorgensen and Berthou.²⁰⁶ In general, agreement to within $\pm 10\%$ was found. Powell and Larson²⁰⁷ have more recently considered the use of the same model from a somewhat more exact viewpoint, including a discussion of potential errors associated with determining experimental peak areas that are directly relatable to all of the processes involved in the differential photoelectric cross-section. Specifically, from 20% to 50% of the one-electron differential photoelectric cross-section is expected to appear as low-energy satellite intensity due to many-electron effects (cf. discussions in Sections III.F.1 and V.D.2). All of the factors in Eq. (115) were considered in detail, with the most accurate approximations being made whenever possible; for three pure compounds with carefully

cleaned surfaces, the agreement between experimental and theoretical relative intensities was $\sim \pm 5\%$. Thus, there are good reasons to be optimistic that XPS can be used for quantitative analyses of well-prepared homogeneous specimens with this accuracy. For systems exhibiting inhomogeneity near the surface (for example, a substrate/overlayer geometry), additional problems are encountered because at least two regions are involved, but, especially when coupled with angular-dependent measurements,¹⁷ accuracies of $\sim \pm 10\%$ again seem achievable (see also discussion in Section VI.B). Thus, XPS does have considerable analytical potential, particularly as a near-surface probe that is at least complementary to, and probably somewhat more quantitative and less destructive than, electron-excited Auger electron spectroscopy (AES). Powell²⁰⁸ has recently comparatively reviewed the use of XPS and AES in surface analysis.

IV. CORE ELECTRON BINDING ENERGY SHIFTS

A considerable fraction of XPS studies to date has been involved primarily with the precise measurement of core electron binding energies, and in particular with the measurement of chemical shifts in these binding energies. Such chemical shifts in fact provided much of the recent impetus for the development of XPS.³ The technique is rather uniquely qualified for such studies, as the usual x-rays utilized ($\text{MgK}\alpha = 1254 \text{ eV}$ and $\text{AlK}\alpha = 1487 \text{ eV}$) can penetrate to levels well below the vacuum level. The more common ultraviolet radiation sources presently limit UPS to valence levels and weakly bound core levels within $\sim 40 \text{ eV}$ of the vacuum level, on the other hand. Synchrotron radiation is also now beginning to be used to excite outer core levels with $E_b^V \lesssim 300 \text{ eV}$.^{15, 209}

The core levels of any atom can by definition be considered to represent filled subshells, and are found in XPS spectra to be relatively sharp in energy, with typical experimental widths of approximately 1–10 eV. The width observed for a core photoelectron peak depends upon several factors of both inherent and instrumental type. The most important inherent sources of width are:

- (1) the lifetime of the k -subshell core hole created by photoemission,
- (2) various possible values for the final state energy $E^f(N-1, K)$, as represented for example by multiplet splittings, multi-electron effects, or vibrational broadening (see Section V), and
- (3) unresolvable chemically-shifted peaks.

For the present discussion, the final-state complexities of item (2) will be neglected so as to yield a description analogous to that for a simple, closed-shell system. The most important instrumental sources and their typical

magnitudes are:

- (1) the exciting x-ray linewidth (approximately 1.0 eV for AlK α without monochromatization and approximately 0.4 eV with),
- (2) the finite resolving power of the electron spectrometer (for example, 0.3 eV for 0.03% resolution at $E_{\text{kin}} = 1000$ eV), and
- (3) non-uniform charging of the specimen (variable magnitude, as discussed in connection with Eq. (2)).

The minimum core linewidths observed to date have been a few tenths of an eV.^{41, 210} Thus, provided that the various inherent sources of linewidth and non-uniform charging are not too large, it is possible in principle to measure chemical shifts of the order of 0.1 eV between two or more photoelectron peaks resulting from emission from the same subshell.

If the same atom A is considered as existing either in two chemically inequivalent sites in the same compound labelled 1 and 2 or in two different compounds which can be similarly labelled 1 and 2, then the chemical shift ΔE_{b} of the k electron binding energy can be written simply as the difference of two binding energies. For gaseous specimens with vacuum-referenced binding energies, this means that

$$\begin{aligned} \Delta E_{\text{b}}^{\text{V}}(A, k, 1-2) &= (E_{\text{b}}^{\text{V}}(k))_1 - (E_{\text{b}}^{\text{V}}(k))_2 \\ &= (E_{\text{kin}})_2 - (E_{\text{kin}})_1 \quad (\text{gases}) \end{aligned} \quad (121)$$

where $A, k, 1-2$ represent the minimum number of parameters required to specify a chemical shift, that is, the atom and level, and the two chemical sites or compounds involved. Here, we have neglected charging effects. For solids with Fermi-referenced binding energies, the corresponding equation is

$$\begin{aligned} \Delta E_{\text{b}}^{\text{F}}(A, k, 1-2) &= (E_{\text{b}}^{\text{F}}(k))_1 - (E_{\text{b}}^{\text{F}}(k))_2 \\ &= (E_{\text{kin}})_2 - (E_{\text{kin}})_1 + (\phi_{\text{spect}})_2 - (\phi_{\text{spect}})_1 + (V_{\text{c}})_2 - (V_{\text{c}})_1 \end{aligned} \quad (122)$$

where possible effects due to spectrometer work function changes or differences in charging potential have been included. Provided that both of the latter effects are negligible, Eq. (122) simplifies to a form identical to that of Eq. (121),

$$\begin{aligned} \Delta E_{\text{b}}^{\text{F}}(A, k, 1-2) &= (E_{\text{b}}^{\text{F}}(k))_1 - (E_{\text{b}}^{\text{F}}(k))_2 \\ &= (E_{\text{kin}})_2 - (E_{\text{kin}})_1 \quad (\text{solids}) \end{aligned} \quad (123)$$

As has been noted previously, many theoretical calculations of chemical shifts have an implicit vacuum reference level. This is quite satisfactory for gas-phase work, but not necessarily for work on solids. For the latter case, the relationship between vacuum-referenced and Fermi-referenced chemical shifts is, from Eq. (5):

$$\Delta E_{\text{b}}^{\text{V}}(A, k, 1-2) = \Delta E_{\text{b}}^{\text{F}}(A, k, 1-2) + (\phi_{\text{s}})_1 - (\phi_{\text{s}})_2 \quad (124)$$

Thus, in directly comparing vacuum-referenced theoretical calculations and Fermi-referenced experimental values, it is required to neglect the work function difference between the two solids, $(\phi_{\text{s}})_1 - (\phi_{\text{s}})_2$. In most work to date, no serious effects of work function differences have been observed, although there is generally more scatter on a plot of measured chemical shifts against calculated chemical shifts for solids than on a corresponding plot for gases.^{3, 4, 7, 211} This additional scatter could be connected with reference level effects or specimen charging or both. Both of these effects deserve further study.

The theoretical interpretation of core-level chemical shifts has been attempted at various levels of sophistication, with each level providing a certain degree of agreement with experiment and interpretive utility. Several reviews of these procedures have been presented previously,^{3, 4, 7, 8, 109} and therefore only a brief outline of the most important models, their uses, and their limitations will be given here. These procedures will be considered in approximate order of descending accuracy. From the outset, it is clear that the major goal of such analyses is to derive chemically-significant information concerning the initial state electronic structure of the system. Various final-state complexities (see Section V) can tend at times to obscure the initial-state chemical information, but it has nonetheless proven possible to derive it relatively straightforwardly for a number of systems.

The most accurate calculation of any binding energy shift must in general involve determining two binding energies, or a total of two initial-state calculations and two final hole-state calculations. The possible errors in shifts are thus approximately twice as large as for a single binding energy when calculations are performed at a given level. Various procedures for calculating binding energies have already been discussed in Sections III.A and III.B. Relative to a Koopmans' Theorem approach, corrections due to relaxation, relativistic, and correlation effects must be considered, as summarized in Eq. (55). A chemical shift in such binding energies between two chemically-inequivalent sites or compounds labelled 1 and 2 is thus

$$\begin{aligned} \Delta E_{\text{b}}^{\text{V}}(A, k, 1-2) &= (E_{\text{b}}^{\text{V}}(k))_1 - (E_{\text{b}}^{\text{V}}(k))_2 \\ &= -(\epsilon_k)_1 + (\epsilon_k)_2 - (\delta E_{\text{relax}})_1 + (\delta E_{\text{relax}})_2 \\ &\quad + (\delta E_{\text{relat}})_1 - (\delta E_{\text{relat}})_2 + (\delta E_{\text{corr}})_1 - (\delta E_{\text{corr}})_2 \end{aligned}$$

or

$$\Delta E_{\text{b}}^{\text{V}}(A, k, 1-2) = -\Delta \epsilon_k - \Delta(\delta E_{\text{relax}}) + \Delta(\delta E_{\text{relat}}) + \Delta(\delta E_{\text{corr}}) \quad (125)$$

In view of the physical origins of the relativistic and correlation corrections for a given core level, they will tend to have values of approximately the same magnitude from one site or compound to another. The same should also be true, but probably to a lesser degree, for relaxation corrections. Thus,

in many cases, it would be expected that $\Delta(\delta E_{relax})$, $\Delta(\delta E_{relat})$, and $\Delta(\delta E_{corr})$ would be considerably smaller in magnitude than the individual corrections to either $(E_b^V(k))_1$ or $(E_b^V(k))_2$, and therefore that the Koopmans' Theorem value $-\Delta\epsilon_k$ would represent a quite good approximation to the chemical shift $\Delta E_b^V(A, k, 1-2)$.¹⁰⁵ (This need not always be true, however, and we discuss both below and in Section V.B a few special examples in which $\Delta(\delta E_{relax})$ is very large.) For similar reasons, the quality of the wave function utilized in obtaining ϵ_k is often not as critical as might be imagined. That is, approximate wave functions with the same degree of self-consistency for both systems 1 and 2 may yield a reasonably accurate value of $\Delta\epsilon_k$ (which is, after all, a small perturbation primarily due to changes in valence electron charge distribution). Thus, the use of Koopmans' Theorem in conjunction with various approximate calculation procedures such as minimal-basis-set or double-zeta-basis-set Hartree-Fock calculations has met with success in analyzing much chemical shift data. It appears that molecular wave functions of double-zeta quality can be utilized to predict chemical shifts from $-\Delta\epsilon_k$ which agree with experiment to within $\sim \pm 1$ eV for a carefully-chosen set of molecules not too much different in size, in spite of the fact that the orbital energies for such levels as C1s and N1s tend to be as much as 10–20 eV higher than the experimental binding energies due to relaxation. In Fig. 18, experimental C1s binding energies for different gaseous molecules are compared to 1s orbital energies from various theoretical calculations of roughly double-zeta accuracy. Although the two scales are shifted relative to one another by about 15 eV, the points lie very close to a straight line of unit slope. Thus, for sets of molecules chosen to minimize $\Delta(\delta E_{relax})$, $\Delta(\delta E_{relat})$, and $\Delta(\delta E_{corr})$, chemical shifts should be calculable from these orbital energies with an accuracy roughly equal to the scatter of points about the straight line or ± 1 eV.^{7, 8, 109}

Although the use of Koopmans' Theorem in estimating binding energy shifts from reasonably accurate molecular-orbital calculations can thus be expected to yield fairly reliable values for well-chosen compounds, it is especially important to be able to include the effects of relaxation in such calculations. Such effects are treated in more detail in Section V.B, but at this point it is appropriate to mention a calculation procedure that lies intermediate between those of Koopmans' Theorem and doing accurate SCF calculations on both initial and final states. This method was developed by Goscinski *et al.*^{212, 213} and is termed the transition-state or transition-operator method. In this method, relaxation effects are allowed for to second order in perturbation theory by solving a set of Hartree-Fock equations in which the Fock operator on the left-hand side of Eq. (42) is adjusted so as to involve an effective 1/2 occupation number as far as electron-electron interactions involving the k th spin-orbital from which emission is to occur. For

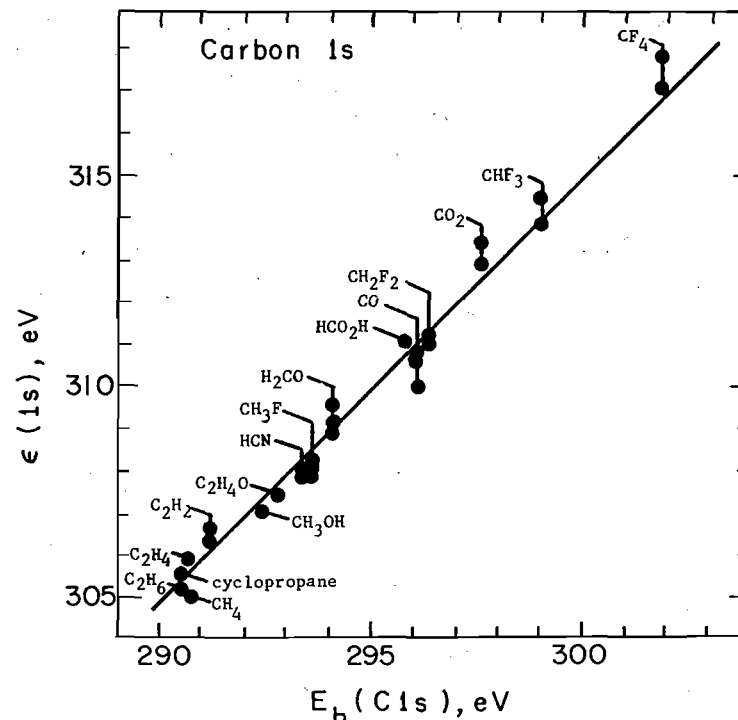


Fig. 18. Plot of carbon 1s binding energies calculated via Koopmans' Theorem against experimental binding energies for several carbon-containing gaseous molecules. For some molecules, more than one calculated value is presented. The slope of the straight line is unity. The two scales are shifted with respect to one another by 15 eV, largely due to relaxation effects. All of the theoretical calculations were of roughly double-zeta accuracy or better. (From Shirley, ref. 7.)

the fictitious "transition state" thus calculated for each initially-occupied spin-orbital, negatives of the one-electron energy eigenvalues yield estimates for binding energies that should include relaxation effects to second order. Comparisons of core- and valence-electron binding energy calculations for He, Li, Be, Ne, and Ar^{212, 213} do indeed show that this method yields results in very good agreement with the more laborious procedure of calculating and subtracting accurate total energies for both the initial and final states.

The next approximation moving away from the Koopmans' Theorem method for calculating chemical shifts is the potential model that was used in the earliest quantitative discussions of chemical shifts by Siegbahn *et al.*³ and Fadley *et al.*¹⁰⁵ In this model, the interaction of a given core electron with all other electrons and nuclei in a molecule or solid is divided into an intra-atomic term and an extra-atomic term. Furthermore, the assumption is made that each atom in the array has associated with it a net charge consistent with

overall electroneutrality. These net changes thus account in some way for the displacement of electronic charge which occurs in the formation of chemical bonds. In very covalent systems, this model is of questionable utility, but several variations of it have been applied to a wide variety of systems with considerable success.^{3, 4, 105, 214-219} More recently, it has been termed a ground-state-potential model (GPM)²¹⁵ to emphasize its usual neglect of final-state effects (especially relaxation). Consider an atom A with a charge q_A situated in an array of atoms to which it is somehow bonded. The binding energy of the k th electron in this atom can then be expressed as a sum of two terms, one intra-atomic free-ion term and one extra-atomic potential:

$$E_b^V(k) = E_b^V(k, q_A) + \frac{V}{\text{Potential due to all other atoms}} \quad (126)$$

Compound Free ion of charge q_A

The first term is a binding energy for the k th electron in a free-ion of charge q_A and the second term is the total potential due to all other atoms in the array. The first term might be evaluated by means of a free-ion Hartree-Fock calculation, for example (although much simpler procedures for dealing with it will also be discussed). The simplest way to calculate the second term is to assume that the other atoms behave as classical point charges in creating the potential V . Thus,

$$V = e^2 \sum_{i \neq A} \frac{q_i}{r_{iA}} \quad (127)$$

where the summation is over all atoms except that of interest in the array. If the array is a crystal, then V represents a convergent infinite sum that is closely related to the Madelung energy of the solid.¹⁰⁵ Thus, both terms in Eq. (126) may be relatively easy to obtain for a number of systems. Calculating a chemical shift using Eq. (126) gives

$$\Delta E_b^V(A, k, 1-2) = E_b^V(k, q_{A, 1}) - E_b^V(k, q_{A, 2}) + V_1 - V_2 \quad (128)$$

where $q_{A, 1}$ and $q_{A, 2}$ are the net charges on atom A in the sites 1 and 2, respectively. It is instructive to consider the predictions of this model for several simple systems, as it is found to explain qualitatively and semi-quantitatively several basic features of chemical shifts.

The difference of free-ion terms in Eq. (128) represents a change in binding energy concomitant with a change in the valence electron orbital occupation of the atom such that the net charge is altered from $q_{A, 2}$ to $q_{A, 1}$. In the first analyses based upon the potential model, Fadley *et al.*¹⁰⁵ calculated such changes for removal of successive valence electrons from various ionic states of I, Br, Cl, F, and Eu, using a minimum-basis-set Hartree-Fock calculation

and Koopmans' Theorem. These results are presented in Figs 19-23, where the shifts are plotted against the location of the maximum magnitude of the radial function for each orbital. Several systematic features of these results can be noted. For iodine, all core levels shift by very nearly the same amount. This is basically true also for Br and Cl, although as the atomic size decreases there is less constancy in the core shifts, with outer orbitals showing slightly

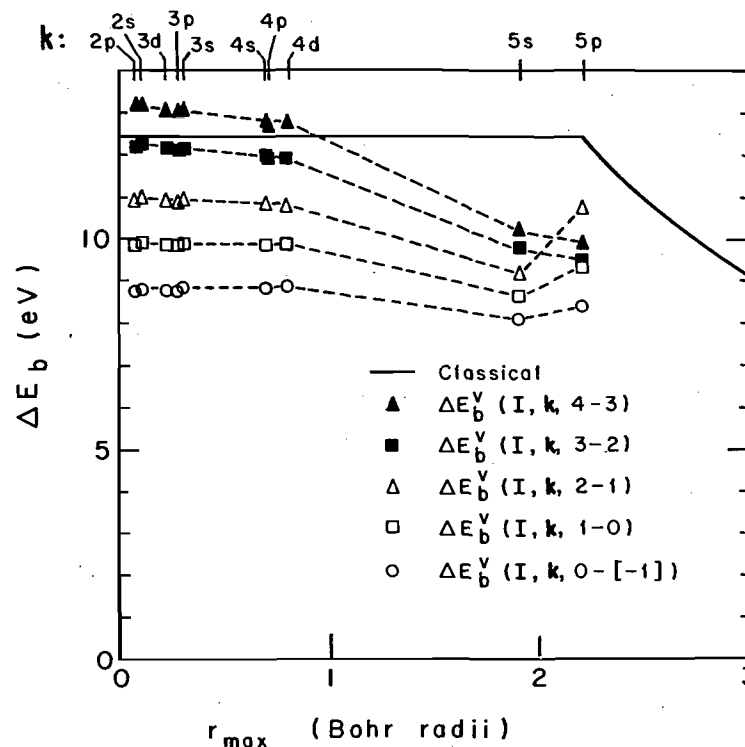


Fig. 19. Koopmans' Theorem free-ion binding energy shifts caused by the removal of a valence $5p$ electron from various configurations of iodine, plotted against the location of the radial maxima for the various orbitals. The configurations are: $+4=5s^25p^2$, $+3=5s^25p^3$, $+2=5s^25p^4$, $+1=5s^25p^5$, $0=5s^25p^6$, and $-1=5s^25p^6$. The solid curve shows the classical shift resulting from the removal of an electron from a thin spherical shell of charge with the radius of the $5p$ maximum. (From Fadley *et al.*, ref. 105.)

lower shifts. In all of the halogens, the p valence electrons are largely external to the core, as is evidenced by the location of the core- and valence-orbital radial maxima. For Eu, which by contrast has valence $4f$ electrons overlapping considerably with the core electrons, the core shifts are not at all constant, and furthermore can be about twice as large per unit change in valence shell occupancy as for the halogens. All of these results are qualitatively consistent with a very simple classical model of the interaction between core

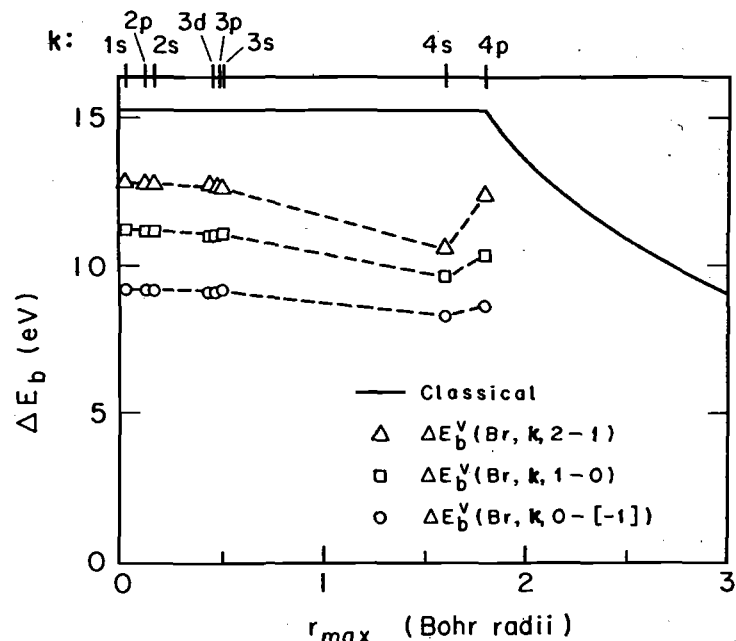


Fig. 20. Calculated free-ion binding energy shifts caused by the removal of a valence $4p$ electron from bromine, plotted as in Fig. 19. The configurations are: $+2=4s^24p^3$, $+1=4s^24p^4$, $0=4s^24p^5$, and $-1=4s^24p^6$. (From Fadley *et al.*, ref. 105.)

and valence electrons. The valence electron charge distribution can be approximated by a spherical charged shell of radius r_v , where r_v can reasonably be taken to be the average radius of the valence orbitals or the location of their radial function maximum. The classical potential inside this spherical shell will be constant and equal to q/r_v , where q is the total charge in the valence shell. If the charge on this shell is changed by δq , the potentials, and thus binding energies, of *all* the core electrons located well inside the shell will shift by an amount $\delta E_b^V = \delta q/r_v$. Such classical calculations are shown as the solid lines in Figs 19–23 and are found to give results that correctly predict the trends in relative shifts from subshell to subshell, as well as being in semi-quantitative agreement with the absolute magnitudes of the more accurate Hartree–Fock calculations. In general then, all core electrons which overlap relatively little with the valence shell are predicted to shift by approximately the same amount, and this prediction is verified experimentally.¹⁰⁵ The magnitude of the shift per unit change in charge should also increase as the valence shell radius r_v decreases, as is illustrated for the case of Eu. A more accurate estimate of $\delta E_b^V/\delta q$ for any atom is given by the change in Hartree–Fock ϵ_k upon removal of one valence electron. From Eq. (47),

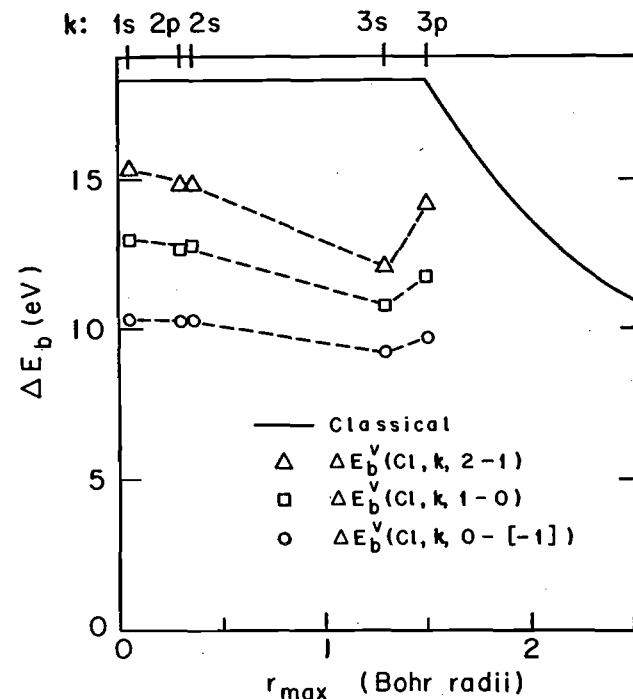


Fig. 21. Calculated free-ion binding energy shifts caused by the removal of a valence $3p$ electron from chlorine, plotted as in Fig. 19. The configurations are: $+2=3s^23p^3$, $+1=3s^23p^4$, $0=3s^23p^5$, and $-1=3s^23p^6$. (From Fadley *et al.*, ref. 105.)

this will be given by $J_{k\text{-valence}} - K_{k\text{-valence}}$ (spins parallel) or $J_{k\text{-valence}}$ (spins anti-parallel). As the core-valence exchange integral $K_{k\text{-valence}}$ will be of significant magnitude only if there is appreciable overlap between the core and valence orbitals, we can neglect $K_{k\text{-valence}}$ in comparison to $J_{k\text{-valence}}$. (For example, in carbon, $J_{1s, 2s} = 22.1$ eV, $K_{1s, 2s} = 1.4$ eV, $J_{1s, 2p} = 20.8$ eV, and $K_{1s, 2p} = 0.6$ eV.) Thus, $\delta E_b^V/\delta q$ should be approximately equal to $J_{k\text{-valence}}$, the core-valence Coulomb integral. The magnitude of such Coulomb integrals are, in fact, found to be in good agreement with the shifts calculated in Figs 19–21 for I, Br, and Cl. As a final point, the free ion term $\delta E_b^V/\delta q$ is of the order of 10–20 eV/electron charge for essentially all elements.

If the potential term V in Eq. (126) is now considered, it is found that its value also will be of the order of 10–20 eV for a transfer of unit electron charge from one atom to its nearest neighbors,^{3, 105} as, for example, in a highly ionic alkali halide crystal. Furthermore, for a given molecule or solid the free-ion term $(\delta E_b^V/\delta q) \cdot \delta q$ will be opposite in sign to V , as V must account for the fact that charge is not displaced to infinity, but only to adjacent atoms during chemical bond formation. Thus, both the free-ion and potential terms

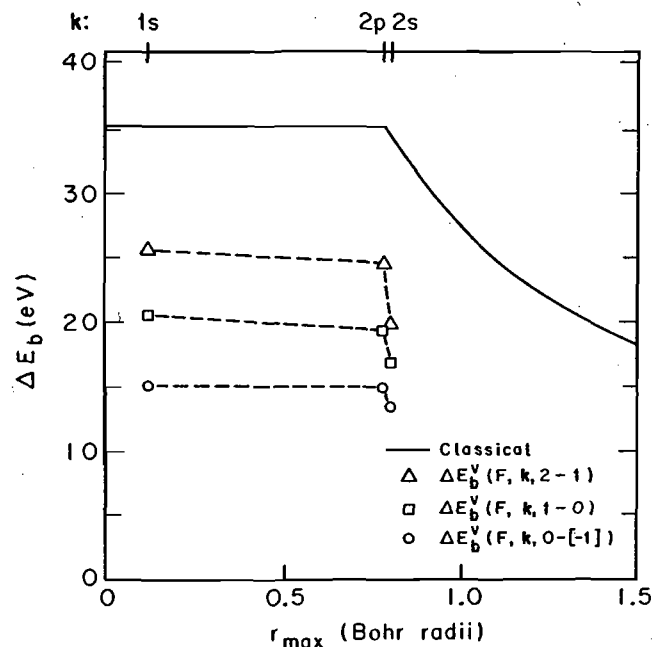


Fig. 22. Calculated free-ion binding energy shifts caused by the removal of a valence $2p$ electron from fluorine, plotted as in Fig. 19. The configurations are: $+2=2s^22p^3$, $+1=2s^22p^4$, $0=2s^22p^5$, and $-1=2s^22p^6$. (From Fadley *et al.*, ref. 105.)

in Eq. (126) must be calculated with similar accuracy if the resultant binding energy (or chemical shift) value is to have corresponding accuracy. This represents one of the possible drawbacks of such potential models.

Several other models based essentially on Eq. (126) have been utilized in analyzing core electron chemical shifts,^{7, 8} and the detailed theoretical justifications for them have been discussed by Manne,²¹⁶ Basch,²¹⁷ and Schwartz.²¹⁸ For example, Siegbahn *et al.*⁴ and Gelius *et al.*²¹¹ have been able to describe the core binding energy shifts for a variety of compounds of C, N, O, F, and S with the following equation:

$$\Delta E_b^V(A, k, 1-2) = C_A q_A + V + I \quad (129)$$

where 2 represents a fixed reference compound. The various atomic charges q_i in each molecule were estimated using CNDO molecular-orbital theory, and these charges were then substituted into Eq. (127) to compute V . Then the constants C_A and I were determined empirically by a least-squares fit to the experimental data. Such fits give a reasonably consistent description of the data, as is shown in Fig. 24 for various compounds of carbon, and, in particular, the parameters C_A are found to be rather close to the $1s$ -valence

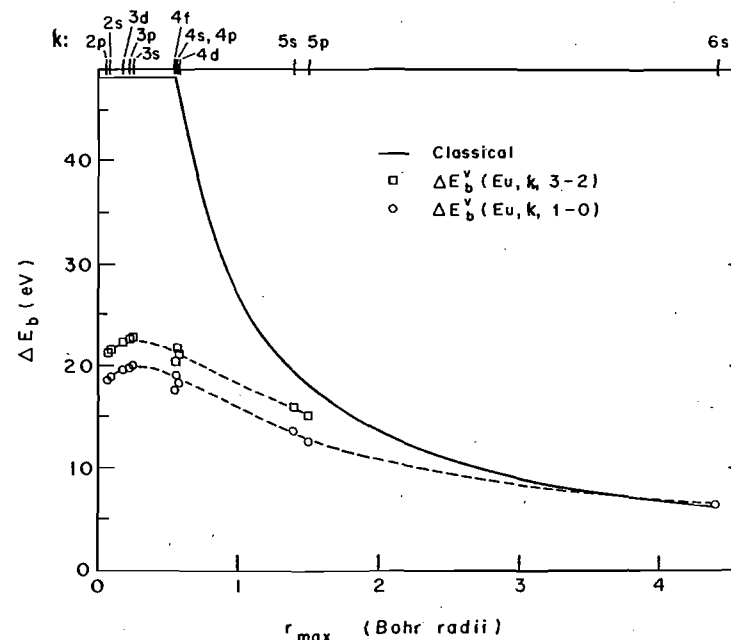


Fig. 23. Calculated free-ion binding energy shifts caused by the removal of a valence $4f$ electron from europium, plotted as in Fig. 19. The configurations are: $+3=4f^6$, $+2=4f^7$, $+1=4f^66s^2$, and $0=4f^76s^2$. Note the non-constancy of the core-level shifts by comparison to Figs 19-22. (From Fadley *et al.*, ref. 105.)

Coulomb integral $J_{1s\text{-valence}}$ computed for atom A . Thus, Eq. (129) as utilized in this semi-empirical way is consistent with a somewhat more exact theoretical model. Note, however, that all molecules are not adequately described by this model and that, for example, the points for CO and CS₂ lie far from the straight line predicted by Eq. (129). As might be expected, if an orbital energy difference based on near Hartree-Fock wave functions is used for the calculated shift of CO, much better agreement with experiment is obtained, as is shown in Fig. 18.

In another variant of the potential model proposed by Davis *et al.*,²¹⁹ a series of chemical shift measurements on core levels in all the atoms of several related molecules are used to derive a self-consistent set of atomic charges. For each atom in each molecule, the measured chemical shift is written in terms of undetermined atomic charges as

$$E_b^V(A, k, 1-2) = C_A' q_A + e^2 \sum_{i \neq A} \frac{q_i}{r_{Ai}} \quad (130)$$

where C_A' is set equal to $J_{1s\text{-valence}}$ for atom A . The resultant set of equations is solved self-consistently for the q_A values on each atom. Such calculations

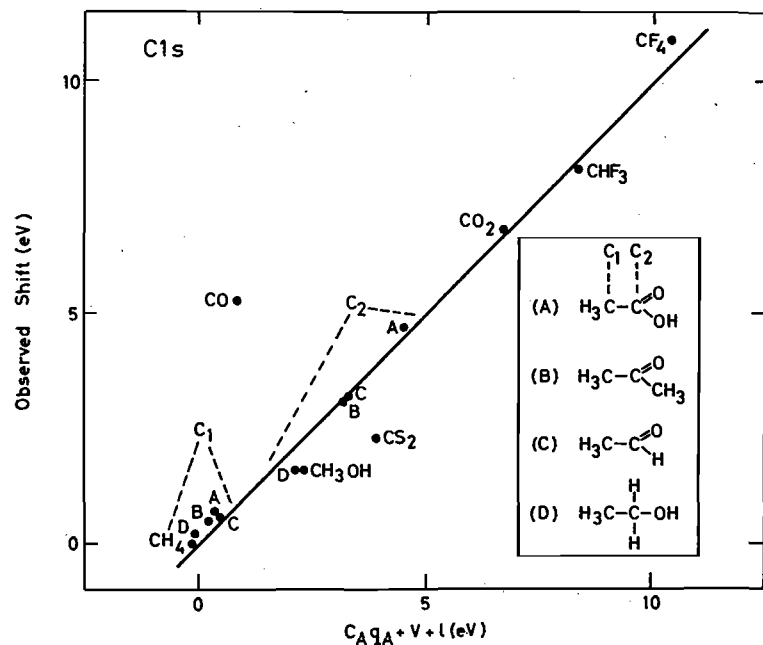


Fig. 24. A comparison of the experimental carbon 1s chemical shift values for several molecules with shifts calculated using the potential model of Eq. (129). The shifts were measured relative to CH_4 . The parameters of the straight line were $C_A = 21.9$ eV/unit charge and $l = 0.80$ eV. (From Siegbahn *et al.*, ref. 4.)

on a series of fluorinated benzenes²¹⁹ give charges which agree rather well with charges obtained from calculations based upon the CNDO/2 method, as is apparent in Fig. 25.

Another procedure for analyzing chemical shift data that can be at least indirectly related to the various potential models is based on summing empirically determined shifts associated with each of the groups bonded to the atom of interest, and has been developed primarily by Gelius, Hedman, and co-workers.^{211, 220} Each group shift is assumed to be constant and independent of the other groups present and is determined from a series of chemical shift measurements on reference compounds representing suitable combinations of the groups. The chemical shift associated with atom A in a given compound is thus written as

$$\Delta E_b(A, k, 1-2) = \sum_{\text{groups}} \Delta E_b(\text{group}) \quad (131)$$

where 2 constitutes some reference compound against which all of the group shifts are determined. The applicability of this procedure has been demonstrated on a large number of carbon- and phosphorous-containing compounds,^{211, 220} and a summary of results obtained for phosphorus compounds

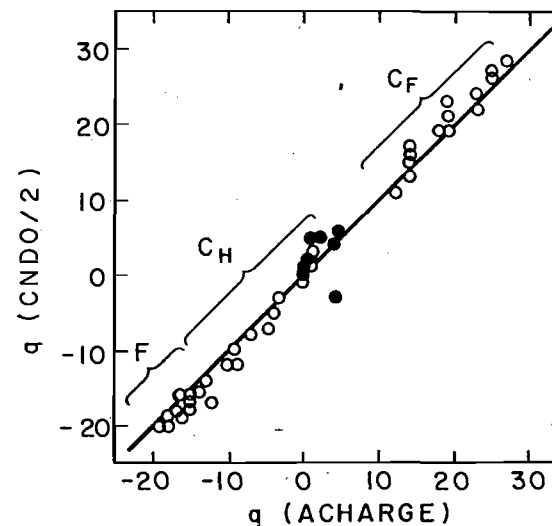


Fig. 25. Atomic charges for the various fluorinated benzenes as calculated by the CNDO/2 method and as derived experimentally ("ACHARGE") from chemical shift measurements on carbon and fluorine and Eq. (130). Charges are in units of 1/100 of an electronic charge. The filled circles represent average hydrogen charges. (From Davis *et al.*, ref. 219.)

is shown in Fig. 26. The relationship of this procedure to a potential model is possible if it is assumed that each group induces a valence electron charge change of $\delta q(\text{group})$ on the central atom and also possesses essentially the same intragroup atomic charge distribution regardless of the other groups present. Then both the free-ion and potential terms in Eq. (126) become simply additive for different groups, as is required in Eq. (131). In addition, however, the group shift can be considered to include empirically an approximately constant intragroup relaxation correction, thus going somewhat beyond a ground-state potential model in one sense.

Some of the first analyses of shift data were performed simply by plotting ΔE_b against atomic charges which were estimated by various procedures, among them CNDO or extended-Hückel calculations, or most crudely by electronegativity arguments. The implicit neglect of the potential terms of Eqs (126) and (128) in such a correlation of ΔE_b against q_A can, however, lead to a rather wide scatter of the points about a straight line or curve drawn through them. Hendrickson *et al.*,²²¹ for example, found two rather distinct clusters of data points described by two different curves in comparing nitrogen 1s shifts with charges calculated via CNDO. However, there is in general a systematic increase in E_b with increasing q_A for most compounds, particularly if the compounds are chosen to be rather similar in bonding type. One such series of compounds for which a simple electronegativity correlation has proven adequate is the halomethanes. Thomas²²² expressed the C1s

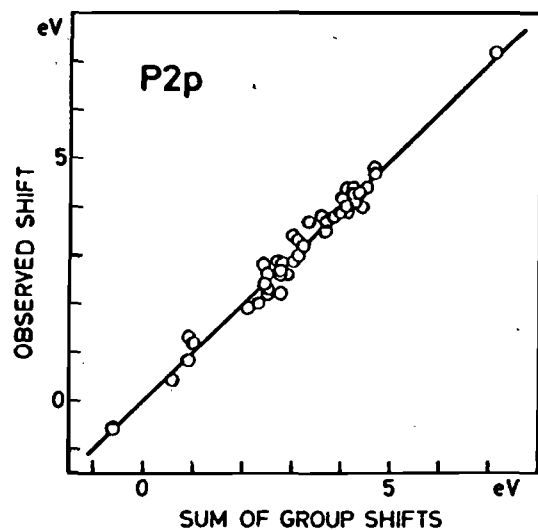


Fig. 26. A comparison of measured phosphorous 2p chemical shifts with shifts calculated using the group shift model of Eq. (131). The compounds were studied as solids. (From Hedman *et al.*, ref. 220.)

shifts between CH_4 and a given halomethane as a linear combination of the electronegativity differences between the various ligands present and hydrogen:

$$\Delta E_{\text{b}}^{\text{V}}(\text{C}1s, \text{halomethane}-\text{CH}_4) = C \sum_i (X_i - X_{\text{H}}) \quad (132)$$

where C is an empirical constant, X_i is the ligand electronegativity, and X_{H} is the electronegativity of hydrogen. Such a correlation is shown in Fig. 27. The explanation for the success of this correlation would seem to be as a further simplification of the group shift approach, in which each monatomic ligand induces a charge transfer δq_i proportional to $X_i - X_{\text{H}}$, and the potential term involved is also simply proportional to δq_i for a nearly constant carbon-ligand bond length. Thus, the potential model of Eq. (128) can be reduced to the form of Eq. (132). Such correlations should be used very cautiously, however, as exceptions are relatively easy to encounter: for example, in the series of molecules generated by adding successive methyl groups to ammonia (NH_3 , $\text{NH}_2(\text{CH}_3)$, $\text{NH}(\text{CH}_3)_2$, and $\text{N}(\text{CH}_3)_3$), the $\text{N}1s$ binding energy is observed to *decrease* with the addition of CH_3 groups,²²³ in complete disagreement with the greater positive charge expected on the central nitrogen because $X_{\text{C}} > X_{\text{H}}$. The major cause of this discrepancy is believed to be the greater relaxation energy associated with the polarization of the $-\text{CH}_3$ group around the $\text{N}1s$ hole,²²³ a type of effect discussed in more detail in Section V.B.

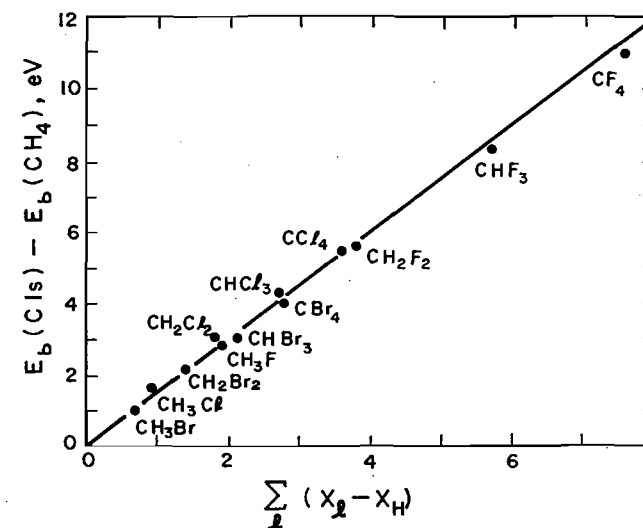


Fig. 27. Carbon 1s chemical shifts for halogenated methanes measured relative to CH_4 and plotted against shifts calculated on the basis of a sum of ligand-hydrogen electronegativity differences, as in Eq. (132). (From Thomas, ref. 222.)

Among the other methods utilized to analyze chemical shift data, mention should also be made of a procedure introduced by Jolly and Hendrickson^{224, 225} for relating chemical shifts to thermochemical data. In this method, it is noted that to a good approximation the atomic core of an atom with nuclear charge Z and a single core-level hole acts on any surrounding electrons in an equivalent way to the filled core of an atom with nuclear charge $Z+1$. If the core electron overlap with the outer electrons is small, then the nuclear shielding should be nearly complete and this assumption is reasonable. As a more quantitative indicator of how good this approximation is for a medium- Z atom, Table I summarizes the results of highly-accurate numerical Hartree-Fock calculations by Mehta, Fadley, and Bagus¹⁰² for atomic Kr with various core-level holes and its equivalent-core analogue Rb^{+1} . With neutral Kr as a reference, the fractional decreases in average subshell radii $1 - \langle r_{ni} \rangle / \langle r_{ni} \rangle_0$ are tabulated for different core-hole locations in Kr^{+1} and for the equivalent-core species Rb^{+1} . For the equivalent-core approach to be fully valid, these fractional changes should be nearly identical between true Kr hole states and Rb^{+1} , thus indicating the same degree of inward relaxation around both a core hole and a nuclear charge that is incremented from Z to $Z+1$. For the various true hole states in subshells that can be designated $n_{\text{hole}}l_{\text{hole}}$, the fractional decreases in $\langle r_{ni} \rangle$ range from ~ 0 for subshells with $n \lesssim n_{\text{hole}}$ up to 11% for the outermost $4p$ orbital. The equivalent-core Rb^{+1} orbitals by contrast show significant relaxation in all

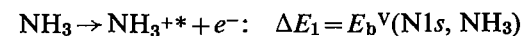
TABLE I

Average radii for the various subshells of neutral Kr $\langle r_{nl} \rangle_0$, together with the fractional changes in average radii between neutral Kr and all possible core-hole states. The changes between neutral Kr and the equivalent-core ion Rb^+ are also given. The units for $\langle r_{nl} \rangle_0$ are bohrs. The Kr^+ values are divided into those for $n \leq n_{\text{hole}}$ and $n > n_{\text{hole}}$ (from Mehta *et al.*, ref. 102)

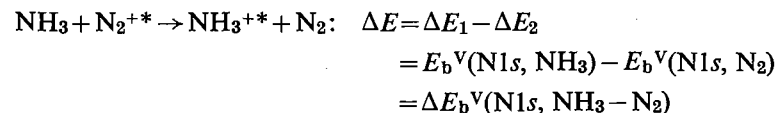
Atom	L, S term	$\frac{\langle r_{1s} \rangle_0}{1 - \langle r_{1s} \rangle_0}$	$\frac{\langle r_{2s} \rangle_0}{1 - \langle r_{2s} \rangle_0}$	$\frac{\langle r_{3s} \rangle_0}{1 - \langle r_{3s} \rangle_0}$	$\frac{\langle r_{2p} \rangle_0}{1 - \langle r_{2p} \rangle_0}$	$\frac{\langle r_{3p} \rangle_0}{1 - \langle r_{3p} \rangle_0}$	$\frac{\langle r_{3d} \rangle_0}{1 - \langle r_{3d} \rangle_0}$	$\frac{\langle r_{4s} \rangle_0}{1 - \langle r_{4s} \rangle_0}$	$\frac{\langle r_{4p} \rangle_0}{1 - \langle r_{4p} \rangle_0}$
$\text{Kr}^+ (-1s)$	3S	0.0424	0.1873	0.5378	0.1619	0.5426	0.5509	1.6294	1.9516
$\text{Kr}^+ (-2s)$	3S	0.0049	0.0185	0.0273	0.0267	0.0381	0.0558	0.0722	0.1142
$\text{Kr}^+ (-2p)$	3P	0.0000	0.0010	0.0194	0.0087	0.0268	0.0534	0.0662	0.1078
$\text{Kr}^+ (-3s)$	3S	0.0008	0.0074	0.0209	0.0026	0.0304	0.0542	0.0683	0.1083
$\text{Kr}^+ (-3p)$	3P	0.0000	-0.0009	0.0016	0.0004	0.0105	0.0251	0.0606	0.1007
$\text{Kr}^+ (-3d)$	3D	0.0001	0.0006	0.0077	-0.0006	0.0028	0.0248	0.0617	0.1019
Rb^+	$1S$	0.0000	0.0003	0.0089	0.0003	0.0119	0.0272	0.0618	0.1003
		0.0275	0.0294	0.0366	0.0306	0.0403	0.0537	0.0799	0.1150

subshells, with a range between 3% for $1s$ and 11% for $4p$. Relaxation for subshells with $n \ll n_{\text{hole}}$ is thus much overestimated by the use of an equivalent core, whereas for $n > n_{\text{hole}}$, the overestimates range from only $\sim 0-1\%$ in absolute fractional radius change. Thus, the equivalent-core model is a reasonable and useful first approximation, although it is certainly expected to overestimate relaxation effects due to core-hole formation.

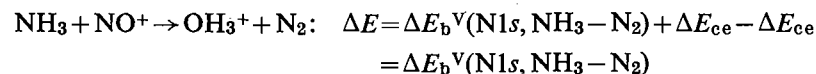
In applying the equivalent-core model to chemical-shift analyses, it is assumed^{224, 225} that an exchange of cores can be made in the final-state ion without appreciably altering the valence electron charge distribution or equilibrium nuclear geometry. (The results in Table I for the $4s$ and $4p$ subshells suggest that this is a good approximation.) Thus, in considering core-level emission from a species containing nitrogen, an $\text{O}^{+6} 1s^2$ core can be exchanged for the $\text{N}^{+6} 1s = \text{N}^{+6*}$ core, where the asterisk denotes the presence of the $1s$ core hole. Such core exchanges can be utilized to write binding energy shifts in terms of thermodynamic heats of reaction, and hence to predict either shifts from thermodynamic data or thermodynamic data from shifts. As one example of the application of this procedure, let us consider $1s$ photoelectron emission from gaseous NH_3 and N_2 as chemical reactions in which the electron is assumed to be formed exactly at the vacuum level and therefore with no kinetic energy:



These reactions are endothermic with internal energy changes ΔE_1 and ΔE_2 given by the $1s$ binding energies in NH_3 and N_2 . Subtracting the second reaction from the first gives



with an internal energy change precisely equal to the $\text{N}1s$ chemical shift between NH_3 and N_2 . However, this reaction involves the unusual and very short-lived species N_2^{+*} and NH_3^{+*} . Now, it is assumed that the N^{6+*} core can be replaced by the O^{6+} core in either N_2^{+*} or NH_3^{+*} with only a small gain or loss of energy that can be termed the core-exchange energy ΔE_{ce} . As long as the core-exchange energy is very nearly the same in both N_2^{+*} and NH_3^{+*} , then the overall energy change associated with the reaction is not affected by core exchange. That is, we have a final reaction of



Therefore, the chemical shift is equal to a thermodynamic heat of reaction involving well-known species. This procedure has been applied to an analysis of $1s$ shifts in compounds of N, C, O, B, and Xe, and very good agreement is obtained between experimental ΔE_b values and thermochemical estimates of these shifts. Such a comparison for nitrogen $1s$ is shown in Fig. 28. This analysis is closely related to the isodesmic processes discussed by Clark,⁹ and is also reviewed in more detail by Jolly¹³ in this series.

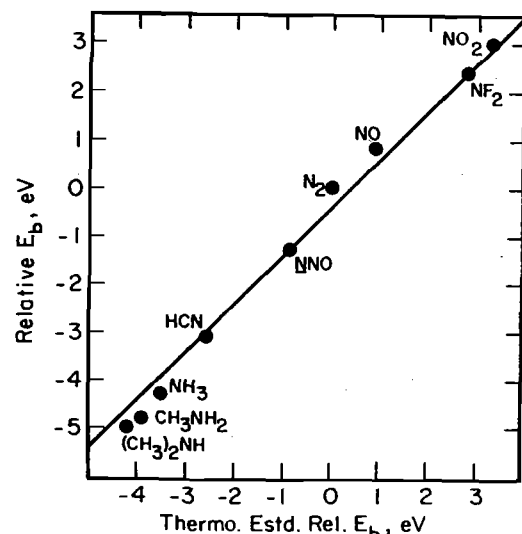


Fig. 28. Plot of experimental $N1s$ binding energy shifts relative to N_2 for several molecules versus values calculated using equivalent-core exchange and thermodynamic data. The slope of the line is unity. (From Jolly, ref. 225.)

Finally, a few other methods in which core electron binding energy shifts can be used should be mentioned:

(1) Attempts have been made to derive bonding information from relative binding energy shifts of different levels in the same atom. From Figs 19–23, it is clear that the outer core and valence levels of a given atom need not shift by the same amount as inner core levels, especially if relatively penetrating valence levels are present as in Eu. Such *relative* shifts of different levels can for certain cases be simply related to the basic Coulomb and exchange integrals involved, and then utilized to determine properties of the valence electron charge distribution. In particular, the relative shifts of the inner core $3d_{3/2}$ and valence $5p_{3/2}$ levels have been measured for iodine in various alkyl iodides and HI, and these shifts have been found by Hashmall *et al.*²²⁶ to be consistent with a simple bonding model of the compounds involved. More

recently, Aono *et al.*²²⁷ have carried out a similar relative shift study of rare-earth compounds that quantitatively confirms the non-constancy of the intra-atomic free-ion shifts as predicted, for example, for Eu in Fig. 23.

(2) In another type of analysis, core-level chemical shifts for several homologous series of the form RXH with $X=O, N, P$, and R =various substituent groups have also been found to be approximately equal to relative proton affinities.²²⁸ Martin *et al.*²²⁸ have explained this correlation by noting that the removal of a core electron from atom X to form a positive hole involves very nearly the same set of R -group relaxation energies (and to a less important degree also potential energies) as the addition of a proton. Thus, changes in X -atom core binding energy with R are expected to be approximately equal to changes in proton affinity with R , even though the absolute magnitudes of the two quantities are very different; this has been found to be true for a rather large number of small molecules.²²⁸

(3) It has also been proposed by Wagner²²⁹ that the difference in kinetic energy between a core photoelectron peak and an Auger electron peak originating totally via core-level transitions in the same atom can be used as a sensitive indicator of chemical state that is free of any uncertainty as to binding energy reference or variable specimen surface charging. This difference, which has been termed the "Auger parameter",²²⁹ changes with alterations in chemical environment because Auger energies are influenced much more strongly than photoelectron energies by final-state relaxation.^{230, 231} In fact, Auger energy chemical shifts are roughly 3–4 times as large as corresponding core binding energy shifts.²²⁹ Although a precise theoretical calculation of such extra-atomic relaxation effects may be difficult (see, for example, Section V.B), the Auger parameter appears to have considerable potential as a fingerprint for different chemical states.

(4) Finally, attempts have been made to correlate core binding energy shifts with the results of nuclear spectroscopic measurements such as NMR^{232, 233} and Mössbauer spectroscopy,²³⁴ as reviewed elsewhere by Carlson.¹⁰ NMR diamagnetic shielding factors have been compared with core shifts, but the difficulty of separating out diamagnetic and paramagnetic contributions to shielding have prevented extensive application of this type of analysis. Also, binding energy shifts for a closely related set of tin compounds correlate reasonably well with Mössbauer chemical shift values,²³⁴ but no detailed theoretical justification for this correlation has been presented.

It is clear that the theoretical interpretation of core electron binding energies or chemical shifts in these energies can be attempted in several ways at varying levels of sophistication. When binding energies are calculated by the most rigorous total-energy-difference method, including perhaps corrections for relativistic effects and electron–electron correlation, values in very good agreement with experiment have been obtained for several atoms and

small molecules. This agreement verifies that all of the basic physical effects involved have been recognized and can be accounted for quantitatively. If binding energies are calculated from orbital energies via Koopmans' Theorem, errors primarily due to neglect of final state relaxation are incurred. Such errors can be from 1% to 10% of the total binding energy and can be estimated in several ways. In calculating chemical shifts of binding energies between two different sites or compounds by means of Koopmans' Theorem, however, a fortuitous cancellation of a large fraction of the relativistic, correlation, and relaxation corrections occurs. Thus, orbital energies can be used with reasonable success in predicting shifts, although anomalously large final-state relaxation around a localized hole represents an ever-present source of error in such analyses (see also Section V.B). The interaction of a core electron with its environment can be simplified even further, giving rise to several so-called potential models with varying degrees of quantum-mechanical and/or empirical input. All of these models can be useful in interpreting shifts, although it may be necessary to restrict attention to a systematic set of compounds for the most approximate of them. The direct connection of chemical shifts with thermochemical heats of reaction via the equivalent-core approximation is also possible. Finally, it is worthwhile to note that one of the primary reasons that chemical shifts can be analyzed by such a wide variety of methods is that their origin is so simply and directly connected to the molecular charge distribution. In turn, it is very often this charge distribution that is of primary interest in a given chemical or physical investigation.

V. FINAL-STATE EFFECTS

A. Introduction

In this section, several effects arising because of complexities in the final state of the photoemission process will be considered. Considerable use will be made of the theoretical developments of Sections III.A–D, from which it is already clear that unambiguously distinguishing various final-state effects in the electronic wave function may not always be possible, primarily due to many-electron effects that might, for example, be described by a configuration-interaction approach. Thus, the first four topics to be dealt with here (relaxation phenomena, multiplet splittings, shake-up and shake-off effects, and other many-electron effects) are all very much interrelated, as will become evident from subsequent discussion. However, for both historical and heuristic reasons, it is reasonable to consider them separately, using several examples for which distinctions can be made relatively easily. (Such final-state electronic effects have also been reviewed by Martin and Shirley¹³ in more detail in this series.) The last subject to be treated here involves the influence

of exciting various final vibrational states, for which theoretical background has already been presented in Sections III.A and III.D.

B. Relaxation Effects

The importance of relaxation corrections in accurately predicting binding energies has been emphasized in several prior discussions in this chapter. As a further example of how large such effects can be, it has been suggested by Ley *et al.*²³⁵ that relaxation is the primary reason why free-atom vacuum-referenced core binding energies are higher by ~5–15 eV than corresponding vacuum-referenced binding energies in the pure elemental solid. Also, inert gas atoms implanted in noble metal lattices have been shown by Citrin and Hamann²³⁶ to exhibit core binding energies 2–4 eV lower than in the free-atom state, again primarily due to relaxation. In a systematic study of the C1s binding energy in a set of linear alkanes C_nH_{2n+2} ($n=1, 2, \dots, 13$), Pireaux *et al.*²³⁷ noted a monotonically increasing C1s chemical shift $\Delta E_b(C1s, CH_4-C_nH_{2n+2})$ with n , and a small overall shift of 0.6 eV between CH_4 and $C_{13}H_{28}$ with sign such that $C_{13}H_{28}$ has the lowest binding energy. Transition-operator calculations for these alkane molecules indicate that the relaxation energy increases by almost 2.0 eV in going from the smallest CH_4 to $C_{13}H_{28}$; thus, relaxation is a major contributing factor in producing these small chemical shifts, although it must act in conjunction with certain other effects with opposite sign to reduce the overall shift to 0.6 eV. Relaxation shifts of ~1–3 eV are also noted in UPS spectra of the valence levels of molecules chemisorbed on surfaces,²³⁸ with the binding energies of molecular orbitals not directly involved in bonding to the surface being lower than in the free molecule, presumably due to extra relaxation in the substrate. In general for these systems, then, it is found that the more near-neighbor atoms there are surrounding a given final-state hole, the more relaxation can occur and the lower is the observed binding energy.

The relaxation energy δE_{relax} can be unambiguously defined as the difference between a Koopmans' Theorem binding energy $-\epsilon_k$ and a binding energy calculated by means of a difference of self-consistent Hartree-Fock total energies for both the initial and final states. Various methods have been utilized for estimating this energy in atoms, molecules, and solids,^{119–121, 235, 239–242} but principal emphasis here will be on a relatively straightforward, yet easily visualized, procedure first used extensively by Shirley and co-workers.^{121, 235, 239}

In this procedure,^{121, 235, 239} the relaxation energy for a given core-level emission process is divided into two parts: an intra-atomic term (the only term present in the free-atom case) and an extra-atomic term that is important in molecules or solids. The extra-atomic term thus includes all relaxation

involving electrons primarily situated in the initial state on other atomic centers. Thus,

$$\delta E_{\text{relax}} = \delta E_{\text{relax}}^{\text{intra}} + \delta E_{\text{relax}}^{\text{extra}} \quad (133)$$

(This division of the relaxation correction was, in fact, made in the first discussion of the potential model for analyzing chemical shifts.¹⁰⁵) The calculation of these two terms makes use of a general result derived by Hedin and Johansson,¹²⁰ which states that, for emission from an initial orbital ϕ_k in an atom of atomic number Z , the relaxation energy is given to a good approximation by

$$\delta E_{\text{relax}} = \frac{1}{2} \langle \phi_k | \hat{V}(N-1, Z) - \hat{V}(N, Z) | \phi_k \rangle \quad (134)$$

in which $\hat{V}(N-1, Z)$ is the total electronic Hartree-Fock potential operator acting on the k th orbital in the $(N-1)$ -electron final state and $\hat{V}(N, Z)$ is the analogous total Hartree-Fock potential operator for the N -electron initial state. (For a neutral atom, of course $N=Z$.) The expectation value in Eq. (134) thus involves sums over Coulomb and exchange integrals between ϕ_k and $(N-1)$ other spin-orbitals $\phi_j \neq \phi_k$. Two sets of orbitals ϕ_j are also needed, an initial-state set $\{\phi_j\}$ in $\hat{V}(N, Z)$ and a relaxed set $\{\phi_j'\}$ in $\hat{V}(N-1, Z)$. The determination of the relaxed orbitals is now further simplified by using the equivalent-core approximation, such that the integrals involving $\hat{V}(N-1, Z)$ are replaced by integrals for $\hat{V}(N+1, Z+1)$, the neutral atom with next higher atomic number; correspondingly, ϕ_k is taken to be an orbital in atom $Z+1$ in evaluating these integrals. This procedure is reasonable because the orbitals at larger mean radii than ϕ_k produce most of the relaxation and such orbitals in neutral atom $Z+1$ are very little different from those in atom Z with a hole in the k subshell (cf. Table I). Furthermore, even though inner-orbital relaxation occurs (including relaxation of ϕ_k), this inner-orbital relaxation is smaller (again see Table I), and thus the Coulomb and exchange integrals between inner and outer orbitals change little in atom $Z+1$ relative to the true hole state in atom Z .¹²¹ Thus, the overall relaxation energy becomes finally

$$\delta E_{\text{relax}} = \frac{1}{2} (\langle \phi_k | \hat{V} | \phi_k \rangle_{Z+1} - \langle \phi_k | \hat{V} | \phi_k \rangle_Z) \quad (135)$$

with all relevant Coulomb and exchange integrals available from existing tabulated data for atoms.¹⁰⁰ Applying this calculation procedure to core emission from noble-gas atoms, Shirley¹²¹ obtained very good estimates for relaxation energies as compared to direct total-energy-difference calculations.

The same procedure has also been applied to metals by Ley *et al.*,²³⁵ for which the separation of Eq. (135) into intra-atomic and extra-atomic terms yields formally

$$\delta E_{\text{relax}} = \frac{1}{2} (\langle \phi_k | \hat{V} | \phi_k \rangle_{Z+1} - \langle \phi_k | \hat{V} | \phi_k \rangle_Z)^{\text{intra}} + \frac{1}{2} (\langle \phi_k | \hat{V} | \phi_k \rangle_{Z+1} - \langle \phi_k | \hat{V} | \phi_k \rangle_Z)^{\text{extra}} \quad (136)$$

The intra-atomic term in Eq. (136) is calculable as described previously. If a free atom A is placed into a pure solid lattice of the same species and it is further assumed that placement in the lattice has a small influence on the initial-state Hartree-Fock energy eigenvalues ϵ_k (corresponding to an extra-atomic potential effect of approximately zero), then the difference between free-atom and solid binding energies is given simply by the extra-atomic relaxation term for the solid:

$$E_b^V(A, k, \text{atom}) - E_b^V(A, k, \text{solid}) = \frac{1}{2} (\langle \phi_k | \hat{V} | \phi_k \rangle_{Z+1} - \langle \phi_k | \hat{V} | \phi_k \rangle_Z)^{\text{extra}} \quad (137)$$

These extra-atomic terms have been derived²³⁵ for a metal by assuming that the conduction electrons polarize to such an extent that a screening charge of approximately unit magnitude occupies an atomic-like orbital centered on the atom containing the core hole. As a reasonable choice for this orbital, that possessing the dominant character of the lowest unoccupied valence band in the solid is used, again together with an equivalent-cores approximation. Although this procedure overestimates screening because the orbital chosen is too localized, it does give approximately correct magnitudes for atom-solid shifts such as those in Eq. (137), as is illustrated in Fig. 29 for the 3d transition-metal series. Note the break in values at $Z=29$ (Cu) when the screening orbital changes from 3d to the more diffuse 4s because of filling of

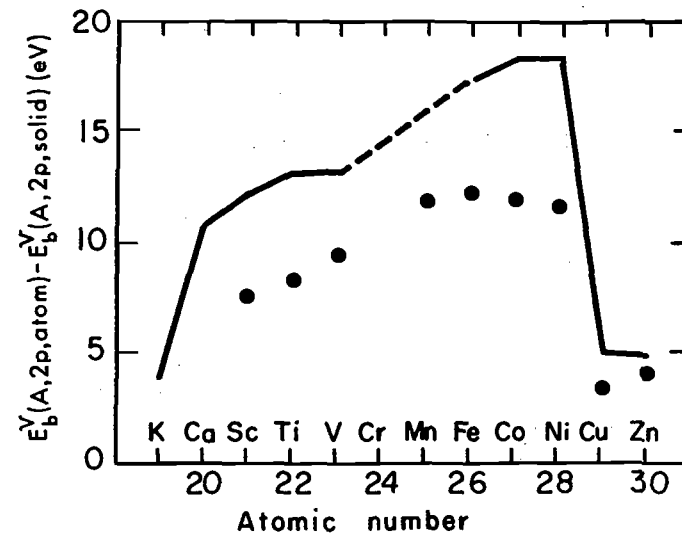


Fig. 29. Differences between vacuum-referenced free-atom 2p core binding energies and analogous binding energies in the corresponding elemental metal. The points represent experimental values and the line calculations based upon Eq. (137), which assumes that extra-atomic relaxation is the main cause of such differences. The break at $Z=29$ is caused by the filling of the 3d valence bands. (From Ley *et al.*, ref. 215 and 235).

the 3d bands. Alternate calculation procedures of a somewhat more rigorous nature have also been proposed to explain such atom-solid shifts^{236, 240-242}, including especially discussions of possible initial-state shifts in the solid. However, the scheme presented here clearly yields a semi-quantitative approximation for one of the most important factors, extra-atomic relaxation, as well as being very easy to apply to various systems.

As noted previously (Section III.B), it has also been pointed out by Ley *et al.*¹¹⁵ that a localized-hole description can be used to estimate relaxation energies associated with *valence-level* excitations in free-electron metals. Such relaxation energies are calculated by assuming that in the final state a full single-electron screening charge occupies an initially unoccupied atomic-like valence orbital. Then, because there is minimal inner-orbital relaxation, the difference operator $\hat{V}(N-1, Z) - \hat{V}(N, Z)$ in Eq. (134) reduces to the single terms $\hat{J}_{\text{valence}} + \hat{K}_{\text{valence}}$, and the final relaxation energy is given by $\frac{1}{2}\langle\phi_{\text{valence}} | \hat{J}_{\text{valence}} + \hat{K}_{\text{valence}} | \phi_{\text{valence}}\rangle \approx \frac{1}{2}\langle\phi_{\text{valence}} | \hat{J}_{\text{valence}} | \phi_{\text{valence}}\rangle = \frac{1}{2}J_{\text{valence, valence}}$.

As a final comment concerning relaxation, the discussion surrounding Eq. (77) and Fig. 8 should be recalled. That is, the occurrence of relaxation requires by virtue of the Manne-Åberg-Lundqvist sum rule given in Eq. (77) that additional photoelectron intensity arises at kinetic energies below that of the relaxed or adiabatic peak position. Thus, relaxation is very closely associated with various kinds of low-energy satellite structure of types to be discussed in Section V.D.

C. Multiplet Splittings

Multiplet splittings arise from the various possible non-degenerate total electronic states that can occur in the final hole states of open-shell systems, whether they be atoms, molecules, or solids with highly localized unfilled valence levels. The way in which multiple final states can be produced has already been briefly introduced in Section III.A, and for most systems it is adequate to consider a total spatial symmetry designation (e.g. $L=0, 1, 2, \dots$ in atoms), a total spin designation (e.g. $S=0, 1, 2, \dots$ in atoms or molecules), and perhaps also the perturbation of these via the relativistic spin-orbit interaction. The simplest interpretation of atomic multiplet splittings is thus in terms of various L, S terms. Such effects can occur in any system in which the outer subshell or subshells are only partially occupied. The partial occupation provides certain extra degrees of freedom in forming total final states relative to the closed-shell case via coupling with the unfilled shell left behind by photoelectron emission. Multiplet effects can occur for both core and valence emission, as long as the valence subshell(s) are not totally occupied initially. Multiplet splittings also possess the important feature of being describable *in first order* in terms of a single set of ground-state Hartree-Fock

one-electron orbitals. Thus, electron-electron correlation effects beyond the ground-state Hartree-Fock approximation are not essential for predicting that multiplet effects will exist, although, as will be shown, the inclusion of correlation effects is absolutely essential for quantitatively describing these phenomena in certain instances.

Multiplet effects involving core-level holes are very commonly encountered in interpretations of the fine structure arising in x-ray emission spectra²⁴³⁻²⁴⁵ and Auger electron spectra.^{3, 246-248} However, it is more recently that such effects were first recognized and studied in detail in connection with core x-ray photoelectron spectra of paramagnetic free molecules^{4, 249} and transition-metal compounds.^{86, 250} Subsequently, numerous studies have been carried out, including applications to systems containing both transition-metal atoms^{86, 157, 250-257} and rare-earth atoms,^{156, 258-261} and a few comprehensive reviews have appeared.²⁶²⁻²⁶⁵ Primary emphasis here will be on the elucidation of a few examples to illustrate the types of effects noted and their modes of interpretation.

As an introductory example of one type of multiplet splitting found in XPS studies,^{86, 250} consider first the ground-state Hartree-Fock description of photoemission from the 3s level of a Mn²⁺ free ion, as shown on the left-hand side of Fig. 30. The ground state of this ion can be described in L, S (Russell-Saunders) coupling as $3d^5 {}^6S$ (that is, $S=\frac{5}{2}, L=0$). In this state, the five 3d spins are coupled parallel. Upon ejecting a 3s electron, however, two final states may result: $3s3d^5 {}^5S$ ($S=2, L=0$) or $3s3d^5 {}^7S$ ($S=3, L=0$). The basic difference between these two is that in the 5S state, the spin of the remaining 3s electron is coupled anti-parallel to those of the five 3d electrons, whereas in the 7S state the 3s and 3d spins are coupled parallel. Because the exchange interaction acts only between electrons with parallel spins, the 7S energy will be lowered relative to the 5S energy because of the favorable effects of 3s-3d exchange. The magnitude of this energy separation will be proportional to the 3s-3d exchange integral $K_{3s, 3d}$, and will be given by¹¹⁸

$$\begin{aligned} \Delta[E_b(3s)] &= E^f(3s3d^5 {}^5S) - E^f(3s3d^5 {}^7S) = \Delta E^f(3s3d^5) \\ &= 6K_{3s, 3d} \\ &= \frac{6e^2}{5} \int_0^\infty \int_0^\infty \frac{r_<^2}{r_>^3} P_{3s}(r_1)P_{3d}(r_2)P_{3s}(r_2)P_{3d}(r_1) dr_1 dr_2 \end{aligned} \quad (138)$$

where e is the electronic charge, $r_<$ and $r_>$ are chosen to be the smaller and larger of r_1 and r_2 in performing the integrations, and $P_{3s}(r)/r$ and $P_{3d}(r)/r$ are the radial wave functions for 3s and 3d electrons. The factor 1/5 results from angular integrations involved in computing $K_{3s, 3d}$. A Hartree-Fock calculation of the energy splitting in Eq. (138) for Mn³⁺ gives a value of $\Delta E^f(3s3d^5) \approx 13$ eV.^{86, 250} As this predicted splitting is considerably larger

momenta requires that

$$\Delta S = S^f - S = \pm \frac{1}{2} \quad (140)$$

and

$$\Delta L = L^f - L = 0, \pm 1, \pm 2, \dots, \pm l \text{ or } L^f = L+l, L+l-1, \dots, |L-l| \quad (141)$$

Also, the overlap factors in Eqs (68) and (74) yield an additional *monopole* selection rule on the passive electrons, as introduced in Section III.D.1. This rule implies that the coupling of the unfilled valence subshell $(n'l)^p$ in the final state must be the same as that in the initial state: that is to total spin and orbital angular momenta of L and S . Finally, any coupling scheme for $(nl)^{q-1}$ or $(n'l)^p$ must of course be consistent with the Pauli exclusion principle. Since $(nl)^{q-1}$ is assumed to represent a single hole in an otherwise filled subshell, it must therefore couple to a total spin of $\frac{1}{2}$ and a total orbital angular momentum of l . Within this model, it has been shown by Cox and Orchard¹⁵⁵ that the total intensity of a given final state specified by L^f, S^f will be proportional to its total degeneracy, as well as to the one-electron matrix element squared. Thus, in Russell-Saunders coupling

$$I_{\text{tot}}(L^f, S^f) \propto (2S^f + 1)(2L^f + 1) \quad (142)$$

For the special case of atomic s -electron binding energy splittings, the relevant selection rules are thus:

$$\Delta S = S^f - S = \pm \frac{1}{2} \quad (143)$$

$$\Delta L = L^f - L = 0 \quad (144)$$

and the total intensity of a given peak is predicted to be proportional to the spin degeneracy of the final state:

$$I_{\text{tot}}(L^f, S^f) \propto 2S^f + 1 \quad (145)$$

Thus, only two final states are possible corresponding to $S^f = S \pm \frac{1}{2}$, and the relative intensities of these will be given by the ratio of their multiplicities, or

$$\frac{I_{\text{tot}}(L, S + \frac{1}{2})}{I_{\text{tot}}(L, S - \frac{1}{2})} = \frac{2S + 2}{2S} \quad (146)$$

The energy separation of these two states can further be calculated from simple atomic multiplet theory and is given by a result often referred to as the Van Vleck Theorem:¹¹⁸

$$\Delta[E_b(ns)] = E^f(L, S - \frac{1}{2}) - E^f(L, S + \frac{1}{2}) \quad (147)$$

$$\Delta[E_b(ns)] = (2S + 1)K_{ns, n'l} \text{ for } S \neq 0 \quad (148)$$

$$\Delta[E_b(ns)] = 0 \text{ for } S = 0 \quad (149)$$

Here $K_{ns, n'l}$ is the $ns - n'l$ exchange integral and can be calculated from

$$K_{ns, n'l} = \frac{e^2}{2l' + 1} \int_0^\infty \int_0^\infty \frac{r < l'}{r > l' + 1} P_{ns}(r_1) P_{n'l}(r_2) P_{ns}(r_2) P_{n'l}(r_1) dr_1 dr_2 \quad (150)$$

where the same notation as that in Eq. (138) has been used. Equations (146)–(150) indicate that such s -electron binding energy splittings should yield a doublet with a more intense component at lower binding energy (corresponding to an exchange-favored final state of $S^f = S + \frac{1}{2}$) and a component separation that is directly associated with both the initial state spin and the spatial distributions of the core and valence electrons as reflected in the exchange integral. Thus, the potential for extracting certain types of useful and unique information from such splittings exists.

That Eq. (148) provides a good description of the systematics of such s -level multiplet splittings has been nicely demonstrated in studies of the $4s$ and $5s$ splittings in rare-earth metals and compounds with varying outer $4f$ subshell occupation numbers and spins S ,^{258, 259} as summarized in Fig. 32.

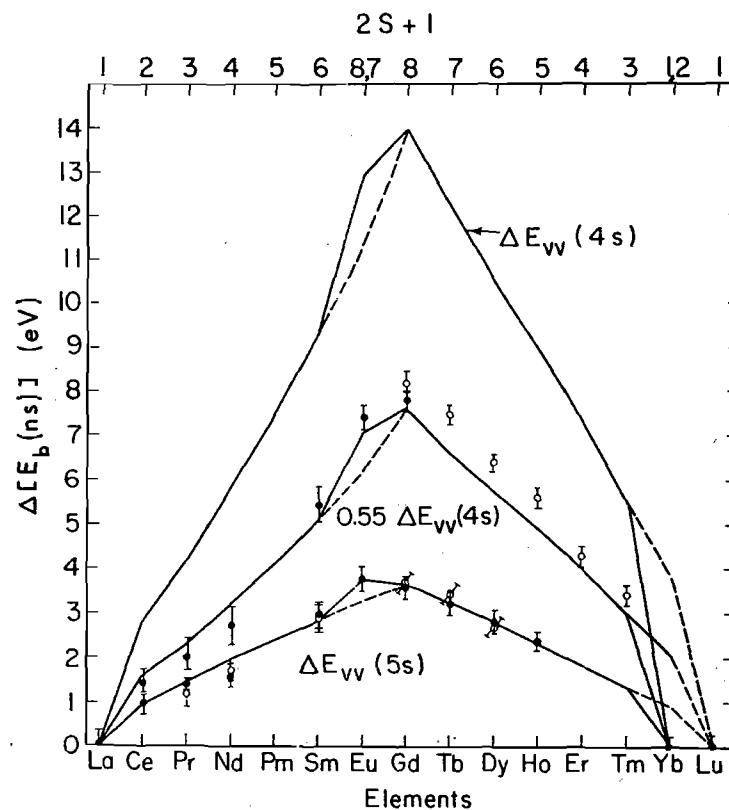


Fig. 32. Experimental (points) and theoretical (lines) $4s$ and $5s$ binding energy splittings in various rare-earth ions. The ΔE_{VV} values are calculated using Van Vleck's Theorem [Eq. (148)]. Experiment and theory are in excellent agreement for $5s$, but the theoretical splittings must be reduced by a factor of 0.55 to agree with the $4s$ data because of correlation effects. (From McFeely *et al.*, ref. 259.)

As the initial state is rather well described by a single configuration $3d^6(1S)3p^6(1S)3d^5(6S)$ possessing the d -electron coupling of Φ_1 , the sudden approximation result of Eq. (84) can immediately be used to show that the four $5S$ intensities will be given by

$$I_1 \propto |C_{11}|^2, \quad I_2 \propto |C_{21}|^2, \quad I_3 \propto |C_{31}|^2, \quad I_4 \propto |C_{41}|^2 \quad (152)$$

with the total intensity $I_1 + I_2 + I_3 + I_4$ still being proportional to the spin degeneracy of $5S$. Evaluating the energies and relative intensities in this way yields a prediction of a total of only *three* observable $5S$ peaks (one is too weak to be seen easily) and one observable $7S$ peak in the Mn^{2+} spectrum. Weak structures in good agreement with these predictions have, in fact, been observed by Kowalczyk *et al.*,²⁵⁸ and their experimental results are shown in Fig. 33. These CI calculations also explain a peak intensity discrepancy noted relative to simple multiplet theory: namely that the intensity ratio $5S(1)/7S$ in Fig. 31 or Fig. 33 is significantly below the $5/7$ predicted by

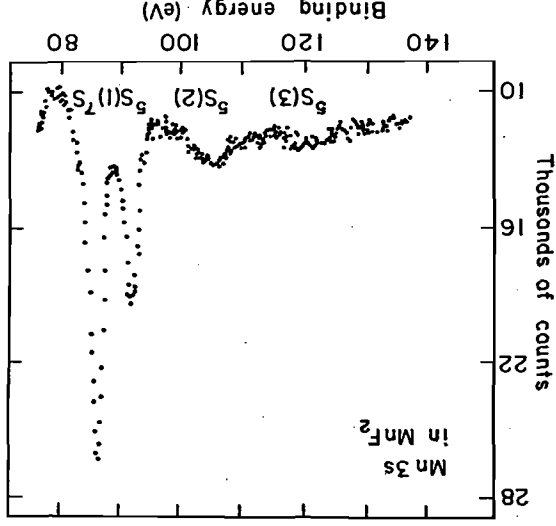


Fig. 33. Higher resolution $Mn3s$ spectrum from MnF_2 obtained with monochromatized $AlK\alpha$ radiation (cf. Fig. 31). The peaks $5S(2)$ and $5S(3)$ arise from final-state configuration interaction (correlation effects) according to Eq. (151). (From Kowalczyk *et al.*, ref. 253.)

Eq. (146). It is thus clear, that, although a first-order description of multiplet effects is possible within a non-correlated Hartree-Fock approach, a detailed description of the numbers, positions, and relative intensities of peaks may require including correlation effects, especially where intrashell interactions

dominate.

The first observations of s -electron core binding energy splittings analogous to those described by Eqs (146)–(150) were in gaseous, paramagnetic

The solid lines connect calculated values based upon Eq. (148) and are in excellent agreement with experiment for the $5S$ splittings, whereas for the $4s$ splittings, this simple theory must be reduced by a factor of ~ 0.55 to agree with experiment. These results also suggest that the $4s$ discrepancy may be due to the same type of correlation correction involved in $Mn3s$, as the $4s$ – $4f$ spatial overlap is high, increasing correlation, whereas the $5s$ – $4f$ overlap is much lower, decreasing it.

Configuration interaction calculations on Mn^{3+} by Bagus *et al.*²⁵² first provided a more quantitative understanding of such correlation corrections to intrashell s -level splittings such as $3s$ – $3d$ and $4s$ – $4f$. They pointed out that, in a CI description of the true Mn^{3+} final states corresponding to $3s$ emission, several configurations would be of special importance in addition to the usual one-electron-transition final configuration as shown in the left half of Fig. 30. (In writing such configurations below, numbers in parentheses will denote the L, S coupling of the subshell to the left.) The $7S$ final state is found to be composed almost completely of $3s^1(2S)3p^6(1S)3d^5(6S)$, the one-electron configuration $\Phi_1(5S) = 3s^1(2S)3p^6(1S)3d^5(6S)$, but also from configurations in which it formally appears that one $3p$ electron has been transferred down to a $3s$ orbital while another $3p$ electron has been transferred up to a $3d$ orbital: $\Phi_2(5S) = 3s^2(1S)3p^4(3P)3d^6(3P_2)$ and $\Phi_4(5S) = 3s^2(1S)3p^4(1D)3d^6(5D)$. (The notations $3d^6(3P_2)$ and $3d^6(3P_2)$ stand for two independent ways in which $3d^6$ can couple to $3P$.) Thus, there will be at least a fourfold manifold of $5S$ states, and the lowest-energy member is expected to be lowered significantly (that is, to move toward $7S$). In fact, the $5S$ state nearest $7S$ is found to be only 4.71 eV away, in much better agreement with the experimental splitting for MnF_2 of 6.5 eV than the estimate of ~ 13 eV obtained from Eq. (138). Such intrashell s -level multiplet splittings can thus only be predicted accurately when correlation is allowed for, whereas intrashell s -level splittings are, by contrast, well predicted by Eq. (148). A further significant effect predicted by these CI calculations for the $Mn^{3+} 5S$ states is the existence of additional experimental fine structure. Specifically, there are four $5S$ states at E_1, E_2, E_3 , and E_4 , that can be written to a good approximation as

$$\begin{aligned} \Psi_1(5S) &= C_{11}\Phi_1(5S) + C_{12}\Phi_2(5S) + C_{13}\Phi_3(5S) + C_{14}\Phi_4(5S) \\ \Psi_2(5S) &= C_{21}\Phi_1(5S) + C_{22}\Phi_2(5S) + C_{23}\Phi_3(5S) + C_{24}\Phi_4(5S) \\ \Psi_3(5S) &= C_{31}\Phi_1(5S) + C_{32}\Phi_2(5S) + C_{33}\Phi_3(5S) + C_{34}\Phi_4(5S) \\ \Psi_4(5S) &= C_{41}\Phi_1(5S) + C_{42}\Phi_2(5S) + C_{43}\Phi_3(5S) + C_{44}\Phi_4(5S) \end{aligned} \quad (151)$$

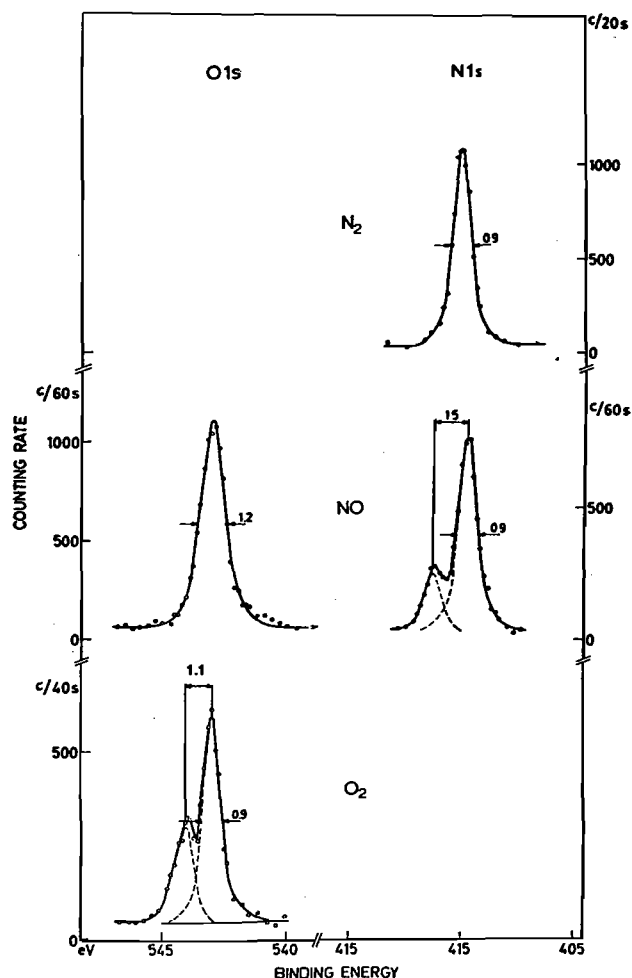


Fig. 34. XPS spectra from the $1s$ core electrons of the gaseous molecules N_2 , NO , and O_2 . The $1s$ peaks from the paramagnetic molecules NO and O_2 are split due to final-state multiplets. Diamagnetic N_2 shows no splitting. (From Siegbahn *et al.*, ref. 4.)

molecules.^{4, 249} Hedman *et al.*²⁴⁹ found splittings as large as 1.5 eV in the $1s$ photoelectron spectra of the molecules NO and O_2 . These results are shown in Fig. 34 along with an unsplit $1s$ spectrum from the diamagnetic molecule N_2 . In each case, it can be shown that the observed energy splitting should be proportional to an exchange integral between the unfilled valence molecular orbital and the $1s$ orbital of N or O,⁴ in analogy with Eq. (148). Theoretical estimates of these splittings from molecular orbital calculations give values in good agreement with experiment,^{4, 107} as expected for such

intershell interactions in which correlation effects are much decreased. The observed intensity ratios of the peaks are furthermore very close to the ratios of the final-state degeneracies, also in agreement with simple theory.

The analysis of binding energy splittings in emission from non- s core levels is not as straightforward as for s -level emission, primarily due to the fact that the core-electron hole represented by $(nl)^{q-1}$ (which now has associated with it a spin of $\frac{1}{2}$ and a non-zero orbital angular momentum of l) can couple in various ways with the valence subshell $(n'l')^p$ (which can have various spins S' and orbital angular momenta L' , including the initial values S and L) to form a final state with a given total spin S^f and total orbital angular momentum L^f . Thus, the number of allowed final states increases and their energy separations will in general be determined by both Coulomb and exchange integrals through different coupling schemes. Additional complexities arising for non- s levels are caused by spin-orbit coupling and crystal-field splittings.

The simplest procedure for calculating such non- s energy separations is again to use non-relativistic atomic multiplet theory.^{86, 250, 262, 263} As an illustrative example, consider $3p$ electron emission from Mn^{2+} , as indicated in the right-hand portion of Fig. 30. For this case, $(nl)^{q-1} = 3p^5$, $(n'l')^p = 3d^5$ and the initial state, as before, is 6S ($S = \frac{5}{2}$, $L = 0$). The previously stated selection rules imply that the allowed final states correspond to 7P ($S = 3$, $L = 1$) and 5P ($S = 2$, $L = 1$). Although a 5S ($S = 2$, $L = 0$) final state would be, consistent with selection rule (141), it requires changing the coupling of $3d^5$ from its initial 6S and so is not allowed. There is only one way for $3p^5$ to couple with $3d^5$ to form a 7P state, that being with $3p^5$ (always coupled to total spin $= s = \frac{1}{2}$ and total orbital angular momentum $= l = 1$) coupled with $3d^5$ in its initial state coupling of 6S ($S = \frac{5}{2}$, $L = 0$). However, there are three ways to form the allowed 5P final state by coupling

$$3p^5(s = \frac{1}{2}, l = 1) \text{ with } 3d^5 \text{ } {}^6S(S'' = \frac{5}{2}, L'' = 0)$$

$$3p^5(s = \frac{1}{2}, l = 1) \text{ with } 3d^5 \text{ } {}^4D(S'' = \frac{3}{2}, L'' = 2)$$

and

$$3p^5(s = \frac{1}{2}, l = 1) \text{ with } 3d^5 \text{ } {}^4P(S'' = \frac{3}{2}, L'' = 1)$$

Thus, four distinct final states are possible for $3p$ emission from Mn^{2+} , one 7P and three 5P . As there are off-diagonal matrix elements of the Hamiltonian between the various 5P coupling schemes,¹¹⁸ they do not individually represent eigenfunctions. The eigenfunctions describing the 5P final states will thus be linear combinations of the three schemes:

$$\begin{aligned} \Psi_1({}^5P) &= C_{11}\Phi({}^6S) + C_{12}\Phi({}^4D) + C_{13}\Phi({}^4P) \\ \Psi_2({}^5P) &= C_{21}\Phi({}^6S) + C_{22}\Phi({}^4D) + C_{23}\Phi({}^4P) \\ \Psi_3({}^5P) &= C_{31}\Phi({}^6S) + C_{32}\Phi({}^4D) + C_{33}\Phi({}^4P) \end{aligned} \quad (153)$$

where each 5P configuration has been labelled by the $3d^5$ coupling involved and the C_{ij} 's are the usual expansion coefficients. The energy eigenvalues corresponding to these eigenfunctions will give the separations between the 5P states. Such eigenfunctions and eigenvalues can most easily be determined by diagonalizing the 3×3 Hamiltonian matrix for the 5P states, where each matrix element is expressed as some linear combination of $J_{3d, 3d}$, $K_{3d, 3d}$, $J_{3p, 3d}$, and $K_{3p, 3d}$.^{33, 118} If Coulomb and exchange integrals from a Hartree-Fock calculation on Mn^{2+} are used, such matrix diagonalization calculations yield the relative separations indicated on the right-hand side of Fig. 30^{86, 250} Once again, the sudden approximation result of Eq. (84) indicates that, because the initial state is rather purely $3d^5(^6S)$, only those components of the 5P states represented by $C_{11}\Phi(^6S)$ are accessible. Thus, the individual intensities of Ψ_1 , Ψ_2 , and Ψ_3 can be computed from $|C_{11}|^2$, $|C_{21}|^2$, and $|C_{31}|^2$, respectively. In determining the total intensity ratios for the 5P and 7P states, Eq. (142) can be used to give:

$$I_{\text{tot}}(^5P) : I_{\text{tot}}(^7P) = [I_1(^5P) + I_2(^5P) + I_3(^5P)] : I_{\text{tot}}(^7P) = 5 : 7$$

The relative peak heights in Fig. 30 have been calculated in this way, and the experimental $3s(1)-3p(1)$ separation and relative intensity for MnF_2 were used to empirically fix the scales between the $3s$ and $3p$ regions. The separations and relative intensities of the peaks observed are found to be at least semi-quantitatively predicted by this simple, atomic L, S coupling model,^{86, 250} and these results have been confirmed in more detail by later experimental²⁵⁵ and theoretical²⁵⁶ studies. The remaining discrepancies between theory and experiment for this $3p$ case could be caused by a combination of effects due to correlation, spin-orbit coupling, and crystal-field splitting, although calculations by Gupta and Sen²⁵⁶ indicate that the latter two are probably not so significant. Ekstig *et al.*²⁴⁵ have carried out matrix diagonalization calculations like those described here but for more complex sets of final $3p$ -hole states in $3d$ transition metal atoms in an attempt to interpret soft x-ray emission spectra from solids. The theoretical aspects of calculating such non- s splittings have also recently been reviewed by Freeman *et al.*²⁶³

Deeper non- s core levels in $3d$ atoms should also exhibit similar splittings, although the magnitudes will be reduced because of the decreased interaction strengths between the core and $3d$ orbitals. For example, Fadley and Shirley⁸⁶ first noted that the $Mn2p$ levels in MnF_2 are broadened by ~ 1.5 eV relative to those in low-spin (filled subshell) compounds, and suggested multiplet splittings as the origin of this broadening. Subsequent measurements at higher resolution by Kowalczyk *et al.*,²⁵⁵ coupled with theoretical calculations by Gupta and Sen,²⁵⁷ have confirmed this suggestion, and also verified the existence of peak asymmetries and anomalous $2p_{3/2}-2p_{1/2}$ separations. For this

$2p$ case, both multiplet effects and spin-orbit coupling are of similar magnitude, and were included in calculations that successfully predicted the observed spectra.²⁵⁷

Analogous non- s core-level splittings have also been studied in systems with partially-filled f subshells,^{86, 260, 266} and the anomalous shape and decreased spin-orbit splitting in the $Eu4d$ spectrum of Fig. 6 is, in fact, attributable to such effects.⁸⁶

Although only multiplet effects on core-level binding energies have been considered up to this point, such phenomena can play a considerable role in determining the fine structure observed in valence spectra (as has been apparent for some time in UPS studies of free molecules⁹⁷). In particular, XPS valence spectra obtained from solids containing highly localized d levels or f levels are expected to be influenced by such multiplet effects,^{82, 156, 157, 261, 266, 267} with the relative intensities of various allowed final states being determined by fractional parentage coefficients, as described in Section III.D.2 and elsewhere.^{156, 157, 262} Heden *et al.*²⁶⁷ first observed such effects in valence spectra of $4f$ metals. As an example of the occurrence and use of such splittings in studies of rare-earth compounds, the XPS results of Campagna *et al.*²⁶¹ and Chazalviel *et al.*²⁶⁶ show strong multiplet splittings in the valence spectra of Sm-chalcogenides and a mixture of two markedly different multiplet structures in certain Sm compounds that are thought to exhibit valence fluctuations between $Sm^{+2} 4f^7$ and $Sm^{+3} 4f^6$. Some of these results for SmB_6 ²⁶⁶ are presented in Fig. 35, in which the L, S multiplets expected for both Sm^{+2} and Sm^{+3} are labelled. Theoretical intensities have been calculated using fractional parentage coefficients,¹⁵⁶ and the agreement between the theoretically simulated spectrum and experiment is excellent. Baer²⁶⁸ has also presented very high-resolution XPS spectra for various $4f$ metals that further confirm the existence of these atomic-like multiplet effects. In analogous multiplet effects in valence d orbitals, the inclusion of crystal-field effects is also expected to be important, as has been emphasized in a recent discussion by Bagus *et al.*¹⁵⁷

In comparison to chemical shifts of core-electron binding energies, multiplet splittings of core- or valence-energies thus represent higher-order effects yielding a different type of information. In their simplest interpretation, chemical shift measurements detect a change in the spatially-averaged potential experienced by an electron, whereas analyses of multiplet effects have the capability of determining the valence electron configuration or the detailed strengths of various higher-order electronic interactions. The two types of measurements are thus complementary. Numerous applications of multiplet splittings measurements are thus possible in the study of the transition series metals, the rare earths, the transuranium elements, and open-shell systems in general.

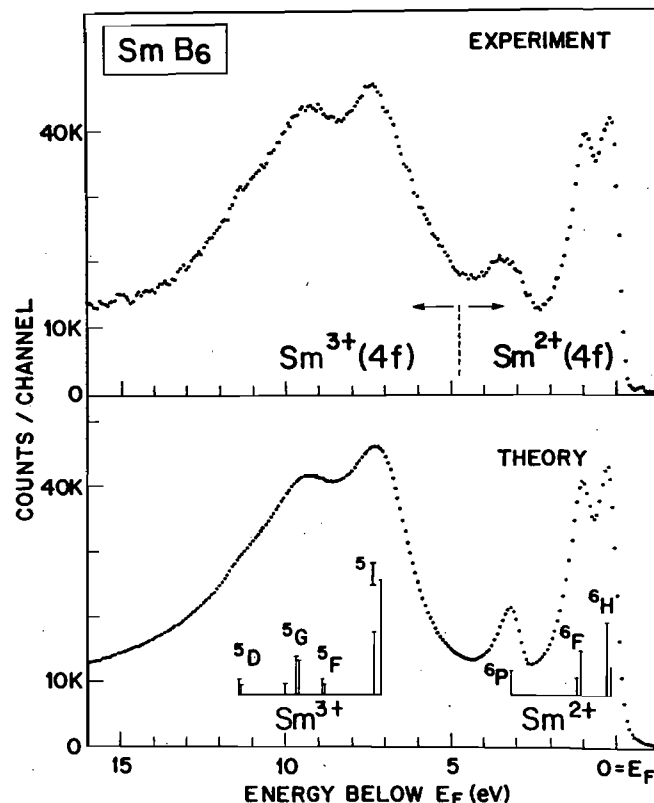


Fig. 35. Experimental and theoretical 4f valence spectra from SmB₆, a "mixed-valence" metallic compound believed to contain both Sm⁺² 4f⁶ and Sm⁺³ 4f⁵. The intensities of the various final-state multiplets for Sm⁺²→Sm⁺³ and Sm⁺³→Sm⁺⁴ were computed using fractional parentage coefficients and are indicated as vertical bars. These calculations were broadened by an empirically-derived function of the form of Eq. (158) to generate the final theoretical curve. Monochromatized AlK α was used for excitation. (From Chazalviel *et al.*, ref. 266.)

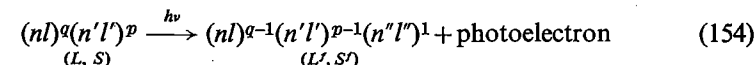
D. Multi-electron Excitations

1. *Introduction.* In this section, several types of final-state effects (and, to a lesser degree, initial-state effects) that involve what appear to be "multi-electron" excitations during the photoemission process are considered. The term multi-electron is judged against a purely one-electron description in which no final-state relaxation occurs. From the outset, it is clear that relaxation *does* occur, so that all transitions are indeed *N*-electron. Also, in a configuration interaction picture, the various mixtures of initial- and final-state configurations involved could easily make it impossible to distinguish clearly a one-electron component of photoemission. Nonetheless, all effects discussed here do somehow represent final states that deviate in a well-defined

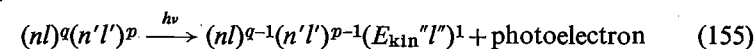
way from the single initial-state Hartree-Fock determinant that best approximates the one-electron photoemission event. The discussion begins with relatively simple forms of multi-electron excitation (shake-up and shake-off), but then comes to involve more complex phenomena that are important in XPS studies of certain atoms, molecules, and solids.

2. *Shake-up, Shake-off, and Related Correlation Effects.* Multi-electron processes in connection with x-ray photoemission were first studied in detail by Carlson, Krause, and co-workers.¹³⁵ In these studies, gaseous neon and argon were exposed to x-rays with energies in a range from 270 eV to 1.5 keV. Measurements were then made of both the charge distributions of the resulting ions and the kinetic energy distributions of the ejected photoelectrons. From these measurements, it was concluded that two-electron and even three-electron transitions occur in photo-absorption, with total probabilities which may be as high as 20% for each absorbed photon. By far the most likely multi-electron process is a two-electron transition, which is approximately ten times more probable than a three-electron transition. Two types of two-electron transitions can further be distinguished, depending upon whether the second electron is excited to a higher bound state ("shake-up"⁴) or to an unbound continuum state ("shake-off"¹³⁵). These are indicated in the transition below (cf. the corresponding one-electron transition in relation Eq. (139)):

Shake-up:



Shake-off:



Here $(n'l')^p$ represents some outer subshell from which the second electron is excited; it can be filled or partially filled. Either shake-up or shake-off requires energy that will lower the kinetic energy of the primary photoelectron. Thus, such multi-electron processes lead to satellite structure on the low-kinetic energy side of the one-electron photoelectron peak, as shown schematically in Fig. 8.

Higher resolution XPS spectra have been obtained more recently for neon and helium by Carlson *et al.*²⁶⁹ and for neon by Siegbahn *et al.*^{41, 270} A high-resolution Nels spectrum obtained by Gelius *et al.*²⁷⁰ is shown in Fig. 36. The two-electron transitions that are believed to be responsible for the observed spectral features labelled 2 to 14 occurring at relative energies from 33 to 97 eV below the one-electron peak are listed in Table II. The total two-electron shake-up intensity in this spectrum is thus estimated to be approximately 12% of that of the one-electron peak. Both shake-up and shake-off together account for ~30% of all emission events.

TABLE II

Summary of data concerning multi-electron transitions accompanying the formation of a 1s hole in atomic neon by AlK α or MgK α x-rays (compare Fig. 36)

(a) Shake-up transitions

Line no.	Type of process	Final state	Experimental ^a excitation energy (eV)	Calculated ^{a, b} excitation energy (eV)	Experimental relative intensity (%)	Calculated ^c relative intensity (%)	Calculated ^d relative intensity (%)
0	One-electron transition	$1s2s^22p^6$ 2S	(870.37)	(870.37)	100.00	100	100
1	Energy loss	$1s^22s^22p^53s$ 2P	16.89 (6)	16.93			
2	Dipole shake-up	$1s2s^22p^53s$ 2P lower	33.35 (9)		0.06 (1)		
3	Monopole shake-up	$1s2s^22p^53p$ 2S lower	37.35 (2)	37.39	3.15 (8)	2.3	2.47
4	Monopole shake-up	$1s2s^22p^53p$ 2S upper	40.76 (3)	41.26	3.13 (10)	2.9	2.60
5	Monopole shake-up	$1s2s^22p^54p$ 2S lower	42.34 (4)	42.30	2.02 (10)		1.48
6	Monopole shake-up	$1s2s^22p^55p$ 2S lower	44.08 (5)	44.18	0.42 (6)		0.43
7	Monopole shake-up	$1s2s^22p^56p$ 2S lower	45.10 (7)		0.50 (15)		0.09
8	Monopole shake-up	$1s2s^22p^54p$ 2S upper	46.44 (5)	46.42	0.96 (11)		0.70
9	Monopole shake-up	$1s2s^22p^55p$ 2S upper	48.47 (7)	48.40	0.17 (5)		0.11
10	Monopole shake-up	$1s2s2p^63s$ 2S lower	59.8 (1)	59.75	0.57 (5)		
11	Monopole shake-up	$1s2s2p^63s$ 2S upper	65.9 (1)	65.93	0.49 (6)		
12	Two electron shake-up	$1s2s^22p^43p^2$ 2S	93.14 (7)		0.08 (2)		
13	Two electron shake-up		95.9 (1)		0.10 (4)		
14	Two electron shake-up		97.23 (5)		0.24 (4)		
	Onset of shake-off	$1s2s^22p^5$ 3P	47.4 (5)	46.96	11.89% = Partial sum of shake-up		
	Onset of shake-off	$1s2s^22p^5$ 1P	51.7 (5)	51.27			

^a From Gelius, ref. 270.

^b All calculated excitation energies have been increased by 1.8 eV to allow for errors due to relativistic and correlation effects, particularly in the $1s2s^22p^6$ one-electron-transition final state.

^c Calculated using one-electron wave functions only from Eq. (156) by Carlson *et al.*, ref. 269.

^d Calculated using initial-state configuration interaction and Eq. (83) by Martin and Shirley, ref. 14.

TABLE II (cont.)

(b) Shake-off transitions

	Experimental ^e relative intensity (%)	Calculated ^e relative intensity (%)
Total intensity for shake-off of one electron from Ne 2s and 2p subshells (Ne \rightarrow Ne $^{2+}$)	16.5	16.1
Total intensity for shake-off of two electrons from Ne 2s and 2p subshells (Ne \rightarrow Ne $^{3+}$)	0.8	

^e From Carlson, Krause, and co-workers, ref. 135. Intensity calculated using an extension of Eq. (156).

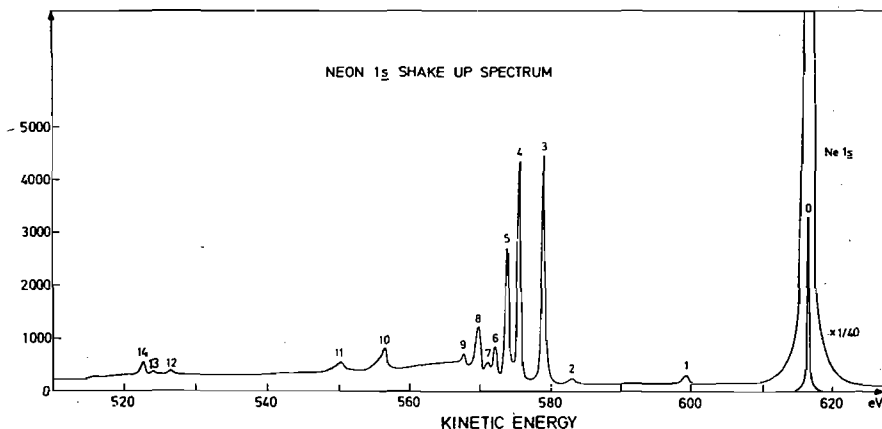


Fig. 36. High-resolution shake-up spectrum associated with excitation from Nels in gaseous neon. Table II lists the origins of the various satellite peaks labelled 1–14. The Nels FWHM was reduced to 0.4 eV in these measurements by using a monochromatized AlK α source. (From Gelius, ref. 270.)

Note that the initial and final states given in Table II are assumed to be composed of a single electronic configuration. This assumption, together with the sudden approximation as outlined in Section III.D.1, permits predicting such shake-up and shake-off peak intensities in a very straightforward way.¹³⁵ Namely, Eq. (75) is used for the relevant matrix element and it is noted that, in the passive-electron manifold, the only major change occurring for a two-electron transition is $\phi_{n'l'} \rightarrow \phi_{n'l'}$, with all other passive orbitals remaining in very nearly the same form. Thus, $\langle \phi_j' | \phi_j \rangle \approx 1.0$ unless the overlap involved is $\langle \phi_{n'l'} | \phi_{n'l'} \rangle$, and the probability of a given transition is in simplest approximation²⁶⁹

$$P_{n'l' \rightarrow n'l'} \propto N_{n'l'} |\langle R_{n'l'} | R_{n'l'} \rangle|^2 \quad (156)$$

where $N_{n'l'}$ is the occupation number of the $n'l'$ subshell, and allows for a summation on $m_l m_s$ (which must equal $m_l m_s$). Here the radial function $R_{n'l'}$ must be calculated in the final-state ionic potential, and $R_{n'l'}$ is a radial function for the initial state. By virtue of symmetry, the overlap in Eq. (156) will only be non-zero if $l'' = l'$, a result that is often termed a one-electron monopole selection rule. Thus, for example, only $2s \rightarrow ns$ and $2p \rightarrow np$ monopole transitions yield large intensities as quoted in Table II (although a single, weak $2p \rightarrow 3s$ dipole transition is also thought to be present). The total symmetries for the $(N-1)$ passive electrons are also predicted to follow a monopole rule of the form predicted by Eq. (69)

$$\Delta J = \Delta L = \Delta S = \Delta M_J = \Delta M_L = \Delta M_S = \Delta \pi = 0 \quad (157)$$

where J is the quantum number for $L+S$, and π is the overall state parity.

Equation (156) has been used with reasonable success in predicting shake-up and shake-off intensities in core-level emission from rare gases,^{4, 135, 269, 270, 271} as well as from alkali-halides²⁷¹ for which the component ions possess rare-gas configurations. Some previous results for Nels emission are summarized in Table II, where calculated two-electron peak separations and relative intensities are compared with experiment. The various final-state configurations are noted and for this case the $\Psi_R(N-1)$ of Eq. (69) corresponds to an *unrelaxed* $\text{Ne}^+ 1s2s^22p^6$ with an overall L, S coupling of 2S . There is reasonable agreement between theoretical and experimental separations, but the theoretical values are uniformly high by about 1.8 eV out of 40 eV, and have been back-corrected by this amount before entry in the table.²⁷⁰ The necessity for this correction has been explained as a $2p-2p$ correlation and relativistic error in the Hartree-Fock calculation for the one-electron $2p^6$ final state that is of much lower magnitude in the various $2p^5np$ two-electron final states because of the reduced $2p-np$ overlap. Theoretical and experimental relative intensities are also in fair agreement. It should also be noted in connection with these data that the various L, S multiplets formed as final states must be considered. For example, the peaks indicated as “lower” and “upper” in Table II are due to a multiplet splitting of the same type noted on the right-hand side of Fig. 30 for the 5P states of Mn^{3+} . In the case of Ne^+ , 2S states can be formed in two ways from the same total configuration $1s2s^22p^5np$: one in which the $1s$ electron is coupled with $2s^22p^5np(^1S)$ and one in which it is coupled with $2s^22p^5np(^3S)$.^{4, 135} A similar effect occurs in $1s2s2p^6ns$ final states. Thus, there may be considerable interaction between multi-electron processes and multiplet splittings, and a complete specification of the final state must include possible multiplet effects.

The assumption of single-configuration final states used in the previous analysis clearly is open to question, especially since the best description of all states would presumably be via a complete configuration-interaction treatment. Martin and Shirley¹⁴ have performed CI calculations for Ne and the isoelectronic molecule HF that do indeed indicate that configuration-interaction effects can be significant. Their analysis proceeds via an equation analogous to Eq. (83), from which it is clear that both final-state CI and initial-state CI can complicate the calculation of intensities by opening up new options for non-zero $(C_j^f)^* C_j^i$ products. In particular, the mixing of both the $1s^22s^22p^6$ and $1s^22s^22p^53p$ configurations into the initial state and the final states corresponding to the observed peaks 0, 3, and 4 is found to significantly alter the calculated intensities so as to yield better agreement with experiment, as shown in Table II.

It should also be noted that the total shake-up intensities associated with *valence-level* emission are generally observed to be higher than predicted by

the simple theory outlined above, a result that is consistent with much stronger intrashell correlation effects.^{135, 269} For example, Chang and Poe²⁷² have recently performed theoretical calculations for Ne2*p* excitation at $h\nu \lesssim 200$ eV using more accurate many-body perturbation theory. Their results are in good agreement with available experimental data.

Similar core-level shake-up phenomena are also well known in molecules^{4, 269, 270} and the same type of sudden approximation analysis as represented by Eqs (69) to (74) has been used with some success to predict intensities.^{273, 274} In connection with valence-level emission a recent CI analysis of low-energy satellite structure in CO by Bagus and Viniikka²⁷⁵ indicates that higher-order correlation effects are also highly significant, in agreement with the similar conclusions reached previously for atomic valence-level shake-up.

3. *Multi-electron Excitations in Metals.* Processes analogous to shake-up and shake-off are also expected to occur during core-level emission from solid metals, where the form of the density-of-states curve above the Fermi energy provides a continuous range of allowed one-electron excitation energies, rather than the discrete set available in atoms or molecules. Thus, rather than a sharp set of satellite lines below a roughly symmetric one-electron-transition peak (cf. Fig. 36), what is expected is an asymmetric tailing of the main peak. The detailed line shapes associated with such processes in XPS core-level emission were first discussed by Doniach and Sunjic²⁷⁶ and are predicted to have the form:

$$I(E) = \frac{\cos [\pi\alpha/2 + (1-\alpha) \tan^{-1}(E/\gamma)]}{(E^2 + \gamma^2)^{(1-\alpha)/2}} \quad (158)$$

where

E = kinetic energy measured from the threshold of the unbroadened one-electron-transition peak

γ = the lifetime of the core hole

α = an asymmetry parameter

$$= 2 \sum_l (2l+1) (\delta_l/\pi)^2 \quad (159)$$

δ_l = the phase shift of the l th partial wave for electrons at the Fermi energy scattering from the core hole.

2γ is thus the natural FWHM of the core-level. If $\alpha=0$ (as it is for insulators), then $I(E)$ merely reduces to a Lorentzian lifetime broadening. The phase shift δ_l thus has a meaning very close to those discussed in connection with atomic differential cross-sections in Section III.D.2 (cf. Fig. 9).

Citrin²⁷⁷ first pointed out that XPS metal spectral shapes exhibited an asymmetry suggestive of Eq. (158). The first quantitative tests of the applicability of this line shape for describing such spectra were performed by Hüfner, Wertheim and co-workers.⁸⁴ They fitted Eq. (158) to core spectra for various simple metals and transition metals, empirically choosing the best values of γ and α . The spectra were corrected for instrumental resolution effects, but not for inelastic scattering. Examples of such a comparison between theory and experiment for Au and Pt⁸⁴ are shown in the right-hand panels of Fig. 37. It is significant here that Au with a low density of states near the Fermi level shows a much lower degree of asymmetry than Pt with a high density of states near the Fermi level. Hüfner, Wertheim *et al.*⁸⁴ concluded that this line shape does well describe the peaks observed in these metals, and that the values of γ and α obtained were physically reasonable. Similar conclusions have been reached in several other studies,^{115, 191} and it thus seems likely that such shake-up-like effects do exert a significant influence on line shapes in metals.

A further closely-related effect that has been predicted to occur in metals is the creation of plasmon excitations during the formation of a core hole.^{194, 278} Such "intrinsic" plasmons are distinguished from the "extrinsic" plasmons created during photoelectron escape from the material, although they occur at the same energy and are thus rather difficult to resolve from the experimental inelastic tail. Debate still continues as to how important intrinsic plasmons are in XPS spectra,²⁷⁹ and some angular-resolved XPS results bearing on this question are discussed in Section VI.B.

4. *Core-peak Satellites in Transition-metal and Rare-earth Compounds.* Very strong low-kinetic-energy satellite lines were first observed in a study of Cu2*p* core levels in compounds such as CuS and Cu₂O by Novakov²⁸⁰. Similar results obtained more recently by Frost *et al.*²⁸¹ are shown in Fig. 38, and it is clear that the satellite peaks have intensities comparable to those of what might be referred to as the one-electron-transition peaks at lowest apparent binding energy. The appearances of these satellites also depend strongly on chemical state, being most intense in cupric compounds containing Cu⁺² 3*d*⁹ ions, and almost unobservable in cupric compounds containing Cu⁺¹ 3*d*¹⁰ ions. Similar strong satellites also occur in the core spectra of other open-shell transition-metal and rare-earth compounds.^{114, 282-286} They are thus much higher in relative intensity than the 10-30% expected from typical atomic-like shake-up processes, and a great deal of discussion has gone on concerning their origins. Summaries of experimental data, as well as analyses of various proposed models, appear in several prior publications.^{114, 280-286}

The most plausible explanation that has emerged for such effects is a significant involvement in the final state of a ligand-to-metal charge transfer

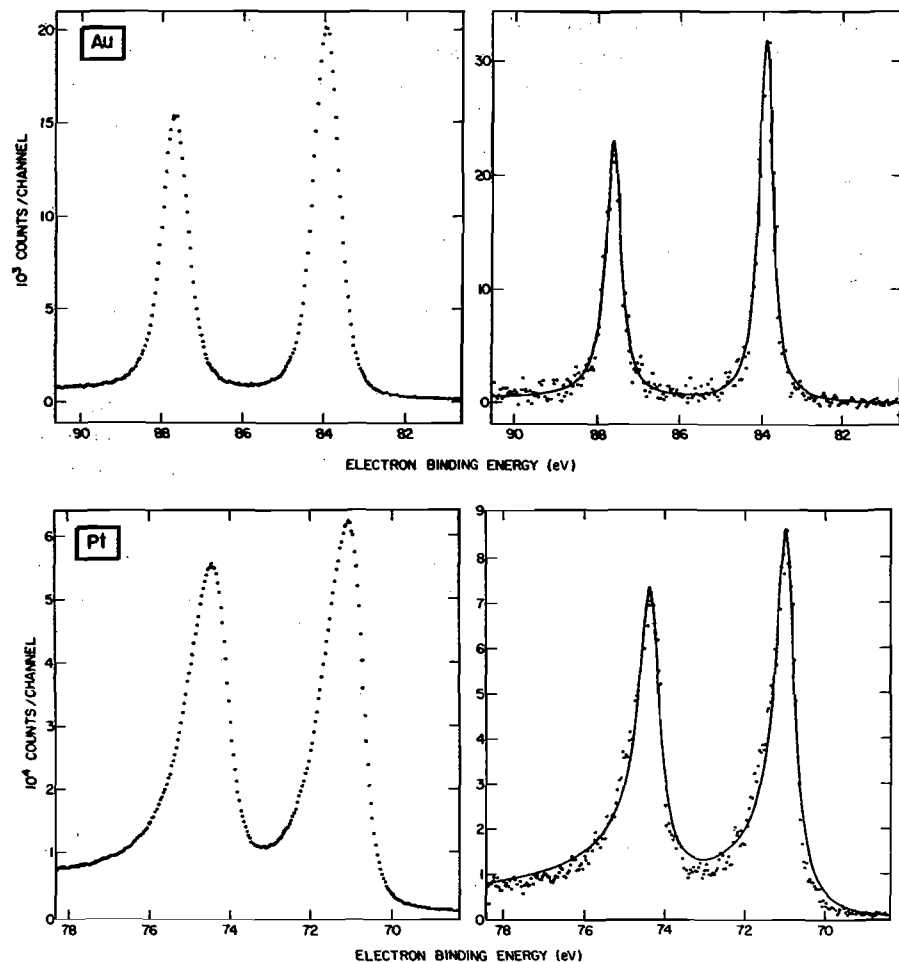


Fig. 37. $4f$ core spectra from polycrystalline Au and Pt (points) in comparison to a best fit of the asymmetric line shape predicted by Eq. (158) (curves). In the right panels, the data have been corrected by deconvolution of the instrumental line shape, but no correction for inelastic scattering effects has been made. The instrumental line shape was derived from the form of the cut-off near E_F (cf. Fig. 13). (From Hüfner and Wertheim, ref. 84.)

that results in a $3d$ or $4f$ configuration with one more d or f electron than in the initial state.^{114, 282, 283, 285, 286} This idea was first suggested and qualitatively discussed by Wertheim *et al.*¹¹⁴ for satellites in $4f$ compounds and by Kim²⁸³ for $3d$ satellites. The importance of such $3d^n \rightarrow 3d^{n+1}$ and $4f^n \rightarrow 4f^{n+1}$ configurations is not surprising, since they represent an attempt to screen very effectively the core hole formed during final-state relaxation. In fact, there is a high degree of similarity between such final-state configurations

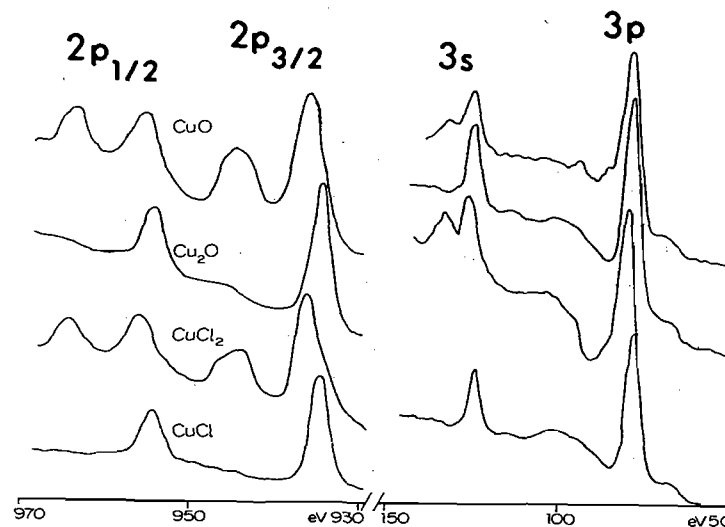


Fig. 38. $2p_{3/2}$, $2p_{1/2}$ and $3s$, $3p$ core-level spectra from the copper compounds CuO, Cu₂O, CuCl₂, and CuCl. The low-energy satellites are very strong in Cu⁺² $3d^9$ compounds (CuO, CuCl₂), and very weak in Cu⁺¹ $3d^{10}$ compounds (Cu₂O, CuCl). (From Frost *et al.*, ref. 281.)

and those used by Ley *et al.*²³⁵ to describe conduction-electron screening in metals (cf. Fig. 29 and discussion in Section V.B). The absence of satellites for closed-shell d or f systems is immediately explained in this picture, as such relaxation mechanisms are not possible. The most quantitative discussions of this model as applied to $3d$ -compound satellites have been presented by Larsson²⁸⁵ and Asada and Sugano.²⁸⁶ A two-configuration manifold is used to describe the final-state core-hole wave functions, with one configuration Φ_1 being the simplest final-state determinant with no change in valence-subshell occupations and the other Φ_2 being a determinant in which a single-electron ligand-to-metal transfer has occurred. Specifically, in an octahedrally-coordinated system, the transfer is ascribed to a monopole-allowed excitation of the type:^{283, 285, 286} $e_g(\text{bonding}) \equiv e_g^b \rightarrow e_g(\text{anti-bonding}) \equiv e_g^a$. Both orbitals are expressed as linear combinations of metal d and ligand valence, with e_g^a being primarily metal $3d$. The crystal-field-split octahedral symmetry designations are used, and the sudden approximation one-electron monopole selection rule must here be applied to these symmetries. If only the active orbitals are considered, the two final-state configurations can thus be written as:²⁸⁶

$$\Phi_1 = (\text{core hole}) (e_g^b)^n (e_g^a)^m$$

$$\Phi_2 = (\text{core hole}) (e_g^b)^{n-1} (e_g^a)^{m+1} \quad (160)$$

Mixing these configurations produces two final states with differing degrees of charge transfer:

$$\begin{aligned}\Psi_1^f &= C_{11}\Phi_1 + C_{12}\Phi_2 \quad \text{at } E_1^f \\ \Psi_2^f &= C_{21}\Phi_1 + C_{22}\Phi_2 \quad \text{at } E_2^f\end{aligned}\quad (161)$$

The "main" line occurs at lower E^f and thus higher kinetic energy and lower binding energy. If Ψ_1^f is chosen to represent this main line, it is found to correspond to a net transfer of ≥ 0.5 electrons to the metal site.^{110, 285} Thus, hole screening is predicted to be very appreciable as far as this state is concerned, and the mixing represented by Eq. (161) is highly significant. If the degree of one-electron-orbital relaxation is small, then Φ_1 is approximately equal to the $(N-1)$ -electron remainder $\Psi_R(N-1)$ in Eq. (69), and the sudden approximation yields peak intensities via Eq. (84) of

$$I_1 \propto |C_{11}|^2, \quad I_2 \propto |C_{21}|^2 \quad (162)$$

Additional splittings due to crystal-field effects, multiplet effects, and spin-orbit interactions cause further fine structure in the predicted energies, and one-electron orbital relaxation has furthermore been included by means of the equivalent-core approximation.²⁸⁶ With a limited degree of empirical parameter choice, numerical results based upon this model are in good agreement with experimental satellite data for $3d$ compounds as to intensities, widths, positions, and systematic trends with ligand character and d -orbital occupations.^{285, 286} Finally, it is important to note that Viniikka and Bagus¹¹⁰ have carried out more accurate self-consistent Hartree-Fock calculations with configuration interaction on fully-relaxed core-hole states in the cluster $[\text{NiO}_6]^{-10}$. These results also show that a significant ligand-to-metal charge transfer of ~ 0.5 electrons is present in the state representing the main line. It is also concluded that the two primary final states contain significant admixtures of both configurations ($C_{11} \approx 0.9$, $C_{12} \approx 0.3$; $C_{21} \approx 0.3$, $C_{22} \approx 0.9$).

The occurrence of such two-configuration charge-transfer satellites has also been suggested in connection with the adsorption of CO on transition-metal surfaces.²⁸⁷ In this case, satellites observed in the O1s spectrum are attributed to the strong involvement of a metal-to-molecule charge transfer (that is, the reverse of the direction discussed previously).

Thus, such satellites and the charge-transfer they represent can be extremely important considerations in the analysis of spectra in many systems. The term "shake-up" has been applied to these effects,^{283, 285, 286} but such nomenclature can be a bit misleading in the sense that the final states are not pure configurations that are as simply related to the initial state as for the neon case of Table II. The most correct view would seem to be

simply that a strong configuration interaction occurs in the final state due to relaxation about the inner hole.

It is finally worth noting that the presence or absence of such satellites has potential for use in a "fingerprint" mode for determining the oxidation state and/or valence configuration of $3d$ or $4f$ atoms in different chemical environments.

5. *Other Multi-electron Effects.* As a final example of multi-electron effects, we consider the observation first made by Gelius²⁷⁰ that, for a series of elements with $Z \approx 50-60$, the $4p$ binding energy broadens into a many-electron resonance with complex structure, as shown in later data obtained by Kowalczyk *et al.*²¹⁵ in Fig. 39. This rather unique occurrence has been observed in both gases²⁷⁰ and solids,²¹⁵ and has been explained by Wendin *et al.*^{288, 289} as being caused by the particular one-electron energy-level spacings involved. Specifically, the single-configuration final-state after $4p$ emission is $\dots 4p^5 4d^{10} 5s^2 \dots$, with the remaining outer occupancies depending upon Z . However, the $4d$ binding energy is approximately $\frac{1}{2}$ that of $4p$ in this region of the periodic table, so that one $4d$ electron can be moved into the lower-energy $4p$ orbital and another $4d$ electron can be placed in a low-energy unoccupied bound orbital or continuum orbital to yield a set of configurations like $\dots 4p^6 4d^8 5s^2 \dots (n'l')^1$ or $\dots 4p^6 4d^8 5s^2 \dots (E_{\text{kin}}' l')^1$ respectively that are nearly degenerate with the one-electron final-state configuration. Strong mixing thus occurs among these configurations, with a resultant smearing of the final states into a broad resonance with fine structure. The mixing in of continuum configurations can also be considered to result from a Coster-Kronig Auger de-excitation of the $4p$ hole via $4d \rightarrow 4p$, $4d \rightarrow$ continuum. The form of the interactions further dictates that orbitals with $l' = 2$ are dominant.^{288, 289} (Note the similarity between the configurational degeneracy discussed here and that noted by Bagus *et al.*²⁵² in their analysis of $3s$ emission from Mn^{2+} , cf. Section V.C). It is thus rather fortunate that such resonances are rare phenomena throughout the periodic table, as one-electron energy levels would otherwise be a much less useful concept.

E. Vibrational Effects

The effects of exciting various final vibrational states on XPS spectra were first clearly observed in gas-phase data obtained with monochromatized radiation by Gelius and co-workers.²⁷⁰ A C1s spectrum obtained from gaseous CH_4 is shown in Fig. 40, and it exhibits a three-component structure that can be explained as arising from the excitation of three different vibrational states of the symmetric C-H stretch type.²⁷⁰ The relative intensities and positions of these peaks are furthermore found to be in good agreement with a theoretical model based upon the Born-Oppenheimer approximation as expressed in Eq. (63), provided that it is noted that the C1s hole alters

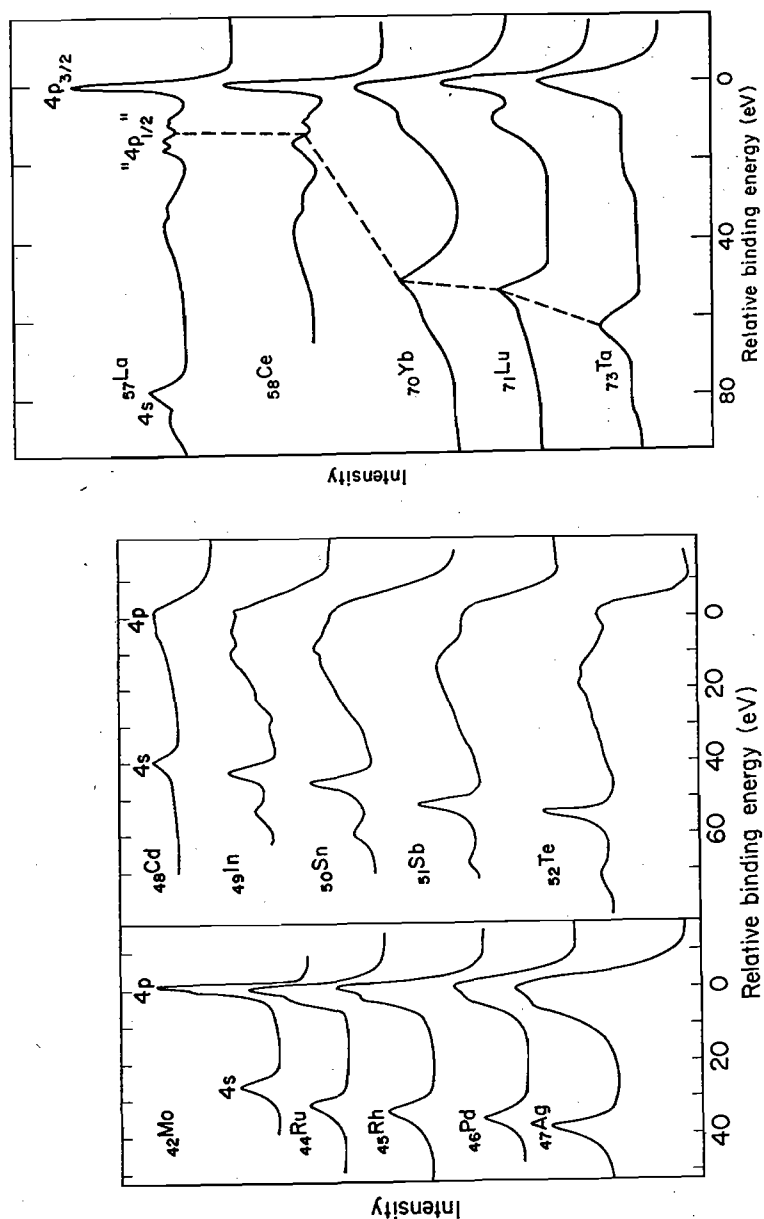


Fig. 39. $4s$, $4p$ core-level spectra for a series of metals from Mo ($Z=42$) to Ta ($Z=73$). Note the broad $4p$ resonance that exists from $Z \approx 49$ to $Z \approx 60$. (From Shirley *et al.*, ref. 215.)

vibrational energies and wave functions appreciably in the final state. Similar vibrational effects appear to be present in other small molecules, and it is thus clear that XPS peak widths and positions can be significantly affected by final-state vibrational excitations.

Vibrational effects have also been noted in XPS studies of solids by Citrin *et al.*⁸⁵ In this work, core peaks in alkali halides were found to exhibit temperature-dependent line widths consistent with the excitation of lattice

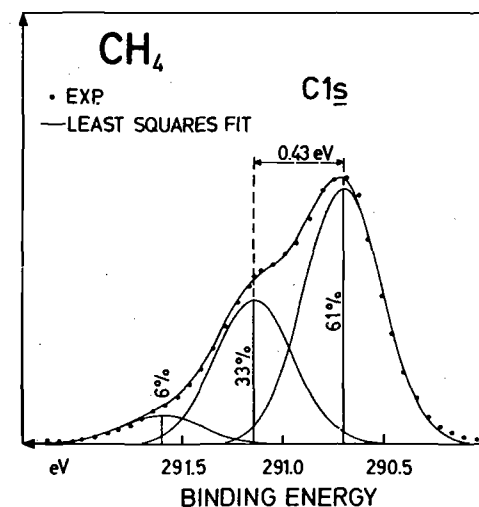


Fig. 40. A $C1s$ spectrum from gaseous CH_4 obtained with very high instrumental resolution ($FWHM \approx 0.3$ eV). The lowest-binding-energy primary peak shown here is found to exhibit three components due to vibrational excitations in the final state. (From Gelius, ref. 270.)

vibrations (phonons) during photoemission as shown in Fig. 41. A solid-state analysis based upon the Born–Oppenheimer approximation and Franck–Condon factors yields the proper variation with temperature, provided that the effects of specimen charging due to low conductivities at low temperatures are corrected for, as shown in the figure. Such effects are thus expected to be important in all polar solids for which electronic relaxation around the core hole cannot be complete enough to leave final vibrational states of very nearly the same form as the initial vibrational states. In metals, on the other hand, conduction electron screening is expected to be complete enough to leave the initial- and final-vibrational manifolds nearly identical. Thus, in metals the distribution of phonon excitation probabilities or Franck–Condon envelope is sharply peaked around the initial states (as can be seen by considering Eq. (63) for a single set of orthonormal functions); therefore, very little extra broadening is expected.

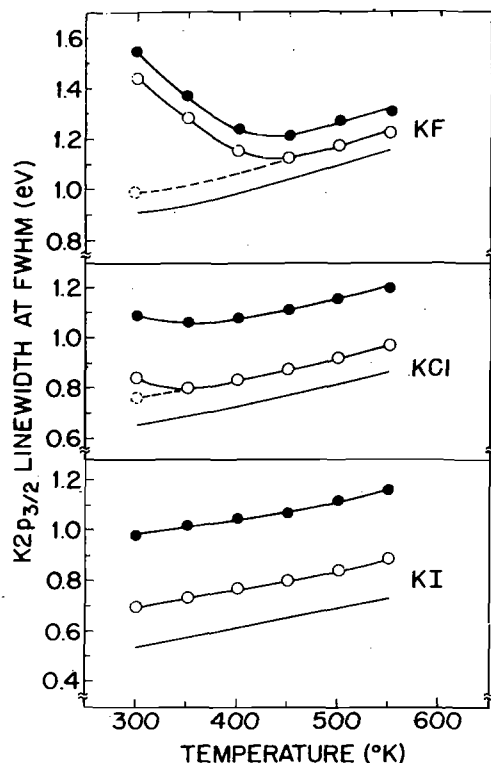


Fig. 41. Variation of the $K2p_{3/2}$ FWHM with temperature in solid KF, KCl, and KI. The curves $\bullet\text{---}\bullet$ are the unaltered experimental data. The curves $\circ\text{---}\circ$ have been corrected for lifetime and instrumental width contributions. The dotted curves represent further corrections for specimen charging that occurred in KF and KI at low temperatures. The solid curves are theoretical calculations based upon final-state vibrational broadening. (From Citrin *et al.*, ref. 85.)

VI. ANGULAR-RESOLVED MEASUREMENTS ON SOLIDS

A. Introduction

Angular-resolved XPS studies of solids have very recently been reviewed by the author,¹⁷ so only a brief outline of the most significant aspects and certain very new results will be presented here. The most generally occurring types of effects are those involving surface sensitivity enhancement for grazing angles of electron exit or x-ray incidence with respect to the surface and two types of anisotropies observed in the angular distributions of photoelectron intensities from single-crystal specimens.

The schematic geometry shown in Fig. 42 both reiterates the definitions of various angles as discussed previously here (cf. Figs 7 and 17) and also indicates that the electron emission direction can be made to have any

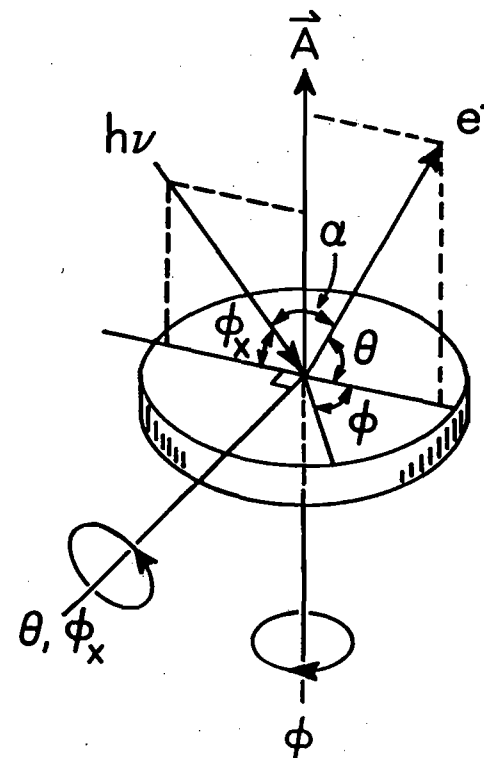


Fig. 42. General geometry for an angular-resolved XPS experiment. Rotations on the two perpendicular axes shown vary θ , ϕ_x and ϕ over their full allowed ranges. The angle α also may be varied, but is most commonly held constant.

orientation with respect to a set of axes fixed in the specimen if externally-actuated rotation is possible on the two perpendicular axes shown. Rotation on the axis perpendicular to the plane containing the photon and electron propagation directions varies the angles θ and ϕ_x describing electron exit and x-ray incidence, respectively. Rotation about the second axis parallel to the specimen surface normal varies the azimuthal angle ϕ as measured with respect to a specimen-fixed reference. Low ϕ or low ϕ_x thus corresponds to a grazing condition. The angle α is held fixed in most current XPS systems. Two-axis specimen goniometers for this purpose have been specially built for use in XPS studies, and various instrumental aspects of carrying out such measurements have been reviewed elsewhere.^{17, 74, 202, 290}

B. Surface Sensitivity Enhancement at Grazing Electron Exit Angles

The achievement of greater relative surface sensitivity at conditions of grazing electron exit angles has already been discussed in connection with the

θ -dependent relationships describing peak intensities in Section III.F.2. The application of this procedure in XPS was first demonstrated by Fadley and Bergström,²⁹¹ and first quantitatively applied by Fraser *et al.*²⁰¹ As a simple illustration of the fundamental mechanism, Fig. 43 illustrates the way in which the mean depth of no-loss emission varies for a homogeneous, semi-infinite substrate. If Λ_e is assumed to be a direction-independent property of the material, this mean depth is given at any angle by $\Lambda_e \sin \theta$, so it is clear that a decrease of θ from say 90° to 5° will decrease the mean depth by about a factor of 6. This is a highly significant change that has by now been used in numerous studies to enable selectively altering the surface sensitivity of the XPS measurement.¹⁷

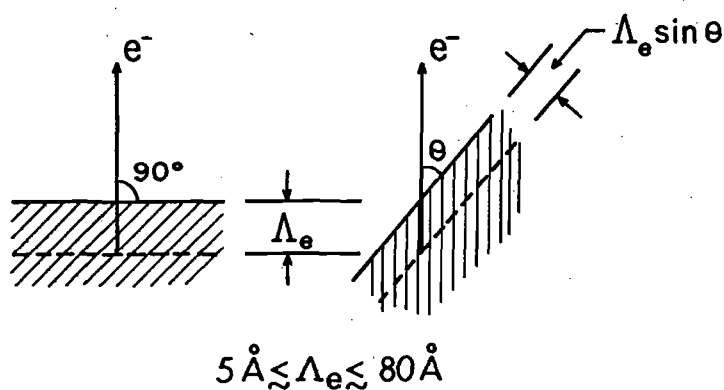


Fig. 43. Illustration of the basic mechanism producing surface sensitivity enhancement for low electron exit angles θ . The average depth for no-loss emission as measured perpendicular to the surface is given by $\Lambda_e \sin \theta$.

The only significant moderating factor that may in certain circumstances render such low- θ measurements somewhat less dramatic in capability is the presence of surface roughness. Surface roughness in general causes the local microscopic true angles of emission θ^t to differ from the experimental value θ as measured relative to the macroscopic planar average of the specimen surface. In general, for low θ values, roughness is expected to cause θ^t to be greater than θ , so that surface sensitivity enhancement is expected to be diminished.^{17, 202, 290-294} Roughness further has the effect of shading certain portions of the surface from x-ray incidence and/or electron exit. Such effects have been studied both experimentally and theoretically for a few systems,^{17, 202, 203, 290-294} and, although it is clear that large-scale roughness can significantly alter the type of surface enhancement achieved,²⁰³ it has also been found for one system that, even with pressed powder pellets of the type often used as specimens in XPS, a usefully large surface enhancement can be achieved at low θ .²⁹³ Thus, although roughness effects always need

to be considered in any quantitative analysis of such XPS data and the preparation of highly planar specimens is essential for some work,²⁹⁴ there are good reasons to expect very general utility of the low- θ surface enhancement procedure. We now consider a few examples of the application of this method.

In Fig. 44, broad-scan spectra are shown at various angles for a highly-polished silicon specimen with an oxide overlayer 1-2 atomic layers in

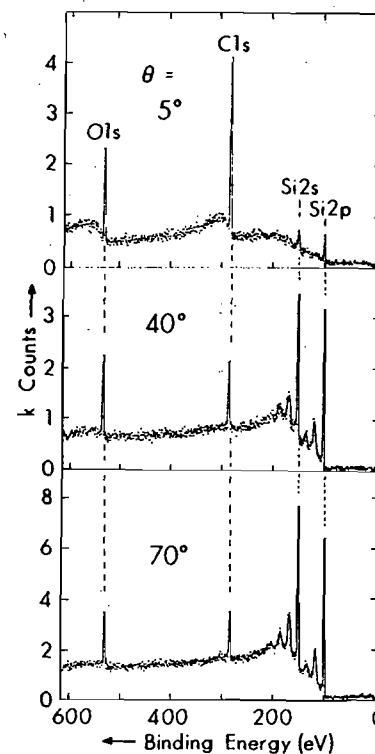


Fig. 44. Broad-scan core spectra at low and high exit angles for a Si specimen with a thin oxide overlayer ($\sim 4 \text{ \AA}$) and an outermost carbon contaminant overlayer approximately 1-2 monolayers in thickness. The C1s and O1s signals are markedly enhanced in relative intensity at low θ due to the general effect presented in Fig. 43. (From Fadley, ref. 17.)

thickness, and an outermost overlayer of carbon-containing residual gas impurities of approximately the same thickness. (These thicknesses were estimated using Eqs such as (117) and (118).) Pronounced peaks due to the O1s, C1s, Si2s, and Si2p core levels are observed. At the higher emission angles of 40° and 70° , plasmon loss structure is also found to be associated with the Si peaks (cf. also Fig. 1 for Al). As θ is lowered to a grazing exit condition, marked changes occur in the relative intensities of all peaks, in

fact causing a complete inversion in ordering. At high θ where maximum bulk sensitivity is expected (Λ_e in Si is $\sim 37 \text{ \AA}$ and Λ_e' in SiO_2 is $\sim 27 \text{ \AA}$ ²⁹⁴), the intensity order is $\text{Si}2s, 2p \gg \text{O}1s > \text{C}1s$, where at low θ with maximum surface sensitivity, it is $\text{C}1s > \text{O}1s \gg \text{Si}2s, 2p$. Such a three-angle scan thus clearly establishes the mean vertical displacement of all dominant species with respect to the surface, yielding very directly a qualitative concentration profile. If the $\text{Si}2p$ region for this specimen is examined more closely, it is further found to exhibit a chemical shift between oxide and element, as shown in Fig. 45. However, the thin oxide layer present yields only a very weak relative intensity in the $\text{Si}2p$ (oxide) peak at the relatively high angle of $\theta = 49^\circ$.

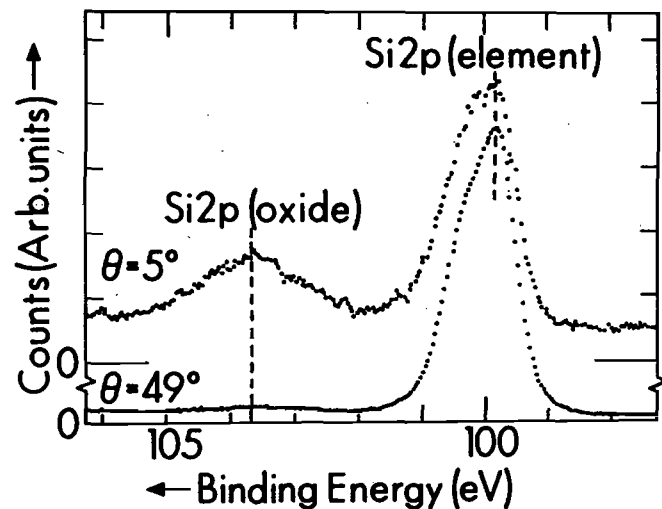


Fig. 45. $\text{Si}2p$ core spectra at $\theta = 5^\circ$ and 49° for the specimen of Fig. 44: The chemically-shifted $\text{Si}2p$ (oxide) peak is enhanced in relative intensity by approximately a factor of 20 between 49° and 5° . (From Fadley, ref. 17.)

The spectrum obtained at $\theta = 5^\circ$ by contrast exhibits marked enhancement by a factor of ~ 20 in the oxide relative intensity. More quantitative studies of such relative intensity changes with angle have also been made by Hill *et al.*,²⁹⁴ and, although certain discrepancies are found to occur at low θ values with respect to the simple intensity expressions given in Section III.F.2, case (c), it nonetheless appears possible to extract highly quantitative data concerning specimen geometry and electron attenuation lengths.

An additional effect that is of interest in connection with the enhanced surface sensitivity achievable at low θ is a change in the relative intensities of various inelastic loss processes. For example, for an atomically clean surface of aluminium (which exhibits well-defined surface- and bulk-plasmon excitations at different energies), it has been found by Baird *et al.*²⁹⁵ that

the surface plasmon losses are markedly enhanced in relative importance at low θ . Some data from this study are shown in Fig. 46. The reason for this enhancement is that the surface- and bulk-plasmons are spatially orthogonal.¹⁹⁷ Because decreasing the angle of exit also decreases the mean depth of emission, the relative probability of exciting a surface plasmon is thus also increased at low exit angles. Comparisons of such data with theoretical calculations for a free electron metal¹⁹⁴ furthermore yield good agreement with experimental relative intensities and further suggest that the creation of plasmons occurs by means of both extrinsic (after excitation) and intrinsic

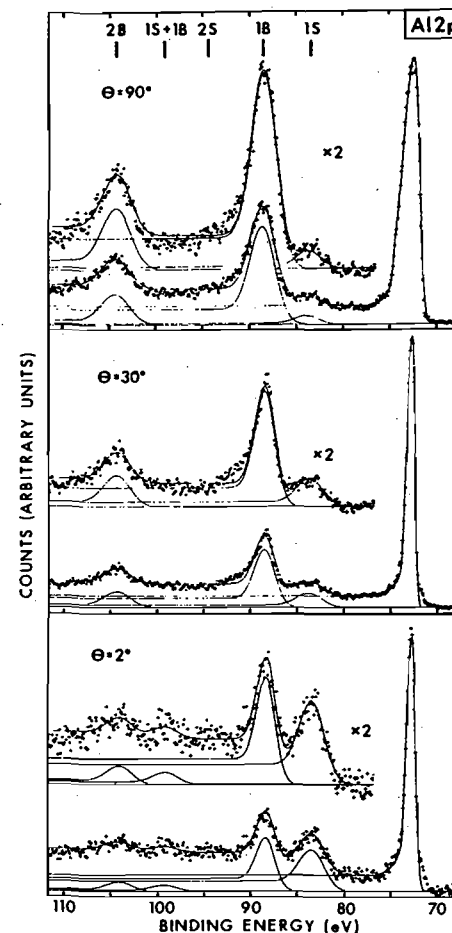


Fig. 46. $\text{Al}2p$ plasmon loss spectra from a clean surface of polycrystalline aluminium at $\theta = 90^\circ, 30^\circ$, and 2° . The positions of various combinations of surface and bulk losses are denoted 1S, 1B, etc. Note the marked enhancement of the relative intensity of the surface plasmon loss (1S) for grazing exit angles. (From Baird *et al.*, ref. 295.)

(during excitation) processes.²⁹⁵ An additional interesting feature of such angular-dependent loss measurements is that they can be used to determine the locations of adsorbed molecules relative to a surface. Specifically, the O1s loss spectrum for an ~ 0.2 monolayer coverage of oxygen on aluminium exhibits only surface plasmon peaks at grazing electron exit, indicating that the oxygen has not penetrated significantly below the surface plane.^{295, 296} Thus, the angular dependence of such adsorbate loss structures should provide useful complementary information concerning adsorption geometries and near-surface electronic structure.

The ground-state valence electronic structure of a solid is also predicted theoretically to change near its surface,²⁹⁷ and it is of interest to determine whether angle-resolved XPS studies can detect this. One effect that should occur in transition metals is a narrowing of the FWHM of the *d*-bands near the surface due to reduced coordination number.²⁹⁷ Such effects have been studied quantitatively by Mehta and Fadley²⁹⁸ for the case of clean polycrystalline copper surfaces, and the experimental and theoretical *d*-band

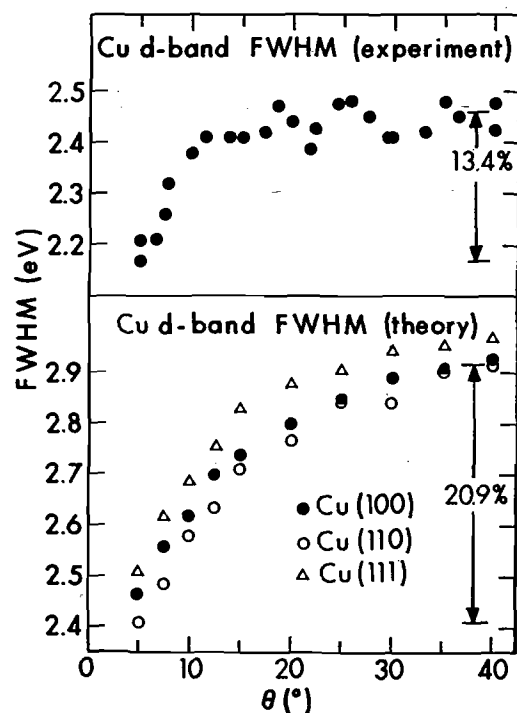


Fig. 47. Experimental and theoretical angular dependence of the FWHM of the Cu3*d* valence-band peak. The width decreases at low θ due to *d*-band narrowing near the surface that is in turn caused by reduced coordination number. (From Mehta and Fadley, ref. 298.)

FWHM values determined are summarized in Fig. 47. The small, but unambiguous decreases in FWHM observed at low θ are consistent with the theoretical calculations, with theory showing somewhat larger relative changes that could easily be explained by several effects.²⁹⁸ Thus, such low- θ measurements can also be used to probe alterations in the near-surface valence electronic structure.

C. Surface Sensitivity Enhancement at Grazing X-ray Incidence Angles

A second mechanism producing enhanced surface sensitivity involves measurements carried out at very low x-ray incidence angles ϕ_x . For $\phi_x \lesssim 1^\circ$, it was first noted by Henke¹⁷⁸ that the mean x-ray penetration depth in a typical XPS experiment (which is 10^3 – 10^5 Å for $\phi_x \gg 1^\circ$) decreases markedly to values of the same order as the electron attenuation length Λ_e . This further suggests that surface-atom signals will be enhanced in relative intensity at low ϕ_x , as was first demonstrated by Mehta and Fadley.¹⁷⁹ The reason for this decrease in x-ray penetration depth is the onset of significant refraction such that $\phi_x' \ll \phi_x$ (cf. Fig. 17) and reflection at the solid surface. The interactions of typical XPS x-rays with a homogeneous medium are furthermore well described by a macroscopic classical treatment,¹⁷⁸ and detailed expressions for predicting penetration depths and expected surface sensitivity

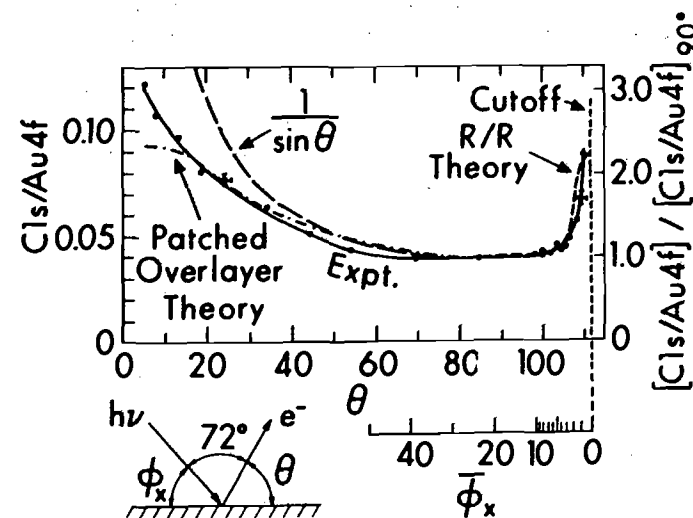


Fig. 48. Angular dependence of the Cl1s/Au4*f* intensity ratio for a gold specimen with a thin carbon-containing overlayer. Enhancement of the near-surface carbon signal is found for both grazing electron exit (low θ) and grazing x-ray incidence (low ϕ_x). The low- ϕ_x enhancement is well predicted by classical calculations allowing for x-ray refraction and reflection (R/R) at the surface, as shown by the dashed curve. (From Mehta and Fadley, ref. 179.)

enhancements in terms of the material optical constants and other parameters have been presented elsewhere.^{17, 178, 179}

As an example of the surface sensitivity enhancement occurring at low ϕ_x , Fig. 48 shows data obtained from a gold specimen with ~ 2 atomic layers of carbon-containing material as an overlayer. The Cl $1s$ /Au $4f$ intensity ratio thus serves as a measure of relative surface sensitivity, and it is observed to increase at both low θ (for reasons discussed in the last section) and low ϕ_x . The increase at low ϕ_x is comparable to that at low θ (approximately a factor of 2–3), and there is good agreement between experiment and theoretical calculations including refraction and reflection effects. Note the very sharp onset of the low- ϕ_x enhancement over a region of only a few degrees near $\phi_x = 0$. Similar effects have also been noted in the Si $2p$ (oxide)/Si $2p$ (element) ratio for silicon with varying oxide overlayer thicknesses.²⁹⁹ Also, the optical properties of several solids at XPS energies of ~ 1.5 keV have been used to predict that such phenomena should be of very general occurrence.¹⁷

It should be noted in connection with low- ϕ_x studies, however, that surface roughness effects can be very important in any attempt at quantitatively analyzing such data.²⁹⁹ This is due to the very small incidence angles involved, so that if the true microscopic incidence angle ϕ_x^t deviates by even $\sim 0.1^\circ$ from the macroscopically measurable ϕ_x , a significant change occurs in the degree of refraction and reflection. Thus, surface preparation and accurate angle measurement are both very critical. A further practical problem is that surface shading by any roughness present will generally act to much diminish absolute photoelectron intensities at low ϕ_x . Thus, low ϕ_x surface enhancements may serve as a useful complement to those at low θ , but the measurement and interpretation of low-incidence-angle data may not be as straightforward.

D. Single-crystal Effects

Two rather distinct types of single-crystal effects have been noted in prior XPS studies. The physical origins and possible interpretations of these will be briefly discussed.

1. *Electron Channeling and Kikuchi Bands.* In measurements of core peak intensities or energy-integrated valence-spectral intensities from single-crystal specimens as a function of the emission angles θ and ϕ in Fig. 42, pronounced fine structure is noted. The first effects of this type were observed by Siegbahn *et al.*³⁰⁰ in NaCl and by Fadley and Bergström²⁹¹ in Au. Baird *et al.*²⁰⁰ have obtained the most detailed set of such data to date for Au $4f$ emission from a Au crystal with (001) orientation and this is summarized in the stereographic projection intensity contour plot of Fig. 49(a). Considerable fine structure is evident in this plot, with many features possessing angular FWHM values of only ~ 5 – 10° and peak height : background ratios as high as $\sim 2 : 1$. It is

thus clear that no peak intensity analysis involving a single crystal can neglect such effects.

The origin of this fine structure is primarily electron diffraction from the various sets of planes in the crystal. These effects are furthermore very closely related to the Kikuchi bands seen in low-energy electron diffraction (LEED) experiments carried out with $E_{\text{kin}} \gtrsim 300$ eV,³⁰¹ as well as to channeling phenomena seen in the emission of high-energy electrons ($\sim 10^4$ – 10^6 eV) from radioactive nuclei imbedded in single crystals.³⁰² Based upon prior experimental and theoretical studies in these two areas,^{301, 302} the qualitative expectation is for each set of planes denoted by Miller indices (hkl) to have associated with it a band of enhanced intensity for photoelectron emission that is parallel with the planes to within plus or minus the first-order Bragg angle θ_{hkl} , as defined from

$$\lambda_e = 2d_{hkl} \sin \theta_{hkl} \quad (163)$$

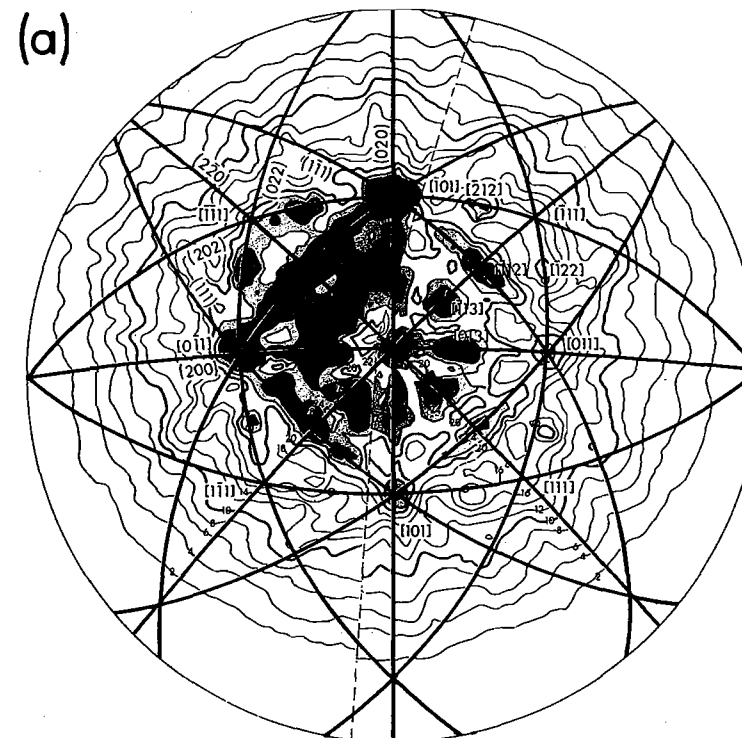


Fig. 49. (a) Experimental photoelectron intensity contours for Au $4f$ emission from a Au(001) single-crystal surface. The contours are plotted in stereographic projection with various low-index directions indicated as $[hkl]$. The normal to the surface therefore lies in the centre of the figure. The arcs represent low-index planes available for electron diffraction or channelling.

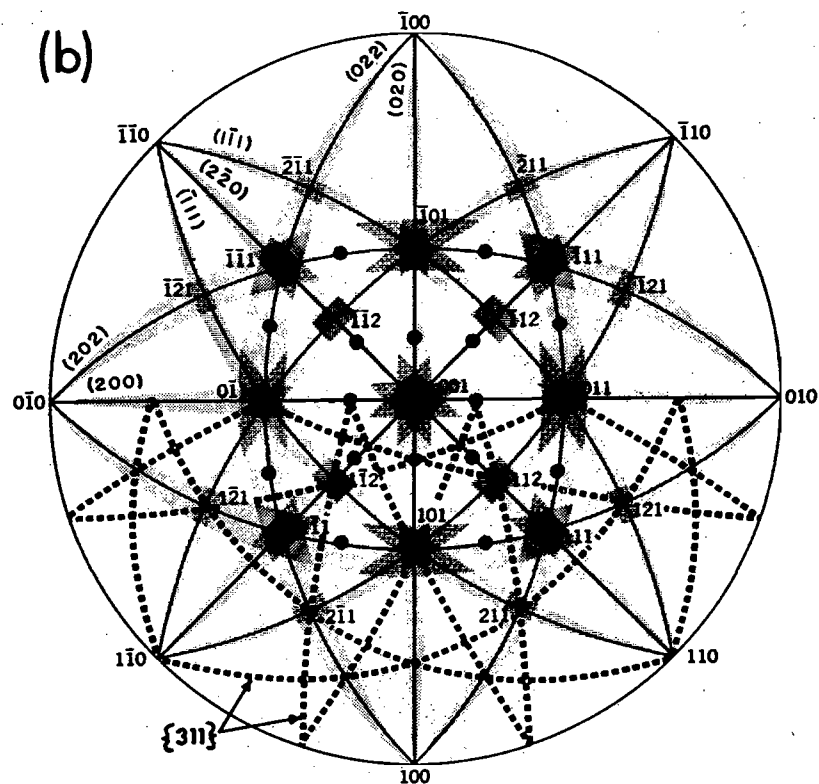


Fig. 49. (b) Qualitative theoretical simulation of the intensity pattern of (a) based on shaded rectangular Kikuchi bands of the form given by the dashed line in Fig. 50. The dotted lines in the lower half of the figure represent the centres of weaker, broader bands from lower-index planes that would also appear at mirror-symmetry-related points in the upper half. (From Baird *et al.*, ref. 200.)

with

$$\begin{aligned} \lambda_e \text{ (in \AA)} &= \text{electron deBroglie wavelength} \\ &= [150/E_{\text{kin}} \text{ (in eV)}]^{1/2} \\ d_{hkl} &= \text{the interplanar spacing} \end{aligned} \quad (164)$$

Such Kikuchi bands are furthermore expected to be approximately uniform in intensity over the $\pm \theta_{hkl}$ range, and to drop off rather sharply at the limits of this range, as shown schematically in Fig. 50. For typical higher-energy XPS photoelectrons and lower-index metal crystal planes, θ_{hkl} is found to lie in the range 3–15°. The overall photoelectron intensity distribution above a single-crystal surface is thus expected to be approximately given by a superposition of such bands for the various low-index planes within the crystal.

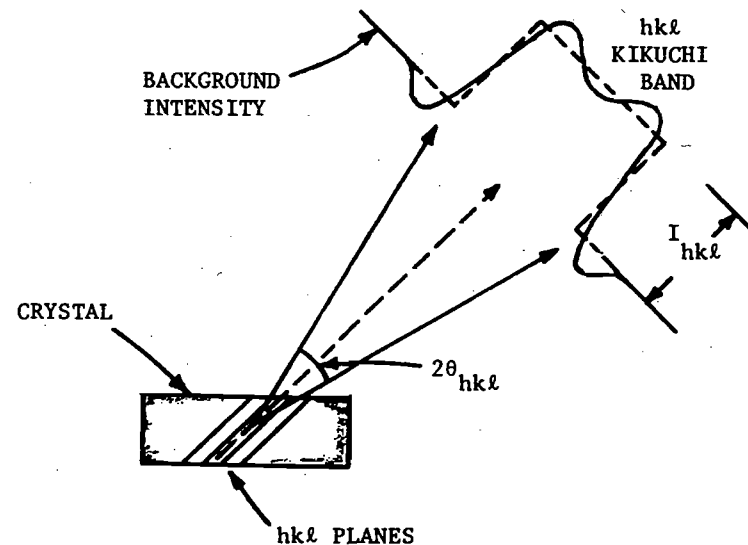


Fig. 50. The approximate form expected for a Kikuchi band from the (hkl) set of planes in a single crystal.

As a qualitative test of this interpretation, Fig. 49(b) presents a stereographic projection on which shaded bands corresponding in width and placement to those expected for the lowest index planes in Au have been inserted. Dotted lines in the lower half of the figure also indicate the centres of broader and weaker bands expected from higher-index planes. Comparison of Figs 49(a) and 49(b) indicates that there is good correspondence between experiment and theory as to the locations of high-intensity regions and fine structure. Recently, more quantitative calculations for copper have been carried out by Baird *et al.*³⁰³ in which each band is given a height proportional to the Fourier coefficient V_{hkl} in the crystal potential; these calculations yield very good agreement with similar intensity contours for copper. Thus, the basic systematics of such effects is well established and relatively easily predicted, and such measurements can provide rather direct information concerning the near-surface atomic order and crystal orientation. Furthermore, in the very near future, more highly accurate theoretical calculations of such effects utilizing methods developed for LEED analyses should become available.³⁰⁴

A final important point in connection with such core-level angular distribution measurements is that it may be possible to utilize them for determining the bonding geometries of atoms or molecules adsorbed on single-crystal surfaces. That is, if core-level emission from an adsorbed atom does exhibit angular anisotropy, it must be primarily associated with final-state scattering effects that should, in turn, be strongly related to the nearest-neighbor

atomic geometry. Very recent measurements in our laboratory do in fact indicate that such anisotropies exist.

2. *Valence Spectra.* It was first noted by Baird *et al.*^{185, 305} that XPS valence spectra from a single crystal exhibit considerable changes in fine structure as the electron emission direction is varied with respect to the crystal axes. As an example of these effects, Fig. 51 presents Au valence

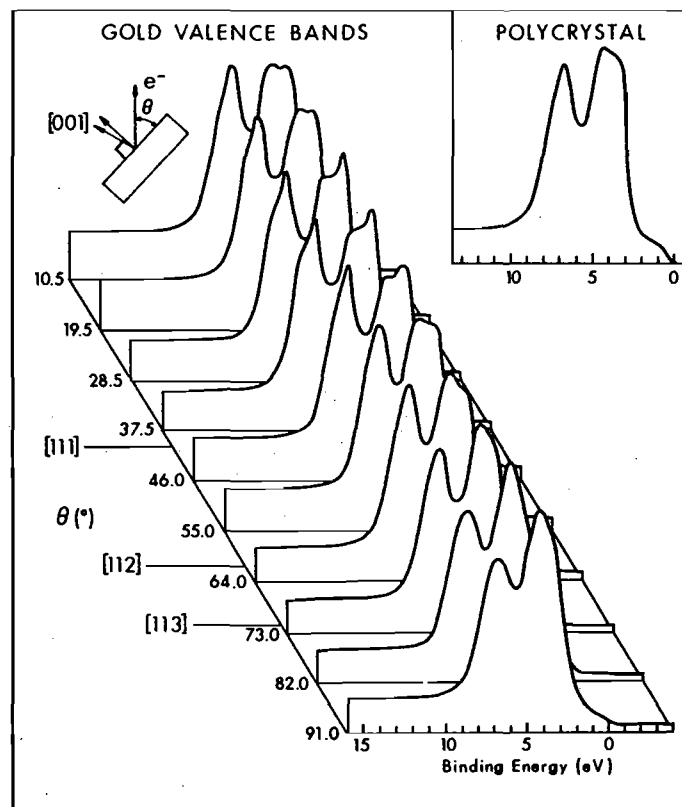


Fig. 51. Au valence spectra from a (001) single-crystal surface obtained at various θ values in a single polar scan passing through the [111], [112], and [113] directions. A polycrystalline spectrum is shown for reference. (From Baird *et al.*, ref. 200.)

spectra obtained with electron emission along various directions in a single θ scan. Although the basic two-peak structure in the dominant d -band peak is present for all directions, there are pronounced changes in the relative intensities and shapes of the two components. In particular, Au spectra obtained with emission along the [001], [101], and [111] directions exhibit probably the most pronounced differences relative to one another, as shown in Fig. 52. Similar changes in single-crystal XPS valence spectra with direction

have by now also been noted in Ag,³⁰⁶ Cu,^{307, 308} Pt,³⁰⁹ and the layer compounds MoS₂, GaSe₂, and SnSe.³¹⁰

The occurrence of such anisotropic effects thus means minimally that considerable care must be exercised in interpreting any XPS valence spectrum from a single crystal in terms of quantities such as the total density of states. That is, the total density of states $\rho(E)$ is by definition a non-directional quantity, as is the mean cross-section $\bar{\sigma}_E(h\nu)$, so that clearly such single-crystal effects add an element beyond the model summarized in Eq. (107). For example the Si spectrum shown in Fig. 14 may well exhibit an extra strength in the peak labelled "L₁" due to such effects.³⁰⁵ As noted in Section III.D.4, the connection of XPS spectra to the density of states in a direct way implies a type of uniform averaging over initial states that need not be possible in a directionally-sensitive single-crystal experiment.

As it is reasonable to expect that the anisotropies noted in XPS valence emission from single crystals are associated somehow with the basic

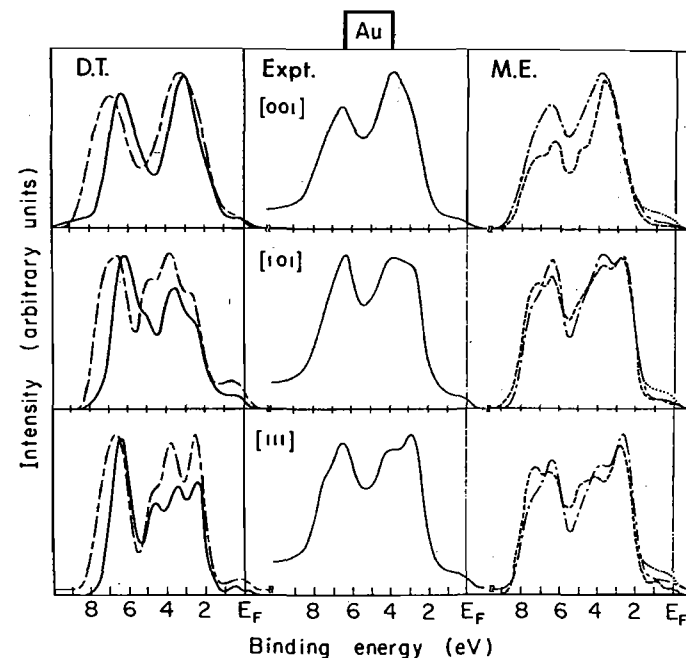


Fig. 52. Experimental and theoretical angular-resolved XPS Au valence spectra for electron emission along the [001], [101], and [111] directions. The data were obtained with monochromatized AlK α radiation. "D.T." represents calculations based upon the direct-transition model. "M.E." represents plane-wave matrix-element calculations. The band structures utilized in the theoretical calculations were: —, Christensen's RAPW³¹⁵ and ---, two slightly different choices for the spin-orbit parameter in Smith's tight-binding interpolation scheme.³¹⁶ (From refs 185, 311, and 317.)

symmetries of the initial states involved, it is of considerable interest to develop theoretical models for the interpretation of such effects. Two different approaches to this problem have been proposed.^{185, 306-312} Both of these models begin with the basic direct-transition expression given in Eq. (106), but the different assumptions made in each yields final predictions of a much different form. These two models are:

(1) *The Direct Transition Model.* In this model, the wave-vector conservation embodied in Eq. (104) is primarily emphasized. This viewpoint has been used previously to analyze angular-dependent UPS data from single crystals,^{182, 313} and suitable modifications to permit its direct application to higher-energy photoemission experiments were first discussed by Baird *et al.*¹⁸⁵ Rigorous wave-vector conservation is used to connect each observed final-state wave vector k^f with a unique initial-state wave vector k within the reduced Brillouin zone by means of a suitable (and unique) reciprocal lattice vector g . The magnitude of k^f is determined from the internal kinetic energy $E_{kin, i'}$ (cf. Fig. 12) by assuming that the free-electron dispersion relation $E_{kin, i'} = \hbar^2(k^f)^2/2m$ is valid at high excitation energies. At XPS energies, k^f furthermore varies very little over the valence spectrum: for example, in gold with lattice constant $a = 4.08 \text{ \AA}$, it is found that $12.84(2\pi/a) \leq k^f \leq 12.88(2\pi/a)$, where $2\pi/a$ is approximately the reduced zone radius. The direction of k^f (or, equivalently, the direction of the photoelectron momentum) with respect to the crystal axes is determined from the known crystal orientation relative to the spectrometer acceptance solid angle. (Small direction corrections due to electron refraction in crossing the surface barrier V_0 are necessary only for very low angles of electron exit.^{17, 307}) The finite solid angle of acceptance of the electron energy analyzer distributes the

observed k^f values over a disc-like region in k -space, as shown in the scale drawing for gold in Fig. 53, where the acceptance solid angle is taken for illustration to be conical with a 2.0° half angle. Each k^f value can then be corrected by the non-negligible $k_{h\nu}$ associated with the photon to yield a set of vectors $k^f - k_{h\nu} = k + g$ (shown as the right-hand shaded disc in the figure) that permits uniquely determining the set of k values in the reduced zone from which allowed transitions can occur (shown as the left-hand shaded disc lying coincidentally very near a reduced-zone face). Due to the finite size of the disc (cf. its size to that of the reduced zone in Fig. 53), more than one g may be involved, depending on the exact placement of the disc in k -space or, equivalently, the observation direction in real space. It is further assumed in this model that the matrix elements for all $k \rightarrow k^f$ transitions are approximately equal, so that an angular-resolved spectrum is finally predicted to be proportional to the density of electronic states over the allowed k region (*not* the total density of states).

This model has been unambiguously demonstrated by Wagner *et al.*³¹⁴ to predict correctly all of the major spectral changes occurring with emission direction and photon energy for copper in the intermediate photon energy range $40 \leq h\nu \leq 200 \text{ eV}$. XPS calculations based upon this model for Au with emission along [001], [101], and [111] are shown in Fig. 52, where they are indicated by "D.T." and compared with experimental spectra. Two different initial-state band structures have been utilized in the calculations,^{315, 316} yielding two different sets of curves. The most accurate band structure was used for the solid curves, and comes from a relativistic augmented plane wave (RAPW) calculation by Christensen.³¹⁵ Both sets of direct-transition curves qualitatively predict the correct changes in both the relative intensities of the two main components and the shapes of each component, although the calculations do predict more change with direction than is noted experimentally. Similar agreement has been found for 9 other directions in Au,³¹⁷ as well as 6 directions in Cu,³⁰⁷ leading to previous conclusions^{185, 307} that the direct-transition model represents a good description of such effects in XPS. However, very recent data obtained by Hussain *et al.*³¹⁸ for Au with both $MgK\alpha$ and $AlK\alpha$ radiation are at variance with his model: specifically, for emission along [001], [111], and [112], theory predicts large changes in the spectra of a given direction when photon energy is changed (because the disc changes position in the reduced zone due to the change in the length of k^f), whereas negligible differences are observed experimentally. In addition,³¹⁸ for excitation with $AlK\alpha$, the free-electron metal Al is found not to exhibit *any* spectral changes with emission direction, again in disagreement with direct-transition predictions. It thus appears that some form of wave-vector smearing or reduced-zone averaging is occurring, probably due to the creation or annihilation of phonons, as suggested first by Shevchik¹⁸⁶ and discussed

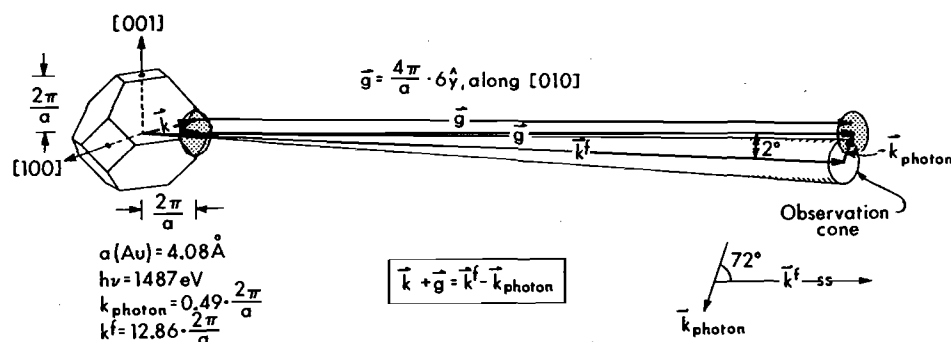


Fig. 53. Scale drawing in k -space of the direct transitions that would be involved in XPS emission along the [010] direction in a Au single crystal. The initial states from which emission could occur are represented by those k values in the shaded disc near the face of the reduced Brillouin zone at left. The additional involvement of variable-magnitude phonon wave vectors due to vibrational effects appears, however, to lead to rather full zone averaging in angular-resolved XPS spectra from Au at room temperatures, as discussed in the text.

previously in Section III.D.4. The fraction of direct transitions for which phonon smearing is absent is most simply estimated from the Debye-Waller factor:¹⁸⁷

$$\text{Debye-Waller factor} = \exp(-\frac{1}{2}\langle u^2 \rangle g^2) \quad (165)$$

where

$\langle u^2 \rangle$ = the mean squared vibrational displacement of atoms in the lattice
 $g^2 = |\mathbf{g}|^2$, with \mathbf{g} the reciprocal lattice vector involved in a given direct transition

$\langle u^2 \rangle$ is thus a function of material and temperature. In XPS, g^2 is of the same order as $(k^f)^2$ (cf. Fig. 53) and therefore is much larger than the corresponding quantity in UPS. Thus, the Debye-Waller factor can be very small in XPS, as, for example, 0.04 in Au at 25 °C. Such small values suggest that rather complete zone averaging may occur in room-temperature angular-resolved XPS measurements on many systems, as previously noted. (In fact, Williams *et al.*³¹⁹ have recently noted the disappearance of direct-transition effects in UPS spectra of Cu obtained at high temperature that very nicely confirm phonon involvement.) The direct transition model as outlined here thus may not be applicable to room-temperature XPS measurements on many materials, even though it clearly is a valid description at lower excitation energies,^{313, 314} and perhaps also at lower temperatures in XPS.

(2) *The Plane-wave Matrix-element Model.* This model was first discussed in connection with angular-dependent XPS spectra by McFeely *et al.*³⁰⁶ Although \mathbf{k} -conserving direct transitions are used as a starting point, it is further assumed that final-state complexities somehow smear out the determination of \mathbf{k} and \mathbf{k}^f to such a degree that essentially all \mathbf{k} values in the reduced zone can contribute to emission in any direction. Mixing of different plane-wave components into the final electronic states by various scattering processes was first suggested as the source of such zone averaging,³⁰⁶ but such effects do not seem to be strong for copper with $h\nu \leq 200$ eV.³¹⁴ More likely, the creation or annihilation of phonons in the photoelectron excitation event is responsible.

In the limit of complete zone averaging, anisotropies in XPS valence spectra are then assumed by McFeely *et al.*³⁰⁶ to be due to directional matrix elements as summed over all occupied initial states. These matrix elements are in turn calculated by assuming a plane-wave final state of the form:

$$\phi_{\mathbf{k}^f}(\mathbf{r}) = \exp(i\mathbf{k}^f \cdot \mathbf{r}) \quad (166)$$

and a tight-binding or LCAO initial state of the form:^{96, 99}

$$\phi_{\mathbf{k}}(\mathbf{r}) = \sum_{\mathbf{R}_i} \exp(i\mathbf{k} \cdot \mathbf{R}_i) \left\{ \sum_{\mu} C_{\mu\mathbf{k}} X_{\mu}(\mathbf{r} - \mathbf{R}_i) \right\} \quad (167)$$

in which

\mathbf{R}_i = the position of an atomic center in the lattice
 $X_{\mu}(\mathbf{r} - \mathbf{R}_i)$ = an atomic orbital centered at \mathbf{R}_i
 $X_{\mu}(\mathbf{r}) = R_{\mu}(r) Y_{\mu}(\theta, \phi)$ [cf. Eq. (36)]
 $C_{\mu\mathbf{k}}$ = an expansion coefficient

Computing matrix elements $\langle \phi_{\mathbf{k}^f} | \mathbf{A} \cdot \nabla | \phi_{\mathbf{k}} \rangle$ can then be shown^{159, 306, 312} to yield a linear combination of the Fourier transforms of the various atomic orbitals making up the initial-state orbital. Such Fourier transforms furthermore exhibit the same angular dependence in \mathbf{k}^f space that the atomic function has in real space, and they can thus be written as

$$X_{\mu}(\mathbf{k}^f) = f_{\mu}(k^f) Y_{\mu}(\theta_{\mathbf{k}^f}, \phi_{\mathbf{k}^f}) \quad (168)$$

with $\theta_{\mathbf{k}^f}, \phi_{\mathbf{k}^f}$ indicating the direction of \mathbf{k}^f , and $f_{\mu}(k^f)$ being a radial integral dependent on $|k^f| = k^f$ only. For radiation with a polarization direction \mathbf{e} , it then directly results that

$$|\langle \phi_{\mathbf{k}^f} | \mathbf{A} \cdot \nabla | \phi_{\mathbf{k}} \rangle|^2 \propto (\mathbf{e} \cdot \mathbf{k}^f)^2 \left| \sum_{\mu} C_{\mu\mathbf{k}} X_{\mu}(\mathbf{k}^f - \mathbf{k}_{h\nu}) \right|^2 \quad (169)$$

In general, $\mathbf{e} \cdot \mathbf{k}^f$ has been held constant in prior experiments, and for a closely related set of orbitals such as d functions, it can further be assumed that the factor $f_{\mu}(k^f)$ is constant. Finally, each initial state is thus predicted to contribute photoelectron intensity with a weight of $\left| \sum_{\mu} C_{\mu\mathbf{k}} Y_{\mu}(\theta_{\mathbf{k}^f - \mathbf{k}_{h\nu}}, \phi_{\mathbf{k}^f - \mathbf{k}_{h\nu}}) \right|^2$ and a summation can be carried out over all such occupied states. Thus, for example, the contribution of a $d_{x^2-y^2}$ atomic orbital to such a matrix element is predicted to be a maximum along the same directions as the orbital maxima, namely the $\pm x$ and $\pm y$ directions. Orbital symmetry is thus predicted to be very directly reflected in the angular-dependent emission probability. Calculations based upon this model are presented in Fig. 52 for Au, where they are indicated by "M.E." Two different types of tight-binding parameterizations have been utilized, and it is clear that the results are sensitive to this choice. Nonetheless, there is generally good agreement between experiment and theory for the three directions shown, as well as others in Au^{306, 311} which have been investigated, and a similar set in Cu.³¹¹ The same type of plane-wave model has also been found by Ley *et al.*³¹⁰ to predict correctly changes in single-crystal valence spectra of the compounds MoS₂, GaSe₂, and SnSe₂. Thus, it at present appears that the plane-wave matrix element approach is the more correct of the two discussed here for describing room temperature XPS experiments on most materials, although significant questions do still remain as to the validity of using a free-electron plane-wave final state for

computing XPS matrix elements.^{165, 186, 318} More accurate theoretical calculations of such effects are thus clearly of interest.

To the degree that such measurements do directly reflect orbital symmetries, such angular-resolved XPS studies should prove to be very useful probes of valence electronic structure.

VII. CONCLUDING REMARKS

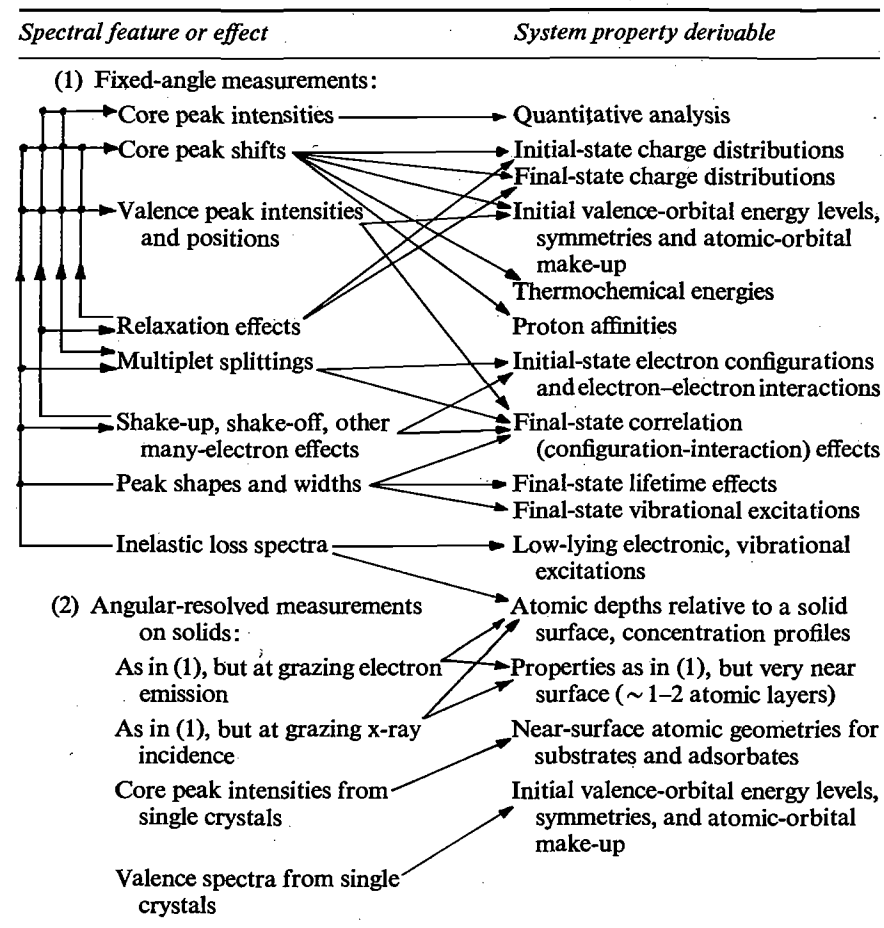
The aim of this chapter has been to discuss in some detail the basic ideas involved in both performing and interpreting XPS measurements. It is clear that a relatively large number of distinct physical and chemical effects can be related to the observed spectra. This diversity can be both an advantage and a disadvantage in using the technique, depending upon the specific problem at hand and the phenomena encountered. On the positive side, however, is the fact that at least some degree of quantitative understanding has been achieved in connection with all of the effects noted to date. The theoretical interpretation of XPS spectra also involves a liberal mixture of concepts from atomic, molecular, and solid-state physics, thus making the technique truly interdisciplinary in character. A major goal of the discussion here has been to present these diverse ideas within a single, unified framework.

As an important example of the interdependency of different phenomena, final-state effects of various types can tend in certain situations to obscure the initial-state information that is of most interest in many applications. But, on the other hand, final-state effects can also be used to determine additional characteristics of the system. The essential reason for this initial-state/final-state dichotomy is that the photoemission event is inherently very disruptive to the system, leaving it with a hole in a certain subshell and thus a significantly altered set of electron-electron interactions. The interpretive material presented in Sections III-V therefore begins with a rather general discussion of the photoemission process that emphasizes the importance of both initial and final states (as well as inelastic scattering effects). However, the first areas of application considered are intentionally those which for many systems can exhibit the strongest initial-state component: valence-level studies in molecules and solids (Sections III.D.3 and III.D.4), quantitative analysis (Section III.F.3), and core-level binding energy shifts (Section IV). Nonetheless, care must always be exercised in analysing data in order to avoid having the different final-state effects discussed in Section V introduce a significant error in any conclusions concerning initial-state properties.

The potential range of information derivable from XPS spectra is indeed very broad, and a schematic summary of the interrelationships between various observable quantities or effects and basic system properties is presented in Table III. In this table, the possible interactions between different observables are also indicated.

TABLE III

Schematic illustration of the interrelationships between various observable XPS spectral features or their associated effects and the basic system properties potentially derivable from an analysis of such observations



XPS has been and will no doubt continue to be fruitfully utilized for the study of free atoms, free molecules, and the *bulk* properties of solids and liquids. However, the inherent *surface* sensitivity of the technique when applied to solids and liquids leads to what is certainly one of the most significant areas of application, namely in studying the physics and chemistry of surfaces and interfaces. In this context, the relatively newly developed angular-resolved studies of solids have also clearly been demonstrated to enhance significantly the amount of information derivable, as is also indicated

in Table III. Two separate procedures exist for selectively increasing surface sensitivity by angle variations. For single-crystal specimens, information concerning both detailed atomic geometries and valence-orbital symmetries can also be derived from angular-distribution measurements.

No exhaustive elucidation of specific areas of application for XPS has been attempted here, but it is sufficient to note that by now the technique has been used in problems related to physical chemistry, inorganic chemistry, organic chemistry, biochemistry, solid-state physics, surface chemistry, surface physics, industrial chemistry, and environmental science. Future developments will no doubt involved all of these areas, but with special emphasis on problems related to surface science. A further significant component of future work will no doubt be the more extended use of XPS in combination with other spectroscopic methods such as, for example, the other surface-sensitive techniques of UPS, photoelectron spectroscopy utilizing synchrotron radiation sources, low-energy electron diffraction (LEED), Auger electron spectroscopy (AES), and secondary ion mass spectrometry (SIMS).

Thus, x-ray photoelectron spectroscopy is by now a relatively mature and well-established experimental tool. However, various major problems still remain to be solved concerning both the measurement and the analysis of XPS spectra. These include the ever-present and conflicting needs for higher resolution and higher intensity, which are at present being sought by means of more efficient x-ray monochromators combined with multichannel detection systems. More novel radiation sources and analyzer/detector systems might also provide a further solution to this problem. From the point of view of theory, more quantitative treatments of various final-state effects and electron-electron correlation effects are needed. More accurate calculations of both wave functions and photoelectric cross-sections for molecules and solids would also be very helpful, especially as related to angular-resolved studies of atoms and molecules interacting with solid surfaces.

Acknowledgements

I would like to thank the following agencies for financial support for those studies involving my research group at the University of Hawaii that are discussed here: The National Science Foundation, The Alfred P. Sloan Foundation, and The Petroleum Research Fund. I am also grateful to Dr S. Kono for helpful comments concerning this manuscript, and to Mr S. M. Goldberg for assistance with theoretical calculations relevant to it. Finally, I would like to thank Ms C. Carnate for invaluable assistance in preparing this manuscript.

REFERENCES

1. H. Robinson and W. F. Rawlinson, *Phil. Mag.* **28**, 277 (1914).
2. R. G. Steinhardt and E. J. Serfass, *Anal. Chem.* **25**, 697 (1953); and R. G. Steinhardt, F. A. D. Granados, and G. I. Post, *Anal. Chem.* **27**, 1046 (1955).
3. K. Siegbahn, C. Nordling, A. Fahlman, R. Nordberg, K. Hamrin, J. Hedman, G. Johansson, T. Bergmark, S.-E. Karlsson, I. Lindgren, and B. Lindberg, "ESCA: Atomic, Molecular, and Solid State Structure Studied by Means of Electron Spectroscopy", *Nova Acta Regiae Soc. Sci. Upsaliensis, Ser. IV*, Vol. 20 (Almqvist and Wiksells, Stockholm, 1967), also available as National Technical Information Service Report No. AD 844315, 1968, Dept of Commerce, Springfield, Va, U.S.A. See also earlier references therein, particularly S. Hagström, C. Nordling, and K. Siegbahn, *Z. Physik*, **178**, 439 (1964), in which the first association of core-binding energy shifts with chemical state was made.
4. K. Siegbahn, C. Nordling, G. Johansson, J. Hedman, P.-F. Hedén, K. Hamrin, U. Gelius, T. Bergmark, L. O. Werme, R. Manne, and Y. Baer, "ESCA Applied to Free Molecules" (North-Holland, Amsterdam, 1969).
5. The extensive XPS literature has been reviewed, for example, in D. M. Hercules, *Anal. Chem.* **44**, 106R (1972); W. E. Schwartz, *Anal. Chem.* **45**, 789A (1973); D. M. Hercules and J. C. Carver, *Anal. Chem.* **46**, 133R (1974), and D. M. Hercules, *Anal. Chem.* **48**, 294R (1976); A. D. Baker, M. Brisk and D. Liotta, *Anal. Chem.* **50**, 328, 1978R. Also, from 1972 on, numerous publications have appeared in the *Journal of Electron Spectroscopy and Related Phenomena*.
6. S. B. M. Hagström, and C. S. Fadley in "X-ray spectroscopy", L. V. Azaroff, ed. (McGraw-Hill, New York, 1974).
7. D. A. Shirley, *Adv. Chem. Phys.* **23**, 85 (1973).
8. C. S. Fadley in "Electron Emission Spectroscopy", W. Dekeyser *et al.*, eds (Reidel, Dordrecht, Netherlands, 1973).
9. D. T. Clark in "Electron Emission Spectroscopy", W. Dekeyser *et al.*, eds (Reidel, Dordrecht, Netherlands, 1973).
10. T. A. Carlson, "Photoelectron and Auger Spectroscopy" (Plenum Press, New York, 1975).
11. D. A. Shirley, ed., "Electron Spectroscopy" (North-Holland, Amsterdam, 1972). The proceedings of an international conference held at Asilomar, California, in September 1971.
12. R. Caudano and J. Verbist, eds, "Electron Spectroscopy: Progress in Research and Applications" (Elsevier, Amsterdam, 1974). The proceedings of an international conference held in Namur, Belgium, in April 1974. Also available as Volume 5 in the *Journal of Electron Spectroscopy* (1974).
13. W. L. Jolly in "Electron Spectroscopy: Theory, Techniques, and Applications", C. R. Brundle and A. D. Baker, eds (Academic Press, London and New York, 1977), Chapter 3, Vol. 1.
14. R. L. Martin and D. A. Shirley in "Electron Spectroscopy: Theory, Techniques, and Applications", C. R. Brundle and A. D. Baker, eds (Academic Press, London and New York, 1977), Chapter 2, Vol 1; and *Phys. Rev.* **A13**, 1475 (1976).
15. Detailed discussions of the application of synchrotron radiation to photoelectron spectroscopy have, for example, been given in papers by D. E. Eastman, by F. C. Brown, R. Z. Bachrach, S. B. M. Hagström, N. Lien,

- and C. H. Pruitt, and by others in "Vacuum Ultraviolet Physics", E. E. Koch *et al.*, eds (Pergamon Press, New York, 1974); as well as in W. E. Spicer, K. Y. Yu. I. Lindau, P. Pianetta, and D. M. Collins in "Surface and Defect Properties of Solids", J. M. Thomas and M. W. Roberts, eds (Chem. Soc., London, 1976), Vol. V.
16. The general area of spin-polarized electron emission experiments has recently been reviewed in: M. Campagna, D. T. Pierce, F. Meier, L. Sattler, and H. C. Siegmann, in *Advances in Electronics and Electron Physics*, **41**, 113 (1976).
 17. C. S. Fadley, *Prog. Sol. St. Chem.* **11**, 265 (1976).
 18. For discussions of energy loss measurements at approximately XPS energies, see, for example, O. Klemperer and J. P. G. Shepherd, *Adv. Phys.* **12**, 355 (1963); H. Raether, *Springer Tracts in Modern Physics*, **38**, 84 (1965); J. Daniels, C. v. Festenburg, H. Raether, and K. Zeppenfeld, *Springer Tracts in Modern Physics*, **54**, 77 (1970), and G. R. Wight and C. E. Brion, *J. Electr. Spectr.* **3**, 191 (1974).
 19. C. Kittel, "Introduction to Solid State Physics", 4th edn (Wiley, New York, 1971), Chapters 7 and 8.
 20. C. J. Powell, *Surf. Sci.* **44**, 29 (1974).
 21. I. Lindau and W. E. Spicer, *J. Electron Spectrosc.* **3**, 409 (1974).
 22. C. R. Brundle, *J. Vac. Sci. Tech.* **11**, 212 (1974).
 23. Kratos, 403 S. Raymond Avenue, Pasadena, California, U.S.A. is now marketing systems formerly manufactured by AEI Scientific Apparatus Ltd.
 24. E. I. DuPont de Nemours and Co., Instrument Products Division, Wilmington, Delaware, U.S.A.
 25. Hewlett Packard Co., Scientific Instruments Division, 1601 California Street, Palo Alto, California, U.S.A. Although no longer marketed, the special properties of this spectrometer are discussed in K. Siegbahn, D. Hammond, H. Fellner-Felldegg, and E. F. Barnett, *Science*, **176**, 245 (1972), as well as by R. J. Baird and C. S. Fadley in reference 74.
 26. GCA/McPherson Instrument Corp., 530 Main Street, Acton, Massachusetts, U.S.A.
 27. Leybold-Heraeus GmbH, Gaedestrasse, 5000 Köln 51, West Germany. The electron optics of this system are described in detail in H. G. Nöller, H. D. Polaschegg, and H. Schillalies, *J. Electron Spectrosc.* **5**, 705 (1974).
 28. Physical Electronics Industries, Inc., 6509 Flying Cloud Drive, Eden Prairie, Minnesota, U.S.A.
 29. Vacuum Generators Inc., Charlwood Road, East Grinstead, Sussex, England.
 30. Varian Associates, Analytical Instrument Devices, Palo Alto, California, U.S.A. This system is no longer marketed.
 31. A. H. Compton and S. K. Allison, "X-rays in Theory and Experiment" (Macmillan and Co., London, 1935).
 32. B. L. Henke in "Advances in X-ray analysis", Vol. 5 (Plenum Press, New York, 1962), p. 285; and in "X-ray Optics and Microanalysis" (Academic Press, New York and London, 1963), p. 157.
 33. C. S. Fadley, Ph.D. Thesis, University of California at Berkeley, 1970 (Lawrence Berkeley Laboratory Report UCRL-19535).
 34. M. O. Krause, *Chem. Phys. Lett.* **10**, 65 (1971).
 35. M. S. Banna and D. A. Shirley, *J. Electr. Spectr.* **8**, 23, 255 (1976).
 36. R. Nilsson, R. Nyholm, A. Berndtsson, J. Hedman, and C. Nordling, *J. Electr. Spectr.* **9**, 337 (1976).
 37. M. O. Krause and J. G. Ferreira, *J. Phys.* **B8**, 2007 (1975).
 38. E. Källne and T. Åberg, *X-ray Spect.* **4**, 26 (1975).
 39. J. E. Castle, L. B. Hazell, and R. D. Whitehead, *J. Electron Spectrosc.* **9**, 246 (1976).
 40. A. Berndtsson, R. Nyholm, R. Nilsson, J. Hedman, and C. Nordling, *J. Electron Spectrosc.* **13**, 131 (1978).
 41. K. Siegbahn, *J. Electr. Spectr.* **5**, 3 (1974) and Uppsala University, *Institute of Physics Report, No. UUIP-909* (1975).
 42. Y. Baer, G. Busch, and P. Cohn, *Rev. Sci. Inst.* **46**, 466 (1975).
 43. C. T. Hovland, *Appl. Phys. Lett.* **30**, 274 (1977).
 44. R. P. Godwin, "Synchrotron Radiation as a Light Source" in *Springer Tracts in Modern Physics*, **51** (1970).
 45. J. F. McGilp and I. G. Main, *J. Electron Spectrosc.* **6**, 397 (1975).
 46. C. S. Fadley, G. L. Geoffroy, S. B. M. Hagström, and J. M. Hollander, *Nucl. Inst. Methods*, **68**, 177 (1969).
 47. G. Johansson, J. Hedman, A. Berndtsson, M. Klasson, and R. Nilsson, *J. Electron Spectrosc.* **2**, 295 (1973), and references therein.
 48. F. J. Grunthaler, N.A.S.A. Technical Brief NPO-13772, Item 57, Spring 1977.
 49. M. O. Krause, *Phys. Rev.* **A140**, 1845 (1965); T. A. Carlson and M. O. Krause, *Phys. Rev.* **A137**, 1655 (1965); **A140**, 1057 (1965); **A151**, 41 (1966).
 50. J. Berkowitz in "Electron Spectroscopy", D. A. Shirley, ed. (North-Holland, Amsterdam, 1972), p. 391; and in "Electron Spectroscopy: Theory, Techniques, and Applications", C. R. Brundle and A. D. Baker, eds (Academic Press, London, 1977), Chap. 7, Vol 1.
 51. See, for example, early gas-phase molecular studies in T. D. Thomas, *J. Chem. Phys.* **52**, 1373 (1970); *J. Am. Chem. Soc.* **92**, 4184 (1970); and D. W. Davis, D. A. Shirley, and T. D. Thomas in "Electron Spectroscopy", D. A. Shirley, ed. (North-Holland, Amsterdam, 1972), p. 707.
 52. J. S. Brinen, *J. Electron Spectrosc.* **5**, 377 (1974); *Accts Chem. Res.* **9**, 86 (1976).
 53. H. P. Hughes and R. A. Pollak, *Phil. Mag.* **34**, 1025 (1976).
 54. T. E. Madey, J. T. Yates, and N. E. Erickson, *Chem. Phys. Lett.* **19**, 487 (1973); *Surf. Sci.* **43**, 526 (1974).
 55. P. A. Redhead, J. P. Hobson, and E. V. Kornelsen, "The Physical Basis of Ultrahigh Vacuum" (Chapman and Hall, London, 1968); D. H. Holkeboer, D. W. Jones, F. Pagano, D. J. Santeler, "Vacuum Engineering" (Boston Technical, Boston, 1967).
 56. Y. Baer, *Sol. St. Comm.* **19**, 669 (1976).
 57. D. E. Eastman in "Electron Spectroscopy", D. A. Shirley, ed. (North-Holland, Amsterdam, 1972), p. 487.
 58. S. Evans, *Chem. Phys. Lett.* **23**, 134 (1973).
 59. H. Siegbahn and K. Siegbahn, *J. Electron Spectrosc.* **2**, 319 (1972); **5**, 1059 (1974).
 60. UPS measurements on liquid Au are, for example, discussed in reference 57.
 61. K. D. Sevier, "Low Energy Electron Spectrometry" (Wiley-Interscience, New York, 1972).
 62. H. Fellner-Felldegg, U. Gelius, B. Wannberg, A. G. Nilsson, E. Basilier, and K. Siegbahn, *J. Electron Spectrosc.* **5**, 643 (1974); B. Wannberg, U. Gelius, and K. Siegbahn, Uppsala University, *Institute of Physics Report No. UUIP-818* (1973).
 63. C. E. Kuyatt, review of electron energy analyzers to appear in this series.

64. C. S. Fadley, C. E. Miner, and J. M. Hollander, *Appl. Phys. Letters*, **15**, 223 (1969); C. S. Fadley, R. N. Healey, J. M. Hollander, and C. E. Miner, *J. Appl. Phys.* **43**, 1085 (1972).
65. E. M. Purcell, *Phys. Rev.* **54**, 818 (1938).
66. H. Z. Sar-el, *Rev. Sci. Instr.* **38**, 1210 (1969).
67. S. Aksela, M. Karras, M. Pessa, and E. Suoninen, *Rev. Sci. Instr.* **41**, 351 (1970); S. Aksela, *Rev. Sci. Instr.* **42**, 810 (1971).
68. R. W. Shaw and T. D. Thomas in "Electron Spectroscopy", D. A. Shirley, ed. (North-Holland, Amsterdam, 1972), p. 105; K. Maeda, *op. cit.* p. 177.
69. K. Siegbahn in "Alpha-, Beta-, and Gamma-ray Spectroscopy", K. Siegbahn, ed. (North-Holland, 1965), Vol. I, Chap. III.
70. K. Mills and D. A. Shirley, private communication.
71. L. B. Leder and J. A. Simpson, *Rev. Sci. Instr.* **29**, 571 (1958); J. A. Simpson, *Rev. Sci. Instr.* **32**, 1283 (1961).
72. C. N. Berglund and W. E. Spicer, *Rev. Sci. Instr.* **35**, 1665 (1964).
73. D. A. Huchital and J. D. Rigden in "Electron Spectroscopy", D. A. Shirley, ed. (North-Holland, Amsterdam, 1972), p. 79.
74. R. J. Baird and C. S. Fadley, *J. Electron Spectrosc.* **11**, 39 (1977).
75. J. C. Helmer, *Am. J. Phys.* **34**, 222 (1966); J. C. Helmer and N. H. Weichert, *Appl. Phys. Lett.* **13**, 266 (1968).
76. O. Klemperer, "Electron Optics", 3rd edn (Cambridge University Press, Cambridge, 1971), Chaps 1 and 2.
77. B. L. Henke, J. A. Smith, and D. T. Attwood, *J. Appl. Phys.* **48**, 1852 (1977).
78. Channeltron electron multipliers were originally marketed under a registered trademark of the Bendix Corporation. They are now available from various manufacturers.
79. The early development of such electron multipliers is reviewed in W. C. Wiley and C. F. Hendee, *I.R.E. Trans. Nucl. Sci.* NS-9, 103 (1962), D. S. Evans, *Rev. Sci. Instr.* **36**, 375 (1965).
80. Ö. Nilsson, L. Hasselgren, K. Siegbahn, S. Berg, L. P. Andersson, and P. A. Tore, *Nucl. Inst. and Meth.* **84**, 301 (1970).
81. C. D. Moak, S. Datz, F. Garcia-Santibanez, and T. A. Carlson, *J. Electron Spectrosc.* **6**, 151 (1975); M. Lampton and F. Paresec, *Rev. Sci. Instr.* **45**, 1098 (1974).
82. C. S. Fadley and D. A. Shirley, *J. Res. Nat. Bur. Stds.* **74A**, 543 (1970).
83. Various self-consistent inelastic loss subtraction procedures such as this have been utilized for XPS valence spectra, as discussed, for example, in references 82, 192, and 298.
84. S. Hüfner and G. K. Wertheim, *Phys. Rev.* **B11**, 678 (1975); *Phys. Rev.* **B11**, 5197 (1975); *Phys. Rev. Lett.* **35**, 53 (1975).
85. P. H. Citrin, P. Eisenberger, and D. R. Hamann, *Phys. Rev. Lett.* **33**, 965 (1974).
86. C. S. Fadley and D. A. Shirley, *Phys. Rev.* **A2**, 1109 (1970).
87. G. K. Wertheim, *J. Electr. Spectr.* **6**, 239 (1975). (As based on mathematical methods developed in ref. 88.)
88. P. H. van Zittert, *Z. Phys.* **69**, 298 (1931).
89. F. J. Grunthaner, Ph.D. Thesis, California Institute of Technology (1974).
90. R. Manne and T. Åberg, *Chem. Phys. Lett.* **7**, 282 (1970).
91. S. T. Manson, *J. Electron Spectrosc.* **9**, 21 (1976).
93. F. Herman and S. Skillman, "Atomic Structure Calculations" (Prentice-Hall, Englewood Cliffs, New Jersey, 1963).
94. T. A. Carlson and B. P. Pullen, Oak Ridge National Laboratory, *Report No. ORNL-4323* (1969).

95. M. Tinkham, "Group Theory and Quantum Mechanics" McGraw-Hill, New York, 1964).
96. J. M. Ziman, "Principles of the Theory of Solids", 2nd edn (Cambridge University Press, Cambridge, 1972).
97. D. W. Turner, C. Baker, A. D. Baker, and C. R. Brundle, "Molecular Photoelectron Spectroscopy" (Wiley, London, 1970).
98. K. Siegbahn in "Electron Spectroscopy", D. A. Shirley, ed. (North-Holland, Amsterdam, 1972), p. 15.
99. J. Callaway, "Quantum Theory of the Solid State" (Academic Press, New York and London, 1974), Chap. 4.
100. J. B. Mann, Los Alamos Scientific Laboratory, *Reports LA-3690* (1967) and *LA-3691* (1968).
101. T. A. Carlson, C. C. Lu, T. C. Tucker, C. W. Nestor, and F. B. Malik, Oak Ridge National Laboratory, *Report ORNL-4614* (1970).
102. M. Mehta, C. S. Fadley, and P. S. Bagus, *Chem. Phys. Lett.* **37**, 454 (1975).
103. P. S. Bagus, *Phys. Rev.* **139**, A619 (1965).
104. A. Rosen and I. Lindgren, *Phys. Rev.* **176**, 114 (1968).
105. C. S. Fadley, S. B. M. Hagström, J. M. Hollander, M. P. Klein, and D. A. Shirley, *Science*, **157**, 1571 (1967); C. S. Fadley, S. B. M. Hagström, M. P. Klein, and D. A. Shirley, *J. Chem. Phys.* **48**, 3779 (1968).
106. M. E. Schwartz, *Chem. Phys. Lett.* **5**, 50 (1970).
107. P. S. Bagus and H. F. Schaefer, *J. Chem. Phys.* **55**, 1474 (1971); **56**, 224 (1972).
108. L. C. Snyder, *J. Chem. Phys.* **55**, 95 (1971).
109. H. Basch, *J. Electron Spectrosc.* **5**, 463 (1974).
110. E.-K. Viinikka and P. S. Bagus, extended abstract for the International Conference on the Physics of X-ray Spectra, 30 August-2 September, 1976, National Bureau of Standards, Gaithersburg, Md.
111. G. Verhaegen, J. J. Berger, J. P. Desclaux, and C. M. Moser, *Chem. Phys. Lett.* **9**, 479 (1971).
112. C. M. Moser, R. K. Nesbet, and G. Verhaegen, *Chem. Phys. Lett.* **12**, 330 (1971).
113. L. S. Cederbaum and W. Domcke, *J. Chem. Phys.* **66**, 5084 (1977).
114. G. K. Wertheim, R. L. Cohen, A. Rosencwaig, and H. J. Guggenheim in "Electron Spectroscopy", D. A. Shirley, ed. (North-Holland, Amsterdam, 1972), p. 813.
115. L. Ley, F. R. McFeely, J. G. Jenkin, and D. A. Shirley, *Phys. Rev.* **11**, 600 (1975).
116. See, for example, J. E. Lennard-Jones and J. A. Pople, *Proc. Roy. Soc.* **A202**, 166 (1950); C. Edmiston and K. Ruedenberg, *Rev. Mod. Phys.* **35**, 457 (1963).
117. P. W. Payne, *J. Am. Chem. Soc.* **99**, 3787 (1977).
118. J. C. Slater, "Quantum Theory of Atomic Structure" (McGraw-Hill, New York, 1960), Vol. II.
119. D. Liberman, *Bull. Am. Phys. Soc.* **9**, 731 (1964).
120. L. Hedin and A. Johansson, *J. Phys.* **B2**, 1336 (1969).
121. D. A. Shirley, *Chem. Phys. Lett.* **16**, 220 (1972).
122. H. F. Schaefer, "The Electronic Structure of Atoms and Molecules" (Addison-Wesley, Reading, Mass., 1972).
123. T. L. Barr, private communication.
124. H. A. Bethe and E. E. Salpeter, Quantum Mechanics of One- and Two-electron Atoms in "Handbuch der Physik" (Springer-Verlag, Berlin, 1955), Vol. 35, p. 88.
125. D. R. Bates, *Mon. Not. Roy. Astr. Soc.* **106**, 432 (1946).

126. J. W. Cooper, *Phys. Rev.* **128**, 681 (1962).
127. U. Fano and J. W. Cooper, *Rev. Mod. Phys.* **40**, 441 (1968).
128. J. W. Cooper, review in "Atomic Inner-shell Processes" (Academic Press, 1975).
129. S. T. Manson, review on atomic cross-section calculations to appear in this series, and S. T. Manson, *Advances in Electronics and Electron Physics*, **41**, 73 (1976).
130. J. J. Huang and J. W. Rabelais, review on molecular cross-sections to appear in this series.
131. See, for example, L. I. Schiff, "Quantum Mechanics" (McGraw-Hill, New York, 1968), Sections 35, 44, and 45, 3rd edn.
132. B. Feuerbacher and R. F. Willis, *J. Phys.* **C9**, 169 (1976).
133. T. Åberg, *Phys. Rev.* **156**, 35 (1967) and in "Inner-shell Ionization Phenomena and Future Applications", R. W. Fink *et al.*, eds (U.S.A.E.C., Conference-72-0404, 1973), p. 1409.
134. J. W. Gadzuk and M. Sunjic, *Phys. Rev.* **B12**, 524 (1975). See also the prior treatment of time scales in photoionization by H. W. Meldner and J. D. Preze, *Phys. Rev.* **A4**, 1388 (1971).
135. T. A. Carlson, *Phys. Rev.* **156**, 142 (1967); M. O. Krause and T. A. Carlson, *Phys. Rev.* **158**, 18 (1967); M. O. Krause, T. A. Carlson, and R. D. Dismukes, *Phys. Rev.* **170**, 37 (1968); M. O. Krause, *Phys. Rev.* **177**, 151 (1968).
136. P. O. Löwdin, *Phys. Rev.* **97**, 1474 (1955).
137. C. S. Fadley, *Chem. Phys. Lett.* **25**, 225 (1974); *J. Electr. Spectr.* **5**, 895 (1974).
138. B. I. Lundqvist, *Phys. Kondens. Materie*, **9**, 236 (1969).
139. F. Wuilleumier and M. O. Krause, *Phys. Rev.* **A10**, 242 (1974).
140. J. Cooper and R. N. Zare, *J. Chem. Phys.* **48**, 942 (1968); and in "Lectures in Theoretical Physics", S. Geltman, K. Mahanthappa, and W. Brittlin, eds (Gordon and Breach, New York, 1969), Vol. XIC.
141. In atomic cross-section calculations based upon typical approximation schemes, the three forms of the dipole operator need not give the same result. Recently, the degree of agreement between calculations using all three forms has been discussed for wave functions including correlation effects in M. S. Pindzola and H. P. Kelly, *Phys. Rev.* **A12**, 1419 (1975).
142. M. O. Krause, *Phys. Rev.* **177**, 151 (1969).
143. A. J. Bearden, *J. Appl. Phys.* **37**, 1681 (1966).
144. G. Rakavy and A. Ron, *Phys. Rev.* **159**, 50 (1967).
145. H. Brysl and C. D. Zerby, *Phys. Rev.* **171**, 292 (1968).
146. S. T. Manson and J. W. Cooper, *Phys. Rev.* **165**, 126 (1968).
147. J. W. Cooper and S. T. Manson, *Phys. Rev.* **177**, 157 (1969).
148. E. J. McGuire, *Phys. Rev.* **175**, 20 (1968).
149. D. J. Kennedy and S. T. Manson, *Phys. Rev.* **A5**, 227 (1972).
150. E. Storm and H. I. Israel, *Nuclear Data Tables A7*, 565 (1970).
151. J. H. Scofield, *J. Electr. Spectr.* **8**, 129 (1976).
152. B. L. Henke and E. S. Ebusu, in "Advances in X-ray Analysis" (Plenum Press, New York, 1974), Vol. 17.
153. S. T. Manson, *Phys. Rev. Lett.* **26**, 219 (1971).
154. R. F. Reilman, Alfred Msezane, and S. T. Manson, *J. Electr. Spectr.* **8**, 389 (1976).
155. P. A. Cox and F. A. Orchard, *Chem. Phys. Lett.* **7**, 273 (1970).
156. P. A. Cox, Y. Baer, and C. K. Jorgensen, *Chem. Phys. Lett.* **22**, 433 (1973); P. A. Cox, *Struct. Bonding*, **23**, 59 (1974).

157. P. S. Bagus, J. L. Freeouf, and D. E. Eastman, *Phys. Rev.* **B15**, 3661 (1977).
158. D. Dill, A. F. Starace, and S. T. Manson, *Phys. Rev.* **A11**, 1596 (1975).
159. J. W. Gadzuk, *Sol. St. Comm.* **15**, 1011 (1974); *Phys. Rev.* **B10**, 5030 (1974); *Phys. Rev.* **B12**, 5608 (1975).
160. D. Dill and J. L. Dehmer, *J. Chem. Phys.* **61**, 692 (1974); J. L. Dehmer and D. Dill, *Phys. Rev. Lett.* **35**, 213 (1975).
161. V. I. Nefedov, N. P. Sergushin, I. M. Band, and M. B. Trzhaskowskaya, *J. Electr. Spectr.* **2**, 383 (1973).
162. F. O. Ellison, *J. Chem. Phys.* **61**, 507 (1974); J. W. Rabelais, T. P. Debies, J. L. Berkosky, J. T. Huang, and F. O. Ellison, *J. Chem. Phys.* **61**, 516, 529 (1974).
163. M. J. S. Dewar, A. Komornicki, and W. Thiel, *Chem. Phys. Lett.* **31**, 286 (1975).
164. B. Ritchie, *J. Chem. Phys.* **60**, 898 (1974); **61**, 3279, 3291 (1974); **64**, 3050 (1976).
165. R. S. Williams and D. A. Shirley, *J. Chem. Phys.* **66**, 2378 (1977).
166. J. W. Davenport, *Phys. Rev. Lett.* **36**, 945 (1976).
167. K. H. Johnson in "Advances in Quantum Chemistry", P. O. Löwdin, ed. (Academic Press, New York and London, 1973), Vol. 7, p. 143.
168. J. L. Dehmer, *J. de Physique*, Coll. **C4**, 42 (1978).
169. T. A. Carlson and G. E. McGuire, *J. Electr. Spectr.* **1**, 209 (1972/73).
170. T. A. Carlson, G. E. McGuire, A. E. Jonas, K. L. Cheng, C. P. Anderson, C. C. Lu, and B. P. Pullen in "Electron Spectroscopy", D. A. Shirley, ed. (North Holland, Amsterdam, 1972), p. 207.
171. D. Dill, *J. Chem. Phys.* **65**, 1130 (1976).
172. U. Gelius in "Electron Spectroscopy", D. A. Shirley, ed. (North-Holland, Amsterdam, 1972), p. 311.
173. U. Gelius, C. J. Allen, G. Johansson, H. Siegbahn, D. A. Allison, and K. Siegbahn, *Phys. Scripta*, **3**, 237 (1971); C. J. Allen, U. Gelius, D. A. Allison, G. Johansson, H. Siegbahn, and K. Siegbahn, *J. Electr. Spectr.* **1**, 131 (1972).
174. R. Prins, *Chem. Phys. Lett.* **19**, 355 (1973).
175. A. Calabrese and R. G. Hayes, *Chem. Phys. Lett.* **27**, 376 (1974); *J. Am. Chem. Soc.* **95**, 2819 (1973); **96**, 505 (1974).
176. S. Kono, T. Ishii, T. Sagawa, and T. Kobayasi, *Phys. Rev. Lett.* **28**, 1385 (1972); *Phys. Rev.* **B8**, 795 (1973).
177. C. N. Berglund and W. E. Spicer, *Phys. Rev.* **A136**, 1030, 1044 (1964).
178. B. L. Henke, *Phys. Rev.* **A6**, 94 (1972).
179. M. Mehta and C. S. Fadley, *Phys. Lett.* **A55**, 59 (1975).
180. G. D. Mahan, *Phys. Rev.* **B2**, 4374 (1970); W. L. Schaich and N. W. Ashcroft, *Phys. Rev.* **B3**, 2452 (1970).
181. P. J. Feibelman and D. E. Eastman, *Phys. Rev.* **B10**, 4932 (1974).
182. N. V. Smith and M. M. Traum, *Phys. Rev. Lett.* **31**, 1247 (1973); M. M. Traum, N. V. Smith, and F. J. DiSalvo, *Phys. Rev. Lett.* **32**, 1241 (1974); N. V. Smith and M. M. Traum, *Phys. Rev.* **B11**, 2087 (1975), and references therein.
183. B. Feuerbacher and F. Fitton, *Phys. Rev. Lett.* **30**, 923 (1973); R. R. Tuttle and T. A. Callcott, *Phys. Rev. Lett.* **34**, 86 (1975); R. F. Willis, *Phys. Rev. Lett.* **34**, 670 (1975).
184. C. Kittel, "Quantum Theory of Solids" (Wiley, New York, 1963), Chap. 1.
185. R. J. Baird, L. F. Wagner, and C. S. Fadley, *Phys. Rev. Lett.* **37**, 111 (1976).
186. N. J. Shevchik, *Phys. Rev.* **16**, 3428 (1977); *J. Phys.* **C10**, L555 (1977).

187. R. W. James, "The Optical Principles of the Diffraction of X-rays" (Cornell University Press, Ithaca, 1967), Chap. V.
188. V. G. Aleshin and Y. N. Kucherenko, *J. Electr. Spectr.* **8**, 411 (1976).
189. L. F. Wagner and C. S. Fadley, unpublished results.
190. See, for example, R. A. Pollak, Ph.D. Thesis, University of California at Berkeley, 1972 (Lawrence Berkeley Laboratory Report LBL-1299); S. P. Kowalczyk, Ph.D. Thesis, University of California at Berkeley, 1976 (Report LBL-4319).
191. A. Barrie and N. E. Christensen, *Phys. Rev.* **B14**, 2442 (1976).
192. L. Ley, S. Kowalczyk, R. A. Pollak, and D. A. Shirley, *Phys. Rev. Lett.* **29**, 1088 (1972).
193. R. G. Cavell, S. P. Kowalczyk, L. Ley, R. A. Pollak, B. Mills, D. A. Shirley, and W. Perry, *Phys. Rev.* **B7**, 5313 (1973); F. R. McFeely, S. P. Kowalczyk, L. Ley, R. G. Cavell, R. A. Pollak, and D. A. Shirley, *Phys. Rev.* **B9**, 5268 (1974).
194. M. Sunjic, D. Sokcevic, and A. Lucas, *J. Electr. Spectr.* **5**, 963 (1974); M. Sunjic and D. Sokcevic, *Sol. St. Comm.* **15**, 165 (1974); **15**, 1703 (1974); **18**, 373 (1976).
195. This compilation of electron inelastic attenuation lengths is intended to contain all published determinations, and information concerning it is available through M. P. Seah, National Physical Laboratory, Electron Mean Free Path Versus Energy Compilation, Teddington, Middlesex, U.K.
196. D. R. Penn, *J. Electr. Spectr.* **9**, 29 (1976).
197. P. J. Feibelman, *Phys. Rev.* **B7**, 2305 (1973).
198. P. J. Feibelman, *Surf. Sci.* **36**, 558 (1973).
199. M. O. Krause and F. Wuilleumier, *Phys. Lett.* **A35**, 341 (1971), and in "Proceedings of the International Conference on Inner Shell Ionization Phenomena", Atlanta, Georgia, 1972.
200. R. J. Baird, C. S. Fadley, and L. F. Wagner, *Phys. Rev.* **B15**, 666 (1977).
201. W. A. Fraser, J. V. Florio, W. N. Delgass, and W. D. Robertson, *Surf. Sci.* **36**, 661 (1973).
202. C. S. Fadley, R. J. Baird, W. Siekhaus, T. Novakov, and S. Å. Bergström, *J. Electr. Spectr.* **4**, 93 (1974).
203. R. J. Baird, C. S. Fadley, S. Kawamoto, and M. Mehta, *Chem. Phys. Lett.* **34**, 49 (1975).
204. W. J. Carter, G. K. Schweitzer, and T. A. Carlson, *J. Electr. Spectr.* **5**, 827 (1974).
205. C. D. Wagner, *Anal. Chem.* **44**, 1050 (1972).
206. C. K. Jorgensen and H. Berthou, *Disc. Far. Soc.* **54**, 269 (1973); H. Berthou and C. K. Jorgensen, *Anal. Chem.* **47**, 482 (1975).
207. C. J. Powell and P. E. Larson, *Appl. Surf. Sci.* **1** (1977), in press.
208. C. J. Powell, in A.S.T.M. Special Technical Publication of the 1977 Symposium on Quantitative Surface Analysis, in press.
209. S. A. Flodström, R. Z. Bachrach, R. S. Bauer, and S. B. M. Hagström, *Phys. Rev. Lett.* **37**, 1282 (1976).
210. K. Siegbahn, Uppsala University, *Institute of Physics Report No. UUIP-940* (1976).
211. U. Gelius, P.-F. Heden, J. Hedman, B. J. Lindberg, R. Manne, R. Nordberg, C. Nordling, and K. Siegbahn, *Physica Scripta*, **2**, 70 (1970).
212. O. Goscinski, B. Pickup, and G. Purvis, *Chem. Phys. Lett.* **22**, 117 (1973).

213. G. Howat and O. Goscinski, *Chem. Phys. Lett.* **30**, 87 (1975).
214. P. H. Citrin, R. W. Shaw, A. Packer, and T. D. Thomas in "Electron Spectroscopy", D. A. Shirley, ed. (North Holland, Amsterdam, 1972), p. 691.
215. D. A. Shirley, R. L. Martin, F. R. McFeely, S. P. Kowalczyk, and L. Ley, *Far. Soc. Disc. No.* **60**, 7 (1975).
216. R. Manne, *J. Chem. Phys.* **46**, 4645 (1967).
217. H. Basch, *Chem. Phys. Lett.* **5**, 3371 (1970).
218. M. F. Schwartz, *Chem. Phys. Lett.* **5**, 50 (1970); **6**, 631 (1970).
219. D. W. Davis, D. A. Shirley, and T. D. Thomas, *J. Chem. Phys.* **56**, 671 (1972).
220. J. Hedman, M. Klasson, B. J. Lindberg, and C. Nordling in "Electron Spectroscopy", D. A. Shirley, ed. (North-Holland, Amsterdam, 1972), p. 681.
221. D. N. Henderickson, J. M. Hollander, and W. L. Jolly, *J. Inorg. Chem.* **8**, 2642 (1969).
222. T. D. Thomas, *J. Am. Chem. Soc.* **92**, 4184 (1970).
223. P. Finn, R. K. Pearson, J. M. Hollander, and W. L. Jolly, *J. Inorg. Chem.* **10**, 378 (1971).
224. W. L. Jolly and D. N. Henderickson, *J. Am. Chem. Soc.* **92**, 1863 (1970).
225. W. L. Jolly in "Electron Spectroscopy", D. A. Shirley, ed. (North-Holland, Amsterdam, 1972), p. 629.
226. J. A. Hashmall, B. E. Mills, D. A. Shirley, and A. Streitwieser, *J. Am. Chem. Soc.* **94**, 445 (1972).
227. M. Aono, M. Okusawa, T. Sagawa, Y. Takehana, and T. Nagatani, "Proceedings of the 7th International Conference on X-ray Optics and Microanalysis" (Moscow); M. Aono, S. Kawai, S. Kono, M. Okusawa, T. Sagawa, and Y. Takehana, *Sol. St. Comm.* **16**, 13 (1975).
228. R. L. Martin and D. A. Shirley, *J. Am. Chem. Soc.* **96**, 5299 (1974); B. E. Mills, R. L. Martin, and D. A. Shirley, *J. Am. Chem. Soc.* **98**, 2380 (1976).
229. C. D. Wagner, *Far. Soc. Disc. No.* **60**, 291 (1975).
230. C. D. Wagner and P. Biloen, *Surf. Sci.* **35**, 82 (1973).
231. D. A. Shirley, *Phys. Rev.* **A7**, 1520 (1973).
232. G. D. Mateescu and J. L. Riemenschneider in "Electron Spectroscopy", D. A. Shirley, ed. (North Holland, Amsterdam, 1972), p. 661; B. J. Lindberg, *J. Electr. Spectr.* **5**, 149 (1974).
233. H. Basch, *Chem. Phys. Lett.* **5**, 3371 (1970).
234. M. Barber, P. Swift, D. Cunnginham, and M. J. Frazer, *Chem. Commun.* **1970**, 1338 (1970).
235. L. Ley, S. P. Kowalczyk, F. R. McFeely, R. A. Pollak, and D. A. Shirley, *Phys. Rev.* **B8**, 2392 (1973).
236. P. H. Citrin and D. R. Hamann, *Phys. Rev.* **B10**, 4948 (1974).
237. J. J. Pireaux, S. Swensson, E. Basilier, P. A. Malmqvist, U. Gelius, R. Caudano, and K. Siegbahn, *Phys. Rev.* **A14**, 2133 (1976).
238. J. E. Demuth and D. E. Eastman, *Phys. Rev. Lett.* **32**, 1123 (1974).
239. D. W. Davis and D. A. Shirley, *Chem. Phys. Lett.* **15**, 185 (1972).
240. R. E. Watson, M. L. Perlman, and J. F. Herbst, *Phys. Rev.* **13**, 2358 (1976).
241. R. Hoogewijs, L. Fiermans, and J. Vennik, *Chem. Phys. Lett.* **37**, 87 (1976).
242. J. W. Gadzuk, *Phys. Rev.* **B14**, 2267 (1976).
243. D. Coster and M. J. Druyvesteyn, *Z. Physik*, **40**, 765 (1927).
244. V. I. Nefedov, *J. Struct. Chem.* **5**, 603, 605 (1964); **7**, 672 (1966).
245. B. Ekstig, E. Källne, E. Noreland, and R. Manne, *Physica Scripta*, **2**, 38 (1970).
246. W. N. Asaad and E. H. S. Burhop, *Proc. Phys. Soc.* **71**, 369 (1958).

247. E. H. S. Burhop, "The Auger Effect and Other Radiationless Transitions" (Cambridge University Press, London, 1952).
248. D. Stalherm, B. Cleff, H. Hillig, and W. Mehlhorn, *Naturforsch.* **24a**, 1728 (1969).
249. J. Hedman, P.-F. Heden, C. Nordling, and K. Siegbahn, *Phys. Lett.* **A29**, 178 (1969).
250. C. S. Fadley, D. A. Shirley, A. J. Freeman, P. S. Bagus, and J. V. Mallow, *Phys. Rev. Lett.* **23**, 1397 (1969).
251. J. C. Carver, T. A. Carlson, L. C. Cain, and G. K. Schweitzer, in "Electron Spectroscopy", D. A. Shirley, ed. (North-Holland, Amsterdam, 1972), p. 803.
252. P. S. Bagus, A. J. Freeman, and F. Sasaki, *Phys. Rev. Lett.* **30**, 850 (1973). These CI calculations actually use seven configurations for 5S rather than the four discussed here, but the dominant contributors are found to be only those four.
253. S. P. Kowalczyk, L. Ley, R. A. Pollak, F. R. McFeely, and D. A. Shirley, *Phys. Rev.* **B7**, 4009 (1973).
254. S. P. Kowalczyk, F. R. McFeely, L. Ley, and D. A. Shirley in "Proceedings of the 20th Annual Conference on Magnetism and Magnetic Materials", 1974.
255. S. P. Kowalczyk, L. Ley, F. R. McFeely, and D. A. Shirley, *Phys. Rev.* **B11**, 1721 (1975).
256. R. P. Gupta and S. K. Sen, *Phys. Rev.* **B10**, 71 (1974).
257. R. P. Gupta and S. K. Sen, *Phys. Rev.* **B12**, 15 (1975).
258. R. L. Cohen, G. K. Wertheim, A. Rosencwaig, and H. J. Guggenheim, *Phys. Rev.* **B5**, 1037 (1972).
259. F. R. McFeely, S. P. Kowalczyk, L. Ley, and D. A. Shirley, *Phys. Lett.* **A49**, 301 (1974).
260. S. P. Kowalczyk, N. Edelstein, F. R. McFeely, L. Ley, and D. A. Shirley, *Chem. Phys. Lett.* **29**, 491 (1974).
261. M. Campagna, E. Bucher, G. K. Wertheim, and L. D. Longinotti, *Phys. Rev. Lett.* **33**, 165 (1974).
262. C. S. Fadley in "Electron Spectroscopy", D. A. Shirley, ed. (North-Holland, Amsterdam, 1972), p. 781.
263. A. J. Freeman, P. S. Bagus, and J. V. Mallow, *Int. J. Magnetism*, **4**, 35 (1973).
264. S. Sugano in "Proceedings of the NATO Advanced Study Institute on Spectroscopy of Excited States" (Plenum Press, New York, 1976).
265. T. A. Carlson, *Far. Soc. Disc.* No. 60, 30 (1975).
266. J. N. Chazalviel, M. Campagna, G. K. Wertheim, and P. H. Schmidt, *Phys. Rev.* **B10**, 4586 (1976).
267. P.-O. Heden, H. Löfgren, and S. B. M. Hagström, *Phys. Rev. Lett.* **26**, 432 (1971).
268. Y. Baer, *J. Electr. Spectr.* **5**, 611 (1974).
269. T. A. Carlson, M. O. Krause, and W. E. Moddeman, *J. de Physique*, **C2**, 102 (1971).
270. U. Gelius, *J. Electr. Spectr.* **5**, 985 (1974).
271. D. P. Spears, H. J. Fischbeck, and T. A. Carlson, *Phys. Rev.* **A9**, 1603 (1974).
272. T. N. Chang and R. T. Poe, *Phys. Rev.* **A12**, 1432 (1975).
273. H. Basch, *Chem. Phys.* **10**, 157 (1975); T. X. Carroll and T. D. Thomas, *J. Electr. Spectr.* **10**, 215 (1977).
274. D. T. Clark in *Far. Soc. Disc.* No. 60, 183 (1975).
275. P. S. Bagus and E.-K. Viinikka, *Phys. Rev.* **A15**, 1486 (1977).

276. S. Doniach and M. Sunjic, *J. Phys.* **C3**, 285 (1970).
277. P. H. Citrin, *Phys. Rev.* **B12**, 5545 (1973).
278. D. C. Langreth, *Phys. Rev. Lett.* **26**, 1229 (1971); J. J. Chang and D. C. Langreth, *Phys. Rev.* **B5**, 3512 (1972); **B8**, 4638 (1973); G. D. Mahan, *Phys. Stat. Solid.* **55**, 703 (1973).
279. W. J. Pardee, G. D. Mahan, D. E. Eastman, R. A. Pollak, L. Ley, F. R. McFeely, S. P. Kowalczyk, and D. A. Shirley, *Phys. Rev.* **B11**, 3614 (1975); J. C. Fuggle, D. J. Fabian, and L. M. Watson, *J. Electr. Spectr.* **9**, 99 (1976).
280. T. Novakov, *Phys. Rev.* **B3**, 2693 (1971).
281. D. C. Frost, A. Ishitani, and C. A. McDowell, *Molec. Phys.* **24**, 861 (1972).
282. T. A. Carlson, J. C. Carver, L. J. Saethre, and F. Garcia Santibanez, *J. Electr. Spectr.* **5**, 247 (1974); T. A. Carlson, J. C. Carver, and G. A. Vernon, *J. Chem. Phys.* **62**, 932 (1975).
283. K. S. Kim and R. E. Davis, *J. Electr. Spectr.* **1**, 251 (1972/73); K. S. Kim, *Phys. Rev.* **B11**, 2177 (1975).
284. L. Yin, I. Adler, T. Tsang, L. I. Matienzo, and S. O. Grim, *Chem. Phys. Lett.* **24**, 81 (1974).
285. S. Larsson, *Chem. Phys. Lett.* **32**, 401 (1975); **40**, 362 (1976).
286. S. Asada and S. Sugano, *J. Phys. Soc. Jap.* **41**, 1291 (1976).
287. E. W. Plummer and W. R. Salaneck in "Proceedings of the 5th International Conference on Vacuum Ultraviolet Radiation Physics", Montpellier, France (1977).
288. S. Lundqvist and G. Wendin, *J. Electr. Spectr.* **5**, 513 (1974).
289. G. Wendin and M. Ohno, *Physica Scripta*, **14**, 148 (1976); G. Wendin, M. Ohno, and S. Lundqvist, *Sol. St. Comm.* **19**, 165 (1976).
290. C. S. Fadley, *J. Electr. Spectr.* **5**, 725 (1974).
291. C. S. Fadley and S. Å. L. Bergström, *Phys. Lett.* **A35**, 375 (1971); in "Electron Spectroscopy", D. A. Shirley, ed. (North-Holland, Amsterdam, 1972), p. 233.
292. C. S. Fadley, *Far. Soc. Disc.* No. 60, 18 (1975).
293. R. J. Baird, C. S. Fadley, S. Kawamoto, M. Mehta, R. Alvarez, and J. A. Silva, *Anal. Chem.* **48**, 843 (1976).
294. J. M. Hill, D. G. Royce, C. S. Fadley, L. F. Wagner, and F. J. Grunthaner, *Chem. Phys. Lett.* **44**, 225 (1976).
295. R. J. Baird, C. S. Fadley, S. M. Goldberg, P. J. Feibelman, and M. Sunjic, *Surf. Sci.* **72**, 495 (1978).
296. A. M. Bradshaw, W. Domcke, and L. S. Cederbaum, *Phys. Rev.* **B16**, 1480 (1977).
297. R. Haydock and M. J. Kelly, *Surf. Sci.* **38**, 139 (1973); M. C. Dejonquieres and F. Cyrot-Lackmann, *Surf. Sci.* **53**, 429 (1975); K. S. Sohn, D. G. Dempsey, L. Kleinmann, and E. Caruthers, *Phys. Rev.* **B13**, 1515 (1976); **B14**, 3185, 3193 (1976).
298. M. Mehta and C. S. Fadley, *Phys. Rev. Lett.* **39**, 1569 (1977).
299. M. Mehta and C. S. Fadley, *Chem. Phys. Lett.* **46**, 225 (1977).
300. K. Siegbahn, U. Gelius, H. Siegbahn, and E. Olsen, *Phys. Lett.* **A32**, 221 (1970).
301. R. Baudouin, R. M. Stern, and H. Taub, *Surf. Sci.* **11**, 255 (1968); E. G. McRae, *Surf. Sci.* **44**, 321 (1974), and earlier references therein.
302. R. E. DeWames and W. F. Hall, *Acta Cryst.* **A24**, 206 (1968), and earlier experimental references therein.
303. R. J. Baird, C. S. Fadley, S. M. Goldberg, and S. Kono, to be published.

304. J. B. Pendry and R. Lindsay, private communication.
305. R. J. Baird, C. S. Fadley, and L. F. Wagner, *Far. Soc. Disc. No. 60*, 143 (1975).
306. F. R. McFeely, J. Stöhr, G. Apai, P. S. Wehner, and D. A. Shirley, *Phys. Rev. B14*, 3273 (1976).
307. L. F. Wagner, Z. Hussain, and C. S. Fadley, *Sol. St. Comm. 21*, 453 (1977).
308. G. Apai, J. Stöhr, R. S. Williams, P. S. Wehner, S. P. Kowalczyk, and D. A. Shirley, *Phys. Rev. B15*, 584 (1977).
309. Z. Hussain, L. F. Wagner, and C. S. Fadley, to be published.
310. L. Ley, R. H. Williams, and P. Kemeny, *Bull. Am. Phys. Soc. 24*, 942 (1976); R. H. Williams, P. C. Kemeny, and L. Ley, *Sol. St. Comm. 19*, 495 (1976).
311. P. S. Wehner, J. Stöhr, G. Apai, F. R. McFeely, and D. A. Shirley, *Phys. Rev. Lett. 38*, 169 (1977).
312. K.-F. Berggren and F. Martino, *Sol. St. Comm. 20*, 1057 (1976).
313. P.-O. Nilsson and L. Ilver, *Sol. St. Comm. 17*, 667 (1975); L. Ilver and P.-O. Nilsson, *Sol. St. Comm. 18*, 677 (1976).
314. L. F. Wagner, Z. Hussain, and C. S. Fadley, *Sol. St. Comm. 21*, 257 (1977).
315. N. F. Christensen and B. O. Seraphin, *Phys. Rev. B4*, 3321 (1972).
316. N. V. Smith, *Phys. Rev. B3*, 1862 (1971). Two different choices of spin-orbit parameter were used in this tight-binding scheme for the calculations of Fig. 52.
317. R. J. Baird, L. F. Wagner, and C. S. Fadley, unpublished results.
318. Z. Hussain, N. F. T. Hall, L. F. Wagner, S. P. Kowalczyk, C. S. Fadley, K. A. Thompson, and R. L. Dod, *Sol. St. Commun. 25*, 907 (1978).
319. R. S. Williams, P. S. Wehner, J. Stöhr, and D. A. Shirley, *Phys. Rev. Lett. 39*, 302 (1977).



Progress in Surface Science

An International Review Journal

EDITOR: Professor Sydney G. Davison

Angle-Resolved X-Ray Photoelectron Spectroscopy CHARLES S. FADLEY

275

ISBN 0 08 030892 9
ISSN 0079-6816
PSSFBP 16(3) 275-388 (1984)

 PERGAMON PRESS

New York / Oxford / Toronto
Paris / Frankfurt / Sydney

ANGLE-RESOLVED X-RAY PHOTOELECTRON SPECTROSCOPY

CHARLES S. FADLEY

Department of Chemistry, University of Hawaii at Manoa,
Honolulu, Hawaii 96822

Abstract

In this review, various aspects of angle-resolved x-ray photoelectron spectroscopy (ARXPS) as applied to solid state- and surface chemical- studies are discussed. Special requirements for instrumentation are first considered. The use of grazing-emission angles to enhance surface sensitivity and study surface concentration profiles of various types is then discussed. Various effects that may limit the accuracy of such measurements such as surface roughness, electron refraction, and elastic scattering are considered. Several examples of surface-specific electronic structure changes as studied by grazing-emission ARXPS (e.g., valence-band narrowing and core-level shifts) are also reviewed. The use of grazing-incidence geometries for surface enhancement is also briefly considered. Single-crystal studies providing additional types of information via ARXPS are next discussed. For core-level emission from single-crystal substrates or adsorbed overlayers, x-ray photoelectron diffraction (XPD) is found to produce considerable fine structure in polar- or azimuthal- scans of intensity. Such XPD effects can be very directly related to the atomic geometry near a surface, for example, through simple intramolecular or intermolecular scattering processes. A straightforward single scattering or kinematical theory also appears to describe such effects rather well, thus far permitting several structures to be solved by analyses of azimuthal intensity scans. Likely future developments and possible limitations of such XPD structure studies are also discussed. Finally, valence-band ARXPS is considered, and it is shown that pronounced direct-transition effects can be observed provided that the specimen Debye-Waller factor is not too small. A simple free-electron final-state model is found to predict these direct-transition effects very well, and future studies at low temperatures and with higher angular resolution seem promising.

Contents

- | | |
|--|-----|
| 1. Introduction | 277 |
| 2. Instrumentation | 280 |
| 3. Surface Sensitivity Enhancement at Grazing Electron Emission Angles | 284 |

A. Introduction	284
B. Simple quantitative models	288
C. Additional complicating effects	296
D. Application to uniform overlayers	302
E. Analysis of adsorbate overlayers at fractional monolayer coverage	304
F. Studies of more complex concentration profiles	306
G. Studies of surface-specific electronic structure changes	311
4. Surface Sensitivity Enhancement at Grazing X-ray Incidence Angles	318
5. Core-Level Emission from Single Crystals: X-ray Photoelectron Diffraction (XPD)	320
A. Introduction	320
B. The single-scattering cluster (SSC) model	327
C. Substrate emission	338
D. Emission from molecular adsorbates	341
E. Emission from atomic adsorbates	345
F. XPD measurements using synchrotron radiation	358
G. Diffraction in core-level Auger emission	362
H. Concluding remarks and comparison to other techniques	364
6. Valence-Level Emission from Single-Crystals	366
A. Introduction	366
B. Simple theoretical models	366
C. Comparisons of experiment and theory	369
D. Concluding remarks	379
Acknowledgements	383
References	384

Abbreviations

ARUPS	Angle-Resolved Ultraviolet Photoelectron Spectroscopy
ARXPS	Angle-Resolved X-ray Photoelectron Spectroscopy
ARXUPS	Angle-Resolved XUV Photoelectron Spectroscopy
DT	Direct Transition
EXAFS	Extended X-ray Absorption Fine Structure
ESDIAD	Electron Stimulated Desorption Ion Angular Distribution
FWHM	Full Width at Half Maximum Intensity
LEED	Low Energy Electron Diffraction
ME	Matrix Element
MS	Multiple Scattering
NDT	Non-Direct Transition
NPD	Normal Photoelectron Diffraction
PhD	Photoelectron Diffraction
RHEED	Reflection High Energy Electron Diffraction
SEXAFS	Surface Extended X-ray Absorption Fine Structure
SIMS	Secondary Ion Mass Spectrometry
SSC	Single Scattering Cluster
UHV	Ultra-High Vacuum
UPS	Ultraviolet Photoelectron Spectroscopy
XPD	X-ray Photoelectron Diffraction
XPS	X-ray Photoelectron Spectroscopy

1. Introduction

Angle-resolved photoelectron spectroscopy in fact has a rather long history, as recently reviewed by Jenkin et al.¹. However, the current interest in angle-resolved x-ray photoelectron spectroscopy (ARXPS) as applied to solids and surfaces is only approximately ten years old, having begun with observations of diffraction-induced channeling effects in single-crystal specimens by Siegbahn et al.² and by Fadley and Bergström³ and of enhanced surface sensitivity for grazing angles of emission by Fadley and Bergström³. A number of other effects of interest in surface science have been noted since these first studies, and several quantitative models have been developed for describing them. This type of measurement has been treated in prior general reviews in 1974⁴, 1976⁵, and 1978⁶, and the present discussion will thus principally stress those developments that have occurred in the past few years, particularly with regard to using ARXPS for quantitative surface analysis, surface atomic geometry investigations, and valence-band studies.

The XPS energy regime will here be defined in what might be termed the classical way so as to involve excitation at photon energies $\gtrsim 1.0$ keV as derivable from standard x-ray tubes (e.g., using MgK α or AlK α radiation). The many very interesting studies performed to date at lower energies in angle-resolved uv- or xuv- photoelectron spectroscopy (ARUPS or ARXUPS) will thus not be considered in detail. However, at various points, comparisons of the characteristics of a given type of measurement (e.g., core-level photoelectron diffraction) as carried out in the low- and high- energy domains will be made. Further details concerning such lower-energy work as based upon both standard radiation sources and synchrotron radiation are contained in other reviews.⁷⁻⁹

It is useful to begin by considering a general experimental geometry for angle-resolved x-ray photoemission from a solid surface, as shown in Fig. 1. X-rays are incident at an angle $\theta_{h\nu}$ with respect to the surface. Photoelectrons are emitted into the acceptance solid angle of the analyzer Ω_0 . The initial direction of a given trajectory into this solid angle is given by its polar angle θ (here measured with respect to the surface) and its azimuthal angle ϕ (measured with respect to some arbitrary direction in the plane of the surface). The angle between the direction of radiation propagation $\hat{k}_{h\nu}$ and the direction of electron emission \hat{k} is defined to be α . In most current XPS systems, α is a constant fixed by the mechanical design, although much UPS work has been carried out with movable analyzers and thus variable α . In addition, the geometry shown here is somewhat special in that the directions of radiation propagation and electron emission

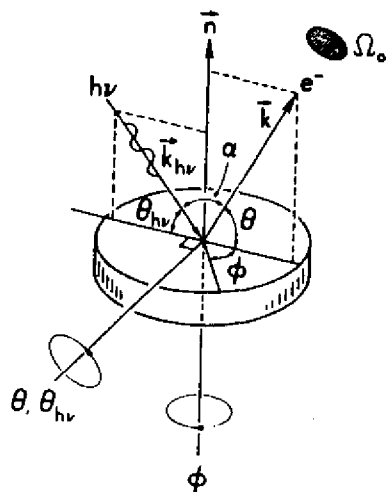


Fig. 1. General geometry for an angle-resolved photoemission experiment. Specimen rotations on the two perpendicular axes shown vary θ , ϕ , and θ_{hv} over their full allowed ranges. \hat{n} is the surface normal. Movement of the electron analyzer relative to the radiation source also can be used to vary α and choose any θ , ϕ , θ_{hv} , α combination, but in XPS this has been done very little to date.

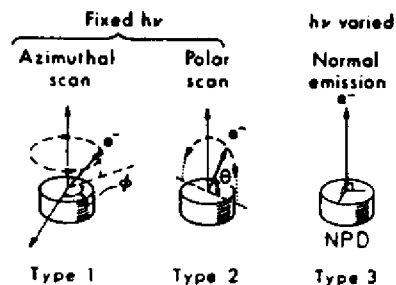


Fig. 2. Schematic illustration of three often-used types of angle-resolved photoemission experiments: (1) an azimuthal scan at constant polar angle, (2) a polar scan at constant azimuthal angle, and (3) a scan of $h\nu$ at fixed normal emission (also referred to as normal photoelectron diffraction or NPD).

define a plane that also contains the surface normal. In this situation, rotation on the two perpendicular axes shown permits varying the angles θ , ϕ , and θ_{hv} over all possible values (consistent, of course with the geometric requirement that $\theta_{hv} + \alpha + \theta = \pi$). The θ , θ_{hv} axis is here taken to be perpendicular to the plane containing \hat{k}_{hv} , \hat{k} and the surface normal, and the ϕ axis is parallel to the surface normal.

More general experimental geometries in which the analyzer can rotate on one or two axes with respect to the specimen and radiation source are also possible. In this case \hat{k}_{hv} and \hat{k} need not be co-planar with the surface normal and the four angles θ , ϕ , θ_{hv} and ϕ_{hv} are in general necessary to fully define the experiment. Such geometries have been used considerably in angle-resolved measurements at lower energies⁷⁻⁹, but very little to date in the XPS regime. A final addition that is possible is the utilization of polarized radiation, as is just become practically possible in XPS studies with synchrotron radiation¹⁰; in this case, the angles θ_c and ϕ_c specifying the orientation of the polarization vector $\hat{\epsilon}$ must also be known. However the standard XPS sources with which virtually all studies at $h\nu \gtrsim 1$ keV have to date been performed yield largely unpolarized radiation, so that we will only later comment briefly on polarization effects as an interesting subject for future investigation.

For a given photon energy $h\nu$, the two basic types of measurements possible in such experiments are thus an azimuthal scan at fixed polar angle (Type 1 of Fig. 2) and a polar scan at fixed azimuthal angle (Type 2 of Fig. 2). A third and more recently developed type of experiment¹¹ requiring the continuously tunable character of synchrotron radiation is also shown in Fig. 2; here, the emission direction is held parallel to the surface normal and $h\nu$ is swept. In core-level studies, this type of measurement has been termed normal photoelectron diffraction or NPD.

The remainder of this discussion will consider specific problems and areas of application. In Section 2, instrumentation requirements are briefly considered. In Section 3, the general ideas relating to surface sensitivity enhancement at grazing emission are introduced, and various examples of the uses of this effect such as concentration profile measurements, overlayer studies, and investigations of surface-specific electronic structure changes are discussed. The less-utilized effect of surface-sensitivity enhancement at grazing x-ray incidence is briefly considered in Section 4. Section 5 discusses various types of effects involved in core-level emission from single crystals, particularly as related to deriving surface atomic geometry information. In Section 6, valence-level emission from single crystals is considered, largely from the point of view of its relationship to bulk valence band structure.

2. Instrumentation

Beyond the normal instrumentation requirements for an XPS experiment, which are reviewed elsewhere⁶, those for adding the capability to do angle-resolved measurements are relatively straightforward.

The solid angle Ω_0 over which electrons are accepted into the analyzer (cf. Fig. 1) needs to be well defined and reasonably small. Depending upon the application intended, a range of angles corresponding to $\Delta\theta \times \Delta\phi$ from a minimum of $\sim 1^\circ \times \sim 1^\circ$ to a maximum of $\sim 10^\circ \times \sim 10^\circ$ could be suitable. For the two most commonly utilized analyzer configurations, the hemispherical electrostatic and cylindrical mirror electrostatic, some degree of baffling thus is in general required to adequately define the solid angle, and this will, of necessity, reduce the overall intensity of the instrument. In certain hemispherical analyzers with pre-retarding lens systems, the solid angle may already be relatively well defined, as discussed in detail for one system by Baird and Fadley¹², but in general this is not at all the case, with much larger angular deflections of $\sim 20^\circ$ - 30° being allowed in a direction perpendicular to the central reference trajectory of the analyzer. This loss of intensity associated with reducing Ω_0 also suggests the use of some form of multichannel detection as a compensating factor. A further problem that may be encountered with any analyzer is that Ω_0 may vary over the effective emitting area of the specimen and also may depend upon electron kinetic energy or other analyzer parameters, as, for example, the degree of retardation.⁵ Such changes in solid angle and also in emitting area can in addition lead to a purely instrumental change in intensity with angle, usually dependent on θ only. Such instrument response functions are discussed in Section 3.C and in prior reviews^{4-6,12}. In addition, some instruments will exhibit a change in energy resolution with θ that must be allowed for in precise analyses of spectra¹². Plummer¹³ has also recently considered general criteria for designing analyzers for angle-resolved studies over a range of energies.

In addition to defining Ω_0 , it is necessary to be able to rotate the specimen so as to change the angles θ , ϕ , and perhaps also θ_{hv} . A single polar axis of rotation varying θ and θ_{hv} is very easy to add in an overall geometry such as that of Fig. 1. A second azimuthal axis for varying ϕ requires additional mechanical complexity, but commercial manipulators providing at least partial azimuthal rotation are available, and custom designs with greater flexibility exist in several laboratories for both ARXPS⁵ and ARUPS^{14,15} measurements.

As one example of a reasonably flexible system for performing ARXPS at ultra-high vacuum conditions, Figs. 3 and 4 show different aspects of one unit currently in use in our laboratory. (An earlier high-vacuum device with a simpler

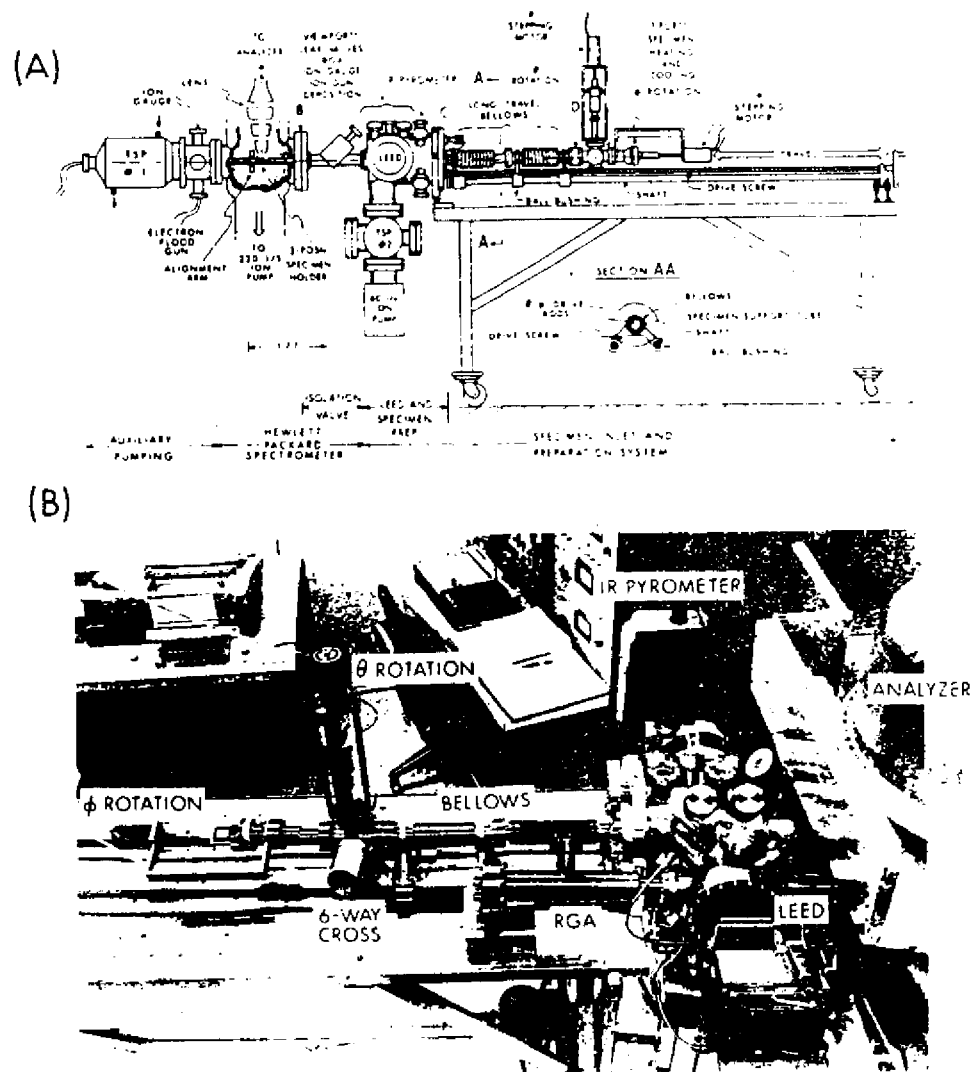


Fig. 3. (a) Schematic drawing of the specimen inlet side of a Hewlett Packard XPS spectrometer that has been specially modified for angle-resolved studies. Various components are labelled. (b) Overall photo of the system in (a) as viewed from the opposite side.

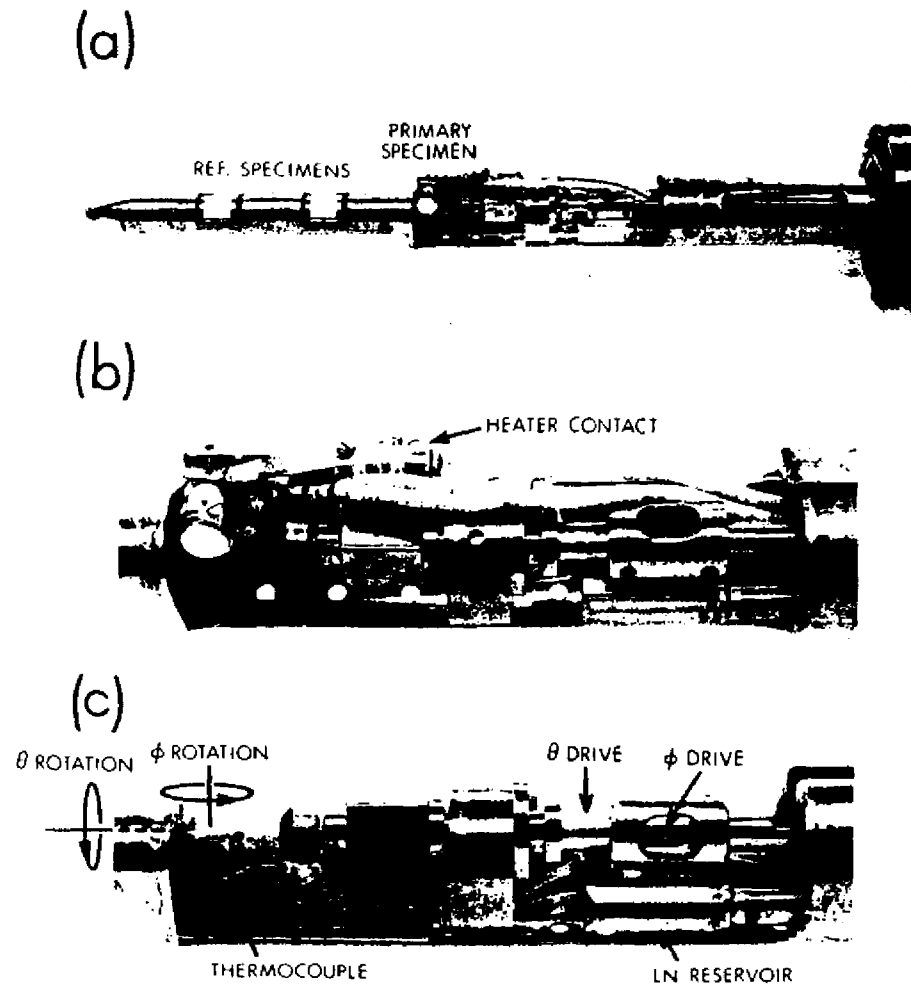


Fig. 4. Three different views of a two-axis goniometer used for variable-temperature ARXPS studies at angular accuracies of $\pm 0.5^\circ$: (a) overview including reference sample positions, and (b),(c) two close ups with different polar orientation. The smaller-diameter section at left in (a) mates with an alignment arm in the analyzer (cf. Fig. 3(a)).

rack-and-pinion drive is described in ref. 5.) The basic XPS analyzer and chamber to which the specimen preparation chamber, specimen goniometer, and translating-bellows inlet system is mounted is a Hewlett-Packard Model 5950A. Fig. 3(a) is a line drawing of the overall system and Fig. 3(b) a photographic view from the isolation valve on the XPS chamber to the preparation chamber and inlet system. The interior specimen support tube translates on external ball bushings, and is controlled by a drive screw. Various standard components such as a LEED unit, residual gas analyzer, ion gun, leak valves, and infrared pyrometer permit cleaning, preparing, and characterizing specimens before admitting them to the XPS chamber through the isolation valve. Two rotary feedthrus driven by computer-controlled stepping motors permit precision scanning on the two axes shown in Fig. 1. These feedthrus are mounted on a six-way cross together with other feedthrus for electrical heating, thermocouple temperature measurement, and liquid nitrogen cooling. Full ultra-high vacuum operation is also achieved with this system, with base pressures in the XPS chamber of $\sim 4-6 \times 10^{-11}$ torr and in the preparation chamber of $\sim 8-10 \times 10^{-11}$ torr.

Fig. 4 shows three photographic views of the specimen end of this goniometer. The θ drive comes in on the vertical port of the six-way cross, turns a right angle with a set of bevel gears, and is then transmitted directly to the rotating specimen support arm via a 1/4" o.d. drive tube. This drive tube is supported on precision ball bearings over its entire length of ~ 110 cm. The ϕ drive enters via the rear port of the six-way cross and is transmitted via a straight internal drive shaft of 1/8" diameter to sets of bevel gears and then spur gears so as effect ϕ motion. The ϕ drive shaft is internal to and concentric with the θ drive tube. Precision stainless steel ball bearings are used at all rotation points. Although there is an overall lash in this system between the coupled θ and ϕ motions of $\sim 1^\circ$ due to the various mechanical linkages involved, the consistent use of identical directions of rotation in making settings permits overall precisions and accuracies of $\pm 0.5^\circ$ in both θ and ϕ . Particularly for the grazing-emission azimuthal scans to be discussed in Section 5, such accuracies appear to be absolutely required for obtaining reproducible data. The specimen can be heated up to $\sim 1000^\circ\text{C}$ with an internal resistive button heater (Varian No. 981-2058) to which current passes via a contact ring and a spring-loaded floating contact. Alternatively, an electron bombardment heater for temperatures up to $\sim 2500^\circ\text{C}$ can also be mounted in the same position. Thus, full azimuthal rotational freedom is maintained, an extremely useful feature in providing a self-consistency check on data from single crystals, where the crystal rotational symmetry should be mirrored in the azimuthal data. Thermocouple and liquid-nitrogen connections can also be made to points near the specimen as needed.

3. Surface Sensitivity Enhancement at Grazing Electron Emission Angles

A. Introduction

The basic mechanism of surface sensitivity enhancement at grazing emission angles is illustrated in Fig. 5 for the case of an idealized homogeneous, semi-infinite, flat-surface specimen in which any effects due to atomic positional order are assumed to be fully averaged over. The mean free path for inelastic scattering Λ_e is further taken to be a constant independent of emission angle. In this case, the mean depth of no-loss photoelectron emission as measured perpendicular to the surface is exactly equal to Λ_e for normal emission or $\theta = 90^\circ$, but it decreases as $\Lambda_e \sin\theta$ for non-normal emission. For typical XPS mean free paths of $15\text{-}20 \text{ \AA}$ ¹⁶⁻¹⁸, this simple model thus predicts that between normal emission and grazing emission at $\theta = 10^\circ$, the mean depth should decrease from roughly 8-10 atomic layers down to only $\sim 2\text{-}3$ atomic layers, respectively. Polar scans of photoelectron intensity are thus expected to exhibit varying degrees of surface sensitivity, as has been demonstrated in numerous prior investigations⁴⁻⁶.

A qualitative illustration of how significant this low- θ effect can be is presented in Fig. 6, where broad-scan spectra are shown at three angles for a highly-polished Si specimen with an oxide overlayer approximately 1-2 atomic layers in thickness and an outermost overlayer of carbon-containing materials from the residual gas of approximately the same thickness¹⁹. The pronounced peaks due to the O1s, C1s, Si2s, and Si2p core levels are found to change dramatically in relative intensity as θ is changed from 70° (near normal) to 5° (grazing). With maximum bulk sensitivity at 70° , the Si peaks are most intense, then O1s, then C1s, but at 5° , this order is completely reversed. These results thus directly provide a qualitative depth profile of the specimen, with C lying outside O (present primarily as a Si oxide) and O lying outside the elemental Si of the substrate.

Closer examination of such oxidized Si spectra also shows Si core-level chemical shifts between oxide and element, with different angular behavior for the two, as illustrated in the results of Kill et al.¹⁹ for a 14 \AA oxide layer in Fig. 7. Here, the Si2p(oxide) peak is enhanced relative to Si2p(element) at low θ , as expected; the quantitative analysis of this type of overlayer data will be discussed further in Section 3.D.

A final and even more subtle example of the qualitative use of variable- θ data is provided by Si in some very recent results due to Grunthaner et al.²⁰ shown in Fig. 8. Here, the Si2p data from a chemically-cleaned surface exhibit a very small change in peak shape in going from $\theta = 38.5^\circ$ to the more surface sensitive $\theta = 18.5^\circ$. These results are also shown after a resolution enhancement procedure

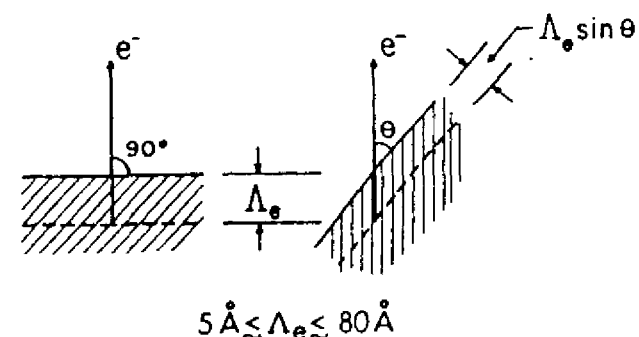


Fig. 5. Illustration of the basic mechanism producing surface sensitivity enhancement for low electron exit angles θ . The average depth for no-loss emission as measured perpendicular to the surface is $\Lambda_e \sin\theta$.

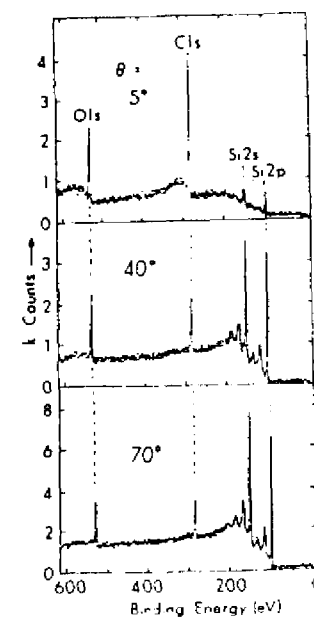


Fig. 6. Broad-scan core-level spectra at three electron exit angles between low and high values for a Si specimen with a thin oxide overlayer ($\sim 4 \text{ \AA}$) and an outermost carbon contaminant layer approximately 1 monolayer in thickness. Note the marked enhancement of the surface-associated O1s and C1s signals for low θ .

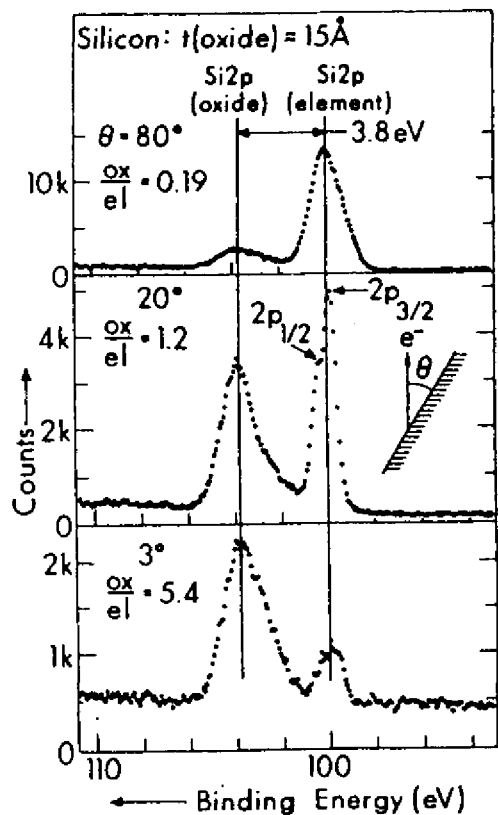


Fig. 7. Si_{2p} spectra at three electron exit angles for a Si specimen with a 15-Å thick oxide overlay. Note the complete reversal of the relative intensities of oxide and element between high and low θ . (From Hill et al., ref. (19).)

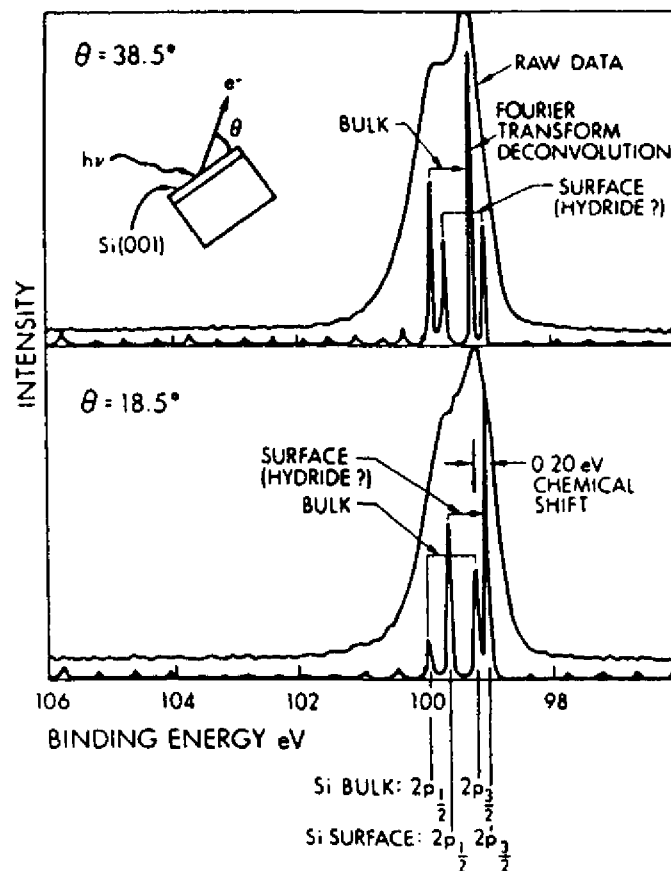


Fig. 8. Si_{2p} spectra at two exit angles from a chemically-cleaned Si surface thought to have a surface hydride present. The raw data and curves obtained via a Fourier-transform (FT) deconvolution procedure are shown. Note the enhancement of the hydride FT peak at $\theta = 18.5^\circ$. (from Vasquez et al., ref. (20).)

using Fourier transform deconvolution to yield two doublets chemically shifted by only 0.30 eV from one another. The lower-binding-energy doublet is enhanced in relative intensity at low θ , suggesting a surface species. The fact that the 2:1 intensity ratio of the expected $2p_{3/2}:2p_{1/2}$ spin-orbit doublet is found in the area ratios of the peaks in each Fourier transform doublet for both angles lends further support to the results of the deconvolution procedure, and provides a further internal consistency check for it. The surface species is thought by the authors to be a chemically-produced hydride²⁰.

B. Simple quantitative models

In more quantitatively discussing such variations of peak intensities with polar angle, it is useful to consider the idealized spectrometer geometry shown in Fig. 9, as has been done in several prior studies^{4-6,21,22}. Here, a uniform flux of x-rays I_0 is taken to be incident at θ_{hv} on the atomically flat surface of a specimen of arbitrary thickness t . The radiation may in general be refracted into $\theta'_{hv} \neq \theta_{hv}$ inside the specimen, after which it penetrates to a depth z below the surface and excites a photoelectron from some level k . X-ray refraction will be negligible for $\theta_{hv} \gtrsim 1-2^\circ$, so that it will not be considered further until the specific discussion of Section 4. Photoelectron excitation is described by the differential photoelectric cross section $d\sigma_k/d\Omega$. The k -level- derived photoelectrons travel to the surface, during which they can be inelastically attenuated according to $\exp(-z/\Lambda_e \sin\theta')$, where θ' is the internal propagation angle and $z/\sin\theta'$ is the path length to the surface. Elastic scattering in travelling to and escaping from the surface is for the moment neglected, although we will consider its possible effects later. In escaping from the surface, the photoelectrons may be refracted from θ' to the external propagation angle θ due to the surface barrier or inner potential V_0 ; refraction will also be neglected for the moment, although an estimate of the low- θ limit of validity of this approximation is presented later in this section. Next, the analyzer is assumed to be adequately described in terms of an effective solid angle of Ω_0 acting over an effective source area of A_0 (as measured perpendicular to the mean electron trajectory), so that all electrons emitted from within the dotted projection of A_0 (the active specimen volume) into Ω_0 are energy analyzed. Possible retardation from an initial energy of $E_{kin} \equiv E_k$ to a final energy of E_0 during analysis is also indicated in Fig. 9. Finally, a detection efficiency D_0 can be included which allows for either less than full counting of the electrons entering Ω_0 (in which case $D_0 < 1$) or the presence of a multichannel detection system (for which $D_0 \gg 1$). In general, the mean free path, the effective solid angle, the effective

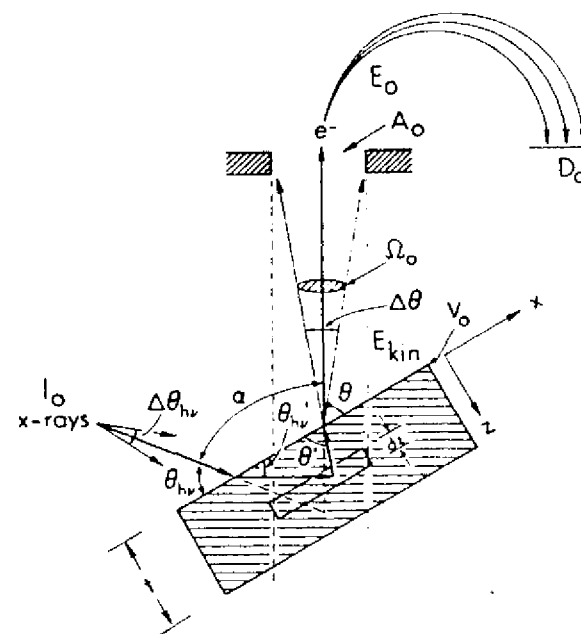


Fig. 9. Idealized spectrometer geometry for calculating angular-dependent photoelectron peak intensities, with various important parameters and variables indicated.

area, and the detection efficiency will depend on electron kinetic energy, so these will be written as $\Lambda_e(E_k)$, $\Omega_o(E_k)$, $A_o(E_k)$, and $D_o(E_k)$.

Within the assumptions of this simple, but for many experimental systems rather realistic, model, expressions for θ -dependent peak intensities can be directly derived for several useful specimen morphologies^{4-6,21,22}. These are depicted in Fig. 10, where $N(\theta)$ denotes a θ -dependent photoelectron intensity, ρ denotes the atomic/molecular number density of the species on which the emitting level is located, a subscript k indicates a substrate level and a subscript l denotes a level originating in an overlayer atom or molecule. Each of these cases will now be discussed, but we will return later in this section to consider several ways in which the model from which the equations have been derived may be somewhat oversimplified.

The different specimen morphologies are:

(i) Semi-infinite specimen, atomically clean surface, peak k with $E_{k1n} \equiv E_k$. No θ dependence is predicted and the intensity is given by:

$$N_k^m \equiv I_o \Omega_o(E_k) A_o(E_k) D_o(E_k) \rho_k (d\sigma_k/d\Omega) \Lambda_e(E_k) \quad (1)$$

This case corresponds to an optimal measurement on a homogeneous specimen for which no surface chemical alteration or contaminant layer is present. The expression given permits predicting the absolute peak intensities resulting for a given specimen, or, of much more interest in practice, the relative intensities of the various peaks. If absolute intensities are to be derived, then the incident flux I_o must be determined, as well as the kinetic energy dependences of the effective solid angle Ω_o , the effective specimen area A_o , and the detection efficiency D_o . In relative intensity measurements in which the quantity of interest is $N_k/N_{k'}$, for two peaks k and k' , the I_o factors will cancel, although the $\Omega_o A_o D_o$ factors need not due to their kinetic energy dependence. The densities ρ_k or $\rho_{k'}$ of the atoms or molecules on which subshell k or k' is located may be known beforehand, or may in many cases be the desired end result in quantitative chemical analyses using XPS. For core levels, the differential cross section $d\sigma_k/d\Omega$ can be calculated for either unpolarized or polarized radiation from a knowledge of the total subshell cross section σ_k and the asymmetry parameter β_k via^{6,23-25}

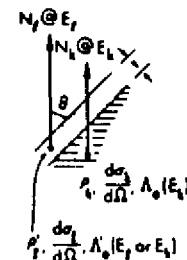
$$\frac{d\sigma_k}{d\Omega} = \frac{\sigma_k}{4\pi} [1 + \beta_k (3 \sin^2 \alpha - 1)] \quad (2)$$

Within a one-electron central-potential model, tabulations of theoretical relativistic σ_{nlj} 's by Scofield²³ and non-relativistic β_{nl} 's by Reilman et al.²⁴ can be used to determine $d\sigma_{nlj}/d\Omega$, or the non-relativistic results of Goldberg et al.²⁵ for σ_{nl} and β_{nl} for a number of atoms can be used. All of these tabulations include the two most common XPS energies (MgK α at 1254.6 eV and AlK α at 1486.6

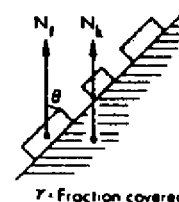
(a) Semi-infinite substrate:



(b) Overlayer on semi-infinite substrate:



(c) Patched overlayer on substrate:



(d) Dilute, non-attenuating overlayer on substrate:



(e) Arbitrary concentration profile:

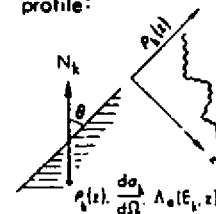


Fig. 10. Several specimen morphologies for which variable- θ peak intensities can be used in order to derive concentration profiles and other analytical information: (a) a uniform semi-infinite substrate, (b) a semi-infinite substrate with a uniform surface overlayer, (c) a semi-infinite substrate with a patched surface overlayer, (d) a semi-infinite substrate with a dilute, non-attenuating overlayer (e.g., a fractional monolayer coverage of an adsorbate), and (e) a semi-infinite substrate with arbitrary concentration profiles inward from the surface.

eV), as well as several lower energies^{23,25}. Possible effects of multi-electron processes on the use of such cross sections are discussed elsewhere⁶. For valence levels involved in bonding, the determination of $d\sigma_k/d\Omega$ is more complex⁶. The last quantity involved is $\Lambda_e(E_k)$ which can either be taken from tabulations of previously measured values¹⁸⁻¹⁸, or, within a given specimen, be estimated from Penn's theoretical treatment²⁶. More simply, its dependence on kinetic energy for $E_k > a$ few hundred eV can be assumed to follow an empirical square-root dependence as^{6,18}: $\Lambda_e(E_k) = (E_k)^{1/2}$; this relationship thus permits determining Λ_e 's at any energy for a given specimen provided that a single value is known.

Note that there is no θ dependence in N_k within this simple model, a prediction that was first made and verified experimentally by Henke²¹. Its origin lies in the fact that the effective emitting depth is $\Lambda_e \sin\theta$ (cf. Fig. 5), while the effective specimen surface area is $A_0/\sin\theta$ (cf. Fig. 9); the effective specimen volume at any θ is thus the product of the two, in which the $\sin\theta$ factors cancel. This behavior is expected to hold as long as θ is not made so small that the edges of the specimen lie within the aperture A_0 ^{4,5}. For such low θ values an additional $\sin\theta$ factor appears in Eq. (1). This is one illustration of the origins of instrument-specific response functions modulating intensities^{4,5,12}. This effect generally leads to the unfortunate characteristic that intensities at grazing emission are markedly reduced compared to those at higher θ .

Prior tests of Eq. (1) in the quantitative analysis of homogeneous samples at relatively high emission angles have generally yielded results in agreement with experimental peak ratios to within $\approx 10\%$, as discussed elsewhere^{6,27-29}.

(ii) Specimen of thickness t , atomically clean surface, peak k with $E_{kin} \equiv E_k$. The intensity in this case is given by

$$N_k(\theta) = I_0 \Omega_0(E_k) A_0(E_k) D_0(E_k) \rho_k(d\sigma_k/d\Omega) \Lambda_e(E_k) [(1 - \exp(-t/\Lambda_e(E_k)\sin\theta))] = N_k^\infty [1 - \exp(-t/\Lambda_e(E_k)\sin\theta)]. \quad (3)$$

Here, the intensity of a peak originating in a specimen of finite thickness is predicted to increase with decreasing θ (again with the proviso that θ not be so small that the specimen edges lie within A_0).

(iii) Semi-infinite substrate with uniform overlayer of thickness t . As first discussed by Fraser et al.²², the two types of intensities here are:

Peak k from substrate with $E_{kin} \equiv E_k$:

$$N_k(\theta) = I_0 \Omega_0(E_k) A_0(E_k) D_0(E_k) \rho_k(d\sigma_k/d\Omega) \Lambda_e(E_k) \exp(-t/\Lambda_e'(E_k)\sin\theta) = N_k^\infty \exp(-t/\Lambda_e'(E_k)\sin\theta). \quad (4)$$

Peak l from overlayer with $E_{kin} \equiv E_l$:

$$N_l(\theta) = I_0 \Omega_0(E_l) A_0(E_l) D_0(E_l) \rho_l'(d\sigma_l'/d\Omega) \Lambda_e'(E_l) [1 - \exp(-t/\Lambda_e'(E_l)\sin\theta)] = N_l^\infty [1 - \exp(-t/\Lambda_e'(E_l)\sin\theta)] \quad (5)$$

where

- Λ_e = an attenuation length in the substrate
- Λ_e' = an attenuation length in the overlayer
- ρ = an atomic density in the substrate
- ρ' = an atomic density in the overlayer.

Or, it is often more convenient to deal with peak ratios in which I_0 and any purely instrumental variations with θ cancel:

Overlayer/substrate ratio:

$$R(\theta) \equiv \frac{N_l(\theta)}{N_k(\theta)} = \frac{\Omega_0(E_l) A_0(E_l) D_0(E_l) \rho_l'(d\sigma_l'/d\Omega) \Lambda_e'(E_l)}{\Omega_0(E_k) A_0(E_k) D_0(E_k) \rho_k(d\sigma_k/d\Omega) \Lambda_e(E_k)} \times \frac{[1 - \exp(-t/\Lambda_e'(E_l)\sin\theta)] \exp(t/\Lambda_e'(E_k)\sin\theta)}{[1 - \exp(-t/\Lambda_e'(E_l)\sin\theta)] \exp(t/\Lambda_e'(E_k)\sin\theta)} = \frac{N_l^\infty}{N_k^\infty} \times [1 - \exp(-t/\Lambda_e'(E_l)\sin\theta)] \exp(t/\Lambda_e'(E_k)\sin\theta).$$

This case represents a much more common experimental situation in which the primary specimen acts as substrate and possesses an intentional or unintentional contaminant overlayer (for example, an oxide on a semiconductor as in Figs. 6 and 7 or a layer deposited from the spectrometer residual gases). Substrate peaks are attenuated by inelastic scattering in the overlayer, an effect that is much enhanced at low θ . The overlayer/substrate ratio is thus predicted to increase strongly as θ decreases, and this model provides a quantitative description of the effects discussed qualitatively in the previous section. It is also useful to consider several trivial modifications of Eqs. (4)-(5) that have been found useful in analyzing data. Rearranging Eq. (4) and taking the logarithm yields³⁰

$$\ln \left[\frac{N_k(\theta)}{N_k^\infty} \right] = - \frac{t}{\Lambda_e'(E_k)\sin\theta}, \quad (7)$$

and proceeding similarly for Eq. (5) gives

$$\ln \left[1 - \frac{N_l(\theta)}{N_l^\infty} \right] = \frac{t}{\Lambda_e'(E_l)\sin\theta}. \quad (8)$$

In Eq. (6), if the two kinetic energies E_k and E_l are very nearly equal (as, for example, in chemically-shifted peaks such as those of Fig. 7), then

$\Lambda_e'(E_k) = \Lambda_e'(E_l)$ (although in general $\Lambda_e'(E_l) \neq \Lambda_e(E_k)$ because they apply to different materials) and the $\Omega_0 A_0 D_0$ products will cancel in the ratio. Defining

$$K \equiv \frac{N_k^0}{N_k^\infty} \text{ then yields after similar manipulation}^{19}$$

$$\ln \left[\frac{R(\theta)}{K} + 1 \right] = \frac{t}{\Lambda_e'(E_k) \sin \theta} \quad (9)$$

Eqs. (7)-(9) thus represent linearized methods for plotting data versus $1/\sin \theta$ that will be considered further in Section (3.D), where the quantitative use of this model is discussed. The slopes of such plots are thus given by plus or minus the effective overlayer thickness $\tau \equiv t/\Lambda_e'$.

(iv) Semi-infinite substrate with a uniform, but patched, overlayer of thickness t ^{5,31,32}. If the fraction of surface area covered by the overlayer is γ , that uncovered is thus $(1-\gamma)$, and the resultant intensities are given by:

Peak k from substrate:

$$N_k(\theta) = (1-\gamma)(\text{Eq. (1)}) + \gamma(\text{Eq. (4)})$$

$$= N_k^\infty [(1-\gamma) + \gamma \exp(-t/\Lambda_e'(E_k) \sin \theta)] \quad (10)$$

Peak l from overlayer:

$$N_l(\theta) = \gamma(\text{Eq. (5)})$$

$$= \gamma N_l^\infty [1 - \exp(-t/\Lambda_e'(E_l) \sin \theta)] \quad (11)$$

Overlayer/substrate ratio:

$$\frac{N_l(\theta)}{N_k(\theta)} = \frac{N_l^\infty}{N_k^\infty} \gamma [1 - \exp(-t/\Lambda_e'(E_l) \sin \theta)]$$

$$\times [(1-\gamma) + \gamma \exp(-t/\Lambda_e'(E_k) \sin \theta)]^{-1} \quad (12)$$

The overlayer/substrate ratio thus has a θ dependence different from Eq. (6), and, in particular, the enhancement of the overlayer relative intensity at low θ is predicted to be less pronounced in the presence of patching or clustering. This model might be expected to apply for overlayer growth in which the overlayer material (for example, a metal) is more compatible with itself than the substrate, or could also be qualitatively useful as an extreme representation of the effects of non-uniform overlayer growth (for example, in certain types of oxide formation). This model has been compared previously with experimental results^{31,32}, although it is not clear that patching effects can be clearly distinguished from those due to other phenomena such as surface roughness (to be discussed below).

(v) Semi-infinite substrate with a very thin, non-attenuating overlayer. One important example of such a specimen type is an adsorbate present on a substrate at fractional monolayer coverage. The relevant intensities are^{5,6}:

Peak k from substrate:

$$N_k(\theta) = N_k^\infty \text{ as Eq. (1)} \quad (13)$$

Peak l from overlayer:

$$N_l(\theta) = I_0 \Omega_0(E_l) A_0(E_l) D_0(E_l) s' (d\sigma_l/d\Omega) (\sin \theta)^{-1} \quad (14)$$

Overlayer/substrate ratio:

$$\frac{N_l(\theta)}{N_k(\theta)} = \frac{\Omega_0(E_l) A_0(E_l) D_0(E_l) s' (d\sigma_l/d\Omega) d}{\Omega_0(E_k) A_0(E_k) D_0(E_k) s (d\sigma_k/d\Omega) \Lambda_e'(E_k) \sin \theta}$$

$$= \left[\frac{s'}{s} \right] \times \frac{D_0(E_l) \Omega_0(E_l) A_0(E_l) (d\sigma_l/d\Omega) d}{D_0(E_k) \Omega_0(E_k) A_0(E_k) (d\sigma_k/d\Omega) \Lambda_e'(E_k) \sin \theta} \quad (15)$$

with

s' = the mean surface density of overlayer atoms in which peak l originates (in cm^{-2})

s = the mean surface density of substrate atoms (in cm^{-2})

s'/s = the fractional monolayer coverage of the atomic species in which peak l originates

d = the mean separation between layers of density s in the substrate (calculable from s/ρ).

These expressions are useful in surface-chemical studies at very low exposures to adsorbate molecules ($s'/s \ll 1$), as they permit an estimation of the fractional monolayer coverage from observed peak intensities. The assumption of no inelastic attenuation in the overlayer is an extreme one, but is justified because the macroscopic Λ_e' of case (iii) is both difficult to estimate and dubious in its application to such thin, non-macroscopic layers, and also because it represents a correct limiting form for zero coverage. A recent attempt to quantitatively assess the utility of this analysis³³ is discussed below in Section 3.E.

(vi) An arbitrary concentration profile $\rho_k(z)$ of a given species in a semi-infinite substrate³⁴.

Peak k from a species of interest:

As a first approximation to such a situation, if the mean free path $\Lambda_e'(E_k)$ can be assumed to be constant with depth z and thus independent of the composition change associated with $\rho_k(z)$, a simple summation over atomic layers with spacing d at depths of $z_n = nd$ ($n = 1, 2, \dots$) can be made to yield:

$$N_k(\theta) = I_0 \Omega_0(E_k) A_0(E_k) D_0(E_k) \Lambda_e'(E_k) (d\sigma_k/d\Omega)$$

$$\times \sum_{n=1}^{\infty} \rho_k(z_n) \exp(-z_n/\Lambda_e'(E_k) \sin \theta) \quad (16)$$

If Λ_e depends on z also as $\Lambda_e(E_k, z)$, the resulting expression is, however, considerably more complex³⁴:

$$N_k(\theta) = I_0 \Omega_0(E_k) A_0(E_k) D_0(E_k) (d\sigma_k/d\Omega) \times \prod_{n=1}^{\infty} [\rho_k(z_n) (1 - \exp(-d/\Lambda_e(E_k, z_n) \sin \theta))] \frac{\pi^{n-1} \exp(-d/\Lambda_e(E_k, z_n) \sin \theta)}{n!} \quad (17)$$

$(n \geq 2)$

Taking ratios of two such intensities N_k and N_k' as derived from species with different concentration profiles has been suggested as a method for deriving profiles by Hollinger et al.³⁴, although a complex, multiparameter fit to the θ -dependent data results, and it appears that physically reasonable constraints must be placed on the forms of $\rho_k(z)$ to yield unique solutions. Vasquez and Grunthaner³⁵ have also considered a very similar model for oxide growth in fixed-angle XPS measurements. This method is discussed in more detail in Section 3.F.

C. Additional complicating effects

With reference to the idealized spectrometer geometry of Fig. 9 and a few further assumptions made in arriving at the results of the last section, there are several additional effects that need to be considered in order to fully understand the behavior of experimental data.

(i) The instrument response function. Beyond the extreme low- θ deviation of intensities from the constancy predicted by Eq. (1) that we have mentioned before, additional purely instrumental effects can be introduced by a non-uniform x-ray flux (as, for example, will be produced by most x-ray monochromators¹²) and a solid angle that varies over the active portion of the specimen. All of these factors can be combined into an effective instrument response function, as discussed in detail in prior reviews⁴⁻⁶. Denoting this by $R_0(E_k, \theta)$, it is conveniently defined in terms of an integral over differential surface elements of the product of spatially varying x-ray flux I , solid angle Ω , and detection efficiency D . The specimen surface can be considered to lie in the x, y plane, thus yielding⁵

$$R_0(E_k, \theta) \equiv \sin \theta \int_A I(\theta, x, y) \Omega(E_k, \theta, x, y) D(E_k, \theta, x, y) dx dy \quad (18)$$

The detection efficiency will depend principally on E_k and so can probably be removed from the integral. With this definition, any of Eqs. (1) and (3)-(17) can be modified so as to apply to an arbitrary spectrometer simply by replacing the

combined factor $I_0(E_k) \Omega_0(E_k) A_0(E_k) D_0(E_k)$ by $R_0(E_k, \theta)$. Inspection of Eq. (1) with and without R_0 inserted shows that the form of such a response function can be empirically determined simply by measuring the θ dependence (and perhaps also the E_k dependence) of the k photoelectron intensity originating from a homogeneous semi-infinite specimen with a clean surface (cf. Fig. 10(a)).

Examples of non-ideal response functions are shown in Fig. 11. Here, curves calculated with a slightly simplified version of Eq. (18) are compared with experimental points obtained with a Hewlett Packard spectrometer¹². These results are for a system with monochromatized radiation in which I is very strongly peaked in the middle of the specimen surface, but for which the Ω_0, A_0 approximation of Fig. 9 is essentially valid. Also shown in Fig. 11 is the measured response function for a Vacuum Generators ESCALAB spectrometer; note that it comes much closer to the constancy with θ predicted by Eq. (1), as its non-monochromatized source yields a much more nearly uniform x-ray flux.

It is finally reasonable to suppose that for some spectrometers, $R_0(E_k, \theta)$ will have the same functional form in θ regardless of E_k ^{5,12}, and in this case, that any intensity ratio $N_k(\theta)/N_k'(\theta)$ from a given specimen will yield θ variations independent of instrument effects. (Clark and co-workers³⁶ have noted, however, that this simplification may not hold for all analyzer systems.) Thus, such peak ratios should in general be more amenable to straightforward analysis, although they still may carry information on the E_k dependence of R_0 . For example, an energy dependence of Ω_0 as shown in Fig. 12³⁷ must be considered in analyzing peak ratios at any θ for the Hewlett Packard instrument of Figs. 3 and 11.

(ii) Surface roughness effects. The qualitative effects of surface roughness are illustrated in Fig. 13(a), and they are twofold: (1) For a given macroscopic or experimental angle of emission θ as measured with respect to the planar average of the roughness, the microscopic or true emission angle θ^t at an arbitrary surface point may be significantly different. Thus, the true degree of surface enhancement at low θ may differ appreciably from that expected on the basis of the macroscopic θ alone. (2) Certain regions on the surface may be shaded for emission at a given θ by adjacent raised areas, as indicated by the cross-hatched regions in Fig. 13(a). Such shading will tend to be fully effective if the roughness contours are large with respect to typical Λ_e values of 10-40 Å, or only partial if the contours are on the scale of Λ_e . In any case, regions of the surface will be selected by shading as being more active in emission, and over these regions, it is an integration of the true-angle emission behavior that will correctly predict the observed intensities.

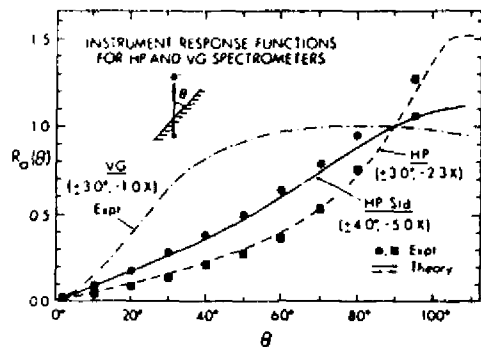


Fig. 11. Instrument response functions $R_0(\theta)$ for two different spectrometer systems, a Hewlett Packard 5950A with monochromatized AlKa x-ray source and $\alpha = 72^\circ$ and a VG ESCALAB5 with a standard AlKa source and $\alpha = 48^\circ$. All curves have arbitrarily been set to 1.0 at $\theta = 90^\circ$ (electron emission normal to the surface). For the HP system, two different entry lens magnifications have been used: standard of 5.0X and a second option of 2.3X. Cls intensities were used for the HP results; Cu2p_{3/2} for the VG. Note the different shapes of the curves, with the monochromatized system showing greater deviations from the simple predictions of Eq. (1) of a constant response function. (From ref. (12) plus R.C. White and C.S. Fadley, unpublished results.)

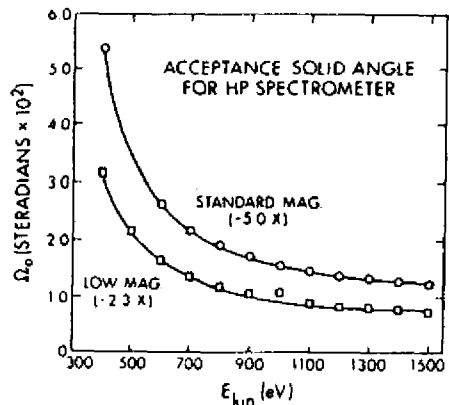


Fig. 12. Kinetic energy dependence of the solid angle of acceptance into a Hewlett Packard 5950A spectrometer, as determined from detailed electron trajectory calculations for two different entry lens magnifications. (From Baird, ref. (37).)

Possible added complexity due to:

- (a) Surface Roughness - Shading and $\theta' \neq \theta$
- (b) Elastic e⁻ Scattering - Decreased surface sensitivity at low θ and θ smearing
- (c) e⁻ Refraction at Surface - $\theta = \theta'$ for $\theta \leq 10^\circ$

Fig. 13. Illustration of three effects providing additional complexities in the analysis of angle-resolved peak intensities: (a) surface roughness, (b) elastic electron scattering, and (c) electron refraction in crossing the surface barrier V_0 .

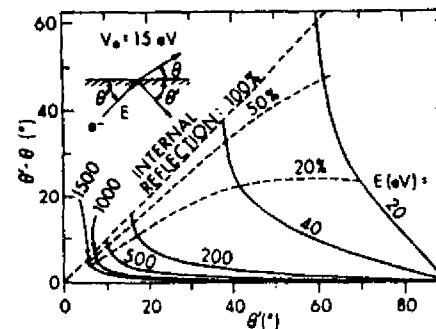


Fig. 14. Calculation of electron refraction effects for different electron kinetic energies and a typical V_0 value of 15eV. The degree of refraction is indicated by the difference $\theta' - \theta$ (internal) - θ (external). Contours of equal probability of internal reflection are also shown. (From ref. (5).)

In prior investigations^{4,5,38,39}, roughness effects have been considered for several idealized topographies from both a theoretical and experimental point of view. For example, the triangular-periodic surfaces of aluminum diffraction gratings with thin oxide overlayers exhibit dramatic angular variations in the Al2p(oxide)/Al2p(metal) ratio that are fully consistent with theoretical calculations incorporating the two effects mentioned above³⁹. The precise form of the effects seen depends strongly on the exact nature of the profile, which is usually not known for an arbitrary specimen unless it has been very carefully prepared. However, it is possible to conclude that the presence of roughness will in general reduce the degree of surface sensitivity enhancement possible at low θ , although in the limit of very low θ , roughness with rounded contours should again give reasonable enhancement (i.e., an average $\theta_t \approx \theta \approx 0^\circ$)⁵.

Thus, roughness must be kept in mind as a possible source of deviations from the simple models of the last section for all specimens. However, even for rather randomly roughened surfaces, such effects do not seem to preclude the use of high- θ and low- θ comparisons to do qualitative depth profiling³⁹, as discussed in Section 3.A. Also, a procedure as simple as unidirectional course polishing of an aluminum surface and subsequent θ scanning in a plane parallel to the polishing grooves and normal to the surface is, for example, found to significantly enhance the amount of surface sensitivity enhancement at low θ ³⁹.

(iii) Elastic electron scattering. Elastic electron scattering during photoelectron travel to and escape from the surface has been neglected in this simple model, but it could lead to several effects. Each interaction of the photoelectron wave with an atomic center will produce scattered intensity deviating from the initial propagation direction. Thus, the simple straight-line paths assumed in the model are not a fully accurate representation. Fortunately, at typical XPS energies of $\sim 10^3$ eV, the scattered intensity due to each atom will be strongly forward peaked; that is, most of the intensity will lie very close to the initial direction and will in fact be within $\sim 10^\circ$ - 15° of it. (Such effects will be discussed in much more detail in Section 5, as they have been found to produce pronounced photoelectron diffraction effects in single-crystal studies.) But even in that case, there may be sufficient displacement of intensity to alter the final emission distribution significantly, especially at low θ . The possible effects of elastic scattering on grazing-emission surface enhancement have been discussed qualitatively for some time^{5,19}, but only rather recently have Nefedov et al.⁴⁰ attempted to quantitatively determine their nature and importance.

One important effect of elastic scattering will be to reduce surface sensitivity enhancement at low θ according to the mechanism of Fig. 13(b). For some very low

emission angle θ , the direct or unscattered wave travels along a long path of inelastic attenuation in reaching the surface. It is possible, however, that a wave initially propagating at some higher angle (and thus with a shorter path length to the surface) can be scattered just before escaping so as to yield significant intensity in the θ direction with respect to that of the direct wave. Thus, higher- θ relative intensities for different peaks can be scattered into lower- θ regions, reducing surface sensitivity enhancement. This discussion implicitly neglects any diffraction or interference effects between waves by assuming that the positions of the atomic scatterers are random and averaged over in different emission events. (For single-crystal specimens, such averaging does not occur and diffraction effects can be very strong.)

A second type of effect discussed by Nefedov et al.⁴⁰ is the effective lengthening of the average path length of a photoelectron caused by a random walk of elastic scattering events. Thus, they postulate that measured inelastic mean free paths Λ_e are too large due to a lack of allowance for such elastic effects.

An example of possible elastic scattering effects is presented in Section 3.D in discussing ARXPS data for the SiO₂/Si system.

(iv) Electron refraction at the surface. As the photoelectron escapes from the surface, it must surmount a potential barrier or inner potential V_0 that can be from 5-25 eV in magnitude for typical clean surfaces^{41,42}. In doing so, the component of momentum perpendicular to the surface will be reduced, along with the kinetic energy, and a net refraction as shown in Fig. 13(c) will be produced. A fraction of the intensity can also be reflected back into the solid. As the internal angle θ' will thus always be greater than the external angle θ , refraction will act to decrease the degree of surface sensitivity enhancement relative to that expected at θ .

Such refraction and reflection effects can be easily calculated provided that V_0 is known⁵, and a family of curves for different kinetic energies E and a typical V_0 of 15 eV is shown in Fig. 14. The equations utilized in calculating θ and the fractional internal reflection R_e for a given θ' are:

$$\theta = \tan^{-1} \left\{ \frac{(\sin^2 \theta' - V_0/E)^{1/2}}{\cos \theta'} \right\} \quad (19)$$

and

$$R_e = \left[\frac{1 - (1 - V_0/E \sin^2 \theta')^{1/2}}{1 + (1 - V_0/E \sin^2 \theta')^{1/2}} \right]^2 \quad (20)$$

The difference $\theta' - \theta$ between the internal and external angles is used as a gauge of the degree of refraction, and contours of equal percentage of internal reflection are also shown. From these results, it is clear that such refraction and

reflection effects can be very serious problems in measurements in the UPS regime of 20-40 eV. In the XPS region of ~500-1500 eV by contrast, refraction and reflection should not be significant for $\theta \gtrsim 10-15^\circ$, where $\theta' - \theta \lesssim 3^\circ$ and the internal reflection is $\lesssim 10\%$. Nonetheless, such effects should be taken into account whenever possible in any fully quantitative analysis of ARXPS data for $\theta \lesssim 20-30^\circ$.

Having considered both the simple quantitative models applicable to ARXPS intensities and several effects which could cause deviations from them, we now turn to illustrative examples involving several specimen morphologies and several types of phenomena that it has been possible to study.

D. Applications to uniform overlayers

As one example of ARXPS as applied to the study of uniform overlayers, we consider work by Clark and co-workers³⁶ on polymer films deposited in situ on metal substrates. In this study, poly(p-xylylene) films of different thicknesses were deposited on a smooth Au substrate. Thicknesses t were measured with a quartz crystal deposition monitor. The Cls intensity from the film and Au4f_{7/2} intensity from the substrate were measured at several θ values for each film, including values obtained in the limit of infinite thickness. Plots of

$$\ln \left[1 - \frac{N_{\text{Cls}}(\theta)}{N_{\text{Cls}}^\infty} \right] \text{ and } \ln \left[\frac{N_{\text{Au4f}_{7/2}}(\theta)}{N_{\text{Au4f}_{7/2}}^\infty} \right] \text{ vs } t/\sin\theta \text{ were then made, according to the}$$

linearized relations of Eqs. (7) and (8). Such data are shown in Fig. 15 and it is clear that the points for various thicknesses and θ values are very well described by a straight line. There is also very good agreement in the overlayer λ_e' values obtained via least-squares fits for data at different θ 's, as given for both the Cls and Au4f_{7/2} kinetic energies on the figure. Varying θ thus provides a very useful additional dimension in such data. We note, however, that high θ values were utilized, being from 90° (normal emission) down to 40° , and thus that various additional effects expected to be stronger at low θ such as roughness, elastic scattering, and refraction have probably been minimized.

As a second case, we consider SiO₂ overlayers thermally grown on highly polished single-crystal Si substrates; some example data have already been shown in Fig. 7. In the first ARXPS study of this type by Hill et al.¹⁹, four oxide thicknesses as determined by ellipsometry were studied and the θ dependence of the Si2p(oxide)/Si2p(element) ratio measured. As the kinetic energies of the two peaks are essentially identical, Eq. (9) provides a useful method for analyzing

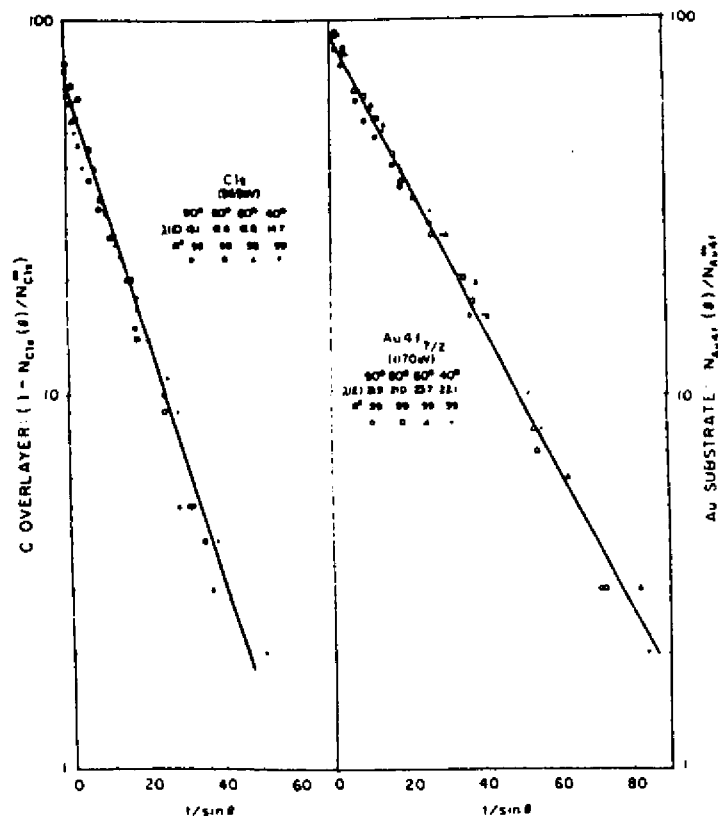


Fig. 15. Angle-resolved core-level intensities from a specimen consisting of a uniform overlayer of poly(p-xylylene) on a polycrystalline Au substrate. Overlayer Cls and substrate Au4f_{7/2} intensities were measured at four θ values and for different overlayer thicknesses, and then plotted according to Eqs. (7) and (8). Line slopes were then used to derive $\lambda_e(E)$ values in the overlayer (here indicated as $\lambda(E)$). (After Clark and Thomas, ref. (36).)

the data, and a plot of $\ln\left[\frac{R(\theta)}{K} + 1\right]$ versus $t/\sin\theta$ is shown in Fig. 16 over a

broad θ range from 90° to as low as 5° . The data were found to be linear over the θ range of 90° to 30° - 40° , but showed similar deviations from linearity for lower θ values in a direction so as to reduce the relative intensity of the oxide peak. These deviations could be due to a combinations of factors: roughness, elastic scattering, electron refraction, incomplete averaging over single crystal effects, and the presence of a non-abrupt transition region between SiO_2 and Si .¹⁹ More recently, Nefedov et al.⁴⁰ have reanalyzed this data with the incorporation of only elastic scattering effects, and they find good agreement as to the qualitative form of the deviations from linearity expected at low θ . Pijolet and Hollinger³⁴ have also very recently analyzed similar $\text{Si}2p(\text{oxide})/\text{Si}2p(\text{element})$ data using a simplified version of Eq. (17) which allows for an interface layer of intermediate composition between SiO_2 and Si ; This analysis suggests that the transition region is rather abrupt and does not exceed $\sim 3 \text{ \AA}$ for an oxide film of $\sim 28 \text{ \AA}$ thickness. However, even this small a transition region also could account for some of the low- θ deviations, as was noted previously in the analysis by Hill et al.¹⁹. But in any case, the use of $\tau = t/\Lambda_e'$ values derived over the linear regions for the three thickest SiO_2 overlayers permitted deriving a $\Lambda_e'(\text{oxide})$ of $37 \pm 4 \text{ \AA}$ and, via the experimentally determined constant K (cf. Eqs. (1) and (9)), also a $\Lambda_e(\text{element})$ of $27 \pm 6 \text{ \AA}$.¹⁹ These values have subsequently been found to be accurate by other investigators^{35,43,44}. Thus, provided that such data are tested via Eq. (9) and the appropriate high- θ range used, this type of analysis seems capable of providing accurate Λ_e' or Λ_e values (or, once Λ_e' is known, accurate t values).

E. Analysis of adsorbate overlayers at fractional monolayer coverage

In chemisorption studies, one is often dealing with fractional monolayer coverages of some adsorbate, and it is thus of interest to ask how accurate ARXPS is for both determining the coverage and also perhaps detecting whether an adsorbate has penetrated into the surface. Single-crystal effects are also often present in such studies, so that some allowance for them needs to be made also.

The example chosen here is from a recent study by Connelly et al.³³ of the very well characterized system $c(2 \times 2)\text{S}$ on $\text{Ni}(001)$, for which an ordered half-monolayer of S atoms is present, occupying every other fourfold hole site on the Ni surface. Previous structural studies⁴⁵ indicate further that the S atoms are 1.3 \AA above the first plane of Ni atoms, as will be discussed further in Section 5.E.

Polar scans of $\text{S}2p(E_{\text{kin}} = 1317 \text{ eV})$, $\text{Ni}2p_{3/2}(627 \text{ eV})$, and $\text{Ni}3p(1413 \text{ eV})$ core-level intensities were made for two different azimuthal orientations

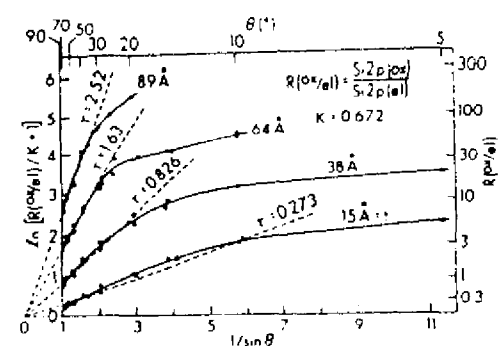


Fig. 16. Angle-resolved core-level intensity ratios from Si specimens with four different oxide overlayer thicknesses from 15 \AA to 89 \AA . The $\text{Si}2p$ oxide/element ratio (cf. Fig. 7) has been plotted according to Eq. (9) so as to derive $\Lambda_e(\text{oxide}) = t/\tau$. (From Hill et al., ref. (19).)

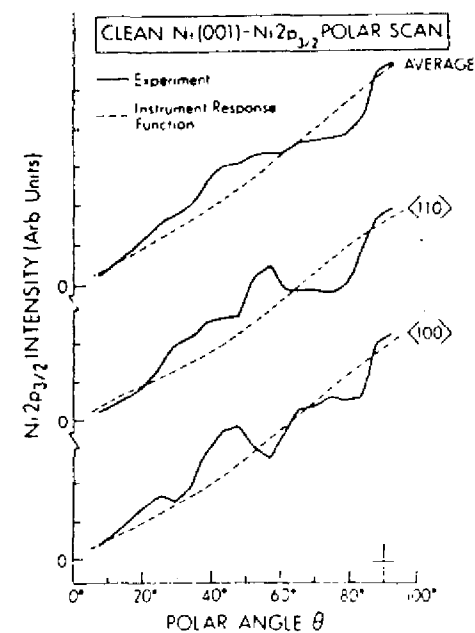


Fig. 17. Polar-scans of $\text{Ni}2p_{3/2}$ intensities above a (001) Ni surface. Shown are two scans along the symmetry-inequivalent azimuths $\langle 100 \rangle$ and $\langle 110 \rangle$, together with an average of these two scans. Before averaging strong diffraction features are evident. Also shown is the instrument response function (cf. Fig. 11). (From ref. (33).)

corresponding to [100] and [111] directions. (For Ni2p_{3/2}, it was important to include the intensity of the satellite at ~6 eV.) As expected, the Ni levels showed marked single-crystal channeling effects in their polar scans, but these were very nearly averaged out in a sum of the two scans at different azimuths. This is illustrated in Fig. 17, where the summed data for each Ni level also fit rather well the form expected for the Hewlett-Packard instrument response function (cf. Fig. 11).

The adsorbate/substrate ratios S2p/Ni3p and S2p/Ni2p_{3/2} were calculated from Eq. (15), with all parameters being evaluated as accurately as possible for the specimen and experimental geometry utilized. This included utilizing the known coverage of s'/s = 0.5, theoretical photoelectric cross sections²⁵, and energy dependences of both λ_e in the substrate as given by $(E_k)^{1/2}$ and Ω_0 as given by Fig. 12. The calculated curves are directly compared with experiment in Fig. 18, and there is very good agreement as to both the 1/sin θ form and the absolute magnitude of the ratio, even though the θ range covered is extremely broad (90°-7°). The two sets of data never disagree with theory by more than ~10%. Theory is however above experiment at low θ for the 2p_{3/2} ratio, whereas it is below in the same region for the 3p ratio. This could be due to the much shorter mean free path for the lower energy Ni2p_{3/2} peak, a fact which could lead to some low- θ inelastic attenuation in the overlayer that is not included in the model of Eq. (15). Nonetheless, these effects are not large, and, particularly if higher energy peaks are utilized, it appears that such azimuthally-summed measurements should permit rather accurate coverage measurements to be made, even in the presence of strong single crystal effects. In addition, differences in the forms of such ratio curves as a function of exposure or annealing could be useful in detecting adsorbate penetration into the substrate, as the degree of increase in an adsorbate/substrate ratio at low θ should decrease in the presence of any penetration. For too high adsorbate coverages, however, there could be concern as to the validity of the non-attenuating assumption for the overlayer⁵.

F. Studies of more complex concentration profiles

In the category of more complex concentration profiles, we begin by considering a single-crystal specimen of LaB₆ with alternating layers of La atoms and B₆ octahedra perpendicular to the (001) surface (cf. Fig. 19(a)). When such a surface is polished, cleaned in situ by ion bombardment, and annealed to form a well-ordered system, the question arises as to whether La or B₆ layers will lie on the surface. Aono et al.⁴⁶ have studied this with ARXPS, measuring polar scans of both La and B core levels, as shown in Fig. 19(b) at two different azimuths. Although there are pronounced single-crystal channeling effects in the intensities

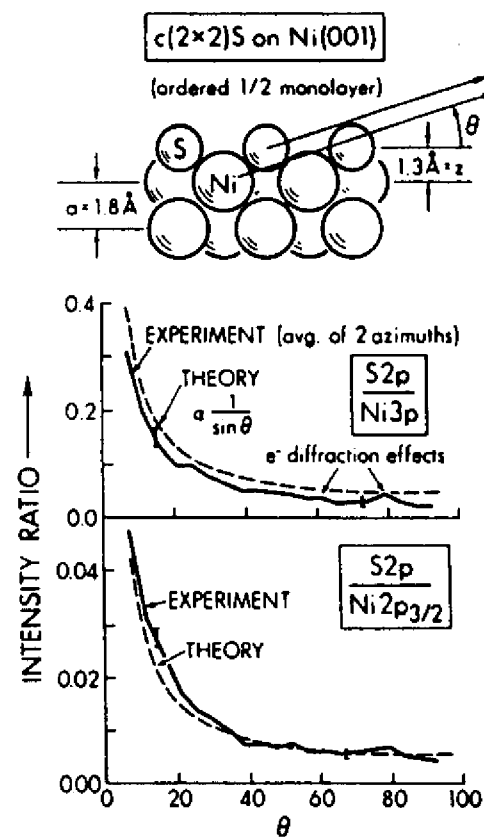


Fig. 18. Comparison of experiment and theory for the polar-angle dependence of an adsorbate/substrate intensity ratio for the very well defined overlayer of c(2x2)S on Ni(001). The Ni2p_{3/2} and Ni3p intensities are averages of two azimuths (cf. Fig. 17). The theoretical curves are calculated according to Eq. (15) with no adjustable parameters. (From ref. (33).)

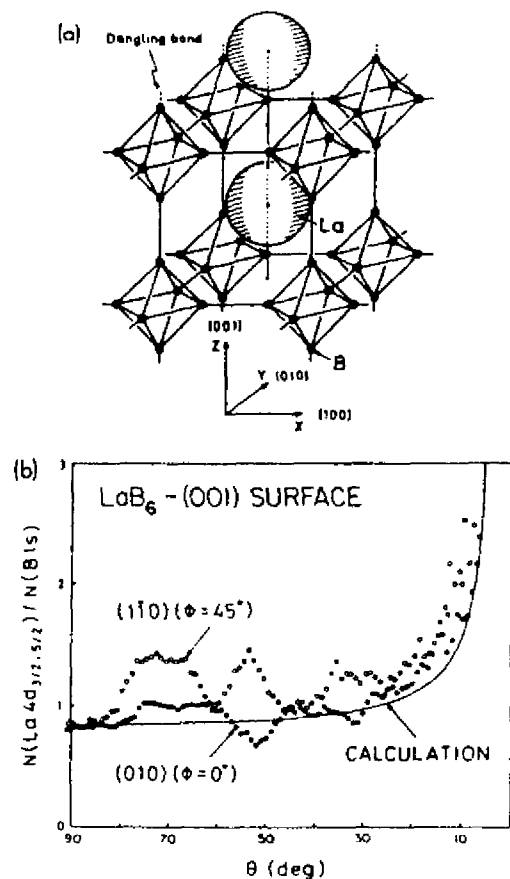


Fig. 19. The crystal structure of LaB₆ is shown in (a), together with the measured and calculated θ dependence of the La4d/B1s intensity ratio in (b). Two different azimuths are shown for the experimental results. (After Aono et al., ref. (46).)

of both peaks, it is nonetheless clear that the relative intensity is enhanced at low θ . This system represents a straightforward application of Eq. (16) in which Λ_e does not vary with z , but it can be set up in two ways depending upon whether La atoms or B₆ moieties make up layer 1 (the surface layer). Aono and co-workers have carried out calculations of the La4d_{3/2,5/2}/B1s ratio in both ways and it is clear that the agreement with experiment is much better for a La surface layer. This observation via ARXPS has thus assisted in explaining the unusually low work function of LaB₆, and should be generally useful for ordered structures with layering of this type.

Binary metal alloys provide another example for which concentration profiles can be much more complex, with one component often segregating preferentially at the surface⁴⁷. The concentration of this species may then monotonically decay into the bulk until it reaches the average bulk value, or it may in certain cases exhibit single-layer oscillations as it approaches the bulk value. Ion bombardment may, on the other hand, cause preferential depletion of one species at such a surface. As a qualitative illustration of such effects, Nefedov et al.⁴⁸ have studied permalloy with a composition of about Fe_{0.2}Ni_{0.8}. They compared the polar dependence of the Fe3p/Ni3p intensity ratio for an air-exposed film and for the same film after ion bombardment. Their results are shown in Fig. 20, where it is clear that Fe is surface segregated for the air-exposed film, but that very little segregation of either species is present after ion bombardment. Thus, it is possible to conclude that the ion bombardment has selectively removed Fe, perhaps leading to a slight enrichment of Ni at the surface.

Beyond such qualitatively useful conclusions concerning alloys, the question also arises as to whether the detailed $\rho_k(z)$ profile can be determined by analyzing such ARXPS data. Pijolet and Hollinger³⁴ have recently discussed this general problem from the point of view of using peak ratios $N_k(\theta)/N_{k_1}(\theta)$ based upon Eq. (17). A simplex method is used to choose the best $\rho_k(z)$ and $\rho_{k_1}(z)$ by minimizing the difference between the experimental and theoretical ratios. However, the ρ curves so derived are found to be extremely sensitive to the exact data points fit and the convergence criteria used, so that effectively, multiple solutions can result if quite arbitrary profiles are utilized. However, by incorporating physically realistic constraints on ρ_k and ρ_{k_1} , as they are derived, much better results can be obtained. These constraints include limiting maximum and minimum values, and usually requiring a monotonically increasing or decreasing function of z . (The latter of course eliminates the possibility of seeing the oscillations in $\rho(z)$ that are expected for certain systems.) An example of their results for a Cu/Ni alloy ion bombarded and annealed in UHV are shown in Fig. 21, together with the % Ni profile yielding the solid curve that

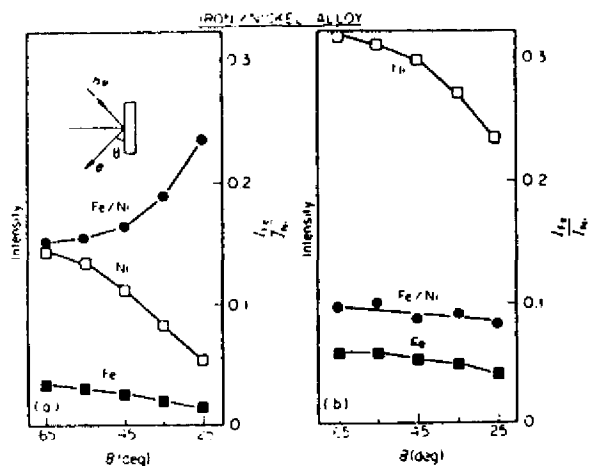


Fig. 20. The θ dependence of Fe 3p and Ni 3p core intensities for an Fe/Ni alloy before and after ion bombardment of the surface. Note particularly the marked change in the variation of the Fe/Ni ratio with bombardment. (After Nefedov et al., ref. (48).)

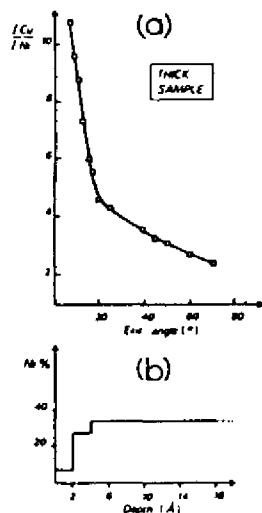


Fig. 21. Experimental $Cu 2p_{3/2}/Ni 2p_{3/2}$ relative intensities from a Cu/Ni alloy are shown as a function of θ in (a). In (b), the Ni concentration profile as derived from these measurements using an analysis based on a simplified revision of Eq. (17) is presented. (From Pijolat and Hollinger, ref. (34).)

very well describes the $Cu 2p_{3/2}/Ni 2p_{3/2}$ ratio data. The profile also agrees qualitatively with that expected from theory. However, the layer-by-layer variation of ρ provides essentially a multiparameter fit, so that good agreement between theory and experiment does not assure meaningful theoretical numbers. Also, the inclusion of low- θ data down to $\sim 6^\circ$ could bring in errors due to roughness, refraction, or elastic scattering; it would be interesting to repeat the analysis for say $\theta \gtrsim 15-20^\circ$ to check self-consistency. Nonetheless, this general idea for trying to derive arbitrary monotonic profiles is promising and well worth further investigation.

As a final and even more complex type of concentration distribution, mention should be made of systems that may exhibit concentration gradients both laterally along the surface as well as inward from the surface. Thus in general the density will be given by $\rho(x,y,z)$. One important class of specimens exhibiting such character is supported heterogeneous catalysts, in which active metal atoms may reside within pores in the support, or may coalesce under sintering to form very small metal particles along the surface of the support. This complex concentration distribution, together with the generally very rough character of the support surface, will make any sort of angle-resolved measurement rather difficult to interpret unambiguously, for reasons we have discussed previously. However, fixed-angle intensity measurements, together with specialized models incorporating some of the ideas in the patched overlayer of Eqs. (10) and (11), have been used to derive useful information concerning atomic migration and particle sizes on heterogeneous catalysts, as discussed recently by Delgass and co-workers⁴⁹ and by Meisel et al.⁵⁰

G. Studies of surface-specific electronic structure changes

(i) Surface core-level shifts. ARXPS has also been used to verify that core-level binding energies of atoms in the outermost layer of a material can be shifted relative to the bulk. This effect was first unambiguously observed by Citrin et al.⁵¹, who used very high resolution (~ 0.25 eV) XPS to study the θ dependence of core levels in Au, Ag, and Cu. Some of their results are summarized in Fig. 22. For Ag and Cu there is little change with θ , but for Au, a shoulder grows in on the low-binding-energy side of the $4f_{7/2}$ peak for low θ . This is reminiscent of the discussion of the Si data in Fig. 8, and suggests a less-tightly-bound species near the surface. The Au data they have analyzed using a two-component model (i.e., a one-monolayer Au(surface) layer and Au(bulk)) with θ -dependent intensities given by Eqs. (4) and (5). This model is found to provide a self-consistent analysis of the data with a surface-to-bulk shift of 0.40 eV and a surface component localized entirely in the first atomic layer. Such

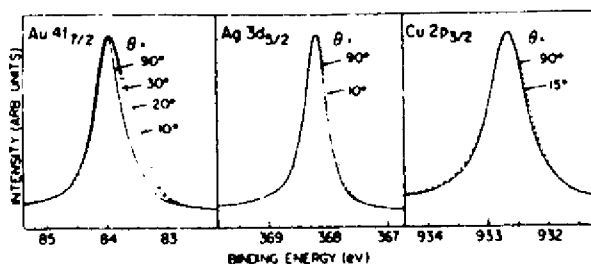


Fig. 22. The θ dependence of core line shapes from the noble metals Au, Ag, and Cu. For near-grazing emission, a shoulder is observed at lower binding energy for Au; this is interpreted as being due to a surface chemical shift of the $Au4f_{7/2}$ binding energy. (From Citrin and Wertheim, ref. (51).)

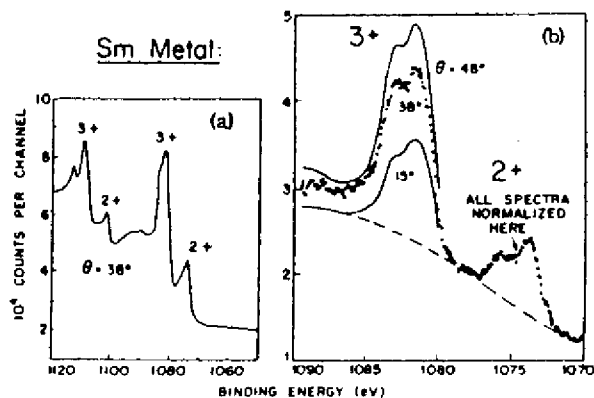


Fig. 23. The θ dependence of 3d core spectra from samarium metal. In (a), the overall 3d spectrum is shown, with both 3/2 and 5/2 regions exhibiting double peaks due to the presence of 3+ and 2+ configurations. In (b), the $3d_{5/2}$ region is shown at three different emission angles, with the 3+ peak being less important for grazing emission angles. (From Wertheim and Creelius, ref. (53).)

surface-layer chemical shifts have subsequently been confirmed for other metals in higher-resolution synchrotron radiation studies⁵². The Si data of Fig. 8 also represents a similar observation of a surface-specific core shift, in this case thought to be due to hydride formation²⁰.

Thus, although both of these examples have strained the resolution of the technique to its limits, the ability to vary angle has provided an absolutely essential feature in arriving at the final conclusions.

(ii) Surface valence-state alterations. A further surface-specific effect that has been detected in ARXPS is a change in the average valency of certain rare earth species near the surface. Wertheim and Creelius⁵³ first noted this effect for metallic Sm. This material is trivalent in the bulk, and exhibits corresponding multiplet splittings in both core and valence levels that can be used as fingerprints of this 3+ state. However, 2+ multiplets are also seen in the XPS spectra and they are found to increase in relative intensity as θ is decreased, as illustrated for the 3d core levels in Fig. 23. These data were successfully analyzed in terms of Eqs. (4) and (5), but with the added assumption that all Sm^{2+} was located in the first layer, although not all first-layer ions were Sm^{2+} .

(iii) Surface density-of-states changes. Inasmuch as the surface atoms of any material experience a different and usually lower coordination number in comparison to their bulk companions, it might be expected that the distribution of valence states in energy would also be different from the bulk. Such a difference, as measured by the density of states, has been predicted in numerous theoretical studies to occur on the surfaces of transition metals, where the general expectation is for a reduced d-band width as measured most accurately by the first moment of the d-band density of states⁵⁴.

One of the most convincing observations of such effects to date is based on ARXPS. Mehta and Fadley⁵⁵ studied clean polycrystalline surfaces of Cu and Ni, and for grazing emission found unambiguous narrowing of the second moment of the d band peaks by $\sim 19\%$ and 21% , respectively. Experimental data for Cu are shown in Fig. 24. Calculations were performed to simulate these effects by taking theoretical densities of states as computed for each layer⁵⁶ $\rho(E)_j$, $j = 1, 2, 3, \dots$ and summing them with allowance for inelastic scattering to yield a weighted density of states that should be seen in first order in the XPS measurement as:

$$\rho(E) = \sum_{j=1}^{\infty} \rho(E)_j \exp(-z_j/\lambda_e \sin\theta^j). \quad (21)$$

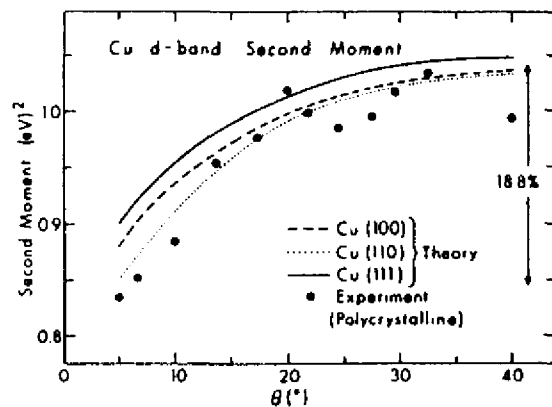


Fig. 24. Comparison of experimental and theoretical Cu 3d-band widths as a function of θ . The width is here measured using the second moment of the 3d intensity, although very similar results are obtained in using the FWHM. Theory is shown for the three lowest-index surfaces. (From Mehta and Fadley, ref. (55).)

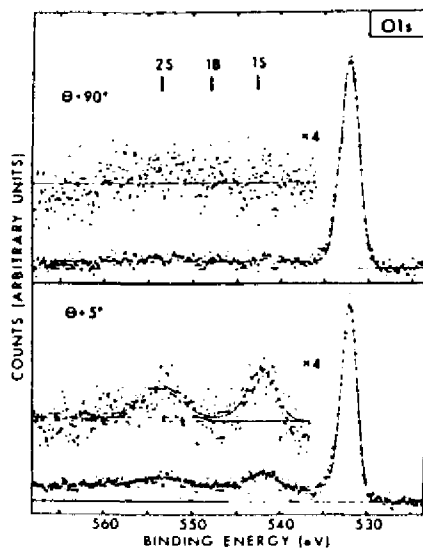


Fig. 25. Polar dependence of plasmon inelastic losses for O1s from oxygen adsorbed on a polycrystalline aluminum surface. The expected positions of bulk- and surface-plasmon loss peaks are also shown. (From Baird et al., ref. (57).)

Here, z_j is the depth of the j th layer and electron refraction has been allowed for in using θ' instead of θ . The curves calculated in this way for three low-index faces of Cu agree very well with the experimental curve, as shown in Fig. 24. The forms of the curves also agree for Ni, although theory predicts a larger effect than that observed. However, in view of the simple initial-state-only model used and the likely greater influence of many-electron effects in nickel d-band emission, the overall conclusion can certainly be made that these ARXPS results display surface d-band narrowing effects for both metals. The fact that decent agreement is obtained even at angles as low as $\theta=5^\circ$ also suggests that surface roughness may not be a major problem for very carefully prepared surfaces (In this case, the metals were deposited in situ on ultra-smooth glass substrates.)

Citrin et al.⁵¹ have subsequently used similar measurements on Au to isolate the surface and bulk components of the density of states, thus illustrating surface narrowing and other featural changes. The model used in analyzing this data is analogous to that described in Section 3.G(i) for surface core-level shifts. Their assumption that only the density of states of the first surface layer differs from that of the bulk deviates somewhat from theory, however,^{54,56} which suggests that the first 2-3 layers may differ. In any case, their results appear to be at least qualitatively correct.

Overall then, such ARXPS measurements have provided another type of information concerning the surface electronic structure of metals, and their application to other classes of materials should also be of interest.

(iv) Surface plasmon losses. A final effect that is of interest in connection with the enhanced surface sensitivity achievable at low θ is a change in the relative intensities of various inelastic loss processes. For example, for an atomically clean surface of aluminum (which exhibits well-defined surface- and bulk-plasmon excitations at different energies), it has been found by Baird et al.⁵⁷ that the surface plasmon losses are markedly enhanced in relative importance at low θ . The reason for this enhancement is that the surface- and bulk-plasmons are spatially orthogonal. Thus, because decreasing the angle of exit also decreases the mean depth of emission, the relative probability of exciting a surface plasmon is also increased at low exit angles. Comparisons of such data with theoretical calculations for a free electron metal furthermore yield good agreement with experimental relative intensities and further indicate that the creation of plasmons occurs by means of both extrinsic processes occurring after photoelectron excitation and intrinsic processes occurring during excitation⁵⁷. A further feature of such angular-dependent loss measurements that is of interest in

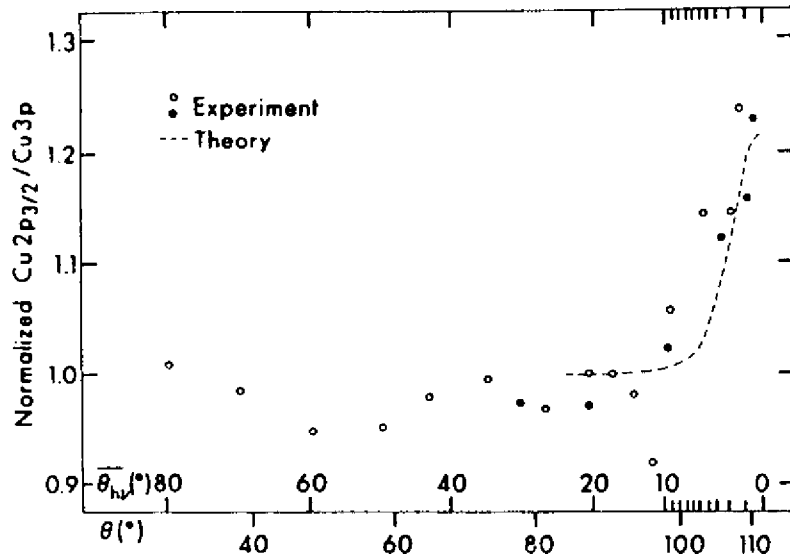


Fig. 26. Experimental and theoretical $\text{Cu}2p_{3/2}/\text{Cu}3p$ ratios for a smooth polycrystalline Cu specimen as a function of x-ray incidence angle $\theta_{\text{h}\nu}$. The $\text{Cu}2p_{3/2}$ intensity is enhanced in relative importance as $\theta_{\text{h}\nu}$ goes to zero due to its lower A_e value and the reduced x-ray penetration depth. (M. Mehta and C. S. Fadley, unpublished results.)

a surface-chemical sense is that they may be useful in determining the locations of adsorbed molecules relative to a surface as noted by Baird et al.⁵⁷ and Bradshaw et al.⁵⁸. Specifically, the O1s loss spectrum for an ~ 0.2 monolayer coverage of oxygen on aluminum exhibits only surface plasmon peaks at grazing electron exit, as shown in Fig. 25, thus suggesting that the oxygen has not penetrated significantly below the surface plane. Thus, the angular dependence of such adsorbate loss structures should provide useful complementary information concerning adsorption geometries and near-surface electronic structure.

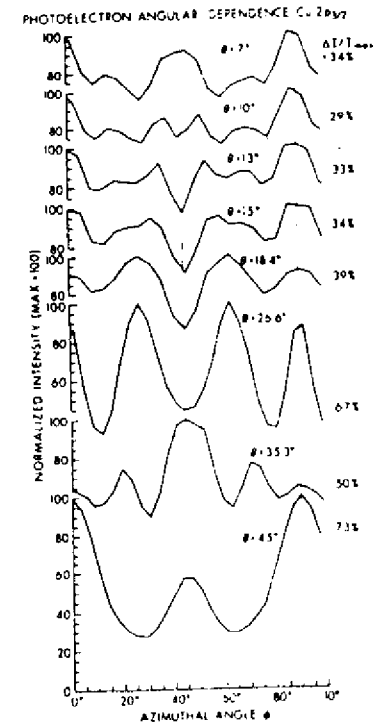


Fig. 27. Experimental azimuthal dependence of $\text{Cu}2p_{3/2}$ intensity above a $\text{Cu}(001)$ surface for 8 different polar angles of emission. The data have been fourfold-averaged into one quadrant from a full 360° scan, but no mirror symmetrization about $\phi = 45^\circ$ has been performed. Overall anisotropies $\Delta I/I_{\text{max}}$ are indicated as percentages. For certain θ values shown here, however (e.g., $\theta = 45^\circ$), it has subsequently been determined that a non-linearity in the vidicon multichannel detector used resulted in $\sim 1.5\times$ overestimates of the degree of an anisotropy. Compare the more accurate $\Delta I/I_{\text{max}}$ values at $\theta = 45^\circ$ of Fig. 31. (From Kono et al., ref. (63).)

4. Surface Sensitivity Enhancement at Grazing X-ray Incidence Angles

A second mechanism producing enhanced surface sensitivity involves measurements carried out at very low x-ray incidence angles θ_{hv} . For $\theta_{hv} \lesssim 1^\circ$, it was first noted by Henke²¹ that the mean x-ray penetration depth in a typical XPS experiment (which is a very large 10^3 - 10^5 Å for $\theta_{hv} \gg 1^\circ$) decreases markedly to values of the same order as the electron attenuation length λ_e . This further suggests that surface-atom signals will be enhanced in relative intensity at low θ_{hv} , as was first demonstrated by Mehta and Fadley⁵⁹. The reason for this decrease in x-ray penetration depth is the onset of significant refraction such that $\theta_{hv}' \ll \theta_{hv}$ (cf. Fig. 9) at the solid surface. The interactions of typical XPS x-rays with a homogeneous medium are furthermore well described by a macroscopic classical treatment,²¹ and detailed expressions for predicting penetration depths and expected surface sensitivity enhancements in terms of the material optical constants and other parameters have been presented elsewhere.^{5,21,59}

As a recent example indicating the surface sensitivity enhancement possible at low θ_{hv} , Fig. 26 shows data obtained from a clean polycrystalline Cu surface for which the $\text{Cu}2p_{3/2}/\text{Cu}3p$ ratio was measured as a function of the mean x-ray incidence angle $\bar{\theta}_{hv}$ ⁶⁰. Because the kinetic energy of the $\text{Cu}2p_{3/2}$ peak (549 eV) is much lower than that of the $\text{Cu}3p$ peak (1406 eV), its mean free path will be significantly lower. Thus, the mean depth of $2p_{3/2}$ emission will be less than that of $3p$ emission under normal circumstances of x-ray incidence, and any significant reduction in the x-ray penetration depth at low θ_{hv} will act preferentially to turn off more of the $3p$ signal. Therefore, the $\sim 25\%$ increase in the $\text{Cu}2p_{3/2}/\text{Cu}3p$ ratio noted for $\bar{\theta}_{hv} \approx 0^\circ$ is a clear indication of surface sensitivity enhancement. There is also good agreement between experiment and theoretical calculations including both refraction and reflection effects, as also shown in Fig. 26. Note the very sharp onset of the low- θ_{hv} enhancement over a region of only a few degrees near $\theta_{hv} = 0^\circ$. More pronounced effects have also been noted in the $\text{Cl}1s/\text{Au}4f$ ratio for Au with a carbonaceous overlayer⁵⁹, and in the $\text{Si}2p(\text{oxide})/\text{Si}2p(\text{element})$ ratio for silicon with varying oxide overlayer thicknesses.⁶¹ Also, the known optical properties of several solids at XPS energies of ~ 1.5 keV have been used to predict that such phenomena should be of very general occurrence.⁵

It should be noted in connection with such grazing-incidence studies, however, that surface roughness effects can be extremely important in any attempt at quantitatively analyzing such data.⁶¹ This is due to the very small incidence angles involved, so that if the true microscopic incidence angle θ_{hv}^t deviates by even $\sim 0.1^\circ$ from the macroscopically measurable θ_{hv} , a significant change occurs

in the degree of refraction and reflection. Thus, surface preparation and accurate angle measurement are both very critical. Further practical problems are that the x-ray source ought to have a very well defined direction of incidence ($\Delta\theta_{hv} \lesssim 1^\circ$ in Fig. 9) and that surface shading by any roughness present will generally act to much diminish absolute photoelectron intensities at low θ_{hv} . Thus, grazing-x-ray-incidence surface enhancements may serve as a useful complement to those at grazing electron emission, but the measurement and interpretation of the former data may not be as straightforward.

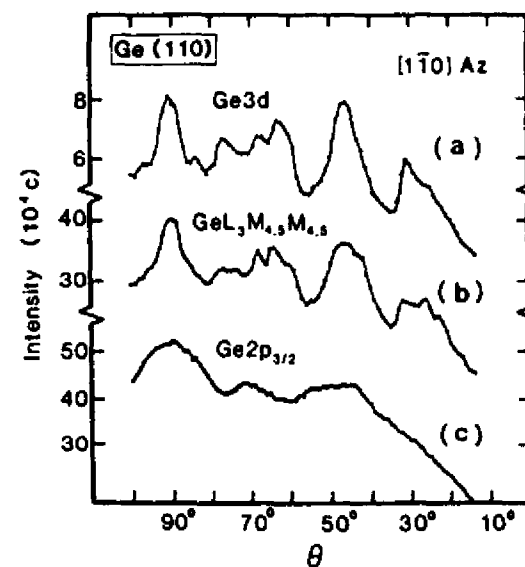


Fig. 28. Experimental polar dependence of Ge XPS and Auger intensities above a $\text{Ge}(110)$ surface for θ scans in a $(1\bar{1}0)$ azimuth. $\text{Ge}3d$ and $\text{Ge}2p_{3/2}$ XPS intensities are shown together with the $\text{Ge}L_3M_{4,5}M_{4,5}$ Auger intensity. No allowance has been made for the instrument response function. (From Owari et al., ref. (64).)

5. Core-Level Emission from Single Crystals:
X-ray Photoelectron Diffraction (XPD)

A. Introduction

In this section, we begin the consideration of effects observed in angle-resolved x-ray photoemission studies of highly-ordered single-crystal specimens. Here, emission from highly-localized, atomic-like core levels will be discussed; in Section 6 following, the more complex case of emission from delocalized valence levels will be considered. In both situations, a consideration of diffraction phenomena associated with the wave character of the emitted photoelectrons will prove essential for understanding the observed angular distributions. It is thus useful to immediately introduce the appropriate non-relativistic relationship between photoelectron wavelength λ_e and kinetic energy E_{kin} :

$$\lambda_e = h/[2mE_{kin}]^{1/2}, \quad (22)$$

where h = Planck's constant and m = the electron mass. In convenient units, this reduces to approximately

$$\lambda_e (\text{in } \text{Å}) = [150/E_{kin}(\text{in eV})]^{1/2}. \quad (23)$$

Thus the relevant wavelengths over the typical XPS range of energies of ~500-1500 will be from 0.55 Å at 500 eV to 0.32 Å at 1500 eV. The magnitude of the associated electron wave vector \vec{k} is in turn given by $k = 2\pi/\lambda_e$, and $\vec{k} = \vec{k}/k$.

In order to qualitatively introduce the different types of effects seen in such x-ray photoelectron diffraction (XPD) experiments, some typical experimental data are shown in Figs. 27-30⁶²⁻⁶⁴. These are illustrative of the various types of data which can be obtained, in that Figs. 27 and 28 both represent emission from core-levels in the single-crystal substrate (Cu with (001) orientation and Ge with (110) orientation, respectively), whereas Figs. 29 and 30 represent emission from species adsorbed on such a substrate ($c(2 \times 2)$ CO on Ni(001) and $c(2 \times 2)$ O on Cu(001), respectively). Also, two of the figures (27 and 30) represent azimuthal scans (cf. Fig. 2) whereas the other two (28 and 29) show polar scans.

From these figures, one can directly draw several useful qualitative conclusions: There are pronounced anisotropies in all of these photoelectron angular distributions. If the degree of anisotropy is measured as $(I_{max} - I_{min})/I_{max} = \Delta I/I_{max}$, we see that the values vary from as large as 73% for Cu2p_{3/2} substrate emission in Fig. 27 to as small as 6% for O1s adsorbate emission at large θ values in Fig. 30. There are also some rather narrow features in these angular distributions, with widths as small as ~4-5°, and this indicates the possible importance of having adequate angular resolution (as discussed further below). Not surprisingly, the patterns seen exhibit certain symmetries of the underlying substrate: for example, the azimuthal data of Figs. 27 and 30 for a Cu(001)

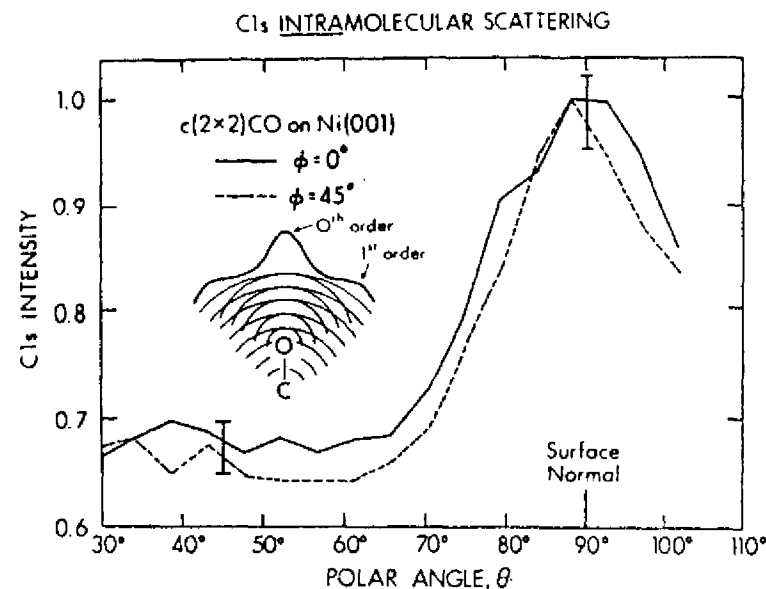


Fig. 29. Experimental polar dependence of the C1s intensity for a $c(2 \times 2)$ overlayer of CO on a Ni(001) surface. The data have been obtained in two symmetry-inequivalent azimuths. Also shown is a schematic illustration of the intramolecular scattering and diffraction producing such effects. (From Petersson et al., ref. (62) and Orders and Fadley, ref. (81).)

surface with C_{4v} symmetry exhibit near mirror symmetry about a $[110]$ azimuth for $\phi = 45^\circ$, a point we will amplify on below. The strongest substrate diffraction features are also most often seen along high-symmetry azimuths as well, and this suggests the possible use of such features for determining crystal orientations. Finally, if the substrate angular distributions of Fig. 28 are considered, it is clear that the lower-energy photoelectron peaks exhibit broader features than those at higher energy: specifically, the $\text{Ge}2p_{3/2}$ angular distribution at 270 eV has less fine structure than that of $\text{Ge}3d$ at 1457 eV. This last observation is a straightforward consequence of the change in de Broglie wavelength with energy, with shorter wavelengths at higher energies being capable of producing sharper diffraction features due to interference effects.

The previous point concerning the desirability of high angular resolution is further illustrated in Fig. 31, where experimental $\text{Cu}2p_{3/2}$ azimuthal data from $\text{Cu}(001)$ at a polar emission angle of 45° is shown for two different analyzer angular acceptances: cones with half angles of 4.5° and 1.5° . The angle steps used in accumulating the data were $\Delta\phi = 1.0^\circ$ for both cases. It is clear that the $\pm 1.5^\circ$ aperture yields data with considerably more fine structure, including some features of only a few degrees in width. Although most of these features can also be seen in the $\pm 4.5^\circ$ data, they are much easier to resolve in the $\pm 1.5^\circ$ curves. Thus the optimum use of XPD in deriving structural information will in many cases require instrumental angular resolutions of approximately $1-2^\circ$.

The azimuthal data of Figs. 27 and 30 further illustrate some important points concerning data analysis. The raw data of Fig. 30 for O1s emission from $c(2 \times 2)0$ on $\text{Cu}(001)$, which is shown as dashed curves, has been obtained by scanning over a full 360° in azimuth. Thus, in view of the C_{4v} symmetry of the surface, there is redundancy in the data that can be used to average out noise and to check for the reliability of various features. One useful method is to fourfold average such data by adding the points at ϕ , $\phi+90^\circ$, $\phi+180^\circ$, and $\phi+270^\circ$, thus partially accounting for the known symmetry associated with the surface; in general, this averaging reduces the anisotropy $\Delta I/I_{\text{max}}$. Subtracting off the minimum intensity and replotting then yields the "flower" patterns shown as solid curves. These can in turn be compared with the raw data to be sure that all features present in the fourfold-averaged data are consistent with similar features in each quadrant of the raw data. Any misalignment of the azimuthal rotation axis with respect to the $[001]$ surface normal also becomes very evident in such comparisons. Finally, since the symmetry operations of mirror reflection across $\phi=0^\circ$, 45° , etc. have not been included in the fourfold averaging, the presence or absence of such mirror symmetry can be used to judge feature accuracy and overall statistical reliability. For example, in Fig. 27, such fourfold-averaged data for $\text{Cu}2p_{3/2}$

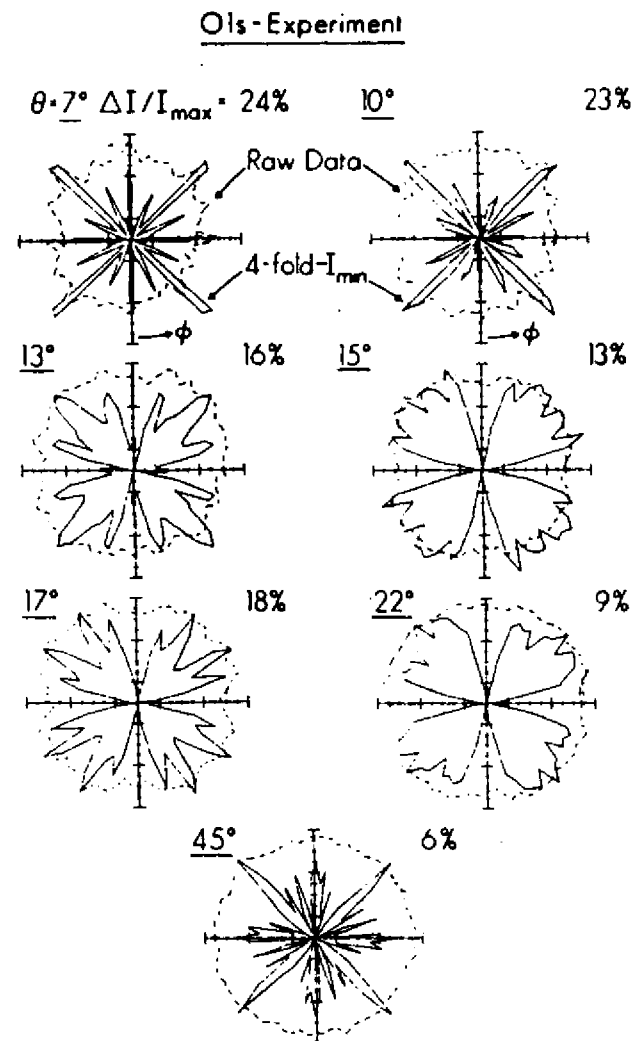


Fig. 30. Experimental azimuthal dependence of the O1s intensity for a $c(2 \times 2)$ overlayer of oxygen on a $\text{Cu}(001)$ surface. Seven different polar angles of emission are shown. Both the raw data of a full 360° scan and fourfold-averaged data from which the minimum intensity has been subtracted are shown. The overall anisotropies $\Delta I/I_{\text{max}}$ are also indicated for each set of fourfold-averaged data. (From Kono et al., ref. (63).)

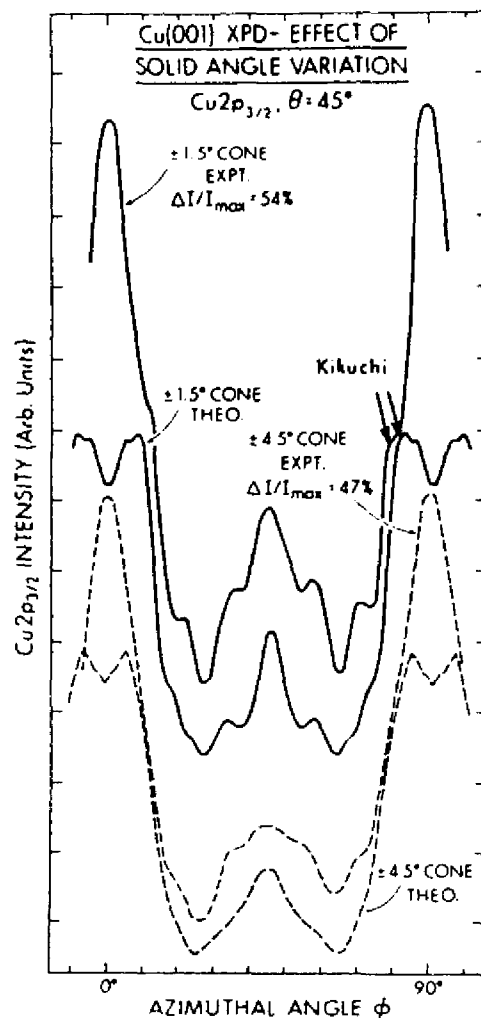


Fig. 31. Effect of analyzer solid angle variation on the experimental and theoretical azimuthal dependences of the Cu₂p_{3/2} intensity observed at 45° above a Cu(001) surface. Curves are shown for both a ±1.5° cone of acceptance solid angle and a ±4.5° cone of acceptance. The theoretical curves are based on the single-scattering cluster model. (R. C. White, B. Sinkovic, P. J. Orders, and C. S. Fadley, unpublished results.)

emission from Cu(001) is plotted in Cartesian form and is found to be very close to mirror symmetric about $\phi = 45^\circ$. Other forms of azimuthal data averaging would be appropriate for surfaces with different symmetry (as a three-fold (111) surface or the stepped surfaces to be discussed in Sec. 5.E.), but in general it seems to be very useful to obtain the fullest angle scans possible to enable carrying out such analyses. Similarly, doing symmetry-equivalent polar scans (e.g., at $\phi = 0^\circ, 90^\circ, 180^\circ, 270^\circ$ for a fourfold surface) and averaging these to check orientational accuracy and reduce spurious intensity variations is also very useful.

It is also worthwhile to note here that the typical mean free paths for inelastic scattering in XPS of $\sim 10\text{-}30 \text{ \AA}$ imply that all of the features seen in Figures 27-30 must be associated with atomic order very near the surface. In fact, we have found in general that the type of surface pre-treatment utilized (for example, as to times and temperatures for ion bombardment and annealing) can have a dramatic effect on the degree of anisotropy found, even when simultaneous observation with low energy electron diffraction (LEED) shows very little visual difference in the sharpness of a pattern for different pre-treatment procedures. Thus, such XPS measurements seem to be very sensitive and quantitative indicators of the degree of near-surface order.

Before proceeding to a more quantitative discussion of these effects, we consider a few examples of how such x-ray photoelectron diffraction patterns can be used in more or less a fingerprint fashion to derive very useful information. First, the fact that substrate photoelectron emission along low-index directions in the crystal is generally associated with pronounced peaks in the XPD pattern can be used to carry out very precise crystal orientations *in situ*. (This peaking along low-index directions can be qualitatively explained in terms of Kikuchi bands associated with different sets of low-index planes⁶⁵, as discussed in more detail in Section 5.8.) For example, in our laboratory, the polar- and azimuthal-orientations of (001)-metal crystals are routinely determined to within $\pm 0.5^\circ$ by using a combination of polar scans through the [001] surface normal and azimuthal scans through a series of $\langle 110 \rangle$ directions at 45° with respect to the normal. For single crystals containing more than one type of atom, a second type of information concerns the nature of the crystal site in which a given substrate atom is sitting: for example, is it in well-defined lattice sites, has it been interstitially incorporated, or has it been randomly incorporated with respect to the other atoms of the lattice? This use of XPD was first made for a Au/Ag alloy by Fadley and Bergstrom³. Some more recent XPD data obtained by Thomas and co-workers⁶⁶ from a single crystal of the mineral muscovite are shown in Figure 32. Here, polar scans of different peak intensity ratios are shown. These have been analyzed by noting that photoelectrons arising from two atoms occupying

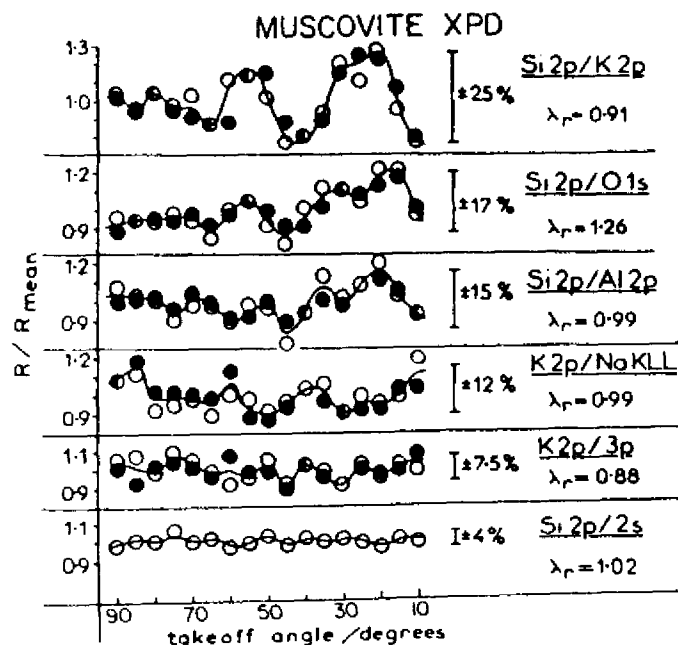


Fig. 32. Experimental polar dependence of normalized core intensity ratios for different peaks resulting from a single crystal of the mineral muscovite ($(KAl_2)(Si_3Al)O_{10}(OH)_2$). The full range of excursion is indicated as a percentage, and λ_r denotes the ratio of de Broglie wavelengths of the two peaks involved in a given ratio. (From Adams, Evans, and Thomas, ref. (66).)

exactly the same type(s) of lattice site(s) in the crystal should show exactly the same XPD pattern, as long as their de Broglie wavelengths are not different by more than $\sim 30\%$; thus, their normalized ratio should be very near unity regardless of polar angle. This is trivially the case for the $K2p/K3p$ and $Si2p/Si2s$ ratios arising in a single atom. By contrast, photoelectrons arising from atoms with very different sites should exhibit the greatest excursions from unity, as for the $\sim 25\%$ deviations in the $Si2p/K2p$ ratio; this is consistent with the known structure of this mineral. The reduced value of the $Si2p/Al2p$ excursions of $\pm 15\%$ (as compared, for example to $Si2p/K2p$) is furthermore suggestive of some Al in stoichiometric excess of that needed to occupy normal octahedral sites going into tetrahedral sites that are predominantly Si. As a second example of site-type determination, Fig. 33 shows polar-scan data obtained by Nihei et al.⁶⁷ for a Au overlayer of $\sim 85 \text{ \AA}$ thickness grown onto a (110) surface of GaSb. With annealing at 400°C only, the Au4f XPD pattern is relatively featureless, suggesting an amorphous overlayer, whereas both the Ga3d and Sb4d patterns exhibit considerable fine structure. After annealing at 540°C , however, the Au4f pattern becomes very nearly identical to the Ga3d pattern; as these two peaks are furthermore very close in kinetic energy, it is thus suggested that Au has preferentially displaced Ga in the GaSb lattice. This kind of atom-specific order and site information would be difficult to obtain in any other way.

As a final introductory comment, we note that Liebsch⁶⁸ first pointed out from a theoretical point of view how adsorbate core-level photoelectron diffraction might be used to determine surface structural information. This work involved multiple-scattering theory for low energies as appropriate to an ARUPS experiment.

B. The single-scattering cluster (SSC) model

In discussing more quantitatively such XPD effects, it is necessary to introduce a more detailed model of the scattering and interference phenomena that are expected to occur for photoelectrons in the ~ 500 - 1500 eV energy regime. Such a model can be formulated at varying levels of complexity from a straightforward single-scattering or kinematical approach^{62,63,69} to more complex dynamical treatments incorporating some degree of multiple scattering^{68,70,71}. Fortunately, we have found that a very simple single-scattering model as applied over a finite cluster of atoms appears to very well describe most of the features in XPD^{62,63,69}, and it is thus this approach that will be discussed below.

The essential elements of this single-scattering cluster (SSC) model are shown schematically in Fig. 34. The basic assumptions are essentially identical to those used in describing extended x-ray absorption fine structure (EXAFS)^{72,73} and a similar model has also been applied (although rather unsuccessfully) to angle-

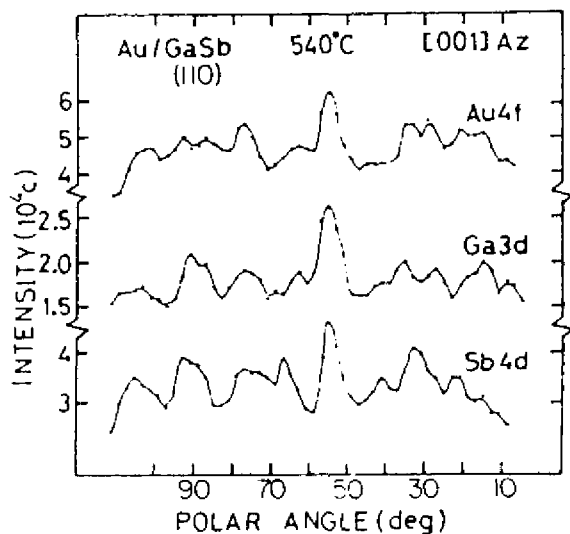
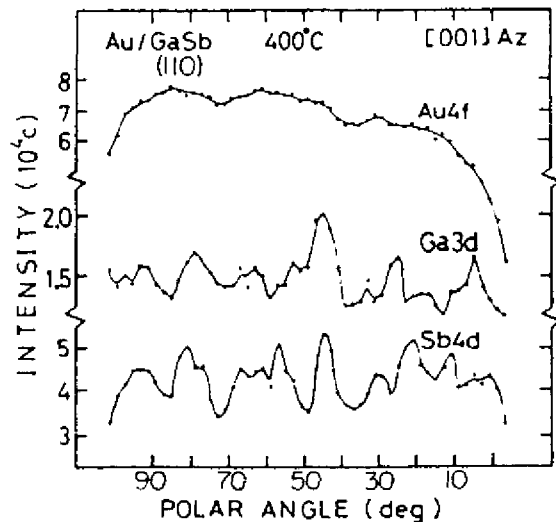


Fig. 33. Experimental polar dependence of the Au4f, Ga3d, and Sb4d peaks resulting from a Au overlayer of approximately 85Å thickness on a GaSb(110) surface. Scanning was in a [001] azimuth, and results for two different annealing temperatures of 400° and 540° are shown. Note the strong similarity of the Au4f and Ga3d curves after the higher temperature anneal. (From Koshizaki et al., ref. (67).)

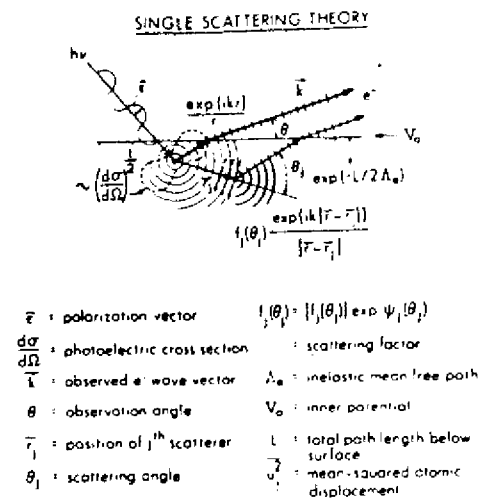


Fig. 34. Schematic illustration of the assumptions used in the single scattering cluster (SSC) model, with various important quantities defined.

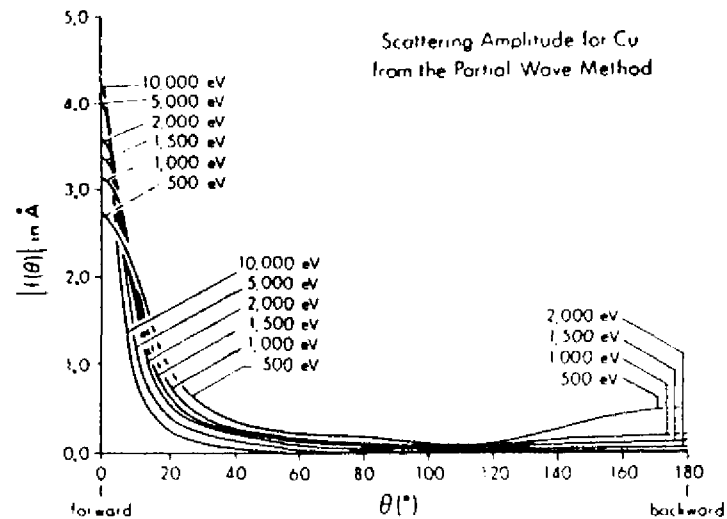


Fig. 35. The magnitude of the atomic scattering factor $|f(\theta)|$ for Cu as a function of scattering angle θ for various electron kinetic energies from 500 to 10,000 eV. Note the enhanced forward peaking as energy increases, and the concomitant decrease in the importance of any backscattering. (From Thompson, ref. (80).)

resolved Auger emission at very low energies of $\lesssim 100$ eV⁷⁴. The SSC model as appropriate to XPD is discussed in more detail elsewhere^{62,63}, so that only the essential assumptions and mathematical results will be outlined here.

Radiation with polarization $\hat{\epsilon}$ is incident on some atom in the cluster, from which it ejects a core-level photoelectron. (In Fig. 34, the emitting atom is shown near the surface, but it could as well be any atom in the substrate.) The problem is then to describe the single scattering of this wave from all other atoms j in the cluster, keeping track of the phase shifts introduced by both the scattering and path length differences and finally to sum the wave amplitudes so produced to yield the total photoelectron amplitude. Squaring this amplitude then yields the intensity expected in a given emission direction, as denoted by the wave vector \vec{k} . That is, if $\phi_0(\vec{r}, \vec{k})$ is the photoelectron wave at \vec{r} as emitted directly into direction \vec{k} and $\phi(\vec{r}, \vec{r}_j, \vec{k})$ is the wave resulting from initial ϕ_0 emission toward a scatterer j at \vec{r}_j and then subsequent scattering so as to emerge from the surface in the direction of \vec{k} , the overall wave amplitude will be given by

$$\psi(\vec{r}, \vec{k}) = \phi_0(\vec{r}, \vec{k}) + \sum_j \phi_j(\vec{r}, \vec{r}_j, \vec{k}) \quad (24)$$

and the photoelectron intensity by

$$I(\vec{k}) \propto |\psi(\vec{r}, \vec{k})|^2 \quad (25)$$

Because the detector is situated at essentially $\vec{r} = \infty$ along \vec{k} , all of the waves in (24) can finally be taken to have the limiting spherical forms $\phi_0 \propto \exp(ikr)/r$ or $\phi_j \propto \exp(ik|\vec{r}-\vec{r}_j|)/|\vec{r}-\vec{r}_j|$, although the actual amplitudes of each type in a given direction will be modulated by the photoexcitation matrix element and, for the ϕ_j 's, also the scattering cross section. It is further assumed that the portion of ϕ_0 which passes to the scatterer j to produce ϕ_j also decays in amplitude according to a spherical wave assumption, or as $1/r_j$. If the scattering angle is θ_j , the overall path length difference between ϕ_0 and ϕ_j is then $r_j(1-\cos\theta_j)$.

The directional modulation of the initial photoelectron wave ϕ_0 would most accurately be treated by considering both the $l+1$ and $l-1$ components produced in a dipole excitation from an $n\ell$ subshell, and determining the matrix element involved⁷⁰⁻⁷². Fujikawa, for example, has recently discussed this approach⁷¹. For the special case of ns emission, however, this reduces simply to an $\hat{\epsilon}\cdot\vec{k}$ dependence²⁵, and it is this form that has been used in most prior XPD analyses^{63,69}. Since the differential photoelectric cross section $d\sigma_{n\ell}(\hat{\epsilon}, \vec{k})/d\Omega$ is proportional to intensity rather than amplitude, another approximation would be to use a ϕ_0 modulation of $[d\sigma_{n\ell}(\hat{\epsilon}, \vec{k})/d\Omega]^{1/2}$ ⁶⁴. Although this is not strictly correct and does not account for possible sign changes in the

matrix element with direction due to the photoelectron parity⁷⁵, it is probably an adequate approximation for XPD in which the electron scattering process will be seen to select out \vec{r}_j choices very nearly parallel to \vec{k} ; that is, for the range of \vec{r}_j directions near the \vec{k} direction that produce significant scattering, the matrix element varies little, so that a very precise description of it is not required. In fact, predicted XPD patterns have not been found to be very sensitive to the exact way in which the matrix-element modulation is included, particularly as regards averaging over $\hat{\epsilon}$ in an unpolarized source^{62,63}. We shall thus use the simple $\hat{\epsilon}\cdot\vec{k}$ form in what follows.

The electron-atom scattering that produces ϕ_j is assumed to be adequately described by a complex scattering factor

$$f_j(\theta_j) = |f_j(\theta_j)| \exp[i\psi_j(\theta_j)], \quad (26)$$

where $\psi_j(\theta_j)$ is the phase shift associated with the scattering. The scattered wave ϕ_j is thus proportional to $f_j(\theta_j) \exp[ik|\vec{r}-\vec{r}_j|/|\vec{r}-\vec{r}_j|]$, with an overall phase shift relative to ϕ_0 of $kr_j(1-\cos\theta_j) + \psi_j(\theta_j)$ that is due to both path length difference and scattering. The use of this form for ϕ_j implicitly assumes that the portion of ϕ_0 incident on the j th scatterer has sufficiently low curvature compared to the scattering potential dimensions to be treated as a plane wave. This is the so-called "small-atom" approximation⁷⁶, and it should be fully adequate in XPD for all but perhaps the nearest-neighbor atoms to the emitter. Even for such nearest-neighbor atoms, the only effect of inclusion of ϕ_0 curvature will probably be to somewhat reduce the amplitudes of certain forward-scattering peaks in $I(\vec{k})$ in comparison to those predicted with the use of Eq. (26)⁷⁷, so that its neglect should not be serious. A further important point here is that, as energy is increased, the region of the potential well that is effective in the scattering is reduced in diameter, so that the small-atom approximation should because of this be more valid than prior criteria⁷⁶ might indicate.

The scattering factor $f_j(\theta_j)$ is most accurately determined by applying the partial-wave method to a suitable spherically symmetric-scattering potential for each atomic type in the cluster. The number of partial-wave phase shifts needed goes up with energy, and for a typical scattering potential of effective radius 1.5 Å, would be $\lambda/8$ for $E_{\text{kin}} = 500$ eV and $\lambda/24$ for 1500 eV. Tabulations of free-atom scattering factors at energies spanning the XPS regime exist⁷⁹. Alternatively, scattering potentials more appropriate to a cluster of atoms with overlapping charge densities and potentials can be constructed via the muffin-tin model employed, for example, in LEED^{41,42}. The free-atom f_j 's generally are larger in magnitude than their muffin-tin counterparts due to their neglect of charge and potential overlap^{62,63}. Both types of f_j 's have been employed in XPD calculations, and they do not yield significantly different $I(\vec{k})$ curves, although

the use of free atom f_j 's might be expected to predict slightly higher peak intensities due to their larger amplitudes. In the limit of very high energy, the use of the first Born approximation⁷⁸ for determining scattering factors might also be expected to be adequate. However, recent studies by Goldberg, Thompson et al. have shown that the Born approximation is not sufficiently accurate for XPD calculations at $\lesssim 5$ keV^{63,80}.

Some typical scattering factor amplitudes and phase shifts for Cu are shown in Figs. 35 and 36. These curves and other available data⁷⁹ show that, over the typical energies in XPS of ~ 500 - 1500 eV, the amplitude $|f_j(\theta_j)|$ is very strongly peaked in the forward direction or near $\theta_j = 0^\circ$, with a FWHM of only ~ 10 - 30° . This forward peaking is even more pronounced at higher energies, as illustrated in Fig. 35. The only other appreciable scattering strength occurs near $\theta_j = 180^\circ$, but this is down by roughly an order of magnitude in comparison to the forward scattering peak. At higher energies, the back scattering peak is reduced even further, essentially disappearing at $10,000$ eV. Considering the phase shifts in Figure 36 and other available data⁷⁹ also permits concluding that for XPD, ψ_j is rather small ($\lesssim 30$ - 50°) for the θ_j region in which $|f_j|$ is large. Thus, for electron elastic scattering in XPD from atoms of low- to moderate- atomic number, the scattered waves ϕ_j are expected to be significant only for θ_j rather near zero, and in this case the scattering phase shift will also be rather small. (The optical theorem prevents ψ_j from being exactly zero unless the total scattering cross section is also zero⁷⁸.) For substrate-atom emission from well below the surface, the condition of near-forward scattering from neighbors above is geometrically possible for emission into a large number of directions \vec{k} above the surface. However, for adsorbates or near-surface substrate atoms, observation at special emission directions may be necessary to see significant XPD. This is why, for example, most of the polar angles θ in Fig. 30 are near-grazing with respect to the surface. It also explains why the anisotropy in Fig. 30 falls off as the polar angle is increased away from the surface, becoming almost undetectable at $\theta = 45^\circ$.

The effects of inelastic scattering on wave amplitudes during propagation below the surface must also be included. Intensity falls off as $\exp(-L/\Lambda_e)$, where L is an arbitrary path length, so that amplitude is expected to fall off as the square root of this or $\exp(-L/2\Lambda_e) \equiv \exp(-\gamma L)$. Thus, $\gamma = 1/2\Lambda_e$, although γ values up to ~ 2 - 3 times this have been suggested in prior EXAFS⁷² and Auger⁷⁴ analyses. Each wave ϕ_0 or ϕ_j can thus be multiplied by such a factor involving an L value which includes the total path length below some surface cutoff point. This surface cutoff is usually chosen to be the substrate surface as defined by hard-sphere atoms^{62,63}, although the exact choice is not found to influence the XPD patterns

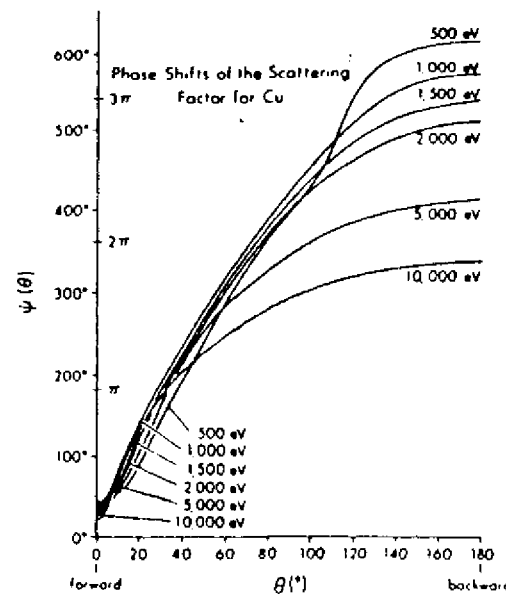


Fig. 36. The phase shift $\psi(\theta)$ for Cu as a function of scattering angle θ for various electron kinetic energies from 500 to $10,000$ eV. (From Thompson, ref. (80).)

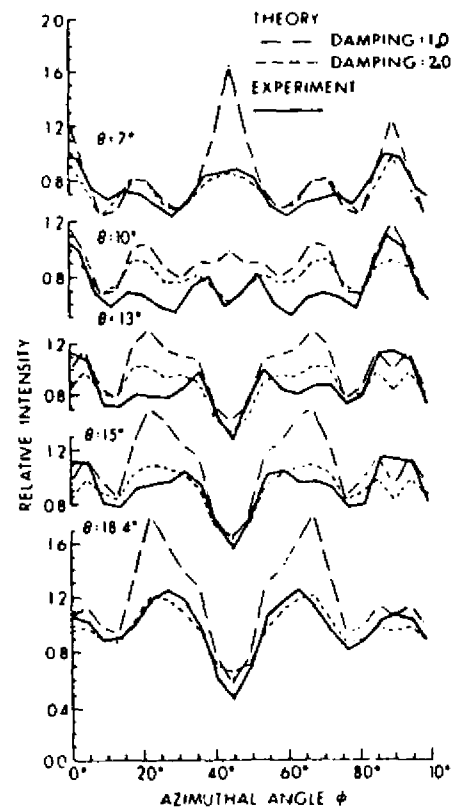
PHOTOELECTRON ANGULAR DEPENDENCE: $\text{Cu } 2p_{3/2}$ 

Fig. 37. Comparison of experiment and single-scattering cluster (SSC) theory for the azimuthal dependence of $\text{Cu } 2p_{3/2}$ emission from $\text{Cu}(001)$ at various polar angles between 7° and 18.4° . The notation damping = 1.0 refers to the use of $|f_j(\theta)_j|$ values with no empirical reduction factor, whereas damping = 2.0 refers to the use of values reduced by $\frac{1}{2}$ to optimize agreement with experiment. Note that the only significant changes produced by the use of such damping are for two fine structure features near $\phi = 45^\circ$ and for $\theta = 7^\circ$ and 10° . (From Kono et al., ref. (63).)

significantly. Λ_e values can be taken from prior experimental or theoretical tabulations, but it is found that this choice also is not critical: for example, Λ_e for Cu has been varied by $\approx 25\%$ without changing the substrate XPD patterns significantly^{62,63}.

Vibrational attenuation of interference effects is furthermore potentially important, and can be included in a standard way by multiplying each ϕ_j by its associated temperature-dependent Debye-Waller factor:

$$W_j(T) = \exp[-\Delta k^2 U_j^2(T)] = \exp[-2k^2(1-\cos\theta_j)U_j^2(T)] \quad (27)$$

where Δk is the magnitude of the change in wave vector produced by the scattering, and $U_j^2(T)$ is the temperature-dependent one-dimensional mean-squared vibrational displacement of atom j with respect to the emitter. At this level of approximation, U_j^2 is assumed to be isotropic in space and any correlations in the movements of near-neighbor atoms are neglected. U_j^2 values can be obtained from, for example, LEED analyses^{62,63}. However, the fact that the electron scattering is significant only when θ_j is rather close to zero acts through the $(1-\cos\theta_j)$ factor in the argument of Eq. (27) to yield W_j 's very close to unity for all important scattered waves. Thus, the U_j^2 values chosen for Cu can in fact be increased by a factor of four without appreciably altering the $I(\vec{k})$ curves⁶³. So, vibrational effects are to first order not very important in forward-scattering dominated XPD, although they are, for example, very important in LEED, EXAFS, and normal photoelectron diffraction where back scattering is the dominant diffraction mode (and thus $\theta_j \approx 180^\circ$). An alternate method for allowing for vibrational effects is to assume some probability distribution of atomic positions due to vibration (as, for example, a harmonic oscillator envelope) and then to sum separate weighted diffraction intensities for all possible combinations of atomic positions. This is cumbersome, but it has been used to quantitatively look at the effects of specific types of molecular vibrations at surfaces^{77,81}.

The expression for intensity $I(\vec{k})$ can now be written down directly as:

$$I(\vec{k}) = \int \left[\hat{e} \cdot \hat{k} e^{-\gamma L} + \sum_j \frac{\hat{e} \cdot \hat{r}_j}{r_j} |f_j(\theta_j)| W_j e^{-\gamma L_j} \exp[i[kr_j(1-\cos\theta_j) + \psi_j(\theta_j)]] \right]^2 d\hat{e} \\ + \sum_j \int (\hat{e} \cdot \hat{r}_j)^2 \frac{|f_j(\theta_j)|^2}{r_j^2} (1-W_j^2) e^{-2\gamma L_j} d\hat{e}. \quad (28)$$

Here, $\hat{e} \cdot \hat{k}$ and $\hat{e} \cdot \hat{r}_j$ represent photoemission matrix-element modulations along the unit vectors \hat{k} and \hat{r}_j , respectively, and $\exp(-\gamma L)$ and $\exp(-\gamma L_j)$ are appropriate inelastic attenuation factors. Thus, $(\hat{e} \cdot \hat{k}) \exp(-\gamma L)$ is the amplitude of the direct wave $\phi_0(\vec{r}, \vec{k})$ and $(\hat{e} \cdot \hat{r}_j) |f_j(\theta_j)| W_j \exp(-\gamma L_j) / r_j$ is the effective amplitude

of $\phi_j(\vec{r}, \vec{r}_j - \vec{k})$ after allowance for both inelastic scattering and vibrational attenuation of interference. The complex exponential allows for the total final phase difference between ϕ_0 and each ϕ_j . The integrals on \hat{e} simply sum over different polarizations perpendicular to the radiation propagation direction, as appropriate to the usual case of a largely unpolarized x-ray source in XPS. The second \int corrects the first absolute value squared for the incorrect inclusion of j

Debye-Waller attenuations in terms involving a product of a scattered wave with itself. That is, in expanding the absolute value squared, only products involving unlike waves as $\phi_0 \phi_j^*$ or $\phi_j \phi_\ell^*$ ($j \neq \ell$) should include Debye-Waller products of W_j or $W_j W_\ell$, respectively. The $(1-W_j^2)$ factor in the second summation is thus necessary to yield overall correct products of the form $\phi_j \phi_j^*$ without any W_j^2 factor. The second sum is termed the thermal diffuse scattering term and it is usually quite small with respect to the overall XPD modulations, because, as we have already noted, W_j is very close to unity for all strong scatterers. Eq. (28) is thus the basic starting point of the single scattering cluster model. It is also worth noting here that such a cluster sum makes no explicit use of the 2- or 3- dimensional translational periodicities that may be present, even though the atomic coordinates \vec{r}_j used as inputs may incorporate such periodicities. Thus, neither surface- nor bulk- reciprocal lattice vectors are explicitly involved, and it makes no sense at this level of description to speak of diffraction "beams" associated with certain \vec{g} 's as in LEED.

Averaging over a totally unpolarized source leads to a more complex expression for $I(\vec{k})$ in terms of various geometric angles, but it can be shown that the strong forward peaking in $f_j(\theta_j)$ permits using the following relatively simple expression^{62,63}:

$$I(\vec{k}) \propto I_0 + \sum_j I_j W_j \exp\{i[kr_j(1-\cos\theta_j) + \psi_j(\theta_j)]\}^2 + \sum_j I_j^2 (1-W_j^2), \quad (29)$$

where θ_k or θ_{r_j} are the angles between the direction of radiation propagation and \vec{k} or \vec{r}_j , respectively, and I_0 and I_j are defined as

$$I_0 = \sin^2 \theta_k \exp(-\gamma L)$$

$$I_j = \sin^2 \theta_{r_j} |f_j(\theta_j)|^2 \exp(-\gamma L_j) / r_j^2.$$

That is, in averaging over \hat{e} , $\hat{e} \cdot \hat{k}$ and $\hat{e} \cdot \hat{r}_j$ by $\sin \theta_k$ and $\sin \theta_{r_j}$. It is this result that has been used in most XPD calculations to date.

The last parameter of importance in actually using Eqs. (28) or (29) is the range of j or the choice of a suitable cluster of atoms. This is done empirically so as to include all significant scatterers by verifying that the predicted XPD patterns do not change in any significant way with the addition of further atoms at the periphery of the cluster. The inherent weakness of all scattering events

for which θ_j is appreciably different from zero tends to limit cluster sizes in most cases. They thus can range from 2 atoms for near-normal emission from a vertically oriented diatomic molecule on a surface⁷⁷ to as many as several hundred atoms for substrate emission in which both the emission and scattering must be summed over several layers into the bulk^{62,63}. However, even for the largest clusters so far considered, the inherent simplicity of Eqs. (28) and (29) still yields calculations which do not consume excessive amounts of computer time, especially by comparison with those necessary for LEED or UPS simulations.

A further physical effect of importance in making comparisons to experiment is the possibility of electron refraction at the surface, as discussed previously in Section 3.C. Fig. 14 indicates that, even at the relatively high energies of XPS, for emission near grazing, angle changes $\theta' - \theta$ of a few degrees can be produced by refraction. Thus, especially for adsorbate studies such as that shown in Fig. 30, a proper allowance for refraction is necessary, at least for θ values $\lesssim 10^\circ$. This is done by using a suitable inner potential V_0 derived from experiment and/or theory and Eq. (19) to predict θ' for a given internal propagation direction θ' . In the presence of an adsorbate, the exact form of the surface potential barrier thus becomes important, as it may not then be possible to assume an abrupt rise to the vacuum level at the substrate surface. Also, the presence of adsorbate atoms may alter V_0 through changes in the work function, and these atoms also may occupy positions above the surface in which only a fraction of V_0 is appropriate. Although a prior study of O on Cu(001) indicates that the predicted XPD results are not particularly sensitive to the choice of V_0 ^{62,63}, it is important to realize that not properly allowing for it may shift theoretical XPD patterns by as much as a few degrees with respect to the actual θ values at which they will be observed.

A final step in any realistic calculation based upon this model is to integrate the direction of emission \vec{k} over the solid angle Ω_0 accepted into the electron analyzer^{62,63}. For most of the calculations reported here, this has been over a cone of ± 3.0 - 3.5° half angle, although for certain cases a smaller cone of $\pm 1.5^\circ$ has been used.

There are several reasons, however, why the XPD effects predicted by such SSC calculations are from the outset expected to be larger in amplitude than those observed experimentally. (This is a common type of discrepancy in other diffraction calculations as well, as, for example, in LEED.) These have been discussed previously in connection with XPD⁶³, and are: (1) The actual surface may have irregularities on an atomic scale that are not included in the usually idealized model cluster. Also, adsorbates may exhibit more than one type of bonding site, especially if unobserved steps or dislocations are present on the surface to

some degree. These effects will in general tend to average out XPD effects in experimental data relative to a highly ideal calculation. (2) The lack of a fully-converged cluster of atoms in the calculations would also tend to produce greater anisotropy, as atoms near the periphery of a larger cluster add so as to produce a nearly isotropic background. (3) The inclusion of spherical-wave character for nearest-neighbor scattering will qualitatively tend to reduce the scattering strength, at least in the forward direction. This effect has been quantitatively estimated in XPD calculations for Cls emission from molecular CO, where it appears to reduce the forward scattering diffraction peak by about 1/2 as measured with respect to the background intensity^{77*}. (4) Vibrational effects, especially at a surface or for an adsorbate, may not be adequately described by simple Debye-Waller factors, and lead to enhanced suppression of XPD features. (5) Multiple-scattering effects also may be present to some degree, and these would generally be expected to smear out some features. (6) The presence of a non-isotropic inelastic scattering mechanism (for example, associated with excitations of rather localized valence electrons) also could reduce the relative intensities of diffraction features. Such phenomena have been noted as a source of reduced diffraction effects in EXAFS back scattering, for example, although it appears that for forward scattering the optical theorem⁷⁸ will require an increase in $|f_j|$ due to inelastic processes⁸². Such effects need to be further investigated for forward scattering at the $\sim 10^3$ eV energies appropriate to XPS. The last four of these effects thus need to be explored in further theoretical treatments of XPD, but we shall show that the much simpler SSC model not incorporating them still seems to describe the observed experimental phenomena rather well.

As a final comment concerning the SSC model, we note that it can be directly reduced to an expression very close to that used in EXAFS analyses⁷² if it is assumed that all scattered waves ϕ_j are small in magnitude in comparison to ϕ_0 . Then, if we begin at Eq. (28) (for simplicity neglecting any averaging over $\hat{\epsilon}$), we see that all terms such as $\phi_j \phi_k^*$ and $\phi_j \phi_j^*$ can be neglected in expanding the absolute value squared. The thermal diffuse scattering term thus can also be neglected. After some simple algebra, it can then be shown that

$$I(\vec{k}) = (\hat{\epsilon} \cdot \vec{k})^2 e^{-2\gamma L} + 2(\hat{\epsilon} \cdot \vec{k}) e^{-\gamma L} \sum_j \frac{\hat{\epsilon} \cdot \vec{r}_j}{r_j} |f_j(\theta_j)| W_j e^{-\gamma L_j} \times \cos(kr_j(1 - \cos\theta_j)) + \psi_j(\theta_j). \quad (30)$$

This simplified form has in fact been used recently by Orders and Fadley in successfully describing several aspects of normal photoelectron diffraction data⁸³.

*This factor of approximately 0.4-0.5 for nearest-neighbor scattering has also been verified in recent much more detailed XPD spherical-wave calculations by Sagurton, Bullock, and Fadley (to be published).

In subsequent sections, we will consider several applications of this SSC model to the interpretation of XPD data, including especially several substrate- and adsorbate- systems of known geometry to test the degree of its validity.

C. Substrate emission

The first quantitative comparisons of theoretical and experimental XPD curves were for azimuthal scans above a Cu(001) surface^{62,63}. Some of this data for Cu2p_{3/2} emission is shown in Fig. 37 (cf. Fig. 27), and a more recent comparison using higher and lower angular resolutions has been presented in Fig. 31. Consider first the theoretical curves labelled "damping = 1.0" in Fig. 37, which represent non-adjusted SSC calculations according to Eq. (29), as do the theoretical curves of Fig. 31. It is clear from these figures that simple SSC calculations are capable of predicting the positions and approximate relative intensities of most of the features observed, even down to the very narrow peaks noted for $15^\circ \lesssim \phi \lesssim 75^\circ$ in Fig. 31. There are, to be sure, some minor discrepancies as to features, as for example, in Figure 37 where the local minimum in experiment is not present in theory for $\phi = 45^\circ$ and $\theta = 10^\circ$ and the maxima in experiment for $\phi = 90^\circ$ and $\theta = 13^\circ, 15^\circ, 18.4^\circ,$ and 45° are local minima in theory. Also, the degree of anisotropy is overestimated by theory by a factor of ~ 1.5 - 2.0 , but this is not surprising in view of our prior discussion of the model.

The overall agreement between theory and experiment for Cu is improved somewhat by the empirical reduction of each scattering amplitude $|f_j|$ by a factor of $1/2$ ⁶³: such curves are denoted by "damping = 2.0" in Figure 37. Such an empirical reduction in $|f_j|$ might be justified in allowing for some or all of the last four factors discussed in the preceding section as being responsible for overestimates of anisotropy by theory,⁴ but its magnitude has been rather arbitrarily chosen to optimize agreement, so that such adjustments will not generally be utilized in what follows and, if so, will be specifically indicated.

As more recent examples of such comparisons, we note that the closely-related crystal Ni(001) exhibits XPD azimuthal patterns very close to those of Cu(001), and somewhat better agreement with non-adjusted SSC calculations⁸⁴.

Also, Kono⁸⁵ has recently compared SSC calculations and experiment for polar scans above a LaB₆ crystal. Fig. 38 shows such a comparison for La4d emission, and it is clear that all main features are correctly predicted as to position and approximate relative intensity. (The experimental data here have not been corrected for a smooth-curve modulation due to the instrument response function.) Takahashi et al.⁸⁶ have also recently compared azimuthal XPD data for Ag3d

*Such empirical adjustments in $|f_j|$ by approximately 0.4-0.5x have also been found to improve agreement with experiment in more recent work (ref. 100 and Trehan and Fadley, to appear in Phys. Rev. B), and their principal origin in spherical-wave effects (ref. 77) has also been confirmed by Sagurton, Bullcock, and Fadley (to be published).

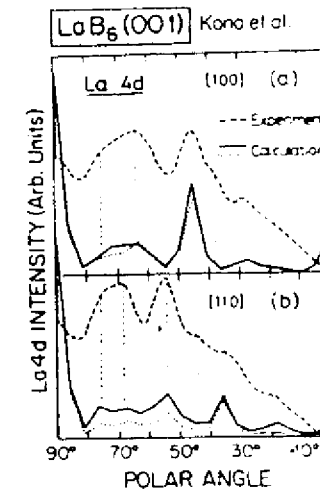


Fig. 38. Comparison of experiment and SSC theory for the polar dependence of La4d emission from LaB₆(001) along the [100] and [110] azimuths. The solid-curve theory includes both La and B atoms as scatterers; the dotted-curve theory includes only the much heavier La atoms as scatterers. No allowance for the instrument response function has been made in plotting the experimental data. (After Kono, ref. (85).)

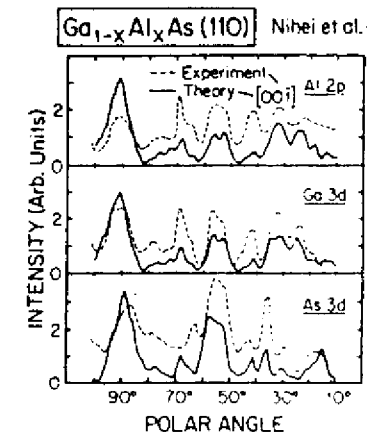


Fig. 39. Comparison of experiment and SSC theory for the polar dependence of Al2p, Ga3d, and As3d emission from Ga_{1-x}Al_xAs(110). (After Owari et al., ref. (87).)

emission from a Ag (110) crystal with SSC theory and found very good agreement for all major features.

As a final example, we show in Figure 39 a very recent comparison of SSC calculations and experimental results obtained by Nihei et al.⁸⁷ for polar scans of three core peaks in a crystal of $Ga_{1-x}Al_xAs$ ($x \approx 0.5$) with (110) orientation. The SSC model utilized was somewhat simplified from that discussed here. Again, almost all of the features are correctly predicted in position and relative intensity, with the sole exception being a shift of $\sim 6^\circ$ of two features for As3d in the range $50^\circ \lesssim \theta \lesssim 70^\circ$.

Overall, the test cases studied to date thus permit tentatively concluding that SSC calculations provide a very good description of the XPD effects associated with substrate core-level emission. The degree of agreement found is even somewhat surprising in view of the fact that emission along or near lines of atoms in the crystal might be expected to enhance the importance of multiple scattering effects. (Perhaps this is the reason for the slight featural disagreements seen in Fig. 31 near $\phi = 0^\circ$ and 90° , as this corresponds to emission along $\langle 110 \rangle$ directions.) Comparing SSC calculations with experimental measurements thus should much increase the certainty of site-type determinations, such as those represented by Figs. 32 and 33. Anticipating the next sections on adsorbate emission, we also note that emission along lines of atoms is generally not possible, so that SSC results might be expected to better describe experiment in at least this respect.

In concluding on substrate emission, we also note an alternate description of such effects in terms of Kikuchi bands^{2,6,65,88}. This emphasizes photoelectron diffraction from different sets of planes in the crystal as denoted by Miller indices (hkl), and each set is expected to have associated with it a band of enhanced intensity for photoelectron emission within plus or minus the Bragg angle θ_{hkl} of being parallel to these planes. If the interplanar spacing is d_{hkl} , then the Bragg angle is determined from

$$\lambda_e = 2d_{hkl} \sin \theta_{hkl} \quad (31)$$

One thus qualitatively expects peaks of intensity for emission along low-index directions in which several sets of planes intersect, as discussed previously. Maxima at $\pm \theta_{hkl}$ away from the planes are also expected and such features are seen in both experiment and SSC theory in Fig. 31 for $\phi \approx 10^\circ, 80^\circ$. This model has been compared to experimental data both qualitatively⁶⁵ and quantitatively (using a simple superposition of independent (hkl) Kikuchi bands)^{88,89}, and found to provide a semi-quantitative zeroth-order description of substrate XPD. A more detailed comparison of the Kikuchi-band and SSC models appears elsewhere⁸⁸.

D. Emission from molecular adsorbates

Although the first adsorbate XPD was actually observed for an atomic adsorbate (O on Cu(001)^{62,63}), it is heuristically useful to begin by considering two simple effects arising in small-molecule adsorption. These have both been studied for the system $c(2 \times 2)CO$ on Ni(001)^{77,81}.

(1) Intramolecular Scattering. Fig. 29 shows polar-scan experimental data for C1s emission from $c(2 \times 2)CO$ on Ni(001) for two different high-symmetry azimuthal orientations^{62,80}. The C1s intensity has been normalized by dividing by the featureless O1s intensity to allow for the instrument response function, and a clear peak along the surface normal is found. A qualitative explanation of this in terms of intramolecular scattering is indicated in the inset of this figure. C1s photoelectrons are preferentially forward-scattered by the O atom in the same molecule so as to produce a constructive interference and therefore a peak in intensity directly along the C-O bond direction. This forward-scattering peak can also be termed a 0th order diffraction peak, as the scattering phase shift is very small (it is shown for simplicity to be zero in the schematic drawing). At larger angles away from the bond direction, 1st order diffraction effects might also be expected, but they cannot be resolved for certain in this data.

A more quantitative description of this data requires using the SSC model, as has been done in two prior studies^{77,81}. Because the electron emission directions of interest are rather near the surface normal, the substrate Ni atoms or other CO molecules around a given emitter will be associated with scattering angles of $\gtrsim 90^\circ$. Thus, it has been shown that they have a negligible influence on such intramolecular XPD and a two-atom cluster (a C emitter and an O scatterer) is sufficient. The other important parameters of the calculation are the tilt angle θ_c of the bond axis away from the surface normal and an rms vibrational amplitude θ_{rms} for a wagging or frustrated rotational motion of the CO. θ_{rms} is incorporated via a ground-state harmonic oscillator probability distribution, and is expected to be near 10° for CO on Ni(001) at ambient temperature.

Fig. 40 compares experiment and theory for $\theta_{rms} = 10^\circ$ and various choices of θ_c . (Again, theory predicts ≈ 2 times larger XPD effects than are observed and at least half of this overestimate has been shown to be neglect of curved-wave effects due to the short C-O distance⁷⁷.) An intensity maximum along the surface normal such as that observed experimentally is found in the SSC curves for all tilt angles $\lesssim 14^\circ$. Considering further the FWHM of this 0th order peak is found to limit the tilt to $\theta_c \lesssim 10^\circ$. This conclusion is also possible in the presence of greater degrees of vibrational motion⁸¹.

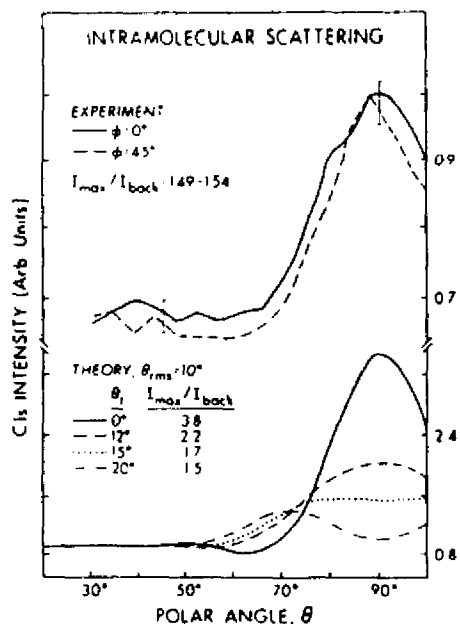


Fig. 40. Comparison of experiment and SSC theory for the polar dependence of C1s emission from $c(2 \times 2)\text{CO}$ on Ni(001). The calculations have been performed with a fixed root-mean-squared vibrational displacement of 10° and several tilt angles θ_c of the CO molecule relative to the Ni surface. The amplitudes of these intramolecular scattering phenomena are indicated here by the maximum-to-background ratio $I_{\text{max}}/I_{\text{back}}$. (From Orders and Fadley, ref. (81).)

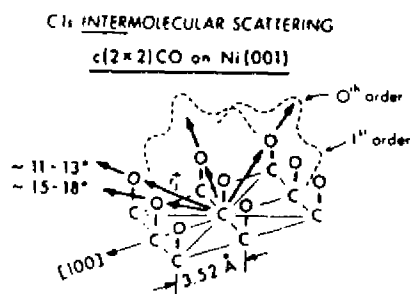


Fig. 41. Schematic illustration of the mechanism by which intermolecular scattering produces azimuthal anisotropy in C1s emission from $c(2 \times 2)\text{CO}$ on Ni(001). (From Orders and Fadley, ref. (81).)

Thus, this analysis permits rather straightforwardly determining the orientation of CO on this surface to within $\sim 10^\circ$. It also suggests the general utility of such effects in studying the orientations of small molecules on surfaces, as the 0th order peak intensity in general follows the bond direction. All that is required is for an atom of reasonable scattering power (that is, of atomic number $\geq 4-8$) to lie between the emitting atom and the detector. Such intramolecular scattering effects thus provide a type of information very similar to that available from electron stimulated desorption ion angular distributions (ESDIAD)⁹⁰ and polarization-dependent core-level absorption edge structure measurements⁹¹. However, the theoretical picture in XPD seems both simpler and more clearly understood than either of these other two methods, and a synchrotron radiation source is not needed to carry out the XPD measurements, although it is for absorption edge studies.

(ii) Intermolecular scattering. A further type of XPD effect possible for an ordered overlayer of adsorbed molecules is illustrated for the case of $c(2 \times 2)\text{CO}$ on Ni(001) in Fig. 41. C1s emission is again considered, but in this case, for near-grazing emission directions for which scattering by O atoms in near-neighbor molecules along the surface is possible. Each O atom thus may generate both 0th order and 1st order XPD structure. For the expected C-O bond length, these effects are expected to occur for emission angles of $\sim 10^\circ-20^\circ$ with respect to the surface. At lower angles, intermolecular scattering by C atoms in adjacent molecules also may be significant. The qualitative expectation is thus that azimuthal scans of C1s intensity should exhibit 0th order peaks at $\phi = 0^\circ, 45^\circ, 90^\circ, \dots$ (as measured from the [100] direction), with extra structure at intermediate angles possible due to 1st order effects.

Such intermolecular effects have been experimentally observed⁸¹, as illustrated in Fig. 42 for scans at various polar angles. These data have been fourfold-averaged over a full 360° scan to reduce noise. As noted previously, the degree of mirror symmetry about $\phi = 45^\circ$ can be used to judge the statistical accuracy of a given feature. Although low intensities make the statistical scatter of these measurements rather high, intermolecular scattering effects are clearly seen at the two lowest angles of $\theta = 7^\circ$ and 11° , including 1st order peaks at ϕ positions of $\sim 22^\circ$ and $\sim 68^\circ$. The overall anisotropies are $\sim 15\%$ for these low θ values, with rapidly decreasing values as θ is increased to a maximum of 18° . Also shown in Fig. 42 are SSC theoretical curves incorporating the effects of both types of adjacent CO molecules (that is, those at $\phi = 0^\circ$ and 45°). Independent wagging vibrations of these molecules have also been included, with a θ_{rms} value of 10° .⁸¹ Although theory again overestimates the degree of anisotropy, this time by ~ 4

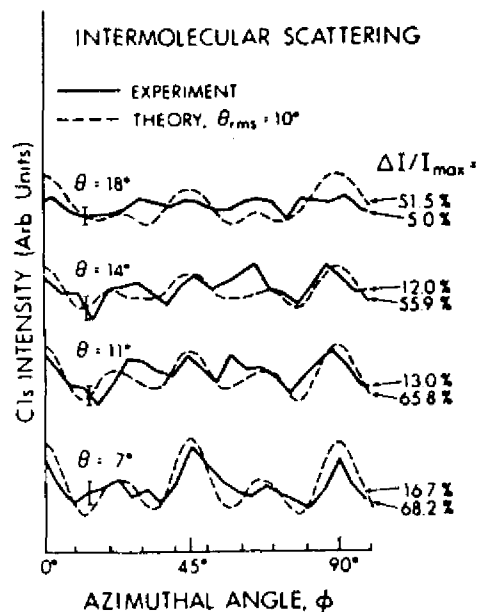


Fig. 42. Comparison of experiment and SSC theory for the azimuthal dependence of Cls emission from $c(2 \times 2)CO$ on Ni(001). The diffraction effects seen are due to intermolecular scattering (cf. Fig. 41). (From Orders and Fadley, ref. (81).)

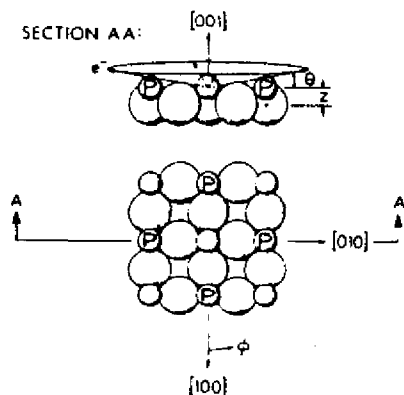


Fig. 43. General atomic geometry for $c(2 \times 2)$ and $p(2 \times 2)$ adsorbate overlayers on a [001] surface of an fcc metal, assuming that adsorption is in fourfold-hollow sites. In $c(2 \times 2)$, all sites are occupied; in $p(2 \times 2)$ only those denoted by "P".

times, the peak positions and approximate relative intensities agree very well with experiment, especially at the two lowest θ values. A more detailed discussion of these effects, including theoretical curves for varying degrees of vibrational motion, appears elsewhere.⁸¹

Thus, such intermolecular scattering effects should provide rather direct information on the short-range order in an adsorbate overlayer. This is by contrast with measurements such as LEED, for which long-range order over distances of $\sim 10^2 \text{ \AA}$ is necessary for sharp patterns to be observed. Particularly with further developments in instrumentation to increase intensity, as well as angular precision and accuracy, such XPD effects thus should provide very useful surface structural information.

E. Emission from atomic adsorbates

We begin here by discussing several recent test cases designed to explore the angular sensitivity of x-ray photoelectron emission from core levels of atomic adsorbates, as well as to determine the degree to which the single scattering cluster model can be used to quantitatively describe such effects. Several practical applications to structural determinations are then discussed, together with estimates of structural sensitivity for different types of adsorption, and suggestions for improving the structural sensitivity. The use of polarized and energy-tunable synchrotron radiation for such XPD studies is also considered.

(1) Well-defined test cases. Fig. 30 makes it clear that XPD effects can be observed in emission from a core level of an atomic adsorbate, and furthermore that the resulting azimuthal patterns are very sensitive to the polar angle of emission. The discussions of the preceding two sections on substrate- and molecular adsorbate- emission also strongly suggest that a single scattering cluster model should be adequate for describing these effects. However, it is nonetheless necessary to test this idea by comparing experiment and SSC calculations for some well-defined adsorbate geometries. This has been done recently by Orders et al.⁶⁹ for $c(2 \times 2)S$ and $c(2 \times 2)Se$ on Ni(001). These overlayers have been studied previously by LEED and NPD and both consist of atomic adsorption in fourfold hollow sites, with S at a vertical distance of $z = 1.30\text{--}1.35 \text{ \AA}$ above the first Ni layer⁴⁵ and Se at a distance of $z = 1.55\text{--}1.60 \text{ \AA}$; every other fourfold site is occupied, as illustrated in Fig. 43.

A series of azimuthal scans for S2p emission from $c(2 \times 2)S$ on Ni(001) at different polar angles θ between 7° and 17° are shown in Fig. 44 in comparison to SSC theoretical curves for $z = 1.30 \text{ \AA}$. Note that some of the θ steps here are only 1° in magnitude. Considering first only the dashed experimental curves, we

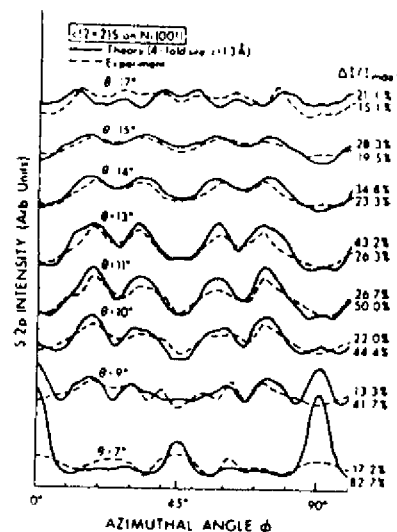


Fig. 44. Comparison of experiment and SSC theory for the azimuthal dependence of S2p emission from c(2x2)S on Ni(001) at eight closely-spaced polar angles. The theoretical calculations were performed for the generally accepted geometry of 4-fold S bonding at a vertical distance of $z = 1.30\text{\AA}$ (cf. Fig. 43). (From Connelly, ref. (33).)

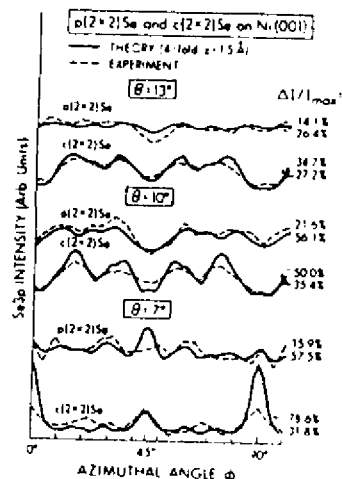


Fig. 45. Comparison of experiment and SSC theory for the azimuthal dependence of Se3p emission from p(2x2)Se and c(2x2)Se on Ni(001) at three different polar angles. The calculations were performed for the accepted geometry of 4-fold Se at $z = 1.5\text{\AA}$. (From R. E. Connelly and R. C. White, unpublished results.)

see that the patterns change very much with θ , particularly in the range of $\sim 7^\circ$ - 11° . The expected mirror symmetry about $\phi = 45^\circ$ is also seen in all of the experimental data, and provides strong confirmation of all of the features present in these curves. A comparison now of experiment with the SSC calculations shows that, with very few exceptions, all of the peak positions and relative intensities, and by implication thus also the changes in structure with θ , are correctly predicted by this simple model. As usual, theory predicts more anisotropy than experiment, here by ~ 1.4 - 4.9 times, depending on the θ value. However, the only significant discrepancies as to features between experiment and theory are associated with the symmetry-identical peaks at $\phi = 0^\circ$ and 90° for $\theta = 7^\circ$ and 9° (and very slightly also for 10°); these peaks are predicted to be ~ 2 - 3 times too high in theory for $\theta = 7^\circ$, and for this reason also persist as significant features at $\theta = 9^\circ$ even though they are not observed experimentally. A consideration of the SSC calculations shows that, for low θ values $\lesssim 7^\circ$, the peaks at $\phi = 0^\circ, 90^\circ$ are produced by forward scattering or 0th order diffraction from nearest-neighbor S atoms to the emitter which are located along $\langle 100 \rangle$ -type directions (cf. Fig. 43). Similarly, the peak for very low θ values at $\phi = 45^\circ$ is associated with forward scattering by next-nearest neighbor S atoms along $\langle 110 \rangle$ -type directions. One likely reason for overestimating the strength of nearest-neighbor scattering is that these SSC calculations assumed no refraction in scattering events from the adsorbate, thereby emphasizing smaller-angle adsorbate events too much in the final angular averaging. Also, for such close distances between emitter and scatterer, the use of the small-atom approximation may not be fully valid, and curved-wave corrections would thus be expected to effectively reduce the forward-scattering strength. It is also possible that surface non-idealities and microscopic roughness could become more important for very low takeoff angles (as discussed in another context in Sec. 3.C), and that both non-isotropic inelastic scattering and multiple scattering effects could be more important for this type of nearest-neighbor forward scattering. In any case, the overall agreement is very encouraging.

A similar comparison of experiment and SSC calculations has also been made for c(2x2)Se or Ni(001)⁶⁹, and it yields essentially identical conclusions. Some of this data is shown in Fig. 45, where the only significant discrepancies are again in the relative intensities of the $\phi = 0^\circ, 90^\circ$ peaks at $\theta = 7^\circ$, as well as in slight position shifts of ~ 3 - 4° in the doublets for $10^\circ \lesssim \phi \lesssim 35^\circ$ and $55^\circ \lesssim \phi \lesssim 80^\circ$. Overall, then, these two test cases thus provide further strong support for the quantitative utility of SSC in describing XPD from adsorbates. (Further experimental and theoretical studies aimed at explaining the few discrepancies noted are nonetheless desirable.)

(ii) Structural sensitivity and structural determinations. In addition to the test cases discussed in the prior section, adsorbate XPD measurements combined with SSC calculations have been used to study the atomic geometries of several more complex systems: $c(2 \times 2)O$ on $Cu(001)$ ^{62,63}, $p(2 \times 2)O$ and $c(2 \times 2)O$ on $Ni(001)$ ⁹², and O on the stepped Cu surfaces (211) and (410) ⁸⁰. We begin by discussing the apparent structural sensitivities seen in some of these studies from both experimental and theoretical points of view.

As a first example of sensitivity to the type of overlayer structure present, Fig. 45 compares experimental and theoretical azimuthal scans from the well-defined overlayers $c(2 \times 2)Se$ on $Ni(001)$ and $p(2 \times 2)Se$ on $Ni(001)$. Considering experiment first, we see that there are major differences between $c(2 \times 2)$ and $p(2 \times 2)$ for all three polar angles shown. Thus, XPD is clearly very sensitive to this change in overlayer structure, albeit a rather large one. Again with only a few exceptions as to relative intensity, the theoretical curves very well predict the experimental curves for both overlayers; in fact, the only points of significant disagreement are for $c(2 \times 2)Se$ at $\theta = 7^\circ$, and have been discussed in the last section. This comparison thus also lends further support to the applicability of the SSC model for describing XPD data.

In proceeding further to consider structural sensitivity, the adsorbate vertical position emerges as a critical parameter of interest. As a first illustration of how this can affect adsorbate XPD, we consider in Figs. 46 and 47 comparisons of experiment and theory at different z values for O_{1s} emission from the expected fourfold hollow sites of $c(2 \times 2)O$ on $Cu(001)$ ^{62,63}. (Although most of the theoretical curves shown are for $\beta \equiv$ damping = 2.0 and thus have had the $|f_j|$ values reduced by 1/2, their forms do not change significantly for $\beta = 1.0$, and thus none of the discussion below is altered with the use of unadjusted $|f_j|$'s.) Comparing experiment and theory here for z values above and below the atomic centers of the Ni surface plane at $z = 0.0 \text{ \AA}$ shows that at $\theta = 10^\circ$ the region of best agreement is for $\sim -0.1 \text{ \AA}$ to $+0.1 \text{ \AA}$. For $\theta = 13^\circ$, it would seem that 0.0 \AA to -0.1 \AA is the region of maximum agreement. Similar comparisons at a total of five θ values ultimately permitted Kono et al.^{62,63} to propose that $c(2 \times 2)O$ is bonded in 4-fold hollow sites at a position that is co-planar with the surface Cu atoms to within $\pm 0.1 \text{ \AA}$ (that is, at $z = 0.0 \pm 0.1 \text{ \AA}$). Including the Cu atom immediately below the hollow, this yields a five-fold coordination for O with a $Cu-O$ bond distance of 1.81 \AA that is not very different from the 1.85 \AA in the compound Cu_2O . Although no prior definitive determination of this structure has been made, very recent NPD measurements on this system are also at least partly consistent with a nearly in-plane adsorption⁹³, and previous LEED⁹⁴ and SIMS

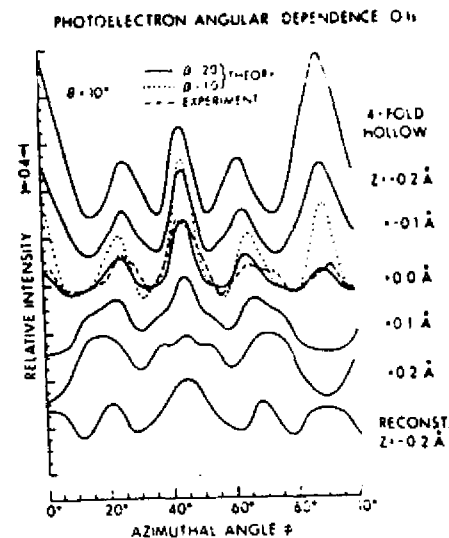


Fig. 46. Comparison of experiment and SSC theory for the azimuthal dependence of O_{1s} emission from $c(2 \times 2)O$ on $Cu(001)$ at $\theta = 10^\circ$ and for different adsorption geometries. $\beta = 2.0$ has the same significance as damping = 2.0 in Fig. 37; $\beta = 1.0$ corresponds to damping = 1.0 or no adjustment of the $|f_j(\theta_j)|$ values. Experiment and theory are compared for five z positions of 4-fold bonding and for the empirically optimum value for a previously proposed reconstructed geometry. (From Kono et al., ref. (63).)

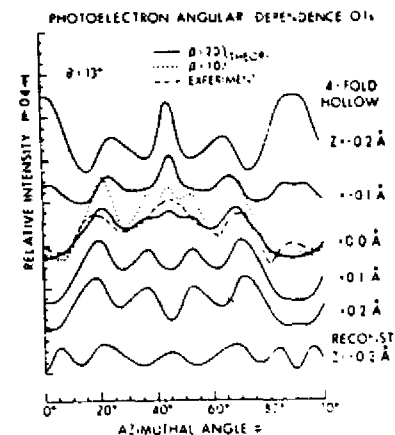


Fig. 47. As Fig. 46, but for $\theta = 13^\circ$.

angular distribution⁹⁵ studies have also found this geometry to give one of the best fits to experiment.

A further indication of structural sensitivity is shown by the bottom curves in Figs. 46 and 47, which were calculated for another trial adsorption geometry: a reconstructed Cu surface in which O replaces every other Cu atom in the first layer. The z distance of -0.2 Å was chosen to optimally fit experiment at all θ values, but this fit is clearly very poor at $\theta = 13^\circ$, even though it is reasonable at $\theta = 10^\circ$. The reconstructed geometry thus could be ruled out. This illustrates both the necessity of using a rather full XPD data set at multiple polar angles and also the potential sensitivity of XPD to the bonding site type.

A similar XPD study of various O exposures on Ni(001) spanning the p(2x2) to c(2x2) transition in LEED^{92,99} also permitted concluding that lower exposures involve fourfold O atoms at $z \approx 0.8 \pm 0.2$ Å, whereas at higher exposures, a considerable fraction of the fourfold O is nearly co-planar with Ni at $z = 0.1 \pm 0.2$ Å. This conclusion has subsequently been confirmed in high-resolution electron energy loss measurements on the same system⁹⁶, although it is at variance with recent NPD⁹⁷ and SEXAFS⁹⁸ measurements, which suggest above-plane adsorptions for both p(2x2) and c(2x2). Possible explanations for this apparent discrepancy are a variable degree of above-plane and co-planar mixing with different specimen preparation treatments, as well as an enhanced sensitivity of XPD to O in the co-planar sites where smaller-angle substrate scattering is possible⁹².

However, the situation concerning vertical sensitivity is not quite as simple for all cases as that illustrated in Figs. 46 and 47. Fig. 48 shows a similar comparison of experiment and theory at different z values for c(2x2)S on Ni(001). Although significant changes in features occur with z for z values up to ~ 1.0 Å, beyond this point, the pattern is rather stable, with only very subtle changes in fine structure. Thus it would be difficult to conclude much more than $z \gtrsim 1.0$ Å by comparing experiment and theory for this case, and similar conclusions obtain for the other polar angles of emission in Fig. 44⁹⁹. The same sorts of trends are seen also for c(2x2)Se on Ni(001)⁹⁹, and lead to the conclusion that vertical position sensitivity is lost if the adsorbate is too far above the surface plane.

The explanation of this lies straightforwardly in the forward-peaked nature of electron-atom scattering in XPS, and is illustrated schematically in Fig. 49. For low θ values and an adsorbate lying closer to the substrate surface, small-angle scattering is possible from both other adsorbate and substrate atoms. Since only substrate scattering can provide information on the adsorbate-substrate distances, a high z sensitivity of the order of ± 0.1 Å results. On the other hand, when the adsorbate is too far above the surface ($\gtrsim 1.3$ Å for O on Ni, $\gtrsim 1.0$ Å for S on Ni, $\gtrsim 0.8$ Å for Se on Ni, and $\gtrsim 0.7$ Å for Te on Ni⁹⁹), the scattering angles from the

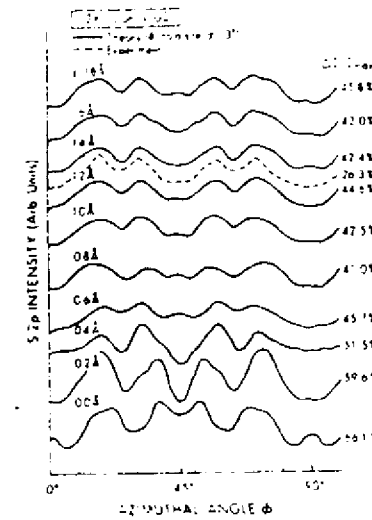


Fig. 48. As Fig. 47, but for c(2x2)S in 4-fold coordination on Ni(001) and a broader range of z values; $B = 1.0$ for all curves. (From Connolly, ref. (33).)

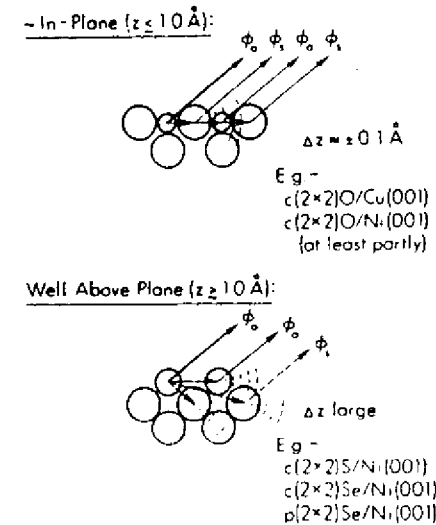


Fig. 49. Schematic explanation of the differing sensitivity of azimuthal XPD depending upon the height of the adsorbate above the substrate, with specific examples of each type of bonding indicated.

near-neighbor substrate atoms of most significance are too large to yield appreciable scattered waves ϕ_j , and the z sensitivity is very low. In fact, the XPD is predominantly produced by scattering in the two-dimensional adsorbate overlayer, as is found to be the case, e.g., for both S and Se on Ni(001). The inherent scattering strengths of the atoms involved also are important parameters here, and one can see a systematic trend through the chalcogenides in the values given above. Thus, a very low atomic number adsorbate on a very high atomic number substrate would tend to show more site type and z sensitivity at higher z values, and vice versa.

Thus, although there are to be sure a great many surface chemical problems for which adsorbed or reacting species will occupy sites at $z \leq 1.0 \text{ \AA}$ with respect to the substrate surface and thus be amenable to high-precision study by XPD, the amount of information derivable for other problems involving greater z distances will be more limited. The question thus arises as to whether the method of carrying out such measurements can be changed in some way so as to improve z sensitivity, and two possible solutions seem promising. The simplest is to increase the angular resolution of the analyzer, so that more fine structure can be resolved in the XPD patterns. A theoretical simulation of this for $c(2 \times 2)S$ on Ni(001) is shown in Fig. 50, where curves for a cone of 3.0° half angle are compared to those for a cone of 1.5° half angle at various z values. Although the $\pm 3.0^\circ$ curves are essentially constant in form for $z > 1.2 \text{ \AA}$, those for $\pm 1.5^\circ$ continue to show changes in fine structure up to the rather high value of 1.8 \AA . Thus, especially if a family of such azimuthal scans at high angular resolution and for various θ values were analyzed simultaneously, it should be possible to increase the sensitivity to both site type and z for higher z values. (On the negative side, however, would be the unavoidable intensity loss in increasing the angular resolution.)

A second possibility for improving z sensitivity is to use polarized synchrotron radiation and preferentially direct the primary photoelectron emission toward the substrate, as shown in Fig. 51. In so-called s polarization with the ϵ vector lying in the plane of the surface, the maximum emission from a level exhibiting a typical XPS differential cross section will be toward the other adsorbate atoms, thus minimizing substrate scattering and lowering the z sensitivity. By contrast, in a p polarization geometry chosen to maximize the emission toward the substrate and minimize that toward the other adsorbate atoms and in the direct wave ϕ_0 , the influence of the substrate should be markedly enhanced in the observed XPD. (Although to be sure a potential disadvantage of such a geometry is that the overall photoelectron intensity may also be markedly reduced.) As an illustration of the possible magnitudes of such polarization effects, Fig. 52 shows a

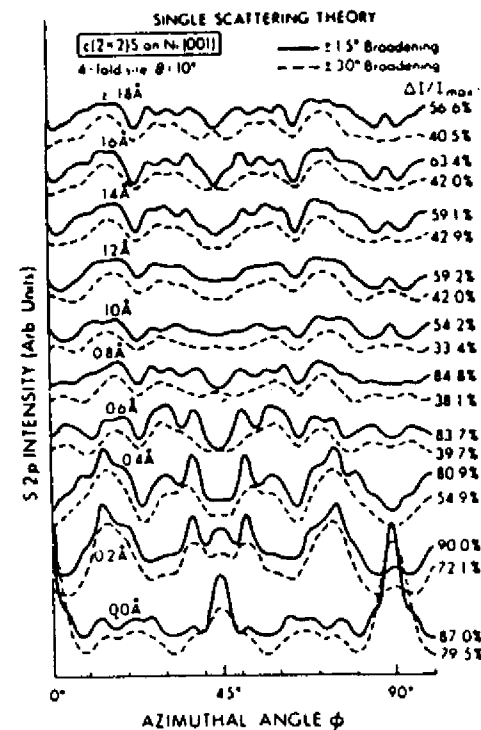


Fig. 50. The effect of reducing analyzer acceptance from $\pm 3.0^\circ$ to $\pm 1.5^\circ$ on azimuthal XPD. Theoretical SSC curves for the azimuthal dependence of S2p intensity from $c(2 \times 2)S$ on Ni(001) at $\epsilon = 10^\circ$ are shown for the two angular acceptances and a range of 4-fold-coordinate z values from 0.0 \AA to 1.8 \AA . (From Connelly, ref. (33).)

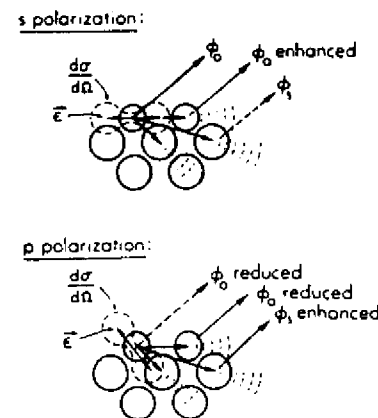


Fig. 51. Schematic explanation of how azimuthal XPD experiments in a p -polarized geometry would be expected to increase the sensitivity to adsorbate-substrate vertical displacement.

comparison of calculated XPD curves for $c(2 \times 2)S$ on $Ni(001)$ with s- and p-polarization, and for various z values. The forms of these curves at $\theta = 10^\circ$ (as well as at other angles not shown) are very much changed by the change in polarization, and the anisotropies for the p-polarized cases are larger by as much as a factor of 2. Recent experiments by our group at the Stanford Synchrotron Radiation Laboratory have confirmed this polarization sensitivity in XPD.¹⁰⁰

Also, although the curves for s polarization cease changing appreciably with z for $z \gtrsim 1.4 \text{ \AA}$ in p polarization, changes in fine structure continue to occur all the way up to $z = 2.0 \text{ \AA}$. Thus, with increased angular resolution and/or the use of polarization variation, it appears that the high- z limitations on z sensitivity in XPD could be substantially improved.

As a further example of structural determinations using XPD, we briefly consider a recent study by Thompson and Fadley⁸⁰ of O adsorbed on the stepped Cu surfaces (211) and (410). Such surfaces are of considerable interest as controlled models of what may be the active sites on metal catalysts. As one illustration from this work, the (211) surface is found via LEED examination to reconstruct under oxygen exposure to the geometry shown in Fig. 53. It consists of a regular series of 5-atom terraces of (111) orientation and 2-atom step faces of (100) orientation. The most likely high-symmetry adsorption sites for atomic oxygen are also shown as A-C, and these can be further designated as A = 4-fold top, B = 4-fold bottom, and C = 3-fold. However, there is no prior evidence to suggest which of these sites will be occupied first, or whether a mixture of occupied sites may arise. Prior chemisorption studies on the separate low-index (111) and (100) faces do suggest however that (100) atoms should be much more reactive than (111) atoms, and it is also expected that atoms on or near step faces may exhibit higher reactivity as well.

It is thus of considerable interest to see whether oxygen adsorbed on this stepped surface exhibits any XPD features that are clearly influenced by the presence of the steps. A 5 Langmuir exposure to O_2 was found via an analysis of XPS core-peak intensities to yield a coverage equivalent to ~ 1 atom per high-symmetry site along the step face (or about 11% of a monolayer); this exposure also occurs at a distinct break in the curve of coverage vs. exposure for which the surface can be considered nearly saturated with O. Full 360° azimuthal scans of the O1s intensity for this system showed pronounced XPD effects, as illustrated in Fig. 54 for $\theta = 10^\circ$. $\phi = 0^\circ$ here corresponds to emission in an azimuth perpendicular to and away from the step faces. The reproducibility of features between the two halves of the scan (which should be mirror symmetric due to the presence of the steps) is also very good, especially for the most pronounced peaks between $\phi \approx 60^\circ$ and $\phi \approx 140^\circ$. Similar reproducibility was found for data obtained

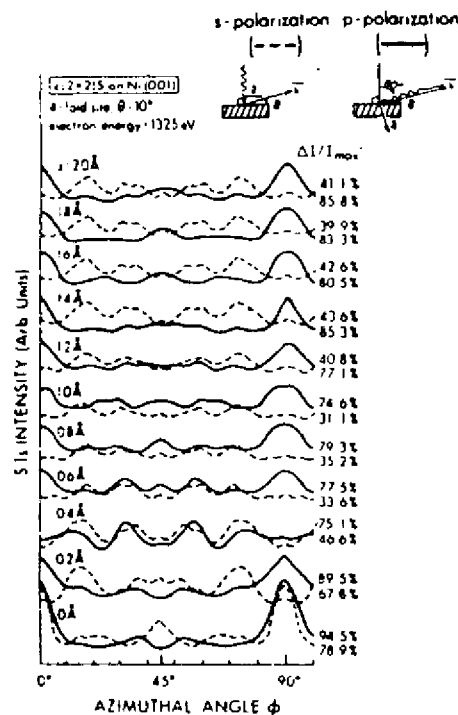


Fig. 52. The effect of changing from s- to p- polarization on azimuthal XPD. Theoretical curves for the azimuthal dependence of S2p intensity from $c(2 \times 2)S$ on $Ni(001)$ at $\theta = 10^\circ$ are shown for the two polarizations and a range of 4-fold-coordinate z values from 0.0 \AA to 2.0 \AA . (P. J. Orders and C. S. Fadley, unpublished results, plus new experimental and theoretical results in ref. 100.)

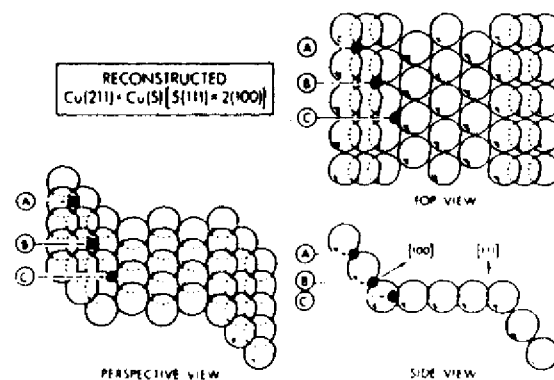


Fig. 53. Three views of a stepped $Cu(211)$ surface as it is found to reconstruct under oxygen exposure. Included are the three possible high-symmetry coordination sites expected for oxygen bonding on or near the step faces: A = 4-fold top, B = 4-fold bottom, and C = 3-fold. (From Thompson, ref. (80).)

from (211) and (410) surfaces at different exposures.⁸⁰ In general, a mirror average of these two halves will give the best representation of the true XPD peaks, and that also is shown in Fig. 54. A full set of such mirror-averaged experimental data for six θ values between 7° and 23° is shown as dashed curves in Fig. 55, and it is clear that the diffraction features are very sensitive to polar angle as well. The anisotropies are as high as 31% for (211) and 40% for (410). The most reliable data range is for $10^\circ \lesssim \theta \lesssim 20^\circ$, as below this the count rates are much lower due to the instrument response function and possible residual roughness effects, and above it, the anisotropies are too low due to the large scattering angles required.

In order to next ask what the experimental data in Fig. 55 can tell us concerning the adsorption geometry, a series of SSC calculations was performed for various physically reasonable vertical positions z of oxygen in the different sites A, B and C of Fig. 53. Comparison of these theoretical curves with experiment showed that the B = 4-fold bottom site clearly gave the best fit to experiment, with A = 4-fold top being reasonably good as well, and C = 3-fold being very poor. Choosing the optimum z value for each site type proceeded via comparisons like Fig. 56 for the 4-fold bottom site at $\theta = 17^\circ$: it is clear here that a z distance of 0.4-0.6 Å above the centers of the Cu atoms in the step face gives the best fit to experiment. Overall use of all six θ values yields 0.6 ± 0.2 Å as the best estimate, and the final theoretical curves for this value are summarized in Fig. 55. Although not all features are correctly predicted, especially as to relative intensity, the overall agreement in the structure-rich region for $\phi > 90^\circ$ is very good, especially for the region $10^\circ \lesssim \theta \lesssim 20^\circ$ expected to be most reliable. The search and optimization procedure used thus strongly suggests a predominant 4-fold bottom adsorption site for this O exposure on Cu(211). A minority admixture of 4-fold top adsorption also is possible.

Having tentatively solved this structure it is also of interest to see whether any of the XPD features are capable of simple physical interpretation. In fact, the strong peaks seen near $\phi = 135^\circ$ for $7^\circ \leq \theta \leq 20^\circ$ are all found to be due to forward scattering or 0th order diffraction from the two nearest-neighbor Cu atoms just above a B-site oxygen on the (100) step face (cf. Fig. 53). (The symmetry of the surface also dictates that similar peaks would arise in A-site emission as well, but they are found to be slightly shifted in position relative to experiment.) Also, the general dip in intensity seen at $\phi \approx 100^\circ$ - 120° is found to be due to enhanced inelastic scattering for emission through the step face at angles nearly parallel to it. The excellent agreement between experiment and theory for these simply explicable features thus further reinforces the 4-fold site assignment.

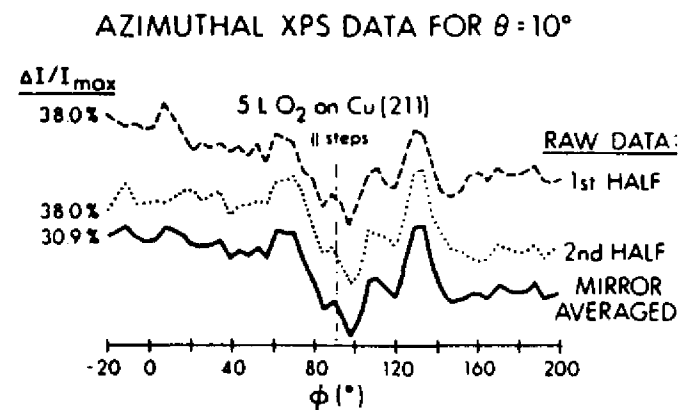


Fig. 54. Azimuthal XPD data for O1s emission from a 5L exposure of O₂ on a stepped Cu(211) surface. The mirror symmetry of the surface across a plane perpendicular to the steps is reflected in the excellent agreement between the two halves of the full 360° scan. The average of these two halves has been used for subsequent structural analysis. (Thompson, ref. (80).)

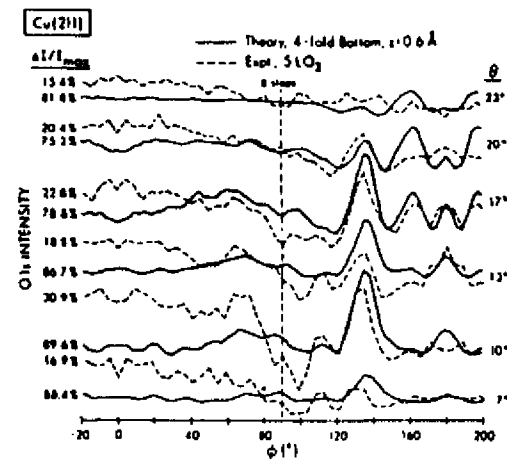


Fig. 55. Comparison of experiment and SSC theory for the data of Fig. 54, with experiment being shown here as dashed curves. The theoretical curves are for oxygen in all sites of type B in Fig. 53 and at a distance of 0.6 Å above the first layer of Cu atoms on the step face; this geometry is found to optimize agreement with experiment.

It has thus been possible using this type of XPD analysis to tentatively suggest adsorption geometries for several exposures of D on Cu(211) and (410)⁸⁰. More importantly, this work indicates that XPD may be able to provide unique structural information for this complex, yet chemically very important, class of surfaces about which rather little is known. Determination of adsorbate bonding geometries from LEED for such surfaces is a very difficult matter, for example, due to the much larger unit cells and relatively weaker substrate effects involved¹⁰¹.

As a final and very recent example of the use of XPD in a surface-structural study, Kono and co-workers¹⁰² investigated the $(\sqrt{3}\times\sqrt{3})R30^\circ$ Ag overlayer on Si(111). They see strong XPD features in azimuthal scans of Ag 3d intensity, and have made use of kinematical theory to propose a new structure for this overlayer. (See below.)

F. XPD Measurements Using Synchrotron Radiation

We have already noted in the last section that the use of polarized synchrotron radiation may permit enhancing the sensitivity of XPD to adsorbate site type and vertical position, and preliminary experiments of this type have recently been performed¹⁰⁰. A further interesting question is whether it would be advantageous to be able to tune the radiation energy so as to have photoelectron energies either below or above those fixed by the usual XPS sources of $h\nu = 1.2-1.5$ keV.

Going to lower kinetic energies of say 200-500 eV would have the advantage of yielding scattering factors less strongly forward peaked, and therefore possibly more substrate sensitivity in azimuthal scans. Also, a useful degree of anisotropy might persist up to higher θ values, thus avoiding the need for extremely small-angle grazing emission with its attendant low intensity and possible surface roughness problems. Possible problems at lower energies, however, are the need for a more complicated theoretical model involving multiple scattering (MS) effects. Very complex MS calculations are, for example, clearly necessary in the very low energy ($\sim 30-100$ eV) adsorbate core-level photoelectron diffraction studies pioneered by Smith, Woodruff, Norman and co-workers¹⁰³.

A partial answer to these questions has been obtained in recent measurements by Orders et al.¹⁰⁰ They obtained SIs azimuthal scans from the well-defined $c(2\times 2)$ S overlayer on Ni(001), tuning the x-ray radiation so as to sweep the photoelectron energy from 230 eV to 900 eV. Some of this experimental data for $\theta = 10^\circ$ is shown as solid curves in Fig. 57, and it is clear that the XPD effects are very sensitive to photoelectron kinetic energy. This directly suggests the alternate possibility of fixing θ at some convenient value and making ϕ scans for various $h\nu$ values to build up a data set for structural determinations. Also shown in Fig. 57 are SSC curves for the known adsorbate geometry and the agreement between theory and experiment for all three energies is extremely good: all peaks are

Since the writing of this review, two additional aspects of XPD have been explored: (1) The use of near-neighbor forward scattering such as that in Figs. 40 and 41 in the analysis of epitaxial overlayer growth (W. F. Egelhoff, *Phys. Rev.*, **B30**, 1052 (1984) - expt.; E. L. Bullock and C. S. Fadley, *Phys. Rev.*, **B31**, 1212 (1985) - theory; and (2) The use of multiplet-split core levels to permit spin-polarized photoelectron diffraction studies of magnetic materials (B. Sinković and C. S. Fadley, *Phys. Rev.*, **B31**, 4665 (1985) - theory; B. Sinković, B. Hermsmeider, and C. S. Fadley - expt., to be published, *Phys. Rev. Lett.* **55**, 1227 (1985))

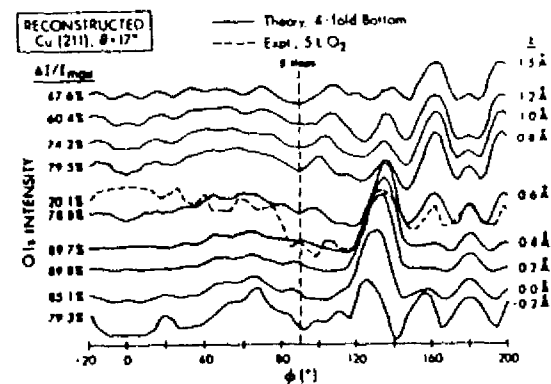


Fig. 56. Illustration of the sensitivity of the theoretical curves of Fig. 55 to the choice of z for the 4-fold bottom site. Calculations for different z values are compared to experiment for a $\theta = 17^\circ$ emission angle.

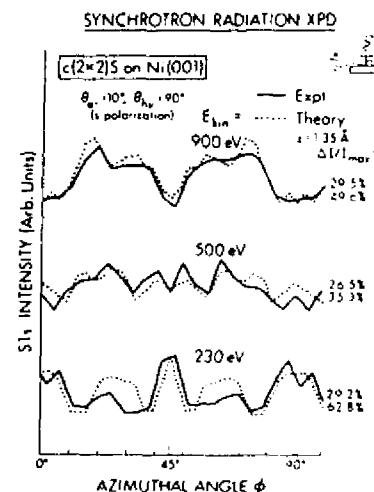


Fig. 57. Comparison of SSC theory to the results of the first azimuthal XPD experiments using synchrotron radiation for excitation. The system is again $c(2\times 2)$ S on Ni(001), and photon energies have been chosen to yield electron kinetic energies of 900 eV, 500 eV, and 230 eV. The electron emission angle is $\theta = 10^\circ$ and the radiation is s-polarized ($\vec{\epsilon}$ is parallel to the surface). (From Orders et al., ref. (100).)

correctly predicted as to position, and generally also as to relative intensity, although a few deviations as to the latter are seen, especially at the lowest energy of 230 eV. Thus, the SSC model definitely seems useful down to a few hundred eV in energy, making this region a potentially very fruitful one for future XPD studies. A more detailed account of this study is in preparation¹⁰⁰.

On the opposite end of the energy scale, would higher photoelectron energies of say 10,000 eV be of any advantage? Scattering factors would be more sharply forward peaked (cf. Fig. 35) and a single-scattering approach probably more likely to be highly accurate. However, on the negative side, the total scattering cross sections would be lower and effects thus smaller, and angles even closer to grazing would be needed to see significant substrate scattering. Also, the smaller deBroglie wavelengths would lead to very fine features in the XPD patterns perhaps difficult to resolve.

A recent theoretical study by Thompson and Fadley⁸⁰ used SSC calculations to compare typical XPD effects at 1000 eV with those at 10,000 eV. The cases chosen for study were polar-scan intramolecular scattering in a vertically-oriented CO molecule with differing degrees of wagging vibration, and grazing emission azimuthal scans from $c(2 \times 2)O$ on Cu(001) at two z positions: in-plane at $z = 0.0 \text{ \AA}$ and above plane at $z = 1.0 \text{ \AA}$. Some of these results are summarized in Figs. 58 and 59. In Fig. 58, the sharper intramolecular peak in a polar scan for 10,000 eV and no vibration ($\theta_{rms} = 0^\circ$) could permit more precisely determining the molecular orientation relative to a surface, but adding in a reasonable amount of vibration ($\theta_{rms} = 10^\circ$) quickly leads to comparable FWHM's for both energies, and an even lower anisotropy $\Delta I/I_{max}$ for 10,000 eV. The negative effect of the lowered total scattering cross section at 10,000 eV is also seen in the larger relative importance of the unscattered waves. In Fig. 59, the overall anisotropy $\Delta I/I_{max}$ in an O1s azimuthal scan is shown as a function of the polar angle at which the scan is made. The two energies and two adsorbate vertical positions are shown separately. These curves make it clear that for either in-plane or above-plane adsorption, the degree of anisotropy falls off much more rapidly with θ for 10,000 eV electrons, and that angles $\lesssim 5-10^\circ$ would be necessary to see significant effects. For $\theta \gtrsim 10^\circ$, almost no anisotropy is seen at 10,000 eV. This is a direct result of the additional peaking in the scattering factors at higher energy. The effects of increasing energy on the detailed form of the azimuthal XPD patterns is also considered elsewhere in detail⁸⁰. Overall, however, it can be concluded that increasing kinetic energy markedly from the present XPD regime of 10^3 eV does not seem to provide any significant advantages for XPD work, even though going to lower energies does seem promising in several respects.

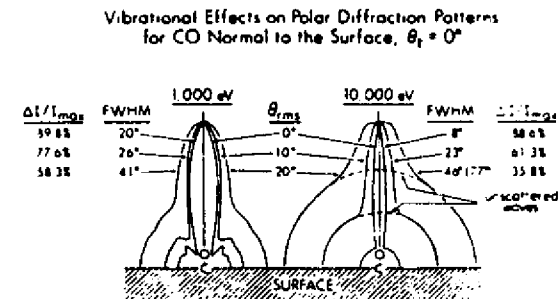


Fig. 58. Vibrational effects on O1s polar dependence in emission from CO oriented normal to a surface ($\theta_t = 0^\circ$) for two electron kinetic energies: 1,000 eV and 10,000 eV. Only the root-mean-squared angular displacement due to vibration is varied from 0° to 20° . (From Thompson, ref. (80).)

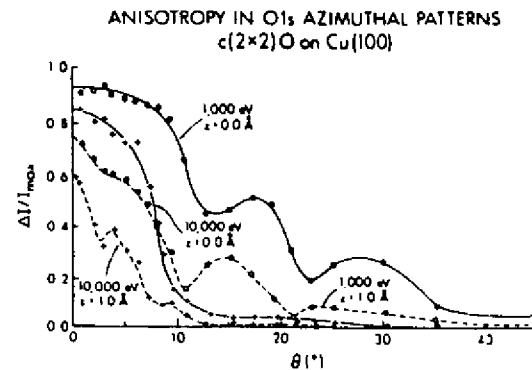


Fig. 59. Dependence of overall XPD anisotropy $\Delta I/I_{max}$ on emission angle θ , adsorbate z position, and electron kinetic energy for $c(2 \times 2)O$ on Cu(001). In general, increasing θ , moving the adsorbate from in-plane ($z = 0.0 \text{ \AA}$) to above-plane ($z = 1.0 \text{ \AA}$), or increasing energy from 1,000 eV to 10,000 eV tends to decrease the anisotropy. (From Thompson, ref. (80).)

G. Diffraction in core-level Auger emission

Inasmuch as Auger emission inevitably accompanies x-ray photoelectron excitation, and also can be produced very easily by other forms of bombardment, for example by electrons, it is of interest to ask whether similar kinds of Auger diffraction effects may arise in emission from a single crystal. For simplicity, we will concentrate on Auger energies in the 500-1500 eV XPS range and on transitions of the core-core-core type that are minimally influenced by chemical effects or valence-level complexities. (In fact, prior studies of the angular distributions of very low energy (≤ 150 eV) core-valence-valence Auger electrons have proven to be rather difficult to interpret, even with the use of multiple-scattering theory^{73,105}.)

Fig. 28 due to Owari et al.⁶⁴ already contains some polar-scan substrate Auger data of this type for the Ge $L_3M_{4,5}M_{4,5}$ transition, which in this case has a kinetic energy of 1147 eV not very different from the Ge3d photoelectron peak at 1457 eV (the deBroglie wavelengths would have a ratio of 1.13, rather close to unity). Comparison of the observed XPD curves (a) and (b) for these two transitions reveals that they are very close in structure. Fig. 60 shows similar azimuthal-scan data due to Orders et al.⁶⁹ for adsorbate core-core-core Auger emission from c(2x2)Se on Ni(001). The Auger transition here is the same as that studied for Ge ($L_3M_{4,5}M_{4,5}$) and it has an energy of 1311 eV extremely close to the Se3p photoelectron peak at 1322 eV; the de Broglie wavelengths here are thus essentially identical. The five curves shown for different polar angles of emission are essentially identical for the Auger and photoelectron peaks. It thus seems clear that in the $\sim 10^3$ eV energy regime and for core-core-core transitions, the predominant source of such Auger anisotropies is final-state scattering and diffraction of exactly the same nature as that discussed in detail here for XPD. By implication, one would also thus expect a single-scattering theory to provide a reasonably good description of such Auger phenomena.

Because of the much different natures of the basic emission processes for photoelectrons and Auger electrons, it might at first sight seem difficult to understand why their overall diffraction effects should be essentially identical for emission at the same kinetic energy. This, however, is easily explained qualitatively in terms of the forward-peaked nature of the electron-atom scattering at these energies. That is, even though the basic Auger emission intensity will be essentially isotropic for a core-core-core transition, in contrast to the polarization-associated directionality of the photoelectron emission (cf. Fig. 34), in either case, it is only for initial emission rather close to the final observation direction \hat{k} that the scattering can be significant enough to produce measureable diffraction effects. Thus, for most current XPS

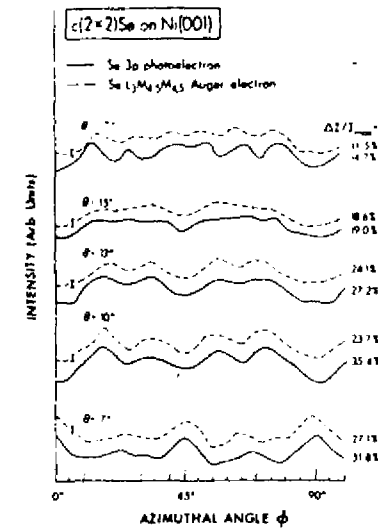


Fig. 60. Comparison of experimentally-observed diffraction effects in azimuthal scans of Se3p photoelectron- and Se $L_3M_{4,5}M_{4,5}$ Auger-emission from c(2x2)Se on Ni(001).

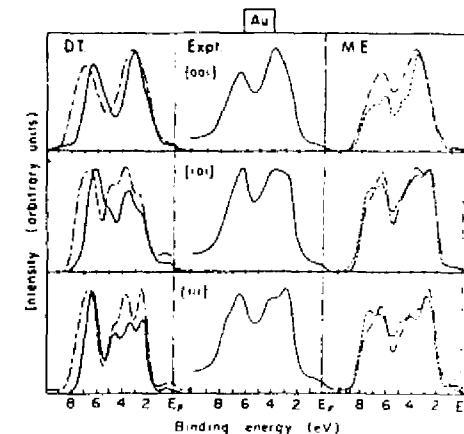


Fig. 61. Some early experimental and theoretical angle-resolved XPS valence spectra for single-crystal Au with electron emission along the [001], [101], and [111] directions. "D.T." represents calculations based upon the direct-transition model, and "M.E." calculations using the plane-wave matrix-element model. The two sets of theoretical curves in each case represent slightly different choices of the band structure used as a starting point (cf. refs. 6, 110, and 111).

experimental geometries, the variation of the primary emission intensity over the solid angle that is effective in producing the diffraction effects will be rather small; overall then, the XPD patterns should look very much like their isotropically-excited Auger counterparts, as is observed experimentally. However, for very special polarization geometries in XPS such as the p case shown in Fig. 51, one would expect the anisotropic character of the primary emission to be more important, and this should lead to inherent differences between photoelectron- and Auger- diffraction effects.

In any case, it is of considerable interest that Auger electrons exhibit effects completely analogous to those of XPD, and this suggests that future cross comparisons of the two types of data could be very useful in structure studies. The same sort of SSC model should also be valuable for interpreting Auger data, perhaps modified so as to assume isotropic initial emission simply by removing the $\hat{e} \cdot \hat{k}$ and $\hat{e} \cdot \hat{p}_j$ factors in Eq. (28).

H. Concluding remarks and comparison to other techniques

Overall then, XPD appears to have considerable potential as a surface structural tool, especially with expected improvements in angular resolution and intensity, as well as with the use of polarized, energy-tunable, synchrotron radiation for excitation. The fact that a very simple single scattering theory appears to describe these effects very well is also an advantage. Intra- and inter-molecular scattering effects can provide very direct and simply interpretable information on adsorbate structures, and similarly simple through-bond scattering has also been observed for adsorption on stepped surfaces. Azimuthal-scan data can also be analyzed by comparison to single-scattering theory so as to derive geometries with accuracies that can be as high as $\pm 0.1 \text{ \AA}$, although for adsorbates situated well above the substrate surface ($\gtrsim 1.0 \text{ \AA}$), further improvements will be needed to achieve high positional accuracy. Analogous Auger diffraction effects at comparable energies of $\sim 500\text{--}1500 \text{ eV}$ may also be useful for structural studies.

A brief comparison to some other currently used surface structural techniques is also worthwhile here. LEED^{41,42} is certainly the most used method to date, but the accumulation of accurate I-V data is a difficult task (certainly of the same order as an XPD experiment) and the final analysis must then proceed via very complex multiple-scattering calculations. Also, rather long-range order over a region of $\gtrsim 100 \text{ \AA}$ in diameter is needed to do LEED, whereas XPD should require only very short range order, or, for certain effects, no long-range order at all beyond that in the substrate. Reflection high-energy electron diffraction (RHEED) with energies of $\sim 10^4 \text{ eV}$ and grazing incidence angles of $\sim 5^\circ$ ¹⁰⁴ is also a close relative of both LEED (in general experimental geometry) and XPD (in using rather high

energies). However, to date only preliminary attempts have been made at deriving quantitative structural information from RHEED¹⁰⁴, even though it is very generally useful in a qualitative sense.

Angle-resolved UPS of valence levels has been shown to provide very useful structural information as well⁷⁻⁹, but this must often rely on a rather complex theoretical analysis of the valence states involved. This analysis may also have to include the detailed matrix elements involved in the photoemission process, although in certain cases, symmetry-based selection rules can be used to semi-quantitatively derive structural information. Angle-resolved UPS of core levels (often referred to as "PhD" for photoelectron diffraction) attempts to do the same thing as XPD, but at much lower energies where a more complex multiple-scattering theory must be used¹⁰⁴; here again long-range order is not necessary. In general, synchrotron radiation is necessary to fully exploit either form of ARUPS.

Two other diffraction-based techniques requiring synchrotron radiation are normal photoelectron diffraction (NPD)^{11,106} (and the closely-related off-normal photoelectron diffraction¹⁰⁷), as well as surface EXAFS or SEXAFS^{98,108}. Neither of these require long-range adsorbate order. Both involve scans of photon energy, but NPD is experimentally more difficult in requiring that a certain core photoelectron peak intensity be monitored accurately throughout this scan; thus the monochromator flux and electron analyzer acceptance must be measured carefully at each $h\nu$, and Auger peaks also may cause interferences at certain $h\nu$ values. By contrast, detection can be much simplified in SEXAFS. NPD seems to require multiple-scattering calculations for comparison to experiment in order to derive adsorbate structures. Prior suggestions of the possibility of Fourier transforming NPD data to more easily derive distance information^{11,106} do not seem to be fully quantitatively justifiable or useful⁸³. By contrast, Fourier transformations of SEXAFS data are routinely used, with accuracies of $\sim 0.05 \text{ \AA}$ appearing to be possible. Thus, although each of these electron-based techniques has certain unique aspects as far as information context, it is also clear that each has certain limitations and/or practical problems of execution.

The use of intramolecular scattering in XPD has already been compared to deriving analogous bond-orientation information from electron stimulated desorption (ESDIAD)⁹⁰ and core-level absorption edge structure measurements⁹¹ in Section 5.c.

Finally, other surface structural techniques involving, for example, different types of ion scattering and x-ray scattering have been reviewed recently by Eisenberger and Feldman¹⁰⁹. It is again clear that each of these techniques has its advantages and disadvantages.

Overall, XPD thus appears to provide various types of structural information that should well complement these other methods and be of general utility in surface science.

6. VALENCE-LEVEL EMISSION FROM SINGLE CRYSTALS

A. Introduction

As the last major subject, we turn to angle-resolved XPS spectra from the valence levels of single-crystals. It was first noted by Baird et al.¹¹⁰ that such angle-resolved valence spectra for Au exhibited significant changes with emission direction, and some of these earliest experimental results are shown in Fig. 61. For electron emission along the three low-index directions [001], [101], and [111], the relative intensities of the two main 5d-band components vary considerably, and there are also noticeable changes in the fine structure within these components. Such angular sensitivity has subsequently been observed in a number of systems encompassing both transition metals and semiconductors, including Ag¹¹¹, Cu¹¹², Pt¹¹³, Si¹¹⁴, MoS₂¹¹⁵, GaSe¹¹⁵, and W¹¹⁶. It is thus clear that there may be no simple connection of a given single-crystal valence band spectrum with something as straightforward as the non-directional total density of electronic states, even though angle-integrated or polycrystalline XPS studies have previously been shown to be capable of deriving density-of-states information⁶. However, the angular dependence of such spectra may provide much more detailed kinds of information concerning the electronic states, and it is toward this end that two rather simple limiting theoretical models have been developed for interpreting such effects. Although much more general treatments of the photoemission process have been presented by several authors¹¹⁷⁻¹¹⁹, these have not been applied to XPS in a quantitative way, and in fact, the higher energy of excitation (vis a vis UPS) makes certain simplifications readily possible. These two simplified models are introduced briefly below, and their likely limitations and domains of applicability are discussed. Comparisons of theory with illustrative experimental spectra are then given.

B. Simple theoretical models

(i) Introduction. A detailed treatment of angle-resolved XPS valence emission would require accurate wave functions for both the initial state and the final state, which involves a photoelectron at $\sim 10^3$ eV. Matrix elements between these two would then have to be evaluated. Although very accurate and complete methods for doing this have been discussed¹¹⁷⁻¹¹⁹, it is convenient and adequate in discussing ARXPS to use as a starting point the simple one-electron, three-step model of photoemission. This model predicts the kinetic energy distribution just outside the surface to be given by:

$$N(E_{kin}) = N(E^f - V_0) = N(E^i + h\nu - V_0) \\ = \sum_{\text{Occ. Bands}} \int \{ \langle \phi_{\vec{k}^f}(E^f = E^i + h\nu) | \vec{A} \cdot \vec{\nabla} | \phi_{\vec{k}^i}(E^i) \rangle \}^2 F(E^i) T(E^f, \vec{k}^f) \\ \times \delta(\vec{k}^f - \vec{k}^i - \vec{g} - \vec{k}_{h\nu}) d^3k^i,$$

where E^f is the final energy of the excitation as measured inside the crystal, E^i is the initial energy from which excitation occurs, $\phi_{\vec{k}^f}$ is a final-state one-electron function corresponding to wave vector \vec{k}^f and energy E^f , $\phi_{\vec{k}^i}$ is the initial-state one-electron function, $\vec{A} \cdot \vec{\nabla}$ is the relevant operator for the radiation, $F(E)$ is the Fermi function (≈ 1.0 for $E < E_{\text{Fermi}}$ and ≈ 0 for $E > E_{\text{Fermi}}$) and T is an escape function that could allow for inelastic scattering effects and internal reflection at the potential barrier V_0 . Energy conservation is implied in setting $E^f = E^i + h\nu$. In XPS, the energies and mean free paths are high enough to assume that emission involves pure bulk states and to set $T = 1.0$ for all but grazing angles of emission (cf. Figs. 5 and 14). The sum is over all occupied bands and the integral over all initial wave vectors \vec{k}^i inside the reduced Brillouin zone. The initial-state band-structure can thus be denoted $E^i(\vec{k}^i)$. The relevant one electron functions are assumed to be Bloch functions due to the full translational periodicity assumed for the crystal, so that the evaluation of the $\vec{A} \cdot \vec{\nabla}$ matrix directly results in a wave-vector conservation relation implied by the delta function:

$$\vec{k}^f = \vec{k}^i + \vec{g} + \vec{k}_{h\nu}. \quad (33)$$

Here \vec{k}^f is the final-state wave vector expressed in an extended zone scheme, \vec{k}^i is the initial-state wave vector expressed in a reduced-zone scheme, \vec{g} is a unique bulk reciprocal lattice vector connecting the two, and $\vec{k}_{h\nu}$ is the wave vector associated with the radiation. In general, $|\vec{k}_{h\nu}| = 2\pi/(\text{radiation wavelength})$. $\vec{k}_{h\nu}$ can be neglected with respect to reduced-zone dimensions in experiments at uv energies, but it cannot be in typical XPS measurements, as will be illustrated below for a specific example. Transitions satisfying Eq. (33) are termed direct transitions or wave-vector conserving transitions. Eqs. (32) and (33) thus implicitly assume long-range order, neglect surface effects except as a potential barrier which may produce refraction at lower takeoff angles, and do not include any consideration of vibrational effects (which can be considered to be the introduction of a type of positional disorder).

At very high energies of excitation such as those in XPS, a further approximation that seems reasonable is to assume a free-electron final state inside the crystal with momentum

$$\vec{p}^f = \hbar \vec{k}^f \quad (34)$$

and energy

$$E^f = E^i + h\nu = \frac{\hbar^2 (k^f)^2}{2m} \quad (35)$$

The observed photoelectron just outside the surface would then have a momentum

$$\vec{p}^f = \hbar \vec{k}^f \quad (36)$$

and energy

$$E_{kin} = E^f - V_0 = \frac{\hbar^2 (k^f)^2}{2m}, \quad (37)$$

with \vec{k}^f being most simply related to \vec{k}^i by refraction at the surface barrier V_0 , as discussed previously in Sec. 3.C. An angle-resolved measurement of E_{kin} and the direction of emission thus determines \vec{k}^f , and, if V_0 is known, \vec{k}^i can then be used to derive \vec{k}^i inside the crystal.

A further point first made by Shevchik¹²⁰ is that vibrational effects can effectively weaken the wave-vector conservation requirement in XPS and introduce a degree of averaging over the entire Brillouin zone such that all \vec{k}^i points can be excited for all emission directions $\vec{k}^f \rightarrow \vec{k}^f$. Such phonon-induced non-direct transitions thus can be described in terms of Eq. (32) simply by removing the delta function so that the integral on \vec{k}^i now can have non-zero contributions for all possible \vec{k}^i values. Let us call this zone-averaged non-direct transition component of emission $N_{NDT}(E_{kin})$ and the direct-transition component as given by Eq. (32) without modification $N_{DT}(E_{kin})$. Since a direct transition can be viewed as a diffraction process, the observed strength of N_{DT} is furthermore reduced by vibrational effects according to a bulk temperature-dependent Debye-Waller factor $W(T)$ as given by Eq. (27); the relevant $\Delta\vec{k}$ is here the reciprocal lattice vector \vec{g} . Then finally the total spectrum can be written as:

$$N_{tot}(E_{kin}, T) = W(T)N_{DT}(E_{kin}) + [1-W(T)]N_{NDT}(E_{kin}). \quad (38)$$

from which it is clear that the Debye-Waller factor represents the fraction of transitions that are direct. Shevchik pointed out that the \vec{g} vectors involved in XPS are sufficiently large that Debye-Waller factors of ~ 0.05 - 0.10 are not uncommon at room temperature, and thus that direct transitions might be very difficult to observe. Experiments with temperature variation also clearly may involve changes in the relative importances of the two component N_{DT} and N_{NDT} .

With this general background, we now discuss the two limiting models.

(ii) The direct-transition model. This model emphasizes the component N_{DT} of Eq. (38) (as calculated from Eq. (32)), and was first proposed by Baird, Wagner, and

Fadley for interpreting angle-resolved XPS spectra¹¹⁰. Rigorous wave-vector conservation according to Eq. (33) is required for a transition to be allowed. The matrix elements $\langle \phi_{\vec{k}^f} | \vec{A} \cdot \vec{p} | \phi_{\vec{k}^i} \rangle$ in Eq. (32) are also assumed to be constant for all allowed transitions, so that each transition is equally weighted in summing and integrating over the band structure $E_i(\vec{k}_i)$. The free-electron dispersion relation of Eq. (35) is also assumed, so that with Eq. (37) and perhaps an allowance for refraction at the surface, the observed energy and wave vector can finally be calculated. As noted previously in XPS, such refraction corrections will only be important for very low take-off angles $\lesssim 10^\circ$, but in applying this same model at lower energies of ~ 40 - 160 eV they have been shown to become more important^{121,122}.

To illustrate the nature of \vec{k} conservation for a typical XPS transition, Fig. 62 shows a scale drawing in \vec{k} space of a possible direct transition in W involving photoelectron emission nearly along the [010] direction. The Brillouin zone radius is approximately $2\pi/a$, where a is the W lattice constant. MgK α radiation is assumed for excitation, leading to k^f values via Eq. (35) that range from $9.18(2\pi/a)$ for emission from the bottom of the 5d bands to $9.20(2\pi/a)$ for emission from the Fermi energy. Thus, the magnitude of \vec{k}^f in XPS is very nearly constant over the full spectrum as judged against the Brillouin zone dimension within which \vec{k}^i is eventually to be located, although this is not true in UPS. The finite solid angle cone of observation of the electron analyzer further distributes the observed \vec{k}^f values over a disc-like region in \vec{k} -space: in Fig. 62, this is taken for illustration to be a cone of 1.5° half angle. \vec{k}_{hv} will in this case be $0.32(2\pi/a)$ and thus clearly non-negligible with respect to Brillouin zone dimensions. Thus, its effect on wave vector conservation must be included. The effect of \vec{k}_{hv} can be allowed for by shifting all points on the \vec{k}^f disc of the observation cone by $-\vec{k}_{hv}$ as shown in Fig. 62. For an assumed angle of 48° between x-ray incidence and electron exit (a characteristic of the spectrometer geometry), this yields the right-hand shaded disc. This disc can then be projected back via one or more \vec{g} vectors to yield \vec{k}^i points within the zone from which emission can occur. The emission geometry here has been arbitrarily chosen so that the \vec{k}^i set is centered along the x axis or [010] direction, and is shown as the left-hand shaded disc. Thus, the large value of \vec{k}^f in XPS produces some degree of averaging in \vec{k}^i via the finite disc sizes involved; in UPS by contrast very little averaging is produced by this effect. Also, this finite size in XPS may make it necessary to use different \vec{g} vectors for different regions of the disc. Thus, this model finally predicts that an angle-resolved N_{DT} spectrum will be proportional to the

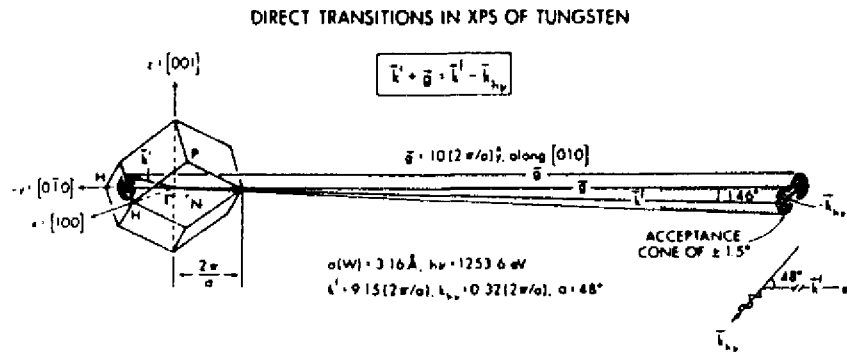


Fig. 62. Scale drawing in \vec{k} -space of the direct transitions that would be allowed for electron emission very nearly along the $[010]$ direction from a W single crystal. An angle α of 48° between photon incidence and electron exit is assumed, together with an analyzer acceptance of $\pm 1.5^\circ$. $\text{MgK}\alpha$ is used for excitation. The emission angle has been chosen so that $\vec{k}^f - \vec{k}_{h\nu} = \vec{k}^i + \vec{g}$ lies exactly along the $[010]$ direction. The angular shift between \vec{k}^f and $\vec{k}^f - \vec{k}_{h\nu}$ is 1.46° , as indicated. Those \vec{k}^i values from which emission could occur will lie on the shaded disc inside of the Brillouin zone at left; the center of this disc lies $-5/8$ of the way from F to H along the $[010]$ direction.

density of electronic states as computed over the allowed \vec{k}^i region or disc, a quantity much different from the total density of states.

This direct-transition model was first shown to successfully describe normal emission angle-resolved UPS spectra from Cu at the lower energies of $40 \lesssim h\nu \lesssim 200 \text{ eV}$ by Wagner et al.¹²³, and it has subsequently also been used to map band structures of metals¹²¹⁻¹²⁵ and semiconductors¹²⁶ in both normal-^{124,125} and off-normal^{121,122,126} emission (where refraction may become important). Its utility in describing XPS spectra we discuss in the next section, but it is important to note that a Debye-Waller factor of too small magnitude would make direct-transition effects very difficult to see. In fact, for the example of Au in Fig. 61 at room temperature, $W = 0.04$, so that direct transition effects would certainly be very weak at that temperature; cooling Au to 4°K would by contrast yield approximately 65% direct transitions in Eq. (38).

(iii) The plane-wave matrix-element model. The second approach was first discussed in connection with XPS by McFeely et al.¹¹¹ Although Eq. (32) is again used as a starting point, it is here assumed that \vec{k} conservation is somehow not an important selection rule, or equivalently that all \vec{k}^i values in the zone can contribute to emission in a given \vec{k}^f direction. The most likely source of this full \vec{k}^i averaging is vibrational effects, as pointed out by Shevchik¹²⁰, but it was also originally suggested that final-state complexities due to electron scattering might cause such averaging as well¹¹¹. In this limit of complete zone averaging, only the matrix elements of Eq. (32) remain as weighting factors of all of the occupied initial states to produce variations in spectra with direction. These matrix elements are further assumed to be calculable by using plane-wave or free-electron final states of the form $\phi_{\vec{k}^f}(\vec{r}) = \exp(i\vec{k}^f \cdot \vec{r})$, and tight-binding or LCAO initial states. The matrix elements then can be shown to have the form of linear combinations of Fourier transforms of atomic orbitals. There is also a further simplification in that the angular shape of the orbital in real space (for example, p_x or $d_{x^2-y^2}$) is preserved in the Fourier transform in \vec{k}^f space (for example, a p_x orbital shows preferred emission along $\pm x$, and a $d_{x^2-y^2}$ orbital along $\pm x, \pm y$). Thus, information concerning the atomic-orbital makeup of a given set of levels is in principle derivable by analyzing the directionality of emission.

This plane-wave matrix-element model would not be expected to be useful at low energies where direct transitions are generally more important, and moreover the final states are expected to be much more complex than plane waves. In fact, the use of such matrix elements in Eq. (32) in an attempt to improve upon

direct-transition model calculations for Cu at ~ 40 -200 eV was found to markedly decrease agreement with experiment¹²³.

C. Comparisons of experiment and theory

Fig. 61 shows results of some of the earliest XPS studies of this type and compares XPS spectra for Au with emission along [001], [101], and [111] with theoretical curves generated by both the direct-transition (DT) and plane-wave matrix-element (ME) models^{6,110,111}. Although the DT model predicts more change than is seen experimentally, both models qualitatively agree with the spectral variations seen experimentally. However, as already pointed out, the Debye-Waller factor for this case is only 0.04, so that the DT model is not appropriate for this particular case and its agreement with experiment must be viewed as fortuitous. However, Sayers and McFeely¹²⁷ and Goldberg et al.²⁵ have subsequently made more accurate matrix-element calculations relevant to zone-averaged tight-binding matrix-elements and they conclude that much of the ME agreement in Fig. 61 is fortuitous as well. Ley et al.¹¹⁵ have however, been able to use this model in describing changes in angle-resolved XPS spectra from MoS₂, GaSe₂, and SnSe₂. Thus, it remains to fully resolve the degree to which the plane-wave matrix-element model can be used in XPS for systems where full zone averaging is expected.

A final important question is thus whether direct transitions can be observed at all in XPS, but this has been unambiguously resolved in the affirmative with recent studies by Hussain and co-workers^{10,116}. The tungsten system chosen for study has an especially high Debye-Waller factor at room temperature: $W = 0.55$ at 300K. Thus $\sim 55\%$ of the transitions at this temperature ought to be direct, and angle scans might be expected to produce spectral variations predictable by the direct-transition model. Also, raising the temperature would be expected according to Eq. (38) to reduce the effect of direct transitions, leading to more importance of zone-averaged matrix elements via N_{NDT} ; thus, any significant change in spectra with temperature would be suggestive of direct transitions.

Fig. 63 shows a room-temperature azimuthal scan of W valence spectra at a polar angle of $\theta = 63.4^\circ$ with respect to the (001)-oriented crystal surface; the azimuthal steps were 5° . The solid-curve experimental spectra show marked changes with angle, particularly as to the relative intensities of the components labelled 1-3. Component 1 at ~ 4.8 eV below E_F in particular is very strong at $\phi = 0^\circ$ and 45° , and very weak at $\phi \sim 15^\circ$. The dashed curves in the figure are based on the direct-transition model and make use of Eq. (38) with N_{NDT} taken to be the total density of states for W as a reasonable first approximation to this quantity that

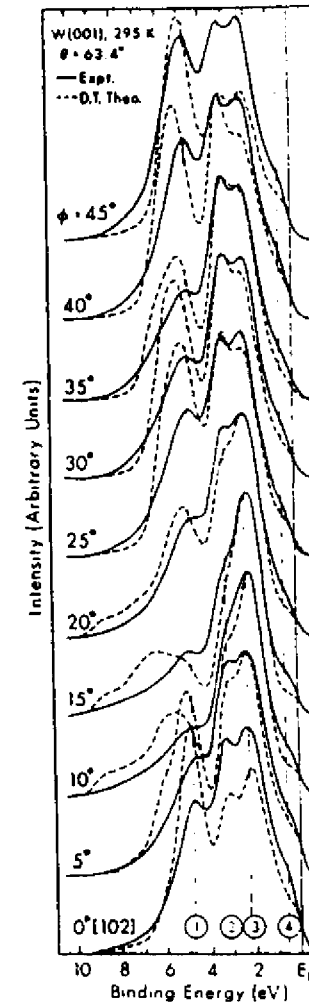


Fig. 63. Tungsten XPS valence-band spectra at $T = 295^\circ\text{K}$ for a 5° -step azimuthal scan from $\phi = 0^\circ$ to 45° and a polar angle of 63.4° . Experimental curves (solid lines) are compared to theoretical curves (dashed lines) as calculated using Eq. (38), with $I_{\text{NDT}}(E)$ assumed to be proportional to the total density of states. (From Hussain et al., ref. (116).)

is in any case not expected to change rapidly with direction. Even though this theory thus totally neglects matrix element effects in both N_{DT} and N_{NDT} , it correctly predicts all of the trends in relative intensity change found experimentally, including for example, the marked drop in importance of the 4.8 eV peak at $\phi \approx 15^\circ$. As a more quantitative indicator of the peak intensity changes with ϕ , Fig. 64 shows the ratio of the 4.8 eV peak to that at 2.3 eV for the azimuthal scan of Fig. 63 and another at $\theta=33^\circ$. Here again all of the experimental features are predicted by the direct-transition model, even if somewhat more dramatically than is actually observed. Some of the small discrepancies remaining are no doubt due to the neglect of matrix elements in the model. Similar agreement is found also for peak intensity ratios from polar scans of spectra¹¹⁶.

A further important observation made in this work¹¹⁶ is that the photon wave vector clearly influences the wave vector conservation in the manner expected. Fig. 65 overlays a pair of 2° -step symmetry-related polar scans around the [102] and [201] directions, and these would be superimposable with the [102] spectrum over that at [201] if \vec{k}_{hv} were not significant. Including the effect of \vec{k}_{hv} (as shown in the figure insets) produces a 4.0° shift in matching the two scans. This shift, together with a 0.6° refraction correction, yields an overall value of 4.6° in very good agreement with the 6.0° empirical shift needed to make the spectra optimally agree with one another. Without such a shift, the agreement is very poor, for example, the [102] and [201] spectra are very different.

The pronounced temperature dependence of W valence spectra also supports the presence of direct transitions in W near room temperature¹¹⁶, as is shown in Fig. 66. Here, spectra obtained at two azimuths that are 6° apart for $\theta = 33^\circ$ are shown as a function of temperature. At 295 K with a Debye-Waller factor of 0.55, the two spectra are very different, particularly as regards the 4.8 eV component, but they become essentially identical at 1000K where the Debye-Waller factor is down to 0.14. The marked difference at 295K suggests direct transitions, as zone-averaged matrix elements by themselves would not be expected to alter intensities that rapidly with ϕ . Conversely, the near identity of the spectra at 1000K is thus attributed to the slow variation of the now dominant zone-averaged matrix elements with direction.

Such temperature-dependent data can also be used to decompose spectra into their N_{DT} and N_{NDT} components¹¹⁶, as Eq. (38) indicates that measurements of N_{tot} at any two temperatures, together with calculated W values at those temperatures, can be used to solve for N_{DT} and N_{NDT} . This is found to yield self-consistent decompositions into components for various spectra and various pairs of temperatures, as shown in Fig. 67. The direct-transition components so isolated

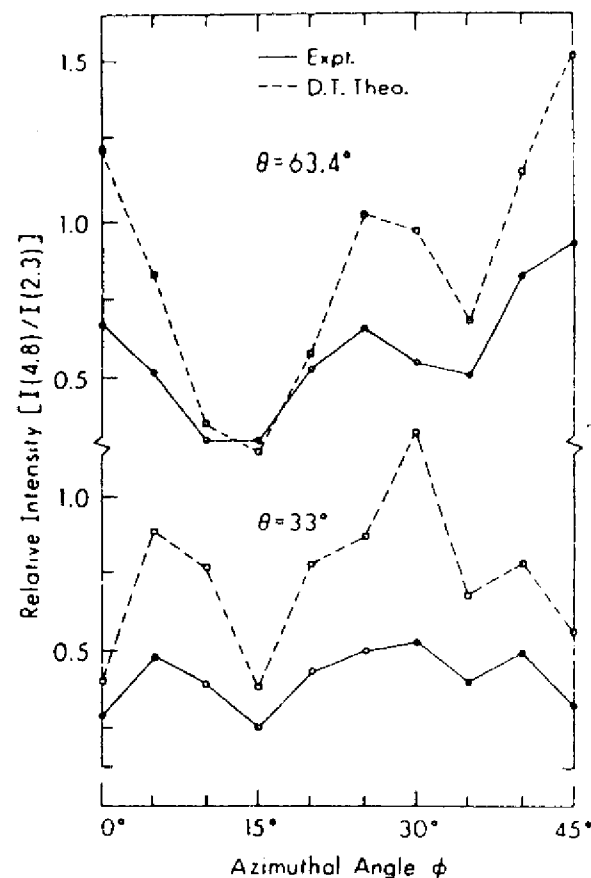


Fig. 64. Azimuthal dependence at $T = 295^\circ\text{K}$ of the relative intensity of the W valence-band peak at -4.8 eV (cf. Fig. 63). The intensity of this peak is measured with respect to that at -2.3 eV, and results are shown for polar angles of both 63.4° and 33° . Both experimental and direct-transition theoretical curves are shown. (From Hussain et al., ref. (116).)

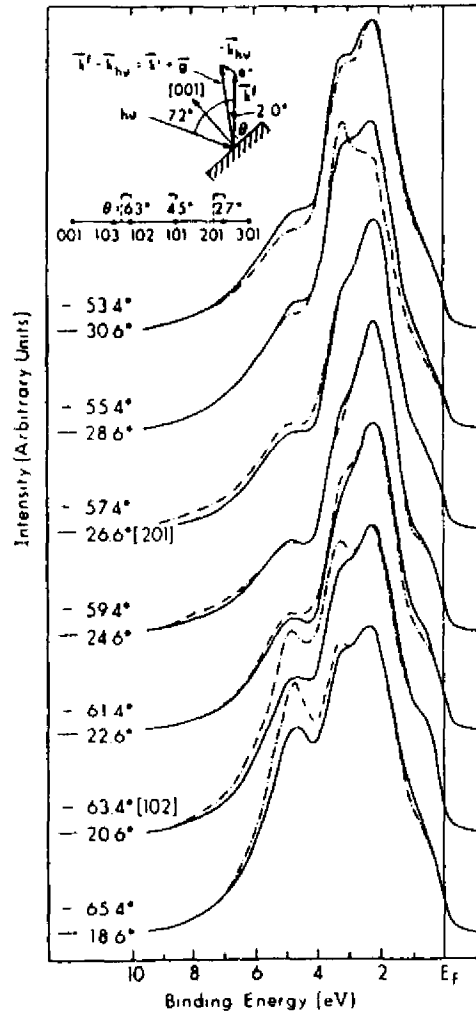


Fig. 55. Effect of photon wave vector $\vec{k}_{h\nu}$ on wave vector conservation in W valence-band emission at $T = 295$ K. A shift of 6.0° is needed in order to match spectra obtained at $\phi = 0^\circ$ and various θ values near the symmetry-equivalent [201] and [102] directions; most of this shift is due to $\vec{k}_{h\nu}$, as explained in the insets. (From Hussain et al., ref. (116).)

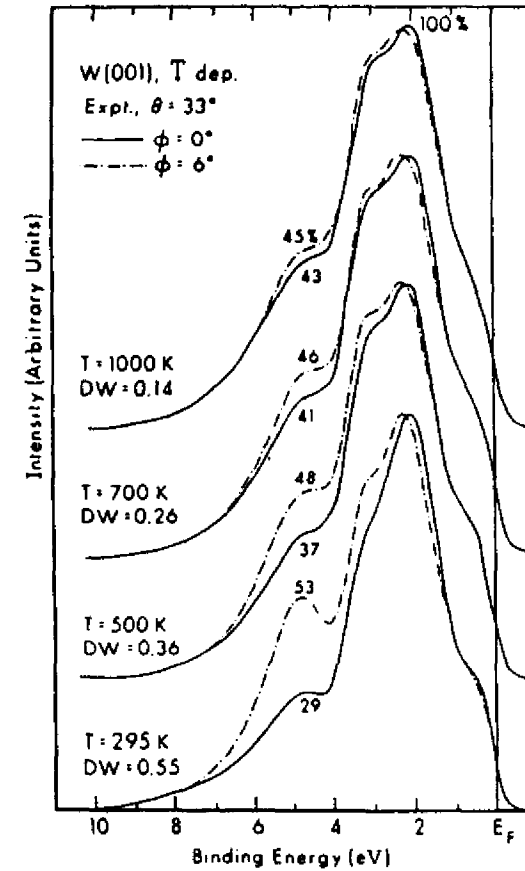


Fig. 56. Temperature dependence of W valence-band spectra for $\theta = 33^\circ$ and emission along two azimuths separated by 6° . The temperatures and their associated Debye-Waller factors are also given, along with the relative intensity of the peak at -4.8 eV (as measured in % of that at -2.3 eV). (From Hussain et al., ref. (116).)

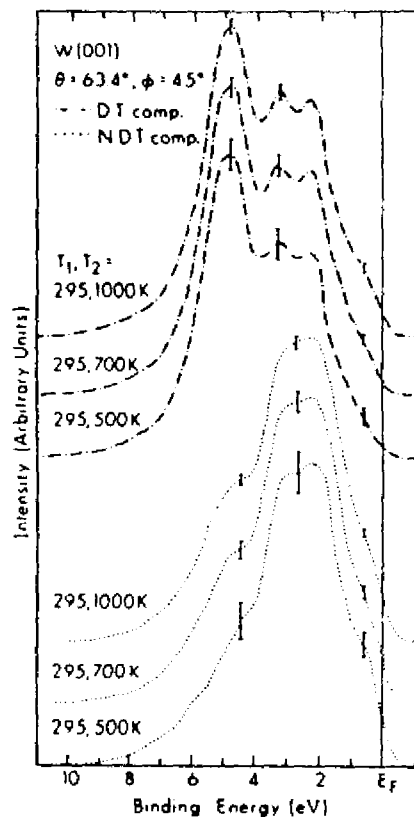


Fig. 67. Use of temperature-dependent W valence spectra to decompose measured intensities into their direct-transition and non-direct transition components with the use of Eq. (38). Different pairs of temperatures yield essentially the same results. (From Hussain et al., ref. (116).)

furthermore agree very well with pure direct-transition calculations of N_{DT} only. This method thus could be very useful in future band-mapping studies using XPS.

As a further example, Hussain et al.¹⁰ have carried out the first swept-hv angle-resolved XPS study of valence spectra, again on tungsten to emphasize direct transition involvement. These measurements were done in normal emission from W (011) with monochromatized synchrotron radiation in the range 1100-1250 eV. Some of the results are shown in Fig. 68 together with direct transition calculations of the same type as those in Fig. 63. The agreement with experiment is thus excellent, especially with regard to the relative intensity change of the peak at ~ 4.8 eV, thereby providing more support for the applicability of the simple direct-transition model.

As a final point concerning the direct-transition model, one can ask why it works as well as it does and why, for example, complexities in the final state wave function do not cause significant deviations from it.^{111,128} Such final-state complexities can be considered most simply as the mixing in of other plane-wave components $\exp(i(\vec{k}^f + \vec{g}') \cdot \vec{r})$ to an initial $\exp(i\vec{k}^f \cdot \vec{r})$ excitation via diffraction events associated with the reciprocal lattice vectors \vec{g}' . Here, \vec{g}' is not the same as the \vec{g} involved in the primary \vec{k} conservation, but may be another bulk \vec{g} vector or a vector associated with the reciprocal lattice of the surface. That such \vec{g}' mixing events may be very weak in XPS is reasonable in view of the forward-peaked nature of the electron-atom scattering factors (cf. discussion of Sec. 5.B) that must be involved in producing such diffracted waves. An additional effect of possible importance is a smearing in \vec{k}^f due to the inelastic scattering that effectively limits the wave function to a region of order Λ_e in size along its propagation direction¹¹⁹. Thus, the uncertainty principle dictates $\Delta k^f \Lambda_e \sim 1/2$ or $\Delta k \sim 1/2\Lambda_e$ as a reasonable estimate of such smearing. That is, a \vec{k}^f disc such as that in Fig. 62 will come to have an added thickness Δk^f along \vec{k}^f . However, for the specific example of W with a mean free path in XPS of ~ 13 Å, $\Delta k^f \sim 0.02(2\pi/a)$, which is not very large compared to the Brillouin zone size as represented by $(2\pi/a)$. Direct calculations also verify that this much smearing along the propagation direction does not significantly alter the predicted XPS spectra,¹¹⁶ even though such Δk^f effects appear to be important for understanding UPS spectra in the 40-200 eV region¹²². Thus neither of these two final-state complexities appears to be highly significant in describing XPS valence spectra.

D. Concluding remarks

In conclusion, although it may at first sight appear to be difficult to see direct-transition effects in the XPS spectra of many systems due to Debye-Waller

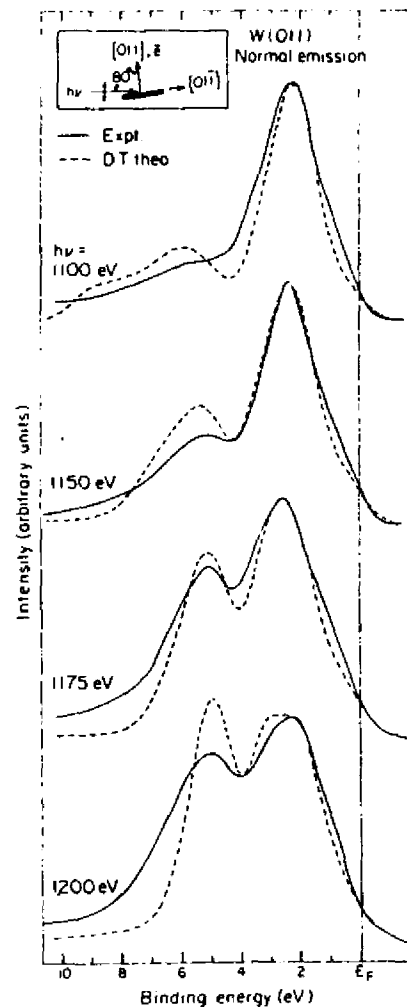


Fig. 6B. Comparison of direct-transition theory to the first XPS valence-band experiments making use of tunable synchrotron radiation. Emission was normal to a W(011) surface; the geometry is shown as an inset. (From Hussain et al., ref. (10).)

attenuation, the inherent simplicity of the theoretical model which describes such effects at high energies of emission makes such measurements very appealing for band-structure studies. In fact, with the possible use of cryogenic cooling to increase W (see table of representative values for different elements in ref. 116) and multi-temperature measurements to permit isolating the direct-transition component, it should be possible to expand the range of systems that could be studied in this way. Using synchrotron radiation at lower energies of ~ 200 -400 eV would also reduce $|\vec{q}|$ and thus increase W while at the same time probably retaining the desired theoretical simplicity. Also, decreasing the angular acceptance of the analyzer would be very beneficial in reducing the size of the disc over which \vec{k}^{\parallel} is averaged, thereby providing more precise band mapping information.

To provide some indication as to how much increased angular resolution might affect such spectra, Fig. 69 shows recent direct-transition theoretical curves by Hussain and Fadley¹²⁹ for several very close-lying emission directions above a W (001) surface at two different angular apertures: $\pm 1.5^\circ$ and $\pm 3.0^\circ$ (at about which all prior XPS experiments have been carried out). It is clear that the $\pm 1.5^\circ$ curves are much more sensitive than the $\pm 3.0^\circ$ curves to small changes in emission direction. The $\pm 3.0^\circ$ curves are expected to show a greater degree of zone averaging, and this is borne out by the fact that at least some non-zero direct-transition intensity is predicted over the entire valence band region from 0-7 eV for all of the angles shown. By contrast, the $\pm 1.5^\circ$ curves exhibit greater differences, sharper features, and regions of zero predicted intensity (e.g., at ~ 3 eV for $\theta = 56^\circ$ and 57°). Furthermore, an analysis of these calculations shows that the $\pm 1.5^\circ$ curves for certain angles directly reflect that the \vec{k}^{\parallel} disc is centered very near a high-symmetry Brillouin zone point. For example, for $\theta = 53^\circ$, the disc center is near N and the 3-peaked structure reflects the 3 bands there¹³⁰, whereas for $\theta = 56^\circ, 57^\circ$, the disc is near H where only a single low-lying band lies below the Fermi level¹³⁰. The positions of the major peaks noted at these angles also correlate very well with band positions. Thus, for the first time, it is possible to predict that high-angular-resolution XPS can provide detailed point-by-point mapping of band structures. Recent experiments on W in our laboratory at a $\pm 1.5^\circ$ resolution¹³¹ also confirm this enhanced sensitivity to angle, and the results are also consistent with direct-transition theory.

Finally, it would certainly be of interest from a theoretical point of view to further explore the calculation of the relevant $\vec{A} \cdot \vec{v}$ matrix elements involved in such studies, as a fully accurate treatment of either direct transitions or zone-averaged non-direct transitions requires accounting for them and it is at present unclear as to whether a simple model can be reliably used to include them.

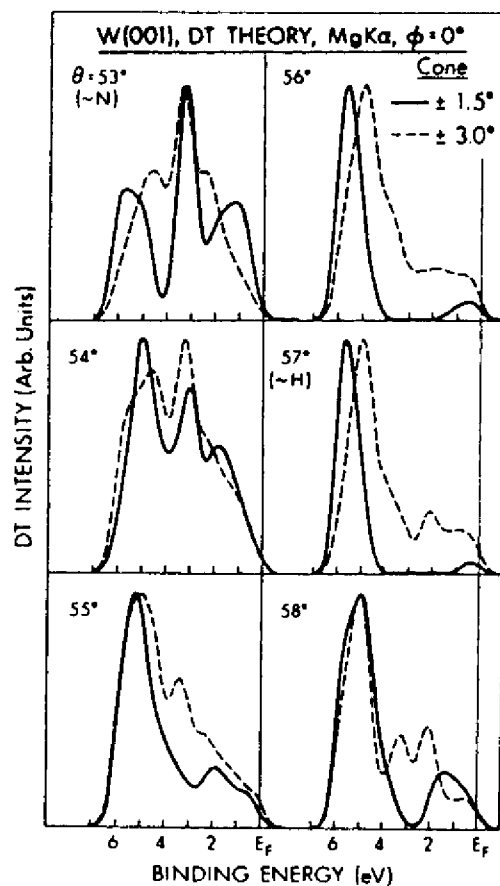


Fig. 69. The effect of increased angular resolution on the direct-transition component of W valence-band emission. Pure direct-transition theoretical curves are compared for a $\pm 3.0^\circ$ analyzer acceptance (dashed curves) and for a $\pm 1.5^\circ$ acceptance (solid curves). ϕ is fixed at 0° and θ is scanned in 1° -steps from 53° to 58° . For $\theta = 53^\circ$ and 57° , the discs of allowed \vec{k} points are very close to the N and H points in the Brillouin zone, respectively, as indicated (cf. Fig. 62).

As a final comparison to the closely-related use of angle-resolved UPS to study valence levels⁷⁻⁹, it is clear that this technique has contributed very much to our understanding of both bulk- and surface- electronic structure. In general, it can be carried out at higher resolutions than ARXPS (~ 0.2 - 0.3 eV in UPS compared to ~ 0.5 - 1.0 eV in XPS), and both phonon effects and \vec{k} smearing due to the finite analyzer acceptance core are much less as problems due to the much smaller energies involved. However, a detailed analysis of ARUPS data may require knowledge of both the initial- and final- state band structures, as well as a proper inclusion of both matrix elements and multiple-scattering effects. In ARXPS, by contrast, a very simple theory seems to describe the data very well, at least as far as the direct transition component is concerned. Thus, it seems that ARXPS will serve as a very useful complement to ARUPS, especially in bulk band structure studies.

Acknowledgements

In connection with those aspects of this review involving work at the University of Hawaii, the author is very much indebted to his several colleagues for their considerable contributions to the development of angle-resolved x-ray photoelectron spectroscopy. This group includes R. J. Baird, S. M. Goldberg, Z. Hussain, P. F. Heden, S. Kono, P. J. Orders, L.-G. Petersson, K. A. Thompson, and L. F. Wagner. Many helpful comments from B. L. Henke are also appreciated. The support of the National Science Foundation, the Petroleum Research Fund, and N.A.T.O. is also gratefully acknowledged. The hospitality of the Department of Physics, Montana State University during a portion of the writing of this manuscript is also very much appreciated. The author is also grateful to E. A. Stern for some very helpful comments concerning EXAFS theory and its relationship to XPD.

References

1. J. Jenkin, *J. Elect. Spect.*, **23**, 137 (1981).
 2. K. Siegbahn, U. Gelius, H. Siegbahn, and E. Olsen, *Phys. Lett.*, **32A**, 221 (1970).
 3. C. S. Fadley and S. A. L. Bergstrom, *Phys. Lett.*, **35A**, 375 (1971); and in *Electron Spectroscopy*, D. A. Shirley, ed., North Holland, Amsterdam (1972), p. 233.
 4. C. S. Fadley, R. J. Baird, W. Siekhaus, T. Novakov, and S. A. L. Bergstrom, review in *J. Elect. Spect.*, **4**, 93 (1974).
 5. C. S. Fadley, review in *Prog. in So. Sci. Chem.*, G. A. Samorjai and J. D. McCaldin, eds., Pergamon Press, New York (1976), Vol. 11, p. 265.
 6. C. S. Fadley, review in *Electron Spectroscopy: Theory, Techniques, and Applications*, C. R. Brundle and A.D. Baker, eds., Academic Press, London (1978), Vol. 2, Ch. 1.
 7. B. Feuerbacher, B. Filton, and R. F. Willis, eds., *Photoemission and the Electronic Properties of Surfaces*, Wiley, New York (1978).
 8. M. Cardona and L. Ley, eds., *Photoemission in Solids*, Springer-Verlag, Berlin (1978), Vols. 1 and 2.
 9. E. W. Plummer and W. Eberhardt, review in *Adv. in Chem. Phys.*, L. Prigogine and S. A. Rice, eds., John Wiley, New York (1982), Vol. XLIX, p. 533.
 10. Z. Hussain, E. Umbach, J. J. Barton, J. G. Tobin, and D. A. Shirley, *Phys. Rev.*, **B 25**, 672 (1982).
 11. S. D. Kevan, D. H. Rosenblatt, D. Denley, B.-C. Lu, and D. A. Shirley, *Phys. Rev.*, **B 20**, 4133 (1979); Z. Hussain, D. A. Shirley, C. H. Li, and S. Y. Tong, *Proc. Nat. Acad. Sci. (U.S.A.)*, **78**, 5293 (1981).
 12. R. J. Baird and C. S. Fadley, *J. Elect. Spect.*, **11**, 39 (1977).
 13. E. W. Plummer, *Nucl. Inst. and Meth.*, **177**, 179 (1980).
 14. N. V. Smith, in *Photoemission in Solids*, M. Cardona and L. Ley, eds., Springer-Verlag, Berlin (1978), Ch. 6.; N. V. Smith, P. K. Larsen, and M. M. Traum, *Rev. Sci. Inst.*, **48**, 454 (1977).
 15. R. Z. Bachrach, S. B. M. Hagstrom, and F. C. Brown, in *Vacuum Ultraviolet Radiation Physics*, E. E. Koch, R. Haensel, and C. Kunz, eds., Pergamon, London (1974), p. 795; G. V. Hansson, B. Goldberg, and R. Z. Bachrach, *Rev. Sci. Inst.*, **52**, 517 (1981).
 16. C. J. Powell, *Surf. Sci.*, **44**, 29 (1974).
 17. I. Lindau and W. E. Spicer, *J. Elect. Spect.*, **3**, 409 (1974).
 18. M. P. Seah and D. P. Dench, *Surf. Int. Anal.*, **1**, 2 (1979).
 19. J. M. Hill, D. G. Royce, C. S. Fadley, L. F. Wagner, and F. J. Grunthaner, *Chem. Phys. Lett.*, **44**, 225 (1976).
 20. R. P. Vasquez, J. D. Klein, J. J. Barton, and F. J. Grunthaner, *J. Elect. Spect.*, **23**, 63 (1981).
 21. B. L. Henke, *Phys. Rev.*, **A 6**, 94 (1972).
 22. W. A. Fraser, J. V. Florio, W. N. Delgass, and W. D. Robertson, *Surf. Sci.*, **36**, 661 (1973).
 23. J. H. Scofield, *J. Elect. Spect.*, **8**, 129 (1976).
 24. R. F. Rielman, Alfred Msezane, and S. T. Manson, *J. Elect. Spect.*, **8**, 389 (1976).
 25. S. M. Goldberg, C. S. Fadley, and S. Kono, *J. Elect. Spect.*, **21**, 285 (1981); *Solid State Commun.*, **28**, 459 (1978).
 26. D. R. Penn, *J. Elect. Spect.*, **9**, 29 (1976) and *J. Vac. Sci. Tech.*, **13**, 221 (1976).
 27. V. I. Nefedov, N. P. Sergushin, I. M. Band, and M. B. Trzhaskowskaya, *J. Elect. Spect.*, **2**, 383 (1973).
 28. W. J. Carter, G. K. Schweitzer, and T. A. Carlson, *J. Elect. Spect.*, **5**, 827 (1974); T. A. Carlson, *Surf. and Int. Anal.*, **4**, 125 (1982).
 29. C. J. Powell and P. E. Larson, *Appl. Surf. Sci.*, **1**, 186 (1977).
 30. D. T. Clark and H. R. Thomas, *J. Polym. Sci. (Polym. Chem. Ed.)*, **15**, 1093 (1977).
 31. C. S. Fadley, *J. Elect. Spect.*, **5**, 725 (1974).
 32. J. Brunner and H. Zogg, *J. Elect. Spect.*, **5**, 911 (1977).
 - *33. R. E. Connelly, M.S. Thesis, Univ. of Hawaii (1982); and R. E. Connelly and C. S. Fadley, to be published.
 34. G. Hollinger and M. Pijolat, *Surf. Sci.*, **105**, 114 (1981); and M. Pijolat, doctoral thesis, Univ. Claude Bernard, Lyon, France (1980).
 35. R. P. Vasquez and F. J. Grunthaner, *Surf. Sci.*, **99**, 681 (1980), and references therein.
 36. D. T. Clark and H. R. Thomas, *J. Polym. Sci. (Polym. Chem., Ed.)*, **15**, 2843 (1977).
 37. R. J. Baird, Ph.D. thesis, Univ. of Hawaii (1977).
 38. R. J. Baird, C. S. Fadley, S. Kawamoto, and M. Mehta, *Chem. Phys. Lett.*, **34**, 49 (1975).
 39. R. J. Baird, C. S. Fadley, S. Kawamoto, M. Mehta, R. Alvarez, and J. A. Silva, *Anal. Chem.*, **48**, 843 (1976).
 40. O. A. Baschenko and V. I. Nefedov, *J. Elect. Spect.*, **17**, 405 (1979); **21**, 153 (1980); and **26**, 109 (1982).
 41. J. B. Pendry, *Low Energy Electron Diffraction*, Academic Press, London (1974).
 42. M. A. Van Hove and S. Y. Tong, *Surface Crystallography by LEED*, Springer-Verlag, New York (1979).
 43. M. F. Ebel and W. Liebe, *J. Elect. Spect.*, **16**, 463 (1979).
 44. J. C. Ashley and V. E. Anderson, *J. Elect. Spect.*, **24**, 127 (1981) and *IEEE Trans. on Nucl. Sci.*, **NS-28**, 4132 (1981).
 45. J. E. Demuth, D. W. Jepsen, and P. M. Marcus, *Phys. Rev. Lett.*, **32**, 1182 (1974); D. H. Rosenblatt et al., *Phys. Rev.*, **B 23**, 3828 (1981); S. Brennan, J. Stöhr, and R. Jaeger, *Phys. Rev.*, **B 24**, 4871 (1981).
 46. M. Aono, C. Oshima, T. Tanaka, E. Bannai, and S. Kawai, *J. Appl. Phys.*, **49**, 2761 (1978).
 47. A. Jablonski, *Adv. in Coll. and Int. Sci.*, **8**, 213 (1977).
 48. V. I. Nefedov, P. P. Pozdeyev, V. F. Dorfman, and B. N. Pypkin, *Surf. and Int. Anal.*, **2**, 26 (1980).
 49. W. N. Delgass, G. L. Haller, and J. H. Lunsford, *Spectroscopy in Heterogeneous Catalysis*, Academic Press, New York (1979), Ch. 8; P. J. Angevine, J. C. Vartuli, and W. N. Delgass, *Proc. 6th Int. Cong. Catal.*, London, 1976, **2**, 611 (1977).
 50. J. Finster, P. Lorenz, and A. Meisel, *Surf. and Int. Anal.*, **1**, 179 (1979).
 51. P. H. Citrin and G. K. Wertheim, *Phys. Rev. Lett.*, **41**, 1425 (1978).
 52. F. M. Duc, C. Guillot, Y. Lassailly, J. Lecante, Y. Jugnet, and J. C. Vedrine, *Phys. Rev. Lett.*, **43**, 789 (1979); J. F. van der Veen, F. J. Himpsel, and D. E. Eastman, *Phys. Rev. Lett.*, **44**, 189 (1980).
 53. G. K. Wertheim and G. Creelius, *Phys. Rev. Lett.*, **40**, 813 (1978).
 54. R. Haydock and M. J. Kelly, *Surf. Sci.*, **38**, 139 (1973); M. C. Dejonqueres and M. Cyrot-Lackmann, *Surf. Sci.*, **53**, 429 (1975); K. S. Sohn, D. G. Dempsey, L. Kleinmann, and E. Caruthers, *Phys. Rev.*, **B 13**, 1515 (1976); **B 14**, 3185, 3193 (1976).
 55. M. Mehta and C. S. Fadley, *Phys. Rev. Lett.*, **39**, 1569 (1977); *Phys. Rev.*, **B 20**, 2280 (1979).
 56. D. G. Dempsey and L. Kleinmann, private communication.
 57. R. J. Baird, C. S. Fadley, S. M. Goldberg, P. J. Feibelman, and M. Sunjic, *Surf. Sci.*, **72**, 495 (1978).
 58. A. B. Bradshaw, W. Domcke, and L. S. Cederbaum, *Phys. Rev.*, **B 16**, 1480 (1977).
-
- * Now appearing as:
33. R. E. Connelly, C. S. Fadley, and P. J. Orders, *J. Vac. Sci. Tech.*, **A2**, 1333 (1984).

59. M. Mehta and C. S. Fadley, *Phys. Lett.*, **A55**, 59 (1975).
 60. M. Mehta and C. S. Fadley, unpublished results.
 61. M. Mehta and C. S. Fadley, *Chem. Phys. Lett.*, **46**, 225 (1977).
 62. S. Kono, S. M. Goldberg, N. F. T. Hall, and C. S. Fadley, *Phys. Rev. Lett.*, **41**, 1831 (1978); L.-G. Petersson, S. Kono, N. F. T. Hall, C. S. Fadley, and J. B. Pendry, *Phys. Rev. Lett.*, **42**, 1545 (1979).
 63. S. Kono, S. M. Goldberg, N. F. T. Hall, and C. S. Fadley, *Phys. Rev.*, **B 22**, 6085 (1980).
 64. M. Owari, M. Kudo, Y. Nihei, and H. Kamada, *J. Elect. Spect.*, **21**, 131 (1981).
 65. R. J. Baird, C. S. Fadley, and L. F. Wagner, *Phys. Rev.*, **8 15**, 666 (1977).
 66. J. M. Adams, S. Evans, J. M. Thomas, *J. Am. Chem. Soc.*, **100**, 3260 (1978); S. Evans, E. Raftery, and J. M. Thomas, *Surf. Sci.*, **89**, 64 (1979).
 67. N. Koshizaki, M. Kudo, M. Owari, Y. Nihei, and H. Kamada, *Jap. J. Appl. Phys.*, **19**, L349 (1980).
 68. A. Liebsch, *Phys. Rev. Lett.*, **32**, 1203 (1974); *Phys. Rev.*, **8 13**, 544 (1976).
 69. P. J. Orders, R. E. Connelly, N. F. T. Hall, and C. S. Fadley, *Phys. Rev.*, **B 24**, 6163 (1981).
 70. R. N. Lindsay, C. G. Kinnibergh, and J. B. Pendry, *J. Elect. Spect.*, **15**, 157 (1979).
 71. T. Fujikawa, *J. Phys. Soc. Jap.*, **50**, 1321 (1981); **51**, 251 (1982); and *J. Elect. Spect.*, **26**, 79 (1982).
 72. P. A. Lee, *Phys. Rev.*, **8 13**, 5261 (1976).
 73. P. A. Lee and G. Beni, *Phys. Rev.*, **8 15**, 2862 (1977).
 74. L. McDonnell, D. P. Woodruff, and B. W. Holland, *Surf. Sci.*, **51**, 249 (1975).
 75. Z. Hussain and D. A. Shirley, XPD results for sulfur s- and p- emission to be published. (Cf. also ref. 107.)
 76. P. A. Lee and J. B. Pendry, *Phys. Rev.*, **B 11**, 2795 (1975).
 77. L.-G. Petersson, S. Kono, N. F. T. Hall, C. S. Fadley, and J. B. Pendry, *Phys. Rev. Lett.*, **42**, 1545 (1979).
 78. L. I. Schiff, *Quantum Mechanics*, McGraw-Hill, New York (1968), pp. 136-137 and 324-325.
 79. M. Fink and A. C. Yates, *At. Data*, **1**, 385 (1970); M. Fink and J. Ingram, *At. Data*, **4**, 129 (1972).
 80. K. A. Thompson, Ph.D. Thesis, Univ. of Hawaii (1981); K. A. Thompson and C. S. Fadley, to be published.
 81. P. J. Orders, S. Kono, C. S. Fadley, R. Trehan, and J. T. Lloyd, *Surf. Sci.*, **119**, 371 (1982).
 82. B. K. Teo and P. A. Lee, *J. Am. Chem. Soc.*, **101**, 2815 (1979).
 83. P. J. Orders and C. S. Fadley, *Phys. Rev.*, **8**, to appear.
 84. P. J. Orders, J. T. Lloyd, and C. S. Fadley, unpublished results for substrate Ni azimuthal XPD.
 85. S. Kono, *Myomen Kagaku (Surface Science)*, **2**, 153 (1981).
 86. S. Takahashi, S. Kono, H. Sakurai, and T. Sagawa, *J. Phys. Soc. Jap.*, **51**, 3296 (1982).
 87. M. Owari, M. Kudo, Y. Nihei, and H. Kamada; and Y. Nihei, M. Owari, M. Kudo, and H. Kamada, papers presented at the 9th Int. Conf. on Atomic Spectroscopy/XXII Colloquium Spectroscopicum Internationale, Sept. 1981, Tokyo, Japan.
 88. S. M. Goldberg, R. J. Baird, S. Kono, N. F. T. Hall, and C. S. Fadley, *J. Elect. Spect.*, **21**, 1 (1980).
 89. M. Kudo, M. Owari, Y. Nihei, Y. Gohshi, H. Kamada, *Jap. J. Appl. Phys.*, **17**, Supp. 17-2, 275 (1978).

* Now appearing as:

80. K. A. Thompson and C. S. Fadley, *J. Elect. Spect.*, **33**, 29 (1984), and *Surf. Sci.*, **146**, 231 (1984).
 83. P. J. Orders and C. S. Fadley, *Phys. Rev.*, **B22**, 781 (1983); E. L. Bullock, C. S. Fadley, and P. J. Orders, *Phys. Rev.*, **B28**, 4867 (1983); M. Sagurton, E. L. Bullock, and C. S. Fadley, *Phys. Rev.*, **B30**, 7332 (1984).
 87. M. Owari et al., *J. Elect. Spect.*, **34**, 215 (1984).

90. Y. E. Madey, *Surf. Sci.*, **79**, 575 (1979) plus earlier references therein.
 91. J. Stohr, K. Baberschke, R. Jaeger, R. Treichler, and S. Brennan, *Phys. Rev. Lett.*, **47**, 381 (1981).
 92. L.-G. Petersson, S. Kono, N. F. T. Hall, S. Goldberg, J. T. Lloyd, and C. S. Fadley, *Mat. Sci. and Eng.*, **42**, 111 (1980).
 93. D. H. Rosenblatt, J. G. Tobin, M. G. Mason, R. F. Davis, S. D. Kevan, D. A. Shirley, C. H. Li, and S. Y. Tong, *Phys. Rev.*, **B 23**, 3823 (1981); D. A. Shirley, private communication.
 94. J. H. Onuferko and D. P. Woodruff, *Surf. Sci.*, **95**, 555 (1980) and references therein.
 95. B. J. Garrison, M. Winograd, and D. E. Harrison, *Phys. Rev.*, **B 18**, 6000 (1978); S. P. Holland, B. J. Garrison, and M. Winograd, *Phys. Rev. Lett.*, **43**, 220 (1979).
 96. T. S. Rahman, J. E. Black, and D. L. Mills, *Phys. Rev. Lett.*, **46**, 1469 (1981) and references therein.
 97. D. H. Rosenblatt, J. G. Tobin, M. G. Mason, R. F. Davis, S. D. Kevan, and D. A. Shirley, private communication.
 98. J. Stohr, R. Jaeger, and T. Kendelewicz, *Phys. Rev. Lett.*, **49**, 142 (1982) and references therein.
 99. N. F. T. Hall, Ph.D. Thesis, Univ. of Hawaii (1982); M. F. T. Hall and C. S. Fadley, to be published.
 100. P. J. Orders, C. S. Fadley, R. Trehan, B. Sinkovic, Z. Hussain, and J. Lecante, to be published.
 101. D. W. Jepsen, *Phys. Rev.*, **B 22**, 5701 (1980) and references therein.
 102. S. Kono, H. Sakurai, K. Higashiyama, and T. Sagawa, *Surf. Sci.*, to appear.
 103. D. P. Woodruff, D. Norman, B. W. Holland, N. V. Smith, H. H. Farrell, and M. M. Traum, *Phys. Rev. Lett.*, **41**, 1130 (1978); N. V. Smith, M. H. Farrell, M. M. Traum, D. P. Woodruff, D. Norman, M. S. Woolfson, and B. W. Holland, *Phys. Rev.*, **B 21**, 3119 (1980); H. H. Farrell, M. M. Traum, N. V. Smith, W. A. Royer, D. P. Woodruff, and P. D. Johnson, *Surf. Sci.*, **102**, 527 (1981); W. M. Kang et al., *Phys. Rev. Lett.*, **47**, 931 (1981).
 104. T. Matsuda, N. Nishijima, and M. Onchi, *Surf. Sci.*, **61**, 651 (1976); O. Aberdam, R. Baudouin, E. Blanc, and C. Gaubert, *Surf. Sci.*, **71**, 279 (1978).
 105. J. L. Beeby, *Surf. Sci.*, **80**, 55 (1979); S. Holloway, *Surf. Sci.*, **80**, 62 (1979); P. A. Maksym and J. L. Beeby, *Surf. Sci.*, **110**, 423 (1981).
 106. S. D. Kevan, R. F. Davis, D. H. Rosenblatt, J. G. Tobin, M. G. Mason, D. A. Shirley, C. H. Li, and S. Y. Tong, *Phys. Rev. Lett.*, **46**, 1629 (1981) and references therein; S. Y. Tong and J. C. Tang, *Phys. Rev.*, **B 25**, 6526 (1982).
 107. D. H. Rosenblatt, S. D. Kevan, J. G. Tobin, R. F. Davis, M. G. Mason, D. A. Shirley, J. C. Tang, and S. Y. Tong, *Phys. Rev.*, **B 26**, 3181 (1982).
 108. P. H. Citrin, P. Eisenberger, and R. C. Hewitt, *Phys. Rev. Lett.*, **41**, 309 (1978); **45**, 1948 (1980); S. Brennan, J. Stohr, and R. Jaeger, *Phys. Rev.*, **B 24**, 4871 (1981); and references therein.
 109. P. Eisenberger and L. C. Feldman, *Science*, **214**, 300 (1981).
 110. C. S. Fadley, *Far. Soc. Disc.*, **60**, 18 (1975); R. J. Baird, C. S. Fadley, and L. F. Wagner, *Phys. Rev. Lett.*, **37**, 111 (1976).
 111. F. R. McFeely, J. Stohr, G. Apai, P. S. Wehner, and D. A. Shirley, *Phys. Rev.*, **B 14**, 3273 (1976).
 112. L. F. Wagner, Z. Hussain, C. S. Fadley, and R. J. Baird, *Solid State Commun.*, **21**, 453 (1977); G. Apai, J. Stohr, R. S. Williams, S. P. Kowalczyk, and D. A. Shirley, *Phys. Rev.*, **B 15**, 584 (1977).

* Now appearing as:

100. B. Sinkovic et al., *Phys. Rev.*, **B30**, 1833 (1984); P. J. Orders et al., *Phys. Rev.*, **B30**, 1838 (1984).
 107. An additional reference for swept-energy studies is: J. J. Barton et al., *Phys. Rev. Lett.*, **51**, 272 (1983).

113. Z. Hussain, L. F. Wagner, and C. S. Fadley, unpublished ARXPS results for the valence bands of Pt.
114. N. Eriksson, Phys. Scr., **16**, 462 (1977).
115. R. H. Williams, P. C. Kemeny, and L. Ley, Solid State Commun., **19**, 495 (1976).
116. Z. Hussain, S. Kono, R. E. Connelly, and C. S. Fadley, Phys. Rev. Lett., **44**, 895 (1980); Z. Hussain, C. S. Fadley, S. Kono, and L. F. Wagner, Phys. Rev., **B 22**, 3750 (1980).
117. G. D. Mahan, Phys. Rev., **B 2**, 4334 (1970), and review in Electron and Ion Spectroscopy of Solids, L. Fiermans, J. Vennik, and W. Dekeyser, eds., Plenum Press, New York (1978).
118. C. Caroli, D. Lederer-Rozenblatt, B. Roulet, and D. Saint-James, Phys. Rev., **B 8**, 4552 (1973).
119. P. J. Feibelman and D. E. Eastman, Phys. Rev., **B 10**, 4932 (1974).
120. N. J. Shevchik, J. Phys., **C 10**, L555 (1977); Phys. Rev., **B 16**, 3428 (1977).
121. L.-G. Petersson, Z. Hussain, S. Kono, and C. S. Fadley, Solid State Commun., **34**, 549 (1980).
122. Z. Hussain, S. Kono, L.-G. Petersson, C. S. Fadley, and L. F. Wagner, Phys. Rev., **B 23**, 724 (1981).
123. L. F. Wagner, Z. Hussain, and C. S. Fadley, Solid State Commun., **21**, 257 (1977).
124. J. Stohr, P. S. Wehner, R. S. Williams, G. Apai, and D. A. Shirley, Phys. Rev., **B 17**, 587 (1978).
125. P. Thiry, D. Chandesri, J. Lecante, C. Guillot, R. Pinchaux, and Y. Petroff, Phys. Rev. Lett., **43**, 82 (1979).
126. T. C. Chiang, J. A. Knapp, M. Aono, and D. E. Eastman, Phys. Rev., **B 21**, 3513 (1980).
127. M. J. Sayers and F. R. McFeely, Phys. Rev., **B 17**, 3867 (1978).
128. G. Paasch, Phys. Status Solidi, **B 87**, 191 (1978).
129. Z. Hussain and C. S. Fadley, unpublished results of ARXPS direct-transition calculations for W with high angular resolution.
130. N. E. Christensen and B. Feuerbacher, Phys. Rev., **B 10**, 2349 (1974).
131. R. C. White, Z. Hussain, D. W. Shinn, and C. S. Fadley, unpublished experimental ARXPS valence data for W with $\pm 1.5^\circ$ resolution.